



Università degli studi di Ferrara

DOTTORATO DI RICERCA IN
“FISICA”

CICLO XXIII

COORDINATORE PROF. FILIPPO FRONTERA

**Small Scale CMB Anisotropies
with *Planck*: Constraints on
Primordial Magnetic Fields and
the Impact of
Foreground/Secondary
Anisotropy Residuals**

Settore Scientifico Disciplinare: FIS/05

Dottorando:

Dott. Paoletti Daniela

Tutore:

Dott. Mandolesi Nazzareno

Co-Tutori:

Dott. Aghanim Nabila

Dott. Finelli Fabio

Dott. Burigana Carlo

ANNI 2008/2010

*He called it freedom, that you can allow yourself...or not.
(from the motion picture "Velvet Goldmine")*

Contents

Introduction	1
1 Cosmology	5
1.1 The Big Bang theory	5
1.2 The cosmological principle	7
1.3 Background metric and equations	7
1.4 Dark Energy	9
1.5 Big Bang problems and inflation	10
2 Cosmological Perturbations	13
2.1 Cosmological perturbations	13
2.2 Synchronous gauge	16
2.3 Longitudinal gauge	16
2.4 Einstein-Boltzmann equations	17
2.4.1 Cold dark matter	20
2.4.2 Baryons	21
2.4.3 Massless neutrinos	21
2.4.4 Photons	22
2.5 Initial conditions for primordial perturbations	24
3 Cosmic Microwave Background Radiation	25
3.1 Introduction	25
3.2 CMB anisotropy statistical analysis	28
3.2.1 Temperature anisotropy angular power spectrum	28

3.2.2	Integration of the photon Boltzmann equation	32
3.2.3	Polarization anisotropy angular power spectra	34
3.3	The CAMB & CosmoMC codes	36
3.4	The <i>Planck</i> satellite	38
4	Primordial Magnetic Fields	43
4.1	Large scale magnetic fields	43
4.2	Primordial magnetic fields	46
4.2.1	Post inflationary generation mechanisms	47
4.2.2	Inflationary generation mechanisms	48
4.3	Magnetism in a cosmological contest	49
5	Stochastic Background of PMF Statistical Properties	53
5.1	Stochastic background of PMF	53
5.1.1	PMF statistical properties	54
5.2	PMF energy momentum tensor	56
5.2.1	PMF EMT spectrum integration technique	58
5.2.2	PMF EMT power spectrum general behavior and com- parison	61
5.2.3	Magnetic energy density	62
5.2.4	Lorentz force	65
5.2.5	Vector EMT spectrum	67
5.2.6	Tensor EMT spectrum	70
5.2.7	PMF EMT spectral fits	71
5.2.8	Cross correlation between energy density and Lorentz force	76
6	Magnetized Cosmological Perturbations	79
6.1	The scalar sector of magnetized cosmological perturbations . .	80
6.1.1	Magnetized metric perturbation equations	80
6.1.2	Fluid equations	81
6.1.3	Tight Coupling	82

6.1.4	Initial conditions	83
6.2	The vector sector of magnetized cosmological perturbations . .	91
6.2.1	Lorentz force	91
6.3	The tensor sector of magnetized cosmological perturbations . .	92
6.3.1	Initial conditions	93
6.4	Magnetized CMB anisotropies	94
6.4.1	Magnetized scalar CMB anisotropies	96
6.4.2	Magnetized vector CMB anisotropies	97
6.4.3	Magnetized tensor CMB anisotropies	99
6.4.4	Magnetized CMB anisotropy dependence on the mag- netic spectral index	99
6.4.5	Comparison of magnetized modes	104
6.5	Magnetized matter power spectrum	107
7	Cosmological Parameters in Presence of PMFs	109
7.1	Constraints with Current CMB data	110
7.2	Forecasts for <i>Planck</i>	116
7.3	Forecasts for CORE	119
7.4	CMB and large scale structure	125
8	Non Gaussianities	131
8.1	CMB temperature spectrum at large angular scales	132
8.2	CMB temperature bispectrum at large angular scales	135
8.3	Magnetic energy density bispectrum	136
8.3.1	Colinear configuration	142
8.3.2	Squeezed configuration	144
8.3.3	Equilateral configuration	147
8.4	The CMB magnetic bispectrum	149
8.5	PMF constraints with current NG data	152
8.5.1	Constraints from the bispectrum	153
8.5.2	Constraints from f_{NL}^{loc}	153

8.6	Preliminary study of the magnetized source term on intermediate scales	156
9	Foregrounds, Secondary Anisotropies and Their Residuals on Small Scales	159
9.1	Diffuse foregrounds	160
9.2	Small scale foregrounds	166
9.2.1	Poissonian contribution	169
9.2.2	Clustering contribution	170
9.3	Secondary anisotropies	172
9.3.1	Sunyaev Zeldovich effect	175
10	Multifrequency Approach to Small Scale Residual Marginalization	181
10.1	Basic concepts	181
10.2	Foreground and secondary anisotropy residuals parametrizations	184
10.2.1	Unresolved thermal Sunyaev Zeldovich effect	184
10.2.2	Unresolved point sources	186
10.3	CMB anistropies with foreground and secondary anisotropy residual contribution	197
10.4	Frequency channel combination	197
11	Cosmological Parameters with Small Scale Foreground and Secondary Anisotropy Residual Marginalization	205
11.1	Cosmological parameters with small scale foreground and secondary anisotropy residuals	207
11.2	Foreground and secondary anisotropy residual marginalization with extended parameter space	215
11.3	Frequency channel combination	220
	Conclusions	233

A	239
A.1 Lorentz force Fourier spectrum	239
A.2 Integrals of Bessel functions	240
A.3 Bispectrum in colinear configuration	241
A.3.1 Integration Domains	243
A.3.2 Domains of I_a	243
A.3.3 Domains of I_b	244
A.3.4 $n=2$	244
A.3.5 $n=-2$	245
Bibliography	247

Introduction

Since its discovery in 1964 the Cosmic Microwave Background (CMB) radiation has been a very good source of information on the primordial and present universe. Its almost perfect black body spectrum, measured by the FIRAS instrument on the COBE satellite [1], proves the equilibrium between matter and radiation in the early epochs, whereas the temperature anisotropies, measured by the DMR instrument of COBE [2, 3] and later by the Boomerang experiment [4, 5], are the footprints of primordial cosmological perturbations which generated the large scale structures we observe nowadays. In particular CMB temperature and polarization anisotropies are a fundamental tool to test and investigate cosmological models. Anisotropies on large angular scales are fundamental to study universe isotropy and possible anomalies, for example the ones observed in WMAP7 data [8], while small scale CMB anisotropies represent a fundamental test for the standard cosmological model and its extensions.

A possible extension of the standard cosmological model is represented by the model which includes the contribution of primordial magnetic fields. Primordial magnetic fields may have left an imprint on CMB anisotropies and therefore CMB data represent the best observational tool to investigate their properties. We will present a study of the impact of a stochastic background of primordial magnetic fields on CMB anisotropies in temperature and polarization. We will investigate their impact on both CMB anisotropy angular power spectrum and also on the CMB bispectrum induced by magnetic non-Gaussianities. We will show the derivation of the constraints on primordial

magnetic fields characteristics using current CMB data and the forecasted constraints for present and future CMB missions.

Small scale CMB anisotropies have a great importance in cosmology and are one of the current frontiers in CMB observations. It is therefore necessary to have data as reliable as possible on these scales. Many experiments have been dedicated to the observations of small scale anisotropies, the *Planck* satellite [6] will cover all the scales up to $\ell \sim 2500$ but there are also ground based or ballon experiments targeting small patches with higher angular resolution, such as: ACBAR [11], CBI [12], QUaD [13], BICEP [14], SPT [15], ACT [16]. At these scales, the Silk damping suppresses the primordial contribution with respect to astrophysical contamination and secondary emission. We will review the main foreground and secondary anisotropy residual contaminants on small scales. We will show the technique we developed to marginalize over such residuals in the perspective of the *Planck* mission.

The work is organized as follows.

- In the first three chapters we will review some basic concepts of cosmology and in particular of the Big Bang theory and the main milestones of observational cosmology. We will review cosmological perturbation evolution in the standard cosmological model and the major aspects of CMB anisotropy analysis. We will introduce a brief overview of the *Planck* mission.
- In the fourth chapter we will approach and introduce the problematic of primordial magnetic fields. In particular we will discuss the observational and theoretical evidences which support the hypothesis of the existence of primordial magnetic fields. We will also review the characteristics of magnetohydrodynamics in a cosmological context.
- In the fifth chapter we will investigate the statistical properties of a stochastic background of primordial magnetic fields. In particular we

will present the study of the Fourier transform of the energy momentum tensor of primordial magnetic fields and the exact results we obtained for its spectra.

- In the sixth chapter we will investigate magnetic cosmological perturbations. We will show the theoretical treatment for the evolution of magnetized perturbations for all types of magnetic perturbations: scalar, vector and tensor. We will show the results for all types of CMB anisotropies induced by primordial magnetic fields that we have obtained with the extension we developed of the Einstein-Boltzmann code CAMB.
- In the seventh chapter we will show the results we obtained with the extension of the Markov chain MonteCarlo public code CosmoMC for the cosmological parameters space exploration we have developed. We will present the constraints we obtained with current cosmological data and the forecasts for present and future CMB missions.
- In the eighth chapter we will investigate the non-Gaussianities induced by a stochastic background of primordial magnetic fields. We will present the derivation of the magnetic CMB bispectrum induced by magnetic scalar perturbations on large scales. We will also show the constraints we have derived on primordial magnetic field characteristics with current non-Gaussianity data by WMAP.
- In the ninth chapter we will review the main foreground contamination to CMB data. We will briefly review the contribution of foregrounds and secondary anisotropies. In particular we will focus on small scales, where the main contaminants are point sources and galaxy clusters. We are interested in the contribution of residuals of small scale foregrounds and secondary anisotropies, which are given by the contribution of unresolved point sources and clusters.
- In the tenth chapter we will present the multifrequency approach to

small scale foreground and secondary anisotropy residuals that we developed for the *Planck* data. We will show how we parametrized each foreground and secondary anisotropy residual signal with an empirical-theoretical-data based approach. We will show how our parametrizations reproduce the expected signal of residuals on small scales. Since we are interested in using single frequency channel combinations we will also address the subject of frequency channel combination. In the context of our multifrequency approach we adopted two different techniques of combination and compared their results. First we will show the standard inverse noise variance weighting technique and then the alternative empirical combination method we have developed for our project.

- In the eleventh chapter we will present the results obtained with an original implementation of the public Markov Chain MonteCarlo code CosmoMC. The implementation considers the marginalization over foreground and secondary anisotropy residuals. We will show the impact of the foreground uncertainties on cosmological parameters and the comparison of different approaches to the combination of different frequency channels.

In great part of the thesis we will use units where the speed of light and the Planck constant are equal 1: $c = 1$ and $\hbar = 1$.

Chapter 1

Cosmology

The goal of cosmology is the understanding of the composition and characteristics of the universe and the investigation of its origin and evolution through theoretical analysis and observations. In particular recent years have seen the blossoming of observational cosmology, driven by the great improvement of instrumental techniques, and the opening of the so-called era of precision cosmology. Three of the fundamental milestones of observational cosmology coincided with the three proofs in support of the Big Bang theory: the discovery of the expansion of the universe, the measurements of primordial element abundances and the discovery of the cosmic microwave background radiation.

1.1 The Big Bang theory

One of the milestones of observational cosmology has been the discovery that the universe is expanding. In the 1920s Lemaitre independently derived the form of the Einstein equations of general relativity for an homogeneous and isotropic universe (already derived by Friedmann) and noticed that these equations predicted an expanding and cooling phase in the universe evolution [20].

Already in 1912 it was observed a sistematic redshift in the spectra of non-

local galaxies by Slipher [17], but at the time the knowledge on galaxies was still too poor to allow a cosmological interpretation of this effect. It was only in 1929 that Hubble and collaborators associated this redshift with a general recession of galaxies one from the others, confirming what had been predicted by Lemaitre few years earlier. In particular, galaxy recession velocities follow the Hubble law, which states that the velocity is directly proportional to the galaxy distance $v = Hd$, where H is the Hubble parameter and varies with time [19]. Lemaitre noticed that since the universe is expanding and cooling, in the past it should have had higher temperature and density. In particular, going back in time at a certain point everything collapses in a point with infinite density and temperature. This was the basic concept of the Big Bang theory. The theory was formalized in 1946 by Gamow and Alpher who introduced also the mechanism of primordial elements creation: the Big Bang nucleosynthesis [21].

The Big Bang theory states that the universe was born from an initial hot and dense state, where the cosmological models based on general relativity and standard theoretical physics are still unable to describe the initial instant without a singularity $\rho \rightarrow \infty$ and $T \rightarrow \infty$ (the so-called “initial singularity problem”). After this initial state the universe started to expand and cool up to its present status, undergoing a series of phase transitions in the early phases of its evolution. In the primordial epochs of very high temperature and density, took place the creation of primordial light elements (the lack of stable nuclei with atomic number 5 allows the primordial generation of only hydrogen, helium and lithium). The introduction of the theory of Big Bang nucleosynthesis has been an incredible improvement in cosmology, in fact, at the time when the Big Bang theory was formulated stellar physics studies still had not discover the nuclear reactions in the stellar interiors, and therefore, there was not an explanation to the generation of elements. The local and non-local element abundances are measured with spectroscopic observations of Sun and planets, with meteors, and with cosmic ray abundances, galaxy spectral observations and other techniques. The observed abundances are in

perfect agreement with the ones predicted by the nucleosynthesis: 75% hydrogen, 23% helium and 2% metals, and their measurements were considered the most important proof in support of the Big Bang theory until 1964 when the Cosmic Microwave Background (CMB) radiation was discovered.

The CMB is an homogeneous and isotropic relic radiation predicted by the Big Bang theory. It represents a picture of the primordial universe at the time when the temperature was low enough to allow the recombination of atoms and the primordial plasma became optically thin. The CMB was first observed in 1964 by chance as an isotropic signal in the microwaves, diffuse in the sky with a temperature of few K. The NASA satellite COBE later discovered anisotropies in the CMB of the order of $\Delta T/T \sim 10^{-5}$ level on an angular scale of 7 degrees [2]. These anisotropies are the picture of the primordial perturbations that have seeded the cosmic structures.

1.2 The cosmological principle

At the base of the standard cosmological model there is the cosmological principle. It is an assumption and states the homogeneity and isotropy of the universe at each fixed time:

The universe spacetime is foliate in hypersurfaces of constant time. These spatial hypersurfaces are homogeneous spaces.

This principle has received several supports from cosmological observations. In particular, large scale structure observations seem to confirm an isotropic distribution of structures at cosmological scales. Another very strong support to the cosmological principle comes from CMB observations, which have confirmed the great degree of isotropy of the primordial universe.

1.3 Background metric and equations

Assuming the cosmological principle, the universe evolution is described by the general relativity theory applied to an homogeneous and isotropic

spacetime. In an expanding universe it is useful to define a comoving dimensionless distance r so that the real distance between two points is given by $d = a(\tau)r$, where τ is the conformal or comoving time related with the cosmic one by: $dt = a(\tau)d\tau$. The function $a(\tau)$ is the scale factor and it incorporates the evolution of the expansion. The metric which describes an homogeneous and isotropic universe is given by the Friedmann-Lemaitre-Robertson-Walker (FLRW) metric, whose line element is:

$$ds^2 = -a^2(\tau)d\tau^2 + a^2(\tau)\left(\frac{dr^2}{1 - Kr^2} + r^2(d\theta^2 + \sin^2\theta d\varphi^2)\right), \quad (1.1)$$

where r, θ, φ are spherical comoving coordinates. The spatial parameter K represents the geometry of the spatial hypersurface. To each value of K , $-1, 0, 1$, is associated a different geometry:

$K = 1 \rightarrow$ Close spacetime \rightarrow Hyperspheric geometry ,

$K = 0 \rightarrow$ Flat spacetime \rightarrow Euclidean geometry ,

$K = -1 \rightarrow$ Open spacetime \rightarrow Hyperbolic geometry .

The Hubble parameter describes the expansion rate and is defined as $H(t) = da(t)/dt$, or in conformal time as: $\mathcal{H}(\tau) = \dot{a}/a$, where the dot denotes the derivative with respect to conformal time. The best independent estimate of the Hubble parameter present value comes from the Hubble space telescope Key project and is: $H_0 = 70.6 \pm 3.1 \text{ Km sec}^{-1} \text{ Mpc}^{-1}$ [22].

The matter and radiation content of the universe is called the cosmological fluid; in the standard model it is composed by: photons, neutrinos, baryons and dark matter. The evolution of universe metric and expansion is described by the Einstein equations with FLRW metric:

$$\left(\frac{\dot{a}}{a}\right)^2 = \frac{8\pi G}{3}a^2\rho - c^2K, \quad (1.2)$$

$$\frac{d}{d\tau}\left(\frac{\dot{a}}{a}\right) = -\frac{4\pi G}{3}(\rho + 3P)a^2. \quad (1.3)$$

We note how the evolution of the scale factor is determined by the cosmological fluid properties such as its total energy and pressure densities. The

energy and pressure densities can be related with the equation of state:

$$P = w\rho. \quad (1.4)$$

The evolution of energy density for a perfect fluid is described by:

$$\dot{\rho}_n = -3H(t)(\rho_n + P_n), \quad (1.5)$$

where the subscript n stands for: photons (γ), neutrinos (ν), baryons (b) and dark matter (c). According to Eq. 1.5 the single fluid components evolve as: $\rho_{\gamma,\nu} \propto a^{-4}$ for radiation, $w = 1/3$, and $\rho_{b,c} \propto a^{-3}$ for pressurless matter, $w = 0$. We can define a critical density which is associated with a flat universe, setting $K = 0$ in the first of Eqs. 1.3 we have: $\rho_c = \frac{3H_0^2}{8\pi G}$. In particular, we can define also a density parameter relative to the critical density: $\Omega_0 = \rho/\rho_c$ for total density and $\Omega_n = \rho_n/\rho_c$ for the single species one. The total density parameter is related with the geometry through:

$$\begin{aligned} \Omega_0 > 1 &\rightarrow K = 1, \\ \Omega_0 = 1 &\rightarrow K = 0, \\ \Omega_0 < 1 &\rightarrow K = -1, . \end{aligned}$$

The current measurements of the density parameter are in agreement with an almost perfectly flat and critical universe, $\Omega_0 \simeq 1$.

1.4 Dark Energy

In Eqs. 1.3 we note that a universe composed only by ordinary matter would be in a decelerated expansion, $\ddot{a} < 0$. But cosmological observations point towards the opposite scenario: a universe in a stage of accelerated expansion. In particular, supernovae Ia are considered standard candles, because their luminosity curve is well known and almost independent on their distance or intrinsic parameters, therefore, they are very good distance indicators. The interpretation of supernova Ia data shows that at late times, around $z \sim 0.3$, the universe expansion accelerates [23, 24]. We note from

Eqs. 1.3 that to have an accelerated expansion it is necessary the presence of an extra component in the cosmological fluid which contributes with negative pressure, and in particular with $w < -1/3$. But supernovae Ia are not the only data to suggest the presence of an extra component in the cosmological fluid; large scale structure data show that the abundances of baryonic, Ω_b , and dark matter, Ω_c , allow a maximum value for the matter density of $\Omega_m = \Omega_b + \Omega_c \simeq 0.3$. Therefore, it is necessary to add an extra component to fill the 70% of missing density in the universe. The first hypothesis for the extra, non-ordinary, component came from the requirement of a static solution of Einstein equations. A cosmological constant, $\rho_\lambda = \Lambda/8\pi G = -P_\lambda$, enters in the Einstein equations as:

$$\begin{aligned} \left(\frac{\dot{a}}{a}\right)^2 &= \frac{8\pi G}{3}a^2\rho - c^2K + \frac{\Lambda}{3}, \\ \frac{d}{d\tau}\left(\frac{\dot{a}}{a}\right) &= -\frac{4\pi G}{3}(\rho_{tot} + 3P_{tot})a^2, \end{aligned} \quad (1.6)$$

where $\rho_{tot} = \rho_b + \rho_c + \rho_\gamma + \rho_\nu + \rho_\Lambda$. The cosmological constant is characterized by a time independent energy density and therefore its contribution is completely subdominant at early times, whereas it starts to dominate the cosmological fluid in recent epochs, driving the acceleration of the universe. Since the value of the cosmological constant required by observations is at odd with theoretical predictions [25], modern cosmology refers to dark energy as the broad class of models which aim to explain the recent acceleration of the universe. Such models include quintessence (scalar fields models) and theories beyond Einstein gravity (for a couple of reviews see [26, 27]).

1.5 Big Bang problems and inflation

The Big Bang model collected a great success, but the original model presents some problems. In particular we refer to three main ones: the cosmological horizon problem, the flatness problem and the magnetic monopole problem.

The horizon problem is related to the fact that every Big Bang model possesses a cosmological horizon. The cosmological horizon delimits the regions which are in causal connection one with the others. Its radius at the cosmic time τ is defined by:

$$r_H(t) = a(t) \int_0^t \frac{dt}{a(t)}. \quad (1.7)$$

The CMB great degree of isotropy implies that the emission region should have been in causal connection and therefore inside the cosmological horizon. In the original Big Bang model this is not true. The CMB ideal emission region is about a factor ten bigger than the horizon at the corresponding time, therefore in the original model it is not possible to explain the CMB isotropy.

The flatness problem is related to the fact that although cosmological data are in agreement with a flat universe, $\Omega_0 = 1$, this model is the least probable from a statical point of view. It requires a fine tuning on the density parameter that has to be equal one not only at present time but at all times, in particular, it should have been equal one with a precision level of 10^{-60} in primordial epochs.

The magnetic monopole problem is related with the Grand Unification Theory (GUT) which predicts the creation of monodimensional relic defects at the GUT phase transition, occurred at $t = 10^{-35}$ sec: the magnetic monopoles. The magnetic monopoles are very massive particles, $m_M \sim 10^{16}$ GeV, and according to their predicted abundance they should be the dominant component of the cosmological fluid with a density parameter Ω_M of the order of 10^{16} . The measurements of the total density of the universe together with the lack of a positive detection of these particles indicates that magnetic monopoles have indeed a very low density.

The solution to these three problems came with the development by Guth [29] and Starobinski [30] in 1980 of the theory of inflation.

Inflation is a phase which takes place just after the GUT phase transition, where the universe expands exponentially:

$$a(t) \propto e^{\int H(t') dt'} , \quad (1.8)$$

where the Hubble parameter is nearly constant. During inflation the horizon grows more slowly than the scale factor, therefore, regions that were in causal connection before this period are pushed outside the Hubble radius ($r_{Hubble} = 1/H$). This solves the problem of the cosmological horizon. In fact, the high degree of isotropy of the CMB is justified by the fact that the emission region was in causal connection before inflation. The solution to the flatness problem is given by the fact that the density parameter evolves as:

$$\Omega - 1 = K/(aH)^2 . \quad (1.9)$$

Since the scale factor grows exponentially during inflation, the density parameter becomes unitary whatever was its initial value. Last, the magnetic monopoles are created before inflation and therefore their density is diluted by the exponential expansion up to a point where their contribution to the cosmological fluid is irrelevant and it is extremely improbable to observe them.

Several models of inflation have been proposed since the first formulation of the theory for a review we refer the reader to [31].

Chapter 2

Cosmological Perturbations

The inflation theory was originally formulated to solve the problems of the original Big Bang theory, but it was soon realized that it can explain also the generation of primordial perturbations [32, 33, 34]. Primordial perturbations are the seeds which evolve forming the large scale structure we observe in the universe. It is crucial to investigate their initial conditions and their evolution to interpret cosmological data. In this chapter we will present a brief summary of the main aspects of linear primordial perturbations treatment. The notation and guide lines follow [66].

2.1 Cosmological perturbations

The evolution of cosmological perturbations is described by linear fluctuations in general relativity. The equations which describe the metric evolution are the Einstein equations:

$$G_{\mu\nu} = 8\pi GT_{\mu\nu}, \quad (2.1)$$

where $G_{\mu\nu}$ is the Einstein tensor is defined by

$$G_{\mu\nu} = R_{\mu\nu} - \frac{1}{2}g_{\mu\nu}R. \quad (2.2)$$

Both the scalar R , the Ricci scalar, and the tensor $R_{\mu\nu}$ derive from contraction of the Riemann tensor:

$$R_{\beta\mu\nu}^{\alpha} = -\Gamma_{\beta\mu,\nu}^{\alpha} + \Gamma_{\beta\nu,\mu}^{\alpha} + \Gamma_{\beta\nu}^{\sigma}\Gamma_{\sigma\mu}^{\alpha} + \Gamma_{\beta\mu}^{\sigma}\Gamma_{\sigma\nu}^{\alpha}, \quad (2.3)$$

where $\Gamma_{\mu\nu}^{\alpha}$ are the Levi-Civita connection coefficients:

$$\Gamma_{\mu\nu}^{\alpha} = \frac{1}{2}g^{\alpha\lambda}(g_{\lambda\nu,\mu} + g_{\mu\lambda,\nu} - g_{\mu\nu,\lambda}). \quad (2.4)$$

In the right hand side of Einstein equations as source term there is the energy-momentum tensor of the fluid, to which is possible to add the contribution of the cosmological constant inserting a term $\Lambda g_{\mu\nu}$. The energy momentum tensor for a perfect fluid is:

$$T_{\mu\nu} = P g_{\mu\nu} + (\rho + P)U_{\mu}U_{\nu}, \quad (2.5)$$

where U_{μ} is the four-velocity of the fluid. The Einstein equations govern the evolution of the metric perturbations, whereas fluid perturbation evolution is described by the conservation equations:

$$T_{\nu;\mu}^{\mu} = 0, \quad (2.6)$$

where ; denotes the covariant derivative.

We can identify three types of primordial perturbations which represent the three possible spatial projections: scalar, vector and tensor perturbations. We can write the perturbed line element as:

$$ds^2 = a(\tau)^2(-(1 - h_{00})d\tau^2 + 2h_{0i}dx^i d\tau + (\delta_{ij} + h_{ij})dx^i dx^j). \quad (2.7)$$

The spatial metric perturbation h_{ij} can be decomposed into its trace h_{ii} and a traceless part h_{ij} that can be decomposed in the sum of three terms: h_{ij}^{\parallel} , h_{ij}^{\perp} , h_{ij}^T with a total metric perturbation $h_{ij} = h\delta_{ij}/3 + h_{ij}^{\parallel} + h_{ij}^{\perp} + h_{ij}^T$. The components of the traceless part have to satisfy :

$$\begin{aligned} \epsilon_{ijk}\partial_i\partial_j h_{ij}^{\parallel} &= 0, \\ \partial_i\partial_j h_{ij}^{\perp} &= 0, \\ \partial_i h_{ij}^T &= 0, \end{aligned} \quad (2.8)$$

where ϵ_{ijk} is the totally antisymmetric tensor. The orthogonal part, h_{ij}^\perp , can be written as function of a divergenceless vector h_i^V , while the parallel one, h_{ij}^\parallel , as function of a scalar field μ :

$$\begin{aligned} h_{ij}^\parallel &= (\partial_i \partial_j - \frac{\delta_{ij}}{3} \nabla^2) \mu, \\ h_{ij}^\perp &= \partial_i h_j^V + \partial_j h_i^V. \end{aligned} \quad (2.9)$$

Scalar perturbations are described by the two scalar potentials h and μ , the vector ones by the divergenceless vector h_i^V while tensor metric perturbations are described by the tensor h_{ij}^T .

General relativity is invariant under diffeomorphism, i.e. two solutions of the Einstein equations are equivalent if diffeomorphic to each other * [35]. This invariance is at the origin of gauge freedom in general relativity, and the evolution of linear perturbations can depend on the gauge choice although results of different gauges can be compared. It is possible to describe linear perturbations also with a gauge-invariant formalism developed by Bardeen [36]. The gauge choice can be seen as the choice of the connection between the unperturbed FLRW background and the perturbations. Among the possible gauge choices, the synchronous and the longitudinal gauges are the most used ones in connection with structure formation.

It is more convenient to describe cosmological perturbation evolution in the Fourier space instead of the real one, therefore, if not otherwise required, we will work in the Fourier space.

*Two differentiable varieties are diffeomorphic to each other if it is possible to create a diffeomorphism between them. A diffeomorphism is a function between two differentiable varieties with three properties: it is differentiable, invertible and its inverse function is differentiable

2.2 Synchronous gauge

In the synchronous gauge the perturbed metric line element is defined as:

$$ds^2 = a(\tau)^2(-d\tau^2 + (h_{ij} + \delta_{ij})dx^i dx^j). \quad (2.10)$$

The scalar metric perturbation in the Fourier space is described by two scalar potentials h and η :

$$h_{ij} = \int d^3k e^{i\vec{k}\cdot\vec{x}} \left(\hat{k}_i \hat{k}_j h(k, \tau) + \left(\hat{k}_i \hat{k}_j - \frac{1}{3} \delta_{ij} \right) 6\eta(k, \tau) \right), \quad (2.11)$$

where h is the trace of h_{ij} . The synchronous gauge is the gauge where the Einstein and fluid equations have the simplest form and this is the reason why it is widely used, especially for Einstein-Boltzmann codes, but the synchronous gauge has two intrinsic issues. The first is represented by coordinate singularities that may appear with this gauge choice. Synchronous gauge coordinates are referred to free fall observers and if the trajectories of two observers intersect each other, the same space-time position would have two different coordinate labels. However it is possible to avoid these singularities with a different choice of the initial hypersurface of constant time. The second issue is represented by two unfixed degrees of freedom generated by the fact that in the synchronous gauge the choice of the initial hypersurface of constant time and the choice of its coordinates are arbitrarily. These two unfixed degrees of freedom originate two unphysical, gauge, modes in the solutions. It is possible to show that fixing the reference system to the rest frame of cold dark matter the two gauge mode contributions disappear. For this reason in our analysis we will always work in the cold dark matter rest frame.

2.3 Longitudinal gauge

The longitudinal gauge perturbed line element (within the convention of [66]) for the scalar sector is:

$$ds^2 = a^2(\tau)(-(1 + 2\psi)d\tau^2 + (1 - 2\phi)dx^i dx_i), \quad (2.12)$$

where ϕ and ψ are scalar potentials. The potential ψ in this gauge plays the role of the Newtonian potential. The perturbed metric tensor is diagonal and this leads to a very simple form for perturbation equations. Newtonian gauge completely fixes the gauge freedom avoiding the issues of synchronous gauge but has an important limit: it requires extensions to describe vector and tensor perturbations. These extensions are rather complex and since in our analysis we will describe all types of perturbations (scalar, vector and tensor) and we will use the Einstein-Boltzmann code CAMB[†] for the results, we chose to use the synchronous gauge for great part of the work. Anyway longitudinal and synchronous gauges are connected to each other by gauge transformations:

$$\begin{aligned}
\psi(\vec{k}, \tau) &= \frac{1}{2k^2} \left[\ddot{h}(\vec{k}, \tau) + 6\ddot{\eta}(\vec{k}, \tau) + \mathcal{H}(\dot{h}(\vec{k}, \tau) + 6\dot{\eta}(\vec{k}, \tau)) \right], \\
\phi(\vec{k}, \tau) &= \eta(\vec{k}, \tau) - \frac{1}{2k^2} \mathcal{H}(\dot{h}(\vec{k}, \tau) + 6\dot{\eta}(\vec{k}, \tau)) \\
\delta^S &= \delta^L - \epsilon \frac{\dot{\rho}}{\rho}, \\
\theta^S &= \theta^L - \epsilon k^2, \\
\delta P^S &= \delta P^L - \epsilon P, \\
\sigma^S &= \sigma^L,
\end{aligned} \tag{2.13}$$

where $\epsilon = \frac{\dot{h} + 6\dot{\eta}}{2k^2}$ is the time translation existing between the two gauges.

2.4 Einstein-Boltzmann equations

The perturbation evolution is described by the coupled system of perturbed Einstein and fluid (or Boltzmann) equations. The perturbed Einstein equations are:

$$\delta G_\nu^\mu = 8\pi G \delta T_\nu^\mu. \tag{2.14}$$

[†]Which uses synchronous gauge to describe perturbation evolution.

The perfect fluid energy momentum tensor Eq. 2.5 perturbed components are:

$$\begin{aligned}\delta T_0^0 &= -\delta\rho, \\ \delta T_y^0 &= (\rho + P)v_y, \\ \delta T_j^y &= \delta P\delta_j^y + \Sigma_j^y,\end{aligned}\tag{2.15}$$

where $\Sigma_j^y = T_j^y - \delta_j^y T_k^k/3$ is the traceless part of the space-space perturbed tensor component and ρ and P are the comoving energy density and pressure. Instead of Σ_j^y and v_y we will use the notation of [66] with $\sigma = -(\hat{k}^y \cdot \hat{k}_j - \delta_j^y/3)\Sigma_j^y/(\rho + P)$ and $\theta = ik_y v^y$. In the synchronous gauge the perturbed Einstein equations become:

$$\begin{aligned}k^2\eta - \frac{1}{2}\mathcal{H}\dot{\eta} &= -4\pi G a^2 \Sigma_n \rho_n \delta_n^S, \\ k^2\dot{\eta} &= 4\pi G a^2 \Sigma_n (\rho_n + P_n) \theta_n^S, \\ \ddot{\eta} + 2\mathcal{H}\dot{\eta} - 2k^2\eta &= -8\pi G a^2 \Sigma_n 3w_n \delta_n^S, \\ \ddot{h} + 6\dot{\eta} + 2\mathcal{H}(\dot{h} + 6\dot{\eta}) - 2k^2\eta &= -24\pi G a^2 \Sigma_n (\rho_n + P_n) \sigma_n.\end{aligned}\tag{2.16}$$

In the longitudinal gauge they become:

$$\begin{aligned}k^2\phi + 3\mathcal{H}(\dot{\phi} + \mathcal{H}\psi) &= 4\pi G a^2 \Sigma_n \rho_n \delta_n^L, \\ k^2(\dot{\phi} + \mathcal{H}\psi) &= 4\pi G a^2 \Sigma_n (\rho_n + P_n) \theta_n^L, \\ \ddot{\phi} + \mathcal{H}(2\dot{\phi} + \dot{\psi}) + \left(2\frac{\ddot{a}}{a} - \frac{\dot{a}^2}{a^2}\right)\psi + \frac{k^2}{3}(\phi - \psi) &= \frac{4\pi}{3} G a^2 \Sigma_n 2w_n \delta_n^L, \\ k^2(\phi - \psi) &= 12\pi G a^2 \Sigma_n (\rho_n + P_n) \sigma_n,\end{aligned}\tag{2.17}$$

where the index n runs over the different components of the fluid: (b) for baryons, (c) for dark matter, (ν) for neutrinos and (γ) for photons. Note that the anisotropic stress is gauge invariant. To derive the fluid equations we have to consider each component of the fluid separately in order to use its specific properties. But before doing that, we will review the general equations for matter and radiation.

The matter component of the fluid is composed by cold dark matter and baryons. In particular the former can be considered collisionless whereas the

latter is fully collisional because baryons interact with photons with Compton scattering prior to the decoupling, in what is called the tight coupling regime. The matter perturbations are in general described by the perturbed conservation equations:

$$\delta T_{;\mu}^{\mu\nu} = \partial_\mu \delta T^{\mu\nu} + \delta \Gamma_{\mu\alpha}^\nu T^{\mu\alpha} + \delta \Gamma_{\beta\alpha}^\alpha T^{\beta\nu} + \Gamma_{\mu\alpha}^\nu \delta T^{\mu\alpha} + \Gamma_{\beta\alpha}^\alpha \delta T^{\beta\nu} = 0. \quad (2.18)$$

In the synchronous gauge these are:

$$\dot{\delta}_n = -(1 + w_n) \left(\theta_n + \frac{\dot{h}}{2} \right) - 3\mathcal{H} \delta P_n - 3\mathcal{H} w_n \delta_n, \quad (2.19)$$

$$\dot{\theta}_n = -\mathcal{H}(1 - 3w_n) \theta_n - \frac{\dot{w}_n}{w_n + 1} \theta_n + \frac{\delta P_n / \rho_n}{1 + w_n} k^2 - k^2 \sigma_n, \quad (2.20)$$

whereas in the longitudinal they become

$$\dot{\delta}_n = -(1 + w_n) (\theta_n - 3\dot{\phi}) - 3\mathcal{H} \delta P_n - 3\mathcal{H} w_n \delta_n, \quad (2.21)$$

$$\dot{\theta}_n = -\mathcal{H}(1 - 3w_n) \theta_n - \frac{\dot{w}_n}{w_n + 1} \theta_n + \frac{\delta P_n / \rho_n}{1 + w_n} k^2 - k^2 \sigma_n + k^2 \psi. \quad (2.22)$$

For radiation as photons and massless (or nearly massless) neutrinos the perfect fluid description is not sufficient. It is instead necessary to evolve the full phase-space distribution function with the Boltzmann equation:

$$\frac{Df}{D\tau} = \frac{\partial f}{\partial \tau} + \frac{dx^i}{d\tau} \frac{\partial f}{\partial x^i} + \frac{dq}{d\tau} \frac{\partial f}{\partial q} + \frac{dn_i}{d\tau} \frac{\partial f}{\partial n_i} = \left(\frac{\partial f}{\partial \tau} \right)_c; \quad (2.23)$$

where f is the phase-space distribution function and the right hand side is the collisional term, which collects all the possible interactions of the particles. The number of particles in a differential volume of the phase-space is defined with the distribution function:

$$f(x_i, P_i, \tau) dP_1 dP_2 dP_3 dx_1 dx_2 dx_3 = dN. \quad (2.24)$$

The zeroth-order solution of the Boltzmann equation is the Bose-Einstein distribution for bosons (assuming the minus sign) and the Fermi-Dirac for fermions (assuming the plus sign):

$$f_0(\epsilon) = g_s \frac{1}{e^{\epsilon/k_B T_0} \pm 1}, \quad (2.25)$$

where k_B is the Boltzmann constant, T_0 is the temperature of the particles today, ϵ is the energy and g_s is the number of spin degrees of freedom. The energy momentum tensor for photons and neutrinos can be written as the integral in the momenta of the distribution function:

$$T_{\mu\nu} = \int dP_1 dP_2 dP_3 (-g)^{-1/2} \frac{P^\mu P^\nu}{P^0} f(x_i, P_i, \tau), \quad (2.26)$$

where g is the metric determinant given by $(-g)^{-1/2} = a^{-4}(1 - \frac{1}{2}h)$ for the synchronous gauge and $(-g)^{-1/2} = a^{-4}(1 - \Psi + 3\phi)$ for the longitudinal one. It is convenient to use the variable q_i instead of the conjugate momenta P_i ; q_i is related with the proper momentum through $q_i = ap_i$. The perturbed distribution function can be written as the sum of two parts, its zeroth-order and a small perturbation:

$$f(x_i, q, n_i, \tau) = f_0(q)(1 + \Upsilon(x_i, q, n_i, \tau)). \quad (2.27)$$

Here q_i has been separated into its modulus and its direction n_i , then $q_i = qn_i$. With this decomposition the components of the energy momentum tensor of Eq. 2.26 can be written as:

$$\begin{aligned} T_0^0 &= -a^{-4} \int q^2 dq d\Omega \sqrt{q^2 + m^2 a^2} f_0(q)(1 + \Upsilon), \\ T_i^0 &= -a^{-4} \int q^2 dq d\Omega q n_i f_0(q) \Upsilon, \\ T_j^i &= -a^{-4} \int q^2 dq d\Omega \frac{q^2 n_i n_j}{\sqrt{q^2 + m^2 a^2}} f_0(q)(1 + \Upsilon), \end{aligned} \quad (2.28)$$

where we used $dP_1 dP_2 dP_3 = (1 + \frac{1}{2}h)q^2 dq d\Omega$ and $dP_1 dP_2 dP_3 = (1 - 3\phi)q^2 dq d\Omega$; $d\Omega$ is the solid angle associated with the direction n_i . To describe radiation perturbation evolution, the Boltzmann equation is decomposed into a hierarchy named the Boltzmann hierarchy. We will now go into the details of each component of the fluid.

2.4.1 Cold dark matter

Cold dark matter is modelled as a collisionless fluid therefore in Eqs. 2.19, 2.20 and 2.21, 2.22 the sound speed and pressure, w , are zero. The

dark matter equations in the synchronous gauge are:

$$\begin{aligned}\dot{\delta}_c &= -\frac{\dot{h}}{2}, \\ \theta_c &= 0,\end{aligned}\tag{2.29}$$

while in the longitudinal gauge we have:

$$\begin{aligned}\dot{\delta}_c &= -\theta_c + 3\dot{\phi}, \\ \dot{\theta}_c &= -\mathcal{H}\theta_c + k^2\Psi.\end{aligned}\tag{2.30}$$

where in the synchronous gauge we choose the rest frame of CDM to avoid the gauge freedom issue.

2.4.2 Baryons

Baryons can be treated as a non relativistic collisional fluid. It is possible to neglect all the pressure contributions except for $k^2 c_s^2 \delta_b / (1 + w)$ in the velocity equation. This term becomes important on small scales and represents the acoustic oscillations. The baryon equations are:

$$\begin{aligned}\dot{\delta}_b &= -\theta_b - \frac{1}{2}\dot{h}, \\ \dot{\theta}_b &= -\mathcal{H}\theta_b + c_s^2 k^2 \delta_b,\end{aligned}\tag{2.31}$$

for the synchronous gauge;

$$\begin{aligned}\dot{\delta}_b &= -\theta_b + 3\dot{\phi}, \\ \dot{\theta}_b &= \mathcal{H}\theta_b + c_s^2 k^2 \delta_b + k^2\Psi,\end{aligned}\tag{2.32}$$

in the longitudinal one.

2.4.3 Massless neutrinos

We will consider only massless neutrinos, their distribution function can be expanded in Legendre polynomials:

$$F_\nu(\vec{k}, \hat{n}, \tau) = \frac{\int q^2 dq q f_0(q) \Phi}{\int q^2 dq q f_0(q)} = \sum_{l=0}^{\infty} (-i)^l F_\nu(\vec{k}, \tau) P_l(\hat{k} \cdot \hat{n}).\tag{2.33}$$

The fluid variables are:

$$\begin{aligned}
\delta_\nu &= 3\delta P_\nu = \frac{1}{4\pi} \int d\Omega F_\nu(\vec{k}, \hat{n}, \tau) = F_{\nu 0}, \\
\theta_\nu &= \frac{3i}{16\pi} \int d\Omega (\vec{k} \cdot \hat{n}) F_\nu(\vec{k}, \hat{n}, \tau) = \frac{3}{4} k F_{\nu 1}, \\
\sigma_\nu &= -\frac{2}{16\pi} \int d\Omega \left[(\hat{k} \cdot \hat{n})^2 - \frac{1}{3} \right] F_\nu(\vec{k}, \hat{n}, \tau) = \frac{1}{2} F_{\nu 2}.
\end{aligned} \tag{2.34}$$

Integrating the Boltzmann equation in q and neglecting the collisional terms, in the synchronous gauge the neutrino equations are:

$$\begin{aligned}
\dot{\delta}_\nu &= -\frac{4}{3}\theta_\nu - \frac{2}{3}\dot{h}, \\
\dot{\theta}_\nu &= k^2 \left(\frac{1}{4}\delta_\nu - \sigma_\nu \right), \\
\dot{F}_{\nu 2} &= 2\dot{\sigma}_\nu = \frac{8}{15}\theta_\nu - \frac{3}{5}kF_{\nu 3} + \frac{4}{15}\dot{h} + \frac{8}{5}\dot{\eta}, \\
\dot{F}_{\nu l} &= \frac{k}{2l+1} (lF_{\nu(l-1)} - (l+1)F_{\nu(l+1)}) \quad \text{for } l \geq 2,
\end{aligned} \tag{2.35}$$

in the longitudinal gauge:

$$\begin{aligned}
\dot{\delta}_\nu &= -\frac{4}{3}\theta_\nu - 3\dot{\phi}, \\
\dot{\theta}_\nu &= k^2 \left(\frac{1}{4}\delta_\nu - \sigma_\nu \right) + k^2\Psi, \\
\dot{F}_{\nu 2} &= 2\dot{\sigma}_\nu = \frac{8}{15}\theta_\nu - \frac{3}{5}kF_{\nu 3}, \\
\dot{F}_{\nu l} &= \frac{k}{2l+1} (lF_{\nu(l-1)} - (l+1)F_{\nu(l+1)}) \quad \text{for } l > 2.
\end{aligned} \tag{2.36}$$

The equation for the truncation multipole of the hierarchy is:

$$F_{\nu(l_{max}+1)} \sim \frac{(2l_{max}+1)}{k\tau} F_{\nu l_{max}} - F_{\nu(l_{max}-1)}. \tag{2.37}$$

2.4.4 Photons

The behaviour of photons is very similar to the one of massless neutrinos with the only difference that in this case the collisional term in the Boltzmann equation is not negligible due to the baryon-photon interaction. The integrated distribution function is composed by two contributions, one is F_γ

which represents the sum of the two linear polarizations and the other is G_γ which their difference. Expanding the two parts in Legendre polynomials the collisional terms are:

$$\begin{aligned} \left(\frac{\partial F_\gamma}{\partial \tau}\right)_c &= an_e \sigma_T \left[\frac{4i}{k} (\theta_\gamma - \theta_b) P_1 + \left(9\sigma_\gamma - \frac{1}{2} G_{\gamma 0} - \frac{1}{2} G_{\gamma 2} \right) P_2 - \right. \\ &\quad \left. \sum_{l \geq 3}^{\infty} (-i)^l (2l+1) F_{\gamma l} P_l \right], \\ \left(\frac{\partial G_\gamma}{\partial \tau}\right)_c &= an_e \sigma_T \left[\frac{1}{2} (F_{\gamma 2} + G_{\gamma 0} + G_{\gamma 2}) (1 - P_2) - \sum_{l \geq 0}^{\infty} (-i)^l (2l+1) G_{\gamma l} P_l \right]. \end{aligned}$$

Substituting the collisional terms in the Boltzmann equation gives the equations for photons:

$$\begin{aligned} \dot{\delta}_\gamma &= -\frac{4}{3} \theta_\gamma - \frac{2}{3} \dot{h}, \\ \dot{\theta}_\gamma &= k^2 \left(\frac{1}{4} \delta_\gamma - \sigma_\gamma \right), \\ \dot{F}_{\gamma 2} &= 2\dot{\sigma}_\gamma = \frac{8}{15} \theta_\gamma - \frac{3}{5} k F_{\gamma 3} + \frac{4}{15} \dot{h} + \frac{8}{5} \dot{\eta} - \frac{9}{5} an_e \sigma_T + \\ &\quad + \frac{1}{10} an_e \sigma_T (G_{\gamma 0} + G_{\gamma 2}), \\ \dot{F}_{\gamma l} &= \frac{k}{2l+1} (l F_{\gamma(l-1)} - (l+1) F_{\gamma(l+1)}) - an_e \sigma_T F_{\gamma l} \quad \text{for } l \geq 3, \\ \dot{G}_{\gamma l} &= \frac{k}{2l+1} (l G_{\gamma(l-1)} - (l+1) G_{\gamma(l+1)}) - \\ &\quad - an_e \sigma_T \left[-G_{\gamma l} + \frac{1}{2} (F_{\gamma 2} + G_{\gamma 2} + G_{\gamma 2}) \left(\delta_{l0} + \frac{\delta_{l2}}{5} \right) \right], \end{aligned} \quad (2.38)$$

in the synchronous gauge. In the longitudinal instead:

$$\begin{aligned} \dot{\delta}_\gamma &= -\frac{4}{3} \theta_\gamma - 3\dot{\phi}, \\ \dot{\theta}_\gamma &= k^2 \left(\frac{1}{4} \delta_\gamma - \sigma_\gamma \right) + k^2 \Psi, \\ \dot{F}_{\gamma 2} &= 2\dot{\sigma}_\gamma = \frac{8}{15} \theta_\gamma - \frac{3}{5} k F_{\gamma 3} - \frac{9}{5} an_e \sigma_T + \\ &\quad + \frac{1}{10} an_e \sigma_T (G_{\gamma 0} + G_{\gamma 2}), \\ \dot{F}_{\gamma l} &= \frac{k}{2l+1} (l F_{\gamma(l-1)} - (l+1) F_{\gamma(l+1)}) - an_e \sigma_T F_{\gamma l} \quad \text{for } l \geq 3, \\ \dot{G}_{\gamma l} &= \frac{k}{2l+1} (l G_{\gamma(l-1)} - (l+1) G_{\gamma(l+1)}) - \\ &\quad - an_e \sigma_T \left[-G_{\gamma l} + \frac{1}{2} (F_{\gamma 2} + G_{\gamma 2} + G_{\gamma 2}) \left(\delta_{l0} + \frac{\delta_{l2}}{5} \right) \right]. \end{aligned} \quad (2.39)$$

2.5 Initial conditions for primordial perturbations

Initial conditions for cosmological perturbations are in general divided between curvature and isocurvature, depending if their gauge invariant curvature perturbation:

$$\zeta = -\frac{1}{2\mathcal{H}} \left[\dot{\eta} - \left(\mathcal{H} \frac{\dot{h} + 6\dot{\eta}}{2k^2} \right) \right] - \frac{\ddot{h} + 6\ddot{\eta}}{4k^2} - \mathcal{H} \frac{\dot{h} + 6\dot{\eta}}{4k^2} - \eta - \frac{1}{6} k^2 \tau^2 \left(\eta - \mathcal{H} \frac{\dot{h} + 6\dot{\eta}}{2k^2} \right), \quad (2.40)$$

is zero or not on long wavelengths ($k \ll 1$). The adiabaticity (or curvature) condition is verified when the stress-energy of the fluid on large scales can be described by a single spatially uniform equation of state [37]. In the initial conditions for the perturbations the adiabaticity condition translates into a relation between the density contrasts of the different species:

$$\frac{\delta_i}{(1 + w_i)} = \frac{\delta_j}{(1 + w_j)}. \quad (2.41)$$

Therefore for the four standard components we would have:

$$\delta_\gamma = \delta_\nu = \frac{4}{3} \delta_b = \frac{4}{3} \delta_c. \quad (2.42)$$

Extensions of the standard cosmological model predict a non-negligible contribution of the so-called isocurvature or entropy perturbations. Isocurvature perturbations are characterized by ratios of the relative abundances which vary spatially and in particular compensate each other in order to maintain the necessary equilibrium. Present data strongly constrain the possible contributions by isocurvature modes but anyway do not exclude completely their presence.

Chapter 3

Cosmic Microwave Background Radiation

The Big Bang theory predicts the existence of a thermal relic isotropic radiation with a few K temperature. After almost 15 years of mistakes and misrecognitions, in 1964 Chance smiled to Penzias and Wilson who observed an isotropic “noise” of 3.5 K at $\lambda = 7.35$ cm [40]. After 25 years from its first observation, in 1990 the NASA satellite COsmic Background Explorer (COBE) finally confirmed the cosmological origin of the CMB with the measurements of its spectrum, showing an almost perfect 2.725 ± 0.002 K black body [1], at the frequencies 31.5, 53, 80 GHz, and of the temperature anisotropies of the order of $\Delta T/T \sim 10^{-5}$, at the angular scale of 7 degrees [2, 3], both in agreement with the predictions of the Big Bang theory.

3.1 Introduction

The CMB is the relic radiation from the Big Bang. The Big Bang theory predicts that at a redshift around $z \sim 1100$ the universe was sufficiently cool to allow the recombination of nuclei with electrons, the so-called recombination epoch. The neutralization of the cosmological fluid decreases the rate of

photon-baryon interaction until photons can propagate up to us, these photons that propagate through the universe history and are observed nowadays are the CMB. The virtual surface where the photons are scattered by electrons for the last time is called *last scattering surface* and can be considered a virtual emission surface of the CMB. At the epoch when CMB was emitted matter and radiation, thanks to their mutual interaction, were in equilibrium and therefore the CMB anisotropies are the mirror of primordial matter inhomogeneities. Also the almost perfect black body spectrum is related to the matter-radiation equilibrium.

Cosmological perturbations are generated at very early epochs and are stretched on wavelengths outside Hubble radius by inflation, re-entering it when the universe expands up to their wavelengths. The CMB anisotropies are a sort of frozen picture of the perturbation status at recombination. We will show in detail later that CMB anisotropies are statistically analyzed in spherical harmonic space. In this space the angular scale, θ , is related with the multipoles, l , and the wavenumber, k , through:

$$\theta \simeq \frac{1}{l} \simeq \frac{k^{-1}}{(\tau_0 - \tau_{Last\ Scattering})}. \quad (3.1)$$

In Fig. 3.1 is shown an example of CMB temperature anisotropy angular power spectrum. We note that we can identify three different characteristic scale ranges. The first are large scale anisotropies ($l < 100$). On these scales the anisotropies are the best representative of primordial perturbations, in fact they represent perturbations which were on super-Hubble scales at recombination. Outside the Hubble scale the only active force is gravity which affects mildly the perturbations. In particular, on these scales the CMB anisotropies are dominated by the Sachs-Wolfe term [173]. This effect is due to the redshifts and blueshifts that photons suffer due to the emission at last scattering surface from a perturbed fluid which presents potential wells and hills. The Sachs-Wolfe temperature fluctuation is directly related to the

gravitational potential by:

$$\frac{\Delta T}{T} = \frac{1}{3}\delta\Phi. \quad (3.2)$$

The second range is where acoustic oscillations are present ($100 < l < 1500$). On intermediate scales which are smaller than the horizon at recombination, the perturbations are inside the Hubble radius and therefore pressure starts to play its role in the behavior of the cosmological fluid. In particular, we have a forced harmonic oscillator in which gravity and pressure both act. In the CMB anisotropy angular power spectrum this region is marked by a series of acoustic peaks which represent the acoustic oscillations of the fluid. The third range is given by very small angular scales ($l > 1500$). On these scales primary anisotropies are suppressed by the Silk damping. This damping is caused by the fact that the radiation mean free path is larger than the cosmological perturbation wavelengths and these are suppressed. In the anisotropy angular power spectrum this region shows a rapid damping tail.

The Compton scattering of photons and electrons polarizes the CMB. In order to produce a polarized signal a photon distribution with a non zero quadrupole moment is necessary; indeed the average effect of different scatterings in a completely isotropic distribution would vanish. Cosmological radiation field carries a quadrupole moment and therefore is polarized: however, since the quadrupole is suppressed by Compton scattering, the resulting polarization signal is much weaker than the temperature one, around some %. The Compton scattering contribution to polarization is linear, circular terms are present only at the next to leading order or in exotic extensions of the standard model. The description of CMB polarization in terms of the Stokes parameters depends on the orientation of the reference system. Linear non-local combinations of Stokes parameters, the scalar E (and its correlation with the temperature TE) and the pseudoscalar B, are often used since they are independent on the system orientation.

3.2 CMB anisotropy statistical analysis

We will now review the basic points of the statistical analysis of CMB anisotropies, first for temperature anisotropies and then for polarization ones.

3.2.1 Temperature anisotropy angular power spectrum

We follow the treatment presented in [38]. We can write the temperature field as the sum of its zeroth-order and the anisotropies $\Delta_T = \delta T/T$:

$$T(\vec{x}, \hat{n}, \tau) = T(\tau)(1 + \Delta_T(\vec{x}, \hat{n}, \tau)); \quad (3.3)$$

here \vec{x} is the space position and \hat{n} is the direction of the incoming photons. The background temperature evolves as radiation temperature, $T \propto a^{-1}$, whereas the temperature anisotropies depend on time, direction and position. Since we work on a sphere temperature anisotropies are expanded in spherical harmonics:

$$\Delta_T(\vec{x}, \hat{n}, \tau) = \sum_{l=1}^{\infty} \sum_{m=-l}^l a_{lm}(\vec{x}, \tau) Y_{lm}(\hat{n}). \quad (3.4)$$

The information about the spatial and temporal distribution of the temperature field is in the expansion coefficients: $a_{lm}(\vec{x}, \tau)$. The spherical harmonics satisfy both completeness and orthonormality relations:

$$\int d\Omega Y_{lm}(\hat{n}) Y_{l'm'}^*(\hat{n}) = \delta_{ll'} \delta_{mm'}, \quad (3.5)$$

$$\sum_{l,m} Y_{lm}^*(\hat{n}) Y_{lm}(\hat{n}') = \delta(\hat{n} - \hat{n}'), \quad (3.6)$$

where Ω is the solid angle. Passing to the Fourier space the temperature anisotropies transform following the convention:

$$\Delta_T(\vec{x}, \hat{n}, \tau) = \frac{1}{(2\pi)^3} \int d^3k e^{i\vec{k}\cdot\vec{x}} \Delta_T(\vec{k}, \hat{n}, \tau). \quad (3.7)$$

By first multiplying Eq. 3.4 for $Y_{lm}^*(\hat{n})$, integrating both its members in $d\Omega$ and finally using the relation of Eq. 3.5, we can express the a_{lm} as a function of the temperature anisotropies:

$$a_{lm}(\vec{x}, \tau) = \int \frac{d^3k}{(2\pi)^3} e^{i\vec{k}\cdot\vec{x}} \int d\Omega Y_{lm}^*(\hat{n}) \Delta_T(k, \hat{n}, \tau). \quad (3.8)$$

The mean of the a_{lm} distribution is zero and therefore the first significant statistical moment of the anisotropy distribution is its variance. The variance of the a_{lm} , called C_l , is the anisotropy angular power spectrum and if the anisotropies, i.e. the cosmological perturbations, are Gaussian it is the only non-zero statistical moment and incorporates all the information on the anisotropies. In non-Gaussian contexts, as we will see in the next chapters, higher statistical moments are non zero. The CMB anisotropy angular power spectrum is defined as:

$$\begin{aligned} \langle a_{lm} \rangle &= 0, \\ C_l &= \frac{1}{2l+1} \sum_m \langle a_{lm}^* a_{lm} \rangle, \end{aligned} \quad (3.9)$$

which implies

$$\langle a_{lm}^* a_{l'm'} \rangle = \delta_{ll'} \delta_{mm'} C_l. \quad (3.10)$$

For an all-sky observation, a statistical analysis of CMB anisotropies is affected by cosmic variance, which is the uncertainty related to the fact that we are applying a statistical analysis to one single realization: the only sky we observe. Each multipole has the same variance at a given l , this means that for each multipole we have $2l+1$ coefficients to draw the underlying distribution. Therefore for high multipoles we have a large information to drawn the distribution while for small multipoles we have only very little information available. In particular the low multipoles are strongly affected by cosmic variance:

$$\frac{\Delta C_\ell}{C_\ell} = \sqrt{\frac{2}{(2\ell+1)}}. \quad (3.11)$$

For a realistic experiment where it is necessary to consider also the noise contribution, the uncertainty on the power spectrum becomes [68]:

$$\frac{\Delta C_\ell}{C_\ell} = \sqrt{\frac{2}{f_{sky}(2\ell+1)}} \left(1 + \frac{A_{pix} \sigma_{pix}^2}{C_\ell e^{-\ell^2 FWHM / \sqrt{8 \log 2}}} \right), \quad (3.12)$$

where f_{sky} is the fraction of the sky considered, A_{pix} , σ_{pix} are the area of the pixel and the sensitivity per pixel and $FWHM$ is the full width half maxi-

mum.

We will now derive the relation between the angular power spectrum and the cosmological perturbations.

The mean value of the temperature anisotropies, $\langle \Delta_T(\vec{k}, \hat{n}) \Delta_T(\vec{k}', \hat{n}') \rangle$, depends on the initial conditions of cosmological perturbations and on their temporal evolution. We can separate these two dependences $\langle \Delta_T(\vec{k}, \hat{n}) \Delta_T(\vec{k}', \hat{n}') \rangle = \xi(\vec{k}) \frac{\Delta_T(\vec{k}, \hat{n})}{\xi(\vec{k})}$, where the $\xi(k)$ represents the initial condition and the ratio represents the temporal evolution. The temporal evolution can be taken out of the averaging:

$$\langle \Delta_T(\vec{k}, \hat{n}) \Delta_T(\vec{k}', \hat{n}') \rangle = \langle \xi(\vec{k}) \xi^*(\vec{k}') \rangle \frac{\Delta_T(\vec{k}, \hat{n})}{\xi(\vec{k})} \frac{\Delta_T^*(\vec{k}', \hat{n}')}{\xi^*(\vec{k}')}. \quad (3.13)$$

We can define the primordial matter power spectrum as*:

$$\langle \xi(\vec{k}) \xi^*(\vec{k}') \rangle = (2\pi)^3 \delta_D^{(3)}(\vec{k} - \vec{k}') P(k). \quad (3.14)$$

Substituting the matter power spectrum of Eq. 3.14 in Eq. 3.13 gives:

$$\langle \Delta_T(\vec{k}, \hat{n}) \Delta_T(\vec{k}', \hat{n}') \rangle = (2\pi)^3 \delta_D^3(\vec{k} - \vec{k}') P(k) \frac{\Delta_T(k, \hat{k} \cdot \hat{n})}{\xi(k)} \frac{\Delta_T^*(k, \hat{k}' \cdot \hat{n}')}{\xi^*(k')}. \quad (3.15)$$

The ratio of Δ_T and ξ depends only on the amplitude of k and its angle with the photon direction, i.e. two modes with the same wavenumber will evolve in the same way. Squaring the Eq. 3.8 and taking its mean value, we can express the angular power spectrum as a function of the temperature anisotropies:

$$C_l = \int \frac{d^3k}{(2\pi)^3} P(k) \int d\Omega Y_{lm}^*(\hat{n}) \frac{\Delta_T(k, \hat{k} \cdot \hat{n})}{\xi(k)} \int d\Omega' Y_{lm}(\hat{n}') \frac{\Delta_T^*(k, \hat{k}' \cdot \hat{n}')}{\xi^*(k)}. \quad (3.16)$$

The temperature anisotropies can be expanded as:

$$\Delta_T(k, \hat{k} \cdot \hat{n}) = \sum_l (-i)^l (2l+1) \mathcal{P}_l(\hat{k} \cdot \hat{n}) \Delta_{Tl}(k), \quad (3.17)$$

*The δ_D is the Dirac distribution.

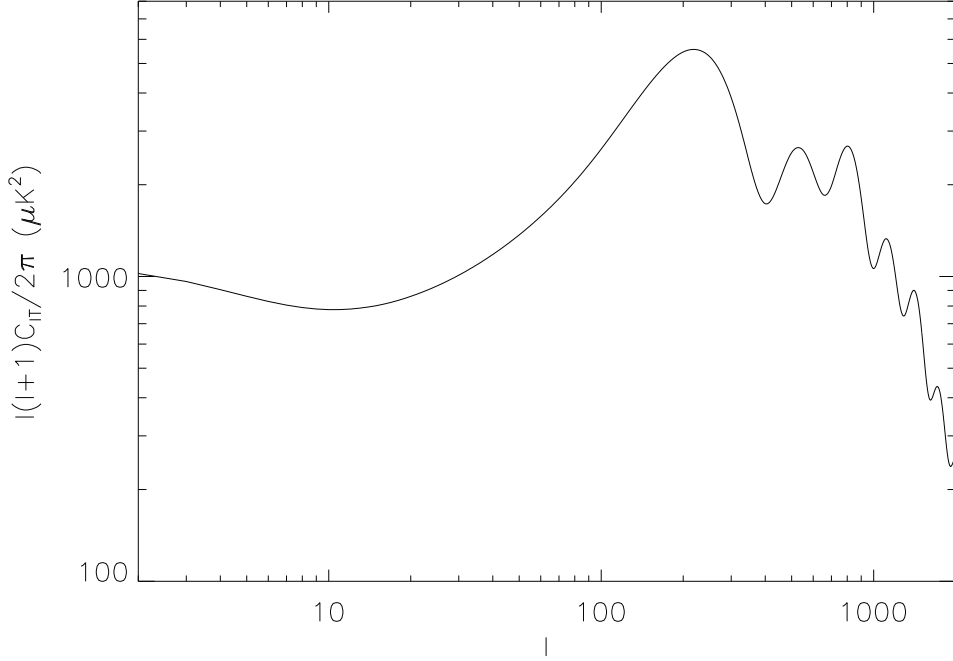


Figure 3.1: Temperature power spectrum, $\Omega_b h^2 = 0.22$, $\Omega_c h^2 = 0.123$, $h = 72$, $\Omega_\lambda = 0.7$, $N_\nu = 3.04$, $n_s = 1$.

where the \mathcal{P} are the Legendre polynomials. Substituting in the previous equation we obtain:

$$C_l = \int \frac{d^3k}{(2\pi)^3} P(k) \Sigma_{l'l''} (-i)^{l'} (i)^{l''} (2l' + 1)(2l'' + 1) \frac{\Delta_{Tl'}(k, \hat{k} \cdot \hat{n}) \Delta_{Tl''}^*(k, \hat{k} \cdot \hat{n})}{|\delta(k)|^2} \times \int d\Omega' \mathcal{P}_{l'}(\hat{k} \cdot \hat{n}) Y_{lm}^*(\hat{n}) \int d\Omega'' \mathcal{P}_{l''}(\hat{k} \cdot \hat{n}') Y_{lm}(\hat{n}'), \quad (3.18)$$

Solving the angular integrations leads to the final expression for C_l as a function of the temperature anisotropies:

$$C_l = \frac{2}{\pi} \int_0^\infty dk k^2 P(k) \left| \frac{\Delta_{Tl}(k)}{\xi(k)} \right|^2. \quad (3.19)$$

3.2.2 Integration of the photon Boltzmann equation

The CMB temperature anisotropy angular power spectrum depends on the integrated evolution with time of the photon multipole distribution. We will now derive the scalar source term of the C_l integrating the Boltzmann equation for photon multipoles, again we will refer to the treatment in [38]. We can define the photon monopole as:

$$\Delta_{T0} = \frac{1}{4\pi} \int d\Omega' \Delta_T(\vec{x}, \hat{n}, \tau) \quad (3.20)$$

The Boltzmann equation with multipole notation is written as:

$$\dot{\Delta}_T + ik(\hat{k} \cdot \hat{n})\Delta_T = -\dot{\phi} - ik(\hat{k} \cdot \hat{n})\psi - \dot{\kappa}(\Delta_{T0} - \Delta_T + (\hat{k} \cdot \hat{n})v_b), \quad (3.21)$$

where ψ and ϕ are the metric perturbations in the longitudinal gauge, v_b is the baryon velocity and κ is the optical depth. Subtracting from both members $\Delta_T\kappa$ the previous equation becomes:

$$\dot{\Delta}_T + (ik\vartheta - \dot{\tau})\Delta_T = e^{-ik\mu + \kappa} \frac{d}{d\tau} (\Delta_T e^{ik\mu - \kappa}) = S, \quad (3.22)$$

where S is the source term and $\vartheta = \hat{k} \cdot \hat{n}$ is the angle between wavenumber and the photon direction. Multiplying by $e^{-\kappa}$ and integrating in τ we obtain:

$$\Delta_T(\tau_0) = \Delta_T(\tau_{rec}) e^{-ik\vartheta(\tau_{rec} - \tau_0) - \kappa(\tau_{rec})} + \int_{\tau_{rec}}^{\tau_0} d\tau S(\tau) e^{ik\vartheta(\tau - \tau_0) - \kappa(\tau)}, \quad (3.23)$$

where it has been used that the present universe is optically thin: $\kappa(\tau_0) = 0$. The optical depth prior to the recombination is very high and the exponential function suppresses the integral before that time. Since every pre-recombination contribution is negligible, the integral lower bound can become zero instead of the recombination time. The temperature anisotropies become:

$$\Delta_T(k, \vartheta, \tau_0) = \int_0^{\tau_0} d\tau S(k, \vartheta, \tau) e^{ik\vartheta(\tau - \tau_0) - \kappa(\tau)}. \quad (3.24)$$

We neglect for the moment the dependence on the angle ϑ in the source term $S(k, \vartheta, \tau) \sim S(k, \tau)$. Multiplying both members of Eq. 3.24 for the Legendre polynomials gives:

$$\mathcal{P}_l \Delta_T(k, \vartheta, \tau_0) = \int_0^{\tau_0} d\tau S(k, \vartheta, \tau) e^{ik\vartheta(\tau - \tau_0) - \kappa(\tau)} \mathcal{P}_l(\vartheta). \quad (3.25)$$

The integration of the Legendre polynomials over the angle gives:

$$\int_{-1}^1 \frac{d\vartheta}{2} \mathcal{P}_l(\vartheta) e^{ik\vartheta(\tau-\tau_0)} = \frac{1}{(-i)^l} j_l(k(\tau-\tau_0)), \quad (3.26)$$

where the j_l is the spherical Bessel function.

In the approximation of negligible angular dependence of the source term the temperature anisotropies would be:

$$\Delta_{Tl}(k, \tau_0) = (-1)^l \int_0^{\tau_0} d\tau S(k, \tau) e^{-\kappa} j_l(k(\tau-\tau_0)). \quad (3.27)$$

To reintroduce the angular dependence of the source term, consider that this term is multiplied by $e^{ik\mu(\tau-\tau_0)}$ therefore everytime there is a μ term it can be written with a conformal derivative:

$$A\mu e^{ik\vartheta(\tau-\tau_0)} = \frac{A}{ik} \frac{d}{d\tau} e^{ik\vartheta(\tau-\tau_0)}, \quad (3.28)$$

where A is a function independent of ϑ . It can be demonstrated that the contribution of the angular dependence is just a sign.

This leads to the equation for the photon anisotropies today:

$$\Delta_{Tl}(k, \tau_0) = \int_0^{\tau_0} d\tau \tilde{S}(k, \tau) j_l(k(\tau-\tau_0)), \quad (3.29)$$

where the source is

$$\tilde{S}(k, \tau) = e^\kappa \left(-\dot{\phi} - \dot{\kappa} \left(\Delta_{T0} + \frac{1}{4} \Pi \right) \right) + \frac{d}{d\tau} \left(e^{-\kappa} \left(\psi - \frac{iv_b \dot{\kappa}}{k} \right) \right) - \frac{3}{4k^2} \frac{d^2}{d\tau^2} (e^{-\tau} \dot{\kappa} \Pi), \quad (3.30)$$

where Π represents the polarization tensor. We can define the visibility function

$$g(\tau) = -\dot{\kappa} e^\kappa, \quad (3.31)$$

that can be seen as the probability that a photon is scattered for the last time at τ . The source term can then be rewritten using the visibility function (neglecting for the moment the polarization term):

$$S(k, \tau) = g(\tau) (\Delta_{T0}(k, \tau) + \psi(k, \tau)) + \frac{d}{d\tau} \left(\frac{iv_b(k, \tau) g(\tau)}{k} \right) + e^{-\kappa} (\dot{\psi}(k, \tau) - \dot{\phi}(k, \tau)). \quad (3.32)$$

Inserting this source term in the Boltzmann equation, and subsequently integrating it in conformal time, we have the expression for the temperature anisotropies today:

$$\begin{aligned} \Delta_{Tl}(k, \tau_0) \sim & (\Delta_{T0}(k, \tau_{rec}) + \psi(k, \tau_{rec}))j_l(k(\tau_0 - \tau_{rec})) + \quad (3.33) \\ & + 3\Delta_1(k, \tau_{rec})(j_{l-1}(k(\tau_0 - \tau_{rec})) - \frac{(l+1)j_l(k(\tau_0 - \tau_{rec}))}{k(\tau_0 - \tau_{rec})}) + \\ & + \int_0^{\tau_0} d\tau e^{-\kappa}(\dot{\psi}(k, \tau) - \dot{\phi}(k, \tau))j_l(k(\tau_0 - \tau_{rec})). \end{aligned}$$

The last term considers the effects on the temperature anisotropies of the potential variations from the recombination until now. This equation together with the expression of C_l as a function of the anisotropies completely determines the temperature anisotropy angular power spectrum.

3.2.3 Polarization anisotropy angular power spectra

We will now review the derivation of the polarization anisotropy angular power spectra following the treatment presented in [147]. The radiation field is characterized by a 2×2 tensor I_{ij} . The temperature intensity is given by $T = (I_{11} + I_{22})/2$, while the two Stokes parameters associated with the linear polarization are given by $Q = (I_{11} - I_{22})/4$ and $U = I_{12}/2$. The parameters Q and U depend on the orientation of the system. In particular under a rotation of an angle ς in the plane perpendicular to the propagation direction \hat{n} they transform as:

$$\begin{aligned} Q' &= Q \cos(2\varsigma) + U \sin(2\varsigma), \\ U' &= -Q \sin(2\varsigma) + U \cos(2\varsigma). \end{aligned} \quad (3.34)$$

Combining the Stokes parameters we can derive two quantities with defined spin

$$(Q \pm iU)'(\hat{n}) = e^{\mp 2\varsigma}(Q \pm iU)(\hat{n}). \quad (3.35)$$

Expanding in spherical harmonics we obtain:

$$\begin{aligned} (Q + iU)(\hat{n}) &= \sum_{lm} a_{2,lm} Y_{2,lm}(\hat{n}), \\ (Q - iU)(\hat{n}) &= \sum_{lm} a_{-2,lm} Y_{-2,lm}(\hat{n}), \end{aligned} \quad (3.36)$$

where the subscript 2, -2 indicates the harmonic spin.

Then coefficients of the expansion are given by:

$$\begin{aligned} a_{2,lm} &= \int d\Omega Y_{2,lm}^*(\hat{n})(Q + iU)(\hat{n}), \\ a_{-2,lm} &= \int d\Omega Y_{-2,lm}^*(\hat{n})(Q - iU)(\hat{n}). \end{aligned} \quad (3.37)$$

It is more convenient to use their linear combinations:

$$a_{E,lm} = -(a_{2,lm} + a_{-2,lm})/2, \quad (3.38)$$

$$a_{B,lm} = i(a_{2,lm} - a_{-2,lm})/2, \quad (3.39)$$

where $a_{E,lm}$ corresponds to the scalar E-mode polarization, while $a_{B,lm}$ to the pseudo scalar B-mode. The polarization power spectra for the E-mode and B-mode autocorrelation and the cross-correlation between temperature and E-mode polarization are defined by:

$$\begin{aligned} C_{El}\delta_{ll'}\delta_{mm'} &= \langle a_{E,lm}^* a_{E,l'm'} \rangle, \\ C_{Bl}\delta_{ll'}\delta_{mm'} &= \langle a_{B,lm}^* a_{B,l'm'} \rangle, \\ C_{TEl}\delta_{ll'}\delta_{mm'} &= \langle a_{T,lm}^* a_{E,l'm'} \rangle. \end{aligned} \quad (3.40)$$

We do not consider the cross-correlations which include the B-mode polarization (both with temperature and E mode) because they are zero under parity symmetry.

We will now derive the angular power spectrum as a function of the polarization anisotropies induced by scalar perturbations. The Boltzmann equation for the polarization anisotropies is given by:

$$\dot{\Delta}_P + ik\vartheta\Delta_P = \dot{\kappa} \left(-\Delta_P + \frac{1}{2}(1 - \mathcal{P}_2(\vartheta))\Pi \right), \quad (3.41)$$

where the polarization tensor is defined by $\Pi = \Delta_{T2} + \Delta_{P0} + \Delta_{P2}$. Applying the same procedure used for the temperature anisotropies we obtain:

$$\Delta_P(k, \vartheta, \tau) = \frac{3}{4}(1 - \vartheta^2) \int_0^{\tau_0} d\tau e^{-ik\vartheta(\tau - \tau_0)} \dot{\kappa} e^{-\kappa} \Pi. \quad (3.42)$$

Writing the polarization anisotropies as $\Delta_P = \xi(\vec{k}) \frac{\Delta_P(\vec{k}, \vartheta)}{\xi(\vec{k})}$ in the same way used for Δ_T gives for the E and B anisotropies:

$$\begin{aligned} E(\hat{n}) &= \int \frac{d^3k}{(2\pi)^3} \xi(\vec{k}) \frac{\Delta_E(k, \vartheta, \tau_0)}{\xi(\vec{k})}, \\ B(\hat{n}) &= \int \frac{d^3k}{(2\pi)^3} \xi(\vec{k}) \frac{\Delta_B(k, \vartheta, \tau_0)}{\xi(\vec{k})}. \end{aligned} \quad (3.43)$$

Using the property $\Delta_P(k, \vartheta, \tau_0) = \Delta_P^*(k, \vartheta, \tau_0)$ we obtain:

$$\begin{aligned} \Delta_E(k, \vartheta, \tau_0) &= -\frac{3}{4} \int_0^{\tau_0} g \Pi \partial_\vartheta^2 ((1 - \vartheta^2)^2 e^{-ik\vartheta(\tau - \tau_0)}) \\ &= \frac{3}{4} \int_0^{\tau_0} g \Pi (1 + \partial_{k(\tau - \tau_0)}^2)^2 (k(\tau - \tau_0) e^{-ik\vartheta(\tau - \tau_0)}), \end{aligned} \quad (3.44)$$

$$\Delta_B(k, \vartheta, \tau_0) = 0. \quad (3.45)$$

We note that scalar perturbations do not generate B-mode polarization, only tensor and vector perturbations do it. The E-mode polarization anisotropy angular power spectrum is:

$$C_{El} = \frac{2}{\pi} \int dk k^2 P(k) |\Delta_{El}(k)|^2, \quad (3.46)$$

where

$$\Delta_{El}(k) = \int_0^{\tau_0} d\tau S_T(\tau, k) \frac{j_l(k(\tau - \tau_0))}{(k(\tau - \tau_0))^2}, \quad (3.47)$$

$$S_T(k, \tau) = \frac{3}{4} g(\tau) \Pi(\tau, k). \quad (3.48)$$

For the TE cross correlation we have:

$$C_{TEl} = \frac{2}{\pi} \int dk k^2 P(k) \Delta_{Tl}(k) \Delta_{El}(k). \quad (3.49)$$

In Fig.3.2 we show the two E-mode and cross TE polarization spectra generated by scalar perturbations and also an example of a B-mode polarization generated by tensor perturbations.

3.3 The CAMB & CosmoMC codes

In order to compute the CMB anisotropy angular power spectrum is necessary to evolve the coupled system of Einstein and Boltzmann equations

in Fourier space, within the chosen cosmological model, for specified initial conditions. The computational tools to accomplish this purpose are the so-called Einstein-Boltzmann codes. The first code made available to the scientific community was the COSMICS package written by Ma and Bertchinger in synchronous and longitudinal gauge [66]. Later this code was improved in computational performances through the integration along the line of sight method [146], such modification is called CMBFAST [41], from which were derived the other codes: CAMB, CMBEASY [43, 42]. These codes evolve the cosmological perturbation equations for a specified set of cosmological parameters and initial conditions giving in output the anisotropy angular power spectra in temperature and polarization and the transfer functions for each species (and the total one) at each time and wavenumber evolved. The results we will present in this work are based on extensions that we implemented of the public Einstein-Boltzmann code CAMB [65, 67].

In order to constrain cosmological models, both standard and its extensions, with current cosmological data is necessary to explore the cosmological parameter space. In particular, to our purpose we extended the public CosmoMC code [64] which is originally connected with CAMB and in our case with our extensions of the CAMB code.

The CosmoMC code explore the parameter space using the Bayesian based Metropolis Hastings Markov Chain MonteCarlo algorithm [119, 45]. The algorithm is based on Bayesian statistics. In particular if we consider an ensemble of variables, $\mathbf{x} = (x_1 \dots x_N)$, and a set of data $\theta = (\theta_1 \dots \theta_C)$ we can define their joint probability distribution with the conditional probability distribution function as:

$$P(\mathbf{x}, \theta) = P(\theta)P(\mathbf{x}|\theta), \quad (3.50)$$

where $P(\theta)$ is the prior probability distribution function of θ and $P(\mathbf{x}|\theta)$ is the sampling distribution or the conditional probability distribution function of \mathbf{x} given the evidence of θ which is also referred to as the likelihood. The

Bayesian theorem states that:

$$P(\theta|\mathbf{x}) = \frac{P(\theta)P(\mathbf{x}|\theta)}{\int d\theta P(\theta)P(\mathbf{x}|\theta)}, \quad (3.51)$$

where $P(\theta|\mathbf{x})$ is the posterior probability distribution function of data θ conditioned to \mathbf{x} . The $\int d\theta P(\theta)P(\mathbf{x}|\theta)$ is simply the marginal probability distribution function of \mathbf{x} and is used as normalizing factor. CosmoMC explores the parameter space using a MCMC Metropolis Hastings algorithm [119, 45], where the equilibrium distribution of the MCMC is the joint posterior distribution. The algorithm starts from a initial point, $\boldsymbol{\varkappa}$, of the parameter space and computes the likelihood associated to it. The following step in the chains, ι , is generated using a proposal density $b(\iota|\boldsymbol{\varkappa})$, this step is accepted as the new point of the chain with a probability:

$$p(\iota|\boldsymbol{\varkappa}) = \min \left\{ \frac{P(\iota)q(\boldsymbol{\varkappa}|\iota)}{P(\boldsymbol{\varkappa})q(\iota|\boldsymbol{\varkappa})}, 1 \right\}. \quad (3.52)$$

The new point of the chain is accepted if:

$$p(\iota|\boldsymbol{\varkappa}) \geq u, \quad (3.53)$$

where u is a random number generated from the uniform distribution $U[0, 1]$. Once the chain reaches the equilibrium the results are independent on the starting point.

CosmomMC code uses all current cosmological data, primary from CMB experiments but also large scale structure and supernovae.

3.4 The *Planck* satellite

The current CMB data come from the WMAP satellite 7 years data in temperature and cross TE polarization and data from small patches experiments like ACBAR [11], CBI [12], QUaD [13], BICEP [14] and more recently SPT [15] and ACT [16]. The *Planck* satellite is an ESA project dedicated to the observation of the microwave sky. It was born from the merger of the two

Instrument	LFI			HFI					
Center frequency GHz	30	44	70	100	143	217	353	545	857
Mean FWHM (arcmin)	32.7	29.5	13.0	9.6	7.0	4.6	4.5	4.7	4.3
$\Delta T/T$ per pixel (Stokes I)	3.3	5.2	8.9	3	2.2	4.8	2.0	150	6000
$\Delta T/T$ per pixel (Stokes $Q&U$)	4.6	7.4	12.7	4.8	4.1	9	38		
Point source sensitivity (1σ ,mJ)	22	59	46	14	10	14	38	44	45

Table 3.1: Planck performance characteristics.

proposals SAMBA and COBRAS in 1996 and subsequently renamed *Planck* in 1998. It represents the third generation of CMB dedicated satellites after COBE and WMAP and its purpose is to improve the current temperature anisotropy measurements up to $\ell \sim 2500$, to accurately measure the E -mode polarization and the cross-correlation TE and improve the constraints on B -mode polarization. The satellite has been launched, together with the HERSCHEL satellite, the 14th of 2009 on Ariane 5 from the launch base of Korou in French Guyana and is orbiting in the second Lagrangian point L2 of the Sun-Earth system and still acquiring data. Each six months it performs a full sky survey. The formerly nominal mission of fourteen months has been extended to one year more, enhancing the number of full sky surveys covered to 4 and half. The satellite is composed of a 1.5 m gregorian telescope and two different instruments in the focal plane: the Low Frequency Instrument (LFI) and the High Frequency Instrument (HFI), which are based on different technologies. The former is made of HEMT amplifier receivers at the temperature of 20 K while the latter is composed by spider web bolometers cooled at a temperature of 0.1 K. The frequency coverage spans from 30 GHz to 857 GHz with nine channels divided between the two instruments: three for LFI and six for HFI. The pre-launch performances have been published recently in a dedicated volume of A&A [39] and are summarized in the table 3.1. The wide frequency coverage of *Planck* will allow the best foreground removal ever, allowing to have the cleanest full sky maps of the CMB. The frequency coverage of *Planck* together with the cleanest CMB full sky maps

will give also the possibility to investigate the Galactic emissions at frequencies never observed. This will allow a better understanding of synchrotron and free-free emission which will be better observed by LFI and of the dust emission from HFI data. Also extragalactic non-CMB science will take a great advantage from *Planck* data thanks to the observation of thousands of known (but also unknown) point sources and galaxy clusters in a frequency range never observed before both in millimetric and in far-infrared. The point source data of *Planck* are the subject of the first product that has been delivered to the scientific community on the 11th of January 2011: the Early Release Compact Source Catalogue (ERCSC) with a series of 25 early papers dedicated to astrophysics [18]. Cosmological data and results instead will be delivered only in late 2012-early 2013.

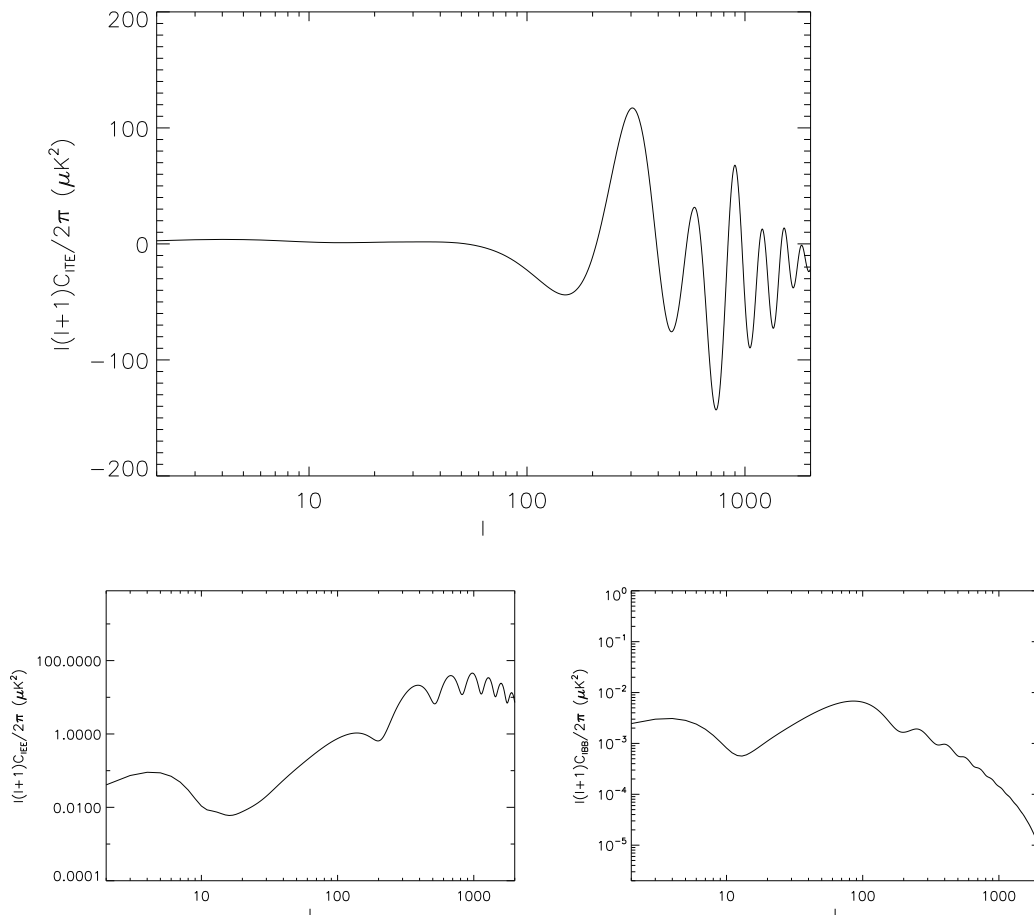


Figure 3.2: Polarization anisotropy angular power spectra. In the upper panel we show the power spectrum of the cross correlation between temperature and E-mode for scalar perturbations; in the lower left panel we show the E-mode polarization; in the bottom right panel we show the B-mode polarization from tensor perturbations with the same cosmological model as scalar and a tensor to scalar ratio of 0.1

Chapter 4

Primordial Magnetic Fields

4.1 Large scale magnetic fields

Magnetic fields are ubiquitous everywhere in the universe from those on small scales in planets and stars to those on large scales in galaxies and galaxy clusters. The first hint of existence of large scale magnetic fields appeared in 1949 from data on polarized star emission, which showed the presence of a diffuse magnetic field in the Galaxy. Few years later in 1962, the existence of a Galactic magnetic field was confirmed by the observations of the diffuse radio background [48]. The complete map of the Galactic field was created using Faraday rotation measures of the polarized emissions from pulsars and extragalactic sources. This was only the beginning. The increasing observational capabilities and the developments of different observational techniques made possible the study of the magnetism far beyond our Galaxy. In particular the main techniques which are used for the observation of large scale magnetic fields are:

- Optic light polarization for near fields.
- Zeeman splitting from hydrogen emission lines (sensitive to the line of sight component of the field).
- Polarimetry in millimetric and infrared bands for the observation of the

emission of dust grains aligned by the magnetic field.

- Synchrotron emission.
- Rotation measure of the Faraday rotation induced on the polarized emission coming from a background source (used for great distance observations).

Some of these techniques as the synchrotron radiation and the Faraday rotation require an independent measurement of the electron density in order to estimate the magnetic field strength.

The use of these techniques made possible to evidence the presence of large scale magnetic fields in every galaxy. The amplitude spans from few to ten μG and is independent on the type of galaxy. The morphology of the magnetic field instead strongly depends on the morphology of the host [49]:

- In spiral galaxies the magnetic field follows the spiral pattern, aligned with the rotation direction, with symmetries with respect to the galactic plane and the spin axis and coherence lengths of the order of the galactic scale.
- In elliptic galaxies instead the magnetic field is randomly distributed and has a coherence length smaller than the galactic scale.

The observation of distant quasars showed the presence of large scale magnetic fields also in high redshift galaxies, $z > 2$, with amplitudes comparable to the low redshift ones and coherence lengths of the order of the galaxy scale [50, 51]. Also damped Ly α systems at very high redshifts show the presence of large scale magnetic fields [49].

Diffuse magnetic fields are observed also in galaxy clusters. The amplitudes are of the order of few μG and seem to increase towards the cluster center. Their presence is not correlated with the presence of radio halos or cooling flows even if clusters with cooling flows present stronger central fields. Weak hints of even larger scale magnetic fields in superclusters are reported

in [52]. Such large scale magnetic fields may have had a strong impact on the structure formation but the observational evidence of their existence is still lacking.

Large scale magnetic fields have been widely investigated and, thanks to the amount of data collected, their present status is well known. Their generation instead is still an open issue. Magnetic fields of the order of μG during structure formation would have had a strong impact on the structure themselves, leaving imprints which are not observed. Therefore large scale magnetic fields must have been generated from the amplification of smaller initial fields. During the gravitational collapse of the forming structure, the adiabatic compression and the stretching of the magnetic field lines amplifies the fields [49], hence magnetic fields are amplified by structure formation itself. Together with the gravitational compression another possible amplification mechanism is the $\alpha\omega$ dynamo. The dynamo is powered by the differential rotation and small scale turbulent motions of the gas in the structure. It can amplify the magnetic fields exponentially up to the equipartition [53]. But all the amplification mechanisms evidently require initial seed magnetic fields to amplify.

The initial seed magnetic fields can be provided by the small scale objects in the structure, for example stars in galaxies and AGNs in galaxy clusters. Stars have magnetic fields and at the end of their life, during supernovae, these fields are ejected in the galactic medium. AGNs have strong emissions on relativistic jets which are extended in the intracluster medium and may diffuse the AGN magnetic fields in the galaxy clusters. The production of the initial seed magnetic fields by astrophysical objects presents two main problems. The first is related to the coherence lengths, these kind of initial seeds produce coherence lengths much smaller than the ones observed in galaxies and galaxy clusters. The second issue concerns the amplitudes of these fields. Astrophysical objects can provide only very weak initial seeds and therefore

require a dynamo amplification. The efficiency of the dynamo amplification is still discussed and in particular it is still unclear if the dynamo can work for large scale structure like galaxy clusters, for almost non rotating objects like elliptical galaxies and for very high redshift galaxies, where the number of e -foldings is very low.

In alternative to the hypothesis of an astrophysical origin of the initial seed magnetic fields, there is the cosmological one. Primordial magnetic fields generated in the early stage of the universe evolution can provide the required seeds. In particular with gravitational and, in case, dynamo amplifications, primordial magnetic fields can reproduce both amplitudes and coherence lengths of the large scale ones.

Upper bounds on the amplitude of diffuse cosmological magnetic fields, are given by the measurements of Faraday rotation of distant quasars, they are still very weak, of the order of $B < 10^{-7}\text{G}$, and model dependent [54, 55]. Very recently data on GeV gamma ray cascades of the FERMI observatory showed the existence of large scale magnetic fields in voids. Large scale magnetic fields in voids can be only of cosmological origin and may represent the present status of primordial magnetic fields. With FERMI data was possible to give lower bounds on cosmological magnetic fields amplitude of the order of $B > 10^{-7}\text{nG}$ [56, 57].

4.2 Primordial magnetic fields

The hypothesis of primordial magnetic fields (PMFs) is present in several cosmological models. Several different processes can generate PMFs in the early epochs, in particular we can identify two main classes related to the generation time: inflationary and post inflationary mechanisms.

4.2.1 Post inflationary generation mechanisms

After inflation causality requires that the maximum coherence length for the fields is about the Hubble distance at the generation time. However the Hubble distance provides only very small coherence lengths and therefore post inflationary mechanisms require a process capable to transfer energy from small to large scales.

Post inflationary generation mechanisms can be associated with phase transitions of both first and second order [58]. One example of process associated with phase transitions can have occurred at QCD phase transition. The nucleation of the hadronic bubbles generates shocks with strong gradients which affect in different ways quarks and leptons. This difference can lead to the development of currents and magnetic fields outside bubble walls. When two or more bubbles collide the magnetic fields merge together randomizing the field lines and increasing the coherence length beyond the bubble scale [49]. Another example is the generation of PMFs at the electroweak phase transition. In this case the generation process of the PMFs is related with the symmetry breaking. After the generation, the MHD turbulence outside the bubble walls enlarges PMF coherence length up to the scale of the larger eddies [49].

A possibility to increase the coherence length is an inverse cascade process. The inverse cascade can take place if the primordial fluid is both magnetically and dynamically turbulent, in particular it requires the injection of helicity in the plasma. The reequilibrium after the injection, which has to conserve both energy and helicity, leads to a transfer of power from small to large scales increasing the coherence length of PMFs. Since it requires particular conditions to take place is still unclear if an inverse cascade process can have occurred in the primordial plasma and there are still no reliable quantitative estimates of the increase of the coherence lengths ([117] and references therein).

PMFs can be generated also at later times. Late time generation processes are typically associated with vorticity or rotational velocities of the

ions and electrons caused by non linear perturbation evolution in the pre-recombination era [59, 60].

We reviewed only few examples of post inflationary generation mechanisms, the complete list would be very long, in particular including also exotic physics.

4.2.2 Inflationary generation mechanisms

The generation of PMFs during inflation naturally provides large coherence lengths. However gravity cannot amplify magnetic fields like happens for gravitons and scalar perturbations, since the electromagnetic field is protected by conformal invariance in four dimensions. The conformal invariance requires that the fluctuations scale as $|B_\kappa|^2 \propto a^{-4}$ for all the wavelengths, which will lead to PMFs with amplitudes too small to be the seeds for the large scale ones. Therefore to generate the required PMFs is necessary to break the conformal invariance. Inflationary models which predict the breaking of conformal invariance involve physical processes like:

- Dynamic couplings[61, 49].
- Extradimensions[61].
- Charged scalar field during inflation [63] and after inflation [62].
- Coupling between photons and axion-like field[49].

Inflationary generation mechanisms have the possibility to create PMFs with very different characteristics, in particular can create PMFs with all the possible spectral indices. Post inflationary ones instead can create PMFs only with spectral indices equal or greater than 2 [116]. The greater variety of inflationary PMFs, with respect to the post-inflationary ones, makes this class of PMFs more difficult to constrain with data. It is not the purpose of this work to investigate in details the generation mechanism of primordial magnetic fields, therefore we reviewed only the main concepts which are useful

for a complete comprehension of the primordial magnetic field subject.

It is not possible a priori to determine which generation mechanism of PMFs is the most likely one. But it is possible to use cosmological data to investigate and constrain PMF characteristics and indirectly discriminate between the different creation models. There have been several attempts to directly observe PMFs in the intercluster space with Faraday rotation of distant quasars, but up to now the results are only weak upper bounds. However PMFs have a strong impact on cosmological perturbations and leave an imprint on cosmological observables. In particular PMFs have an impact on CMB anisotropies in temperature and polarization, therefore CMB data represent a powerful tool to investigate and constrain PMF properties. In particular since CMB data are becoming more and more accurate, it is possible to constrain PMF characteristics up to a great accuracy level. In the following chapters we will investigate the impact of PMF on cosmological perturbations and on CMB anisotropies.

4.3 Magnetism in a cosmological contest

Before going into the details of the contribution of PMFs to cosmological perturbations, we will briefly review the properties of electromagnetism in the peculiar context of the primordial universe. The primordial plasma is fully ionized and can be considered globally neutral. Therefore we can assume vanishing charge density: $J_0 = 0$, where J_μ is the current density quadrivector. The electric conductivity of the ionized plasma can be considered infinite: $\sigma_{cond} \rightarrow \infty$, which is the so-called infinite conductivity limit.

With these assumptions the Maxwell equations reduce to:

$$\begin{aligned}
\nabla \cdot \mathbf{B} &= 0 \\
\nabla \cdot \mathbf{E} &= 0 \\
\nabla \times \mathbf{E} &= -\dot{\mathbf{B}} \\
\nabla \times \mathbf{B} &= \dot{\mathbf{E}} + 4\pi\mathbf{J},
\end{aligned} \tag{4.1}$$

Note how both the magnetic and the electric field are solenoidal. The density current evolves following $\mathbf{J} = \sigma_{cond}(\mathbf{E} + \mathbf{v} \times \mathbf{B})$. The term $\mathbf{v} \times \mathbf{B}$ is the electric field induced by the dragging of the PMF lines by the plasma, since it is a second order contribution, can be neglected for our analysis. At the first order we have $\mathbf{E} \propto \mathbf{J}/\sigma_{cond}$, which shows that electric fields vanish in the infinite conductivity limit. The electromagnetic Energy Momentum Tensor (EMT) within the infinite conductivity limit is:

$$\begin{aligned}
\tau_0^0 &= -\rho_B = -\frac{1}{8\pi G a^4} |\mathbf{B}(\mathbf{x})|^2 \\
\tau_i^0 &= \frac{1}{4\pi G a^4} (\mathbf{E} \times \mathbf{B}) = 0 \\
\tau_j^i &= \frac{1}{4\pi G a^4} (\delta_j^i \frac{|\mathbf{B}(\mathbf{x})|^2}{2} - \mathbf{B}_j(\mathbf{x})\mathbf{B}^i(\mathbf{x})).
\end{aligned} \tag{4.2}$$

Note how the space-time component of the PMF EMT is zero. Since this component is related with the PMF velocity: $\tau_i^0 = (\rho + P)v_i = 0$, its disappearance means that in the infinite conductivity limit PMFs are stationary.

The contribution of PMFs to cosmological perturbation is through their EMT, the PMF EMT is considered at the same footing as first order perturbations. Since the PMF EMT is quadratic in the fields, PMFs are considered half order perturbations.

The conservation equations for PMFs are given by:

$$\partial_\mu \tau_\nu^\mu + \Gamma_{\alpha\beta}^\alpha \tau_\nu^\beta - \Gamma_{\nu\beta}^\alpha \tau_\alpha^\beta = -F_\nu^\mu J_\mu \tag{4.3}$$

Setting $\nu = 0$ Eq. 4.3 gives to the energy conservation equation, in the infinite conductivity limit, where $F_0^\mu = 0$, it becomes:

$$\begin{aligned}
\partial_0 \tau_0^0 + \partial_i \tau_0^i + \Gamma_{0\beta}^0 \tau_0^\beta + \Gamma_{j\beta}^j \tau_0^\beta - \Gamma_{0\beta}^0 \tau_0^\beta - \Gamma_{0\beta}^j \tau_j^\beta &= 0, \\
\partial_0 \tau_0^0 + \Gamma_{j0}^j \tau_0^0 - \Gamma_{0k}^j \tau_j^k &= 0.
\end{aligned} \tag{4.4}$$

Substituting the EMT components:

$$\tau_0^0 = -\delta\rho_B, \quad (4.5)$$

$$\tau_j^i = \delta P \delta_j^i + \Sigma_j^i, \quad (4.6)$$

and expliciting the connection coefficients in FRW spacetime we obtain:

$$-\dot{\rho}_B - 3\mathcal{H}\rho_B - \delta_k^j \mathcal{H} \delta P \delta_j^k - \mathcal{H} \delta_k^j \Sigma_j^k = 0. \quad (4.7)$$

Using the equation of state for relativistic species ($\delta P = \rho_B/3$) we have:

$$\delta \dot{\rho}_B = -4\mathcal{H} \delta \rho_B. \quad (4.8)$$

Which simply gives to the temporal evolution law for the magnetic energy density in the infinite conductivity limit:

$$\rho_B \propto a^{-4}. \quad (4.9)$$

Note how the magnetic energy density evolves with time like radiation. Since the energy density is quadratic in the fields, PMFs evolve like $B(x, \tau) = B(x)/a^2(\tau)$.

PMFs carry energy density and anisotropic stress at the level of perturbations, but they carry also a third contribution which is the Lorentz force induced on baryons. In particular the Lorentz force is given by:

$$\nabla^2 L = \frac{1}{4\pi} [(\nabla_i B_j(\mathbf{x}, \tau)) \nabla_j B_i(\mathbf{x}, \tau) - \frac{1}{2} \nabla^2 B^2(\mathbf{x}, \tau)], \quad (4.10)$$

which is quadratic in the fields and therefore evolves as $L_B(x, \tau) = L_B(x)/a^4(\tau)$.

Fixing $\nu = i$ in Eq. 4.3 we obtain the momentum constraint equation:

$$\partial_\mu \tau_i^\mu + \Gamma_{\alpha\beta}^\alpha \tau_i^\beta - \Gamma_{i\beta}^\alpha \tau_\alpha^\beta = -F_i^j J_j, \quad (4.11)$$

which reduces to:

$$\begin{aligned} \partial_j \tau_i^j &= -F_i^j J_j, \\ i^2 k^i k_i \delta P + i^2 k^i k_j \Sigma_i^j &= \frac{-i^2 k^i}{4\pi} (B^k k_k B_i - B^k k_i B_k). \end{aligned} \quad (4.12)$$

We can explicitate the Lorentz force as $L_B = k^i L_i = \frac{1}{4\pi} k^i (B^j k_j B_i - \frac{1}{2} B^k k_i B_k)$ and we can express the anisotropic stress with the notation of [66] $\sigma = -(\hat{k}_i \hat{k}_j - \frac{1}{3} \delta_{ij}) \Sigma_j^i$:

$$\sigma_B = \frac{\rho_B}{3} + L_B. \quad (4.13)$$

This relation is crucial for scalar perturbations where we have the combined effect of all the three contributions. These properties are valid independently on the model of PMFs chosen. In the next chapter we will describe in details the model we adopted for our treatment.

Chapter 5

Stochastic Background of PMF Statistical Properties

5.1 Stochastic background of PMF

One possible model of PMFs is an homogeneous field. An homogeneous PMF, or any homogeneous component of PMFs, would break isotropy and is not supported in an homogeneous and isotropic universe. The cosmological model which includes the presence of an homogeneous PMF is represented by an anisotropic universe filled with blackbody radiation (the CMB) and homogeneous PMF, where the anisotropy evolution is governed by the PMF anisotropic pressure [109]. The great degree of isotropy of the CMB can put strong bounds on anisotropic cosmological models. In particular, with CMB data is possible to constrain this model of PMFs. The first constraints on an homogeneous PMF have been derived in [109] with COBE data: $B < 3.4 (\Omega_0 h_{50}^2)^2$ nG. A more recent theoretical analysis on the impact of an homogeneous PMF on CMB has been done in [110]. An homogeneous field induces a correlation between $a_{l-1,m}$ and $a_{l+1,m}$ which has a particular shape [112, 114]. In [111, 113] this correlation has been used to derive constraints on the PMF with WMAP data, these constraints are of the order of few nG. PMFs affect CMB polarization with Faraday rotation. In particular

in [115] are analyzed the forecasts for the constraints from Faraday rotation with future CMB polarization dedicated missions. These forecasts show an improvement of one or two orders of magnitude with respect to the current constraints.

The constraints with current data still allow the presence of an homogeneous component in PMF model, however an anisotropic universe would hardly agree with nucleosynthesis constraints at early times. For this reason we are mainly interested in a stochastic background of PMFs. A stochastic background of PMFs carries neither energy density nor pressure at the homogeneous level and therefore leaves unperturbed the homogeneous and isotropic cosmological background.

5.1.1 PMF statistical properties

We will now review the properties of a stochastic background of PMFs. PMFs evolve like a stiff source and therefore back reactions of fluid and gravity onto the fields are zero. Since we are interested in studying the impact of PMFs on cosmological perturbations, we will work in the Fourier space. In Fourier space we can define the two point correlation function for a stochastic background of PMFs as:

$$\langle B_i(\mathbf{k})B_j^*(\mathbf{k}') \rangle = (2\pi)^3 \delta(\mathbf{k} - \mathbf{k}') \left[(\delta_{ij} - \hat{k}_i \hat{k}_j) \frac{P_B(k)}{2} + \epsilon_{ijt} \frac{k_t}{k} P_H(k) \right], \quad (5.1)$$

where ϵ_{ijt} is the totally antisymmetric tensor and P_B and P_H are respectively the non-helical and helical part of the PMF power spectrum. Our analysis concerns only the non helical part of PMFs, therefore we will neglect all helical contributions: $P_H = 0$. We considered power law power spectrum PMFs:

$$P_B(k) = Ak^{n_B}, \quad (5.2)$$

where the spectrum is characterized by two parameters: the amplitude, which is related to the amplitude of the PMFs, and the spectral index n_B .

In order to relate the results obtained for PMFs with large scale magnetic fields, it is a common convention to smooth the fields on a comoving scale λ . The smoothing scale is typically of the order of coherence lengths of large scale magnetic fields, from 0.1 Mpc to 1 Mpc:

$$\begin{aligned}\langle B_\lambda^2 \rangle &= \frac{1}{2\pi} \int dk k^2 P_B(k) e^{-\lambda^2 k^2} \\ \langle B_\lambda^2 \rangle &= 2\pi A \lambda^{n_B+3} \Gamma\left[\frac{n_B+3}{2}\right].\end{aligned}\quad (5.3)$$

The spectral index has to satisfy the condition: $n_B > -3$ to avoid infrared divergences and ensure the convergence of the integral .

In the second chapter we showed that matter perturbations on small scales are suppressed by the Silk damping. This suppression is the responsible for the high multipole damping tail in the CMB anisotropy angular power spectrum. Differently from standard cosmological perturbations, magnetic ones survive Silk damping. Large wavelenght magnetic modes have too little oscillations and small wavelenght ones are overdamped oscillators, therefore magnetic modes on every scale are not affected by Silk damping. However PMFs are suppressed on small scales, but much smaller than the Silk one, by radiation viscosity. In particular the magnetic damping scale k_D depends on the field amplitude and on the spectral index [77, 70]:

$$k_D \sim (1.7 \times 10^2)^{\frac{2}{(n_B+3)}} \left(\frac{B_\lambda}{10^{-9}G}\right)^{\frac{-2}{n_B+5}} \times \left(\frac{k_\lambda}{Mpc^{-1}}\right)^{\frac{n_B+3}{n_B+5}} h^{\frac{1}{n_B+5}}. \quad (5.4)$$

We modelled the small scale suppression of PMFs with a sharp cut off at k_D in the PMF power spectrum. The root mean square of the fields is given by:

$$\langle B^2 \rangle = \frac{1}{2\pi^2} \int_0^{k_D} k^2 P_B(k), \quad (5.5)$$

where the upper bound of the integration is given by the sharp cut off. The relation between the root mean square of PMFs and the amplitude of the smoothed PMFs is:

$$\langle B^2 \rangle = \langle B_\lambda^2 \rangle \frac{(k_D \lambda)^{n_B+3}}{(n_B+3) \Gamma\left[\frac{n_B+3}{2}\right]}. \quad (5.6)$$

Through great part of our analysis we will use the smoothed fields B_λ .

5.2 PMF energy momentum tensor

The contribution of PMFs to cosmological perturbations depends the scalar, vector and tensor projections of their EMT. The EMT of PMFs is quadratic in the fields:

$$\begin{aligned}\tau_0^0 &= -\frac{1}{8\pi G a^4} |\mathbf{B}(\mathbf{x})|^2 \\ \tau_i^0 &= 0 \\ \tau_j^i &= \frac{1}{4\pi G a^4} \left(\delta_j^i \frac{|\mathbf{B}(\mathbf{x})|^2}{2} - \mathbf{B}_j(\mathbf{x}) \mathbf{B}^i(\mathbf{x}) \right),\end{aligned}\quad (5.7)$$

therefore its Fourier transform is a convolution. In particular the two point correlation function of the spatial part of the EMT is given by:

$$\begin{aligned}\langle \tau_{ab}^*(\mathbf{k}) \tau_{cd}(\mathbf{k}') \rangle &= \frac{1}{(64\pi^5)} \int d^3 q d^3 p \delta_{ab} \delta_{cd} \langle B_l(\mathbf{q}) B_l(\mathbf{k} - \mathbf{q}) B_m(\mathbf{p}) B_m(\mathbf{k}' - \mathbf{p}) \rangle \\ &\quad - \frac{1}{(32\pi^5)} \int d^3 q d^3 p \langle B_a(\mathbf{q}) B_b(\mathbf{k} - \mathbf{q}) B_c(\mathbf{p}) B_d(\mathbf{k}' - \mathbf{p}) \rangle.\end{aligned}\quad (5.8)$$

Since PMFs modelled as a stochastic background are Gaussianly distributed, we can apply the Wick theorem:

$$\begin{aligned}\langle B_a(\mathbf{q}) B_b(\mathbf{k} - \mathbf{q}) B_c(\mathbf{p}) B_d(\mathbf{k}' - \mathbf{p}) \rangle &= \langle B_a(\mathbf{q}) B_b(\mathbf{k} - \mathbf{q}) \rangle \langle B_c(\mathbf{p}) B_d(\mathbf{k}' - \mathbf{p}) \rangle + \\ &\quad \langle B_a(\mathbf{q}) B_c(\mathbf{p}) \rangle \langle B_b(\mathbf{k} - \mathbf{q}) B_d(\mathbf{k}' - \mathbf{p}) \rangle + \\ &\quad \langle B_a(\mathbf{q}) B_d(\mathbf{k}' - \mathbf{p}) \rangle \langle B_b(\mathbf{k} - \mathbf{q}) B_c(\mathbf{p}) \rangle.\end{aligned}\quad (5.9)$$

Substituting the two point correlation functions with the power spectra and integrating over d^3q we obtain:

$$\begin{aligned}
\langle \tau_{ab}^*(\mathbf{k}) \tau_{cd}(\mathbf{k}') \rangle = & \\
& \frac{1}{(64\pi^5)} \int \frac{d^3p}{4} \delta_{ab} \delta_{cd} P_B(\mathbf{p}) P_B(\mathbf{k} - \mathbf{p}) \times \\
& [(\delta_{lm} - \hat{\mathbf{p}}_l \hat{\mathbf{p}}_m)(\delta_{lm} - \widehat{(\mathbf{k} - \mathbf{p})}_l \widehat{(\mathbf{k} - \mathbf{p})}_m) + \\
& (\delta_{lm} - \hat{\mathbf{p}}_l \hat{\mathbf{p}}_m)(\delta_{lm} - \widehat{(\mathbf{k} - \mathbf{p})}_l \widehat{(\mathbf{k} - \mathbf{p})}_m)] \\
& - \frac{1}{(32\pi^5)} \int \frac{d^3p}{4} P_B(\mathbf{p}) P_B(\mathbf{k} - \mathbf{p}) \times \\
& [(\delta_{ac} - \hat{\mathbf{p}}_a \hat{\mathbf{p}}_c)(\delta_{bd} - \widehat{(\mathbf{k} - \mathbf{p})}_b \widehat{(\mathbf{k} - \mathbf{p})}_d) + \\
& (\delta_{ad} - \hat{\mathbf{p}}_a \hat{\mathbf{p}}_d)(\delta_{bc} - \widehat{(\mathbf{k} - \mathbf{p})}_b \widehat{(\mathbf{k} - \mathbf{p})}_c)], \quad (5.10)
\end{aligned}$$

which simplifies to:

$$\begin{aligned}
\langle \tau_{ab}^*(\mathbf{k}) \tau_{cd}(\mathbf{k}') \rangle = & \\
& \frac{\delta_{ab} \delta_{cd}}{(64\pi^5)} \int \frac{d^3p}{4} P_B(\mathbf{p}) P_B(\mathbf{k} - \mathbf{p}) 2(\delta_{lm} - \hat{\mathbf{p}}_l \hat{\mathbf{p}}_m) \\
& (\delta_{lm} - \widehat{(\mathbf{k} - \mathbf{p})}_l \widehat{(\mathbf{k} - \mathbf{p})}_m) \\
& - \frac{1}{(32\pi^5)} \int \frac{d^3p}{4} P_B(\mathbf{p}) P_B(\mathbf{k} - \mathbf{p}) \\
& [P_{ac}(\mathbf{p}) P_{bd}(\mathbf{k} - \mathbf{p}) + P_{ad}(\mathbf{p}) P_{bc}(\mathbf{k} - \mathbf{p})] \}. \quad (5.11)
\end{aligned}$$

We have used the definition of the projector onto the orthogonal plane $P_{ab}(k) = \delta_{ab} - \hat{k}_a \hat{k}_b$. To estimate the impact on cosmological perturbations it is necessary to compute the scalar, vector and tensor correlation functions:

$$\begin{aligned}
\langle \Pi^{*(S)}(\mathbf{k}) \Pi^{(S)}(\mathbf{k}') \rangle &= \delta_{ab} \delta_{cd} \langle \tau_{ab}^*(\mathbf{k}) \tau_{cd}(\mathbf{k}') \rangle \\
\langle \Pi_i^{*(V)}(\mathbf{k}) \Pi_j^{(V)}(\mathbf{k}') \rangle &= k_a P_{ib}(\mathbf{k}) k'_c P_{jd}(\mathbf{k}') \langle \tau_{ab}^*(\mathbf{k}) \tau_{cd}(\mathbf{k}') \rangle \\
\langle \Pi_{ij}^{*(T)}(\mathbf{k}) \Pi_{tl}^{(T)}(\mathbf{k}') \rangle &= (P_{ia}(\mathbf{k}) P_{jb}(\mathbf{k}) - \frac{1}{2} P_{ij}(\mathbf{k}) P_{ab}(\mathbf{k})) \times \\
& (P_{tc}(\mathbf{k}') P_{ld}(\mathbf{k}') - \frac{1}{2} P_{tl}(\mathbf{k}') P_{cd}(\mathbf{k}')) \langle \tau_{ab}^*(\mathbf{k}) \tau_{cd}(\mathbf{k}') \rangle, \quad (5.12)
\end{aligned}$$

Such convolutions can be written in terms of spectra as follows:

$$\begin{aligned}\langle \Pi^{*(S)}(\mathbf{k})\Pi^{(S)}(\mathbf{k}') \rangle &= |\Pi^{(S)}(k)|^2 \delta(\mathbf{k} - \mathbf{k}') \\ \langle \Pi_i^{*(V)}(\mathbf{k})\Pi_j^{(V)}(\mathbf{k}') \rangle &= \frac{1}{2} |\Pi^{(V)}(k)|^2 P_{ij}(\mathbf{k}) \delta(\mathbf{k} - \mathbf{k}') \\ \langle \Pi_{ij}^{*(T)}(\mathbf{k})\Pi_{tl}^{(T)}(\mathbf{k}') \rangle &= \frac{1}{4} |\Pi^{(T)}(k)|^2 \mathcal{M}_{ijtl}(\mathbf{k}) \delta(\mathbf{k} - \mathbf{k}'),\end{aligned}$$

where $\mathcal{M}_{ijtl} = P_{it}P_{jl} + P_{il}P_{jt} - P_{ij}P_{tl}$. With this choice the spectra take the form:

$$|\rho_B(k)|^2 = \frac{1}{1024\pi^5} \int d\mathbf{p} P_B(p) P_B(|\mathbf{k} - \mathbf{p}|) (1 + \mu^2) \quad (5.13)$$

$$\begin{aligned}|\Pi^{(V)}(k)|^2 &= \frac{1}{512\pi^5} \int d\mathbf{p} P_B(p) P_B(|\mathbf{k} - \mathbf{p}|) \times \\ &\quad [(1 + \beta^2)(1 - \gamma^2) + \gamma\beta(\mu - \gamma\beta)]\end{aligned} \quad (5.14)$$

$$\begin{aligned}|\Pi^{(T)}(k)|^2 &= \frac{1}{512\pi^5} \int d\mathbf{p} P_B(p) P_B(|\mathbf{k} - \mathbf{p}|) \times \\ &\quad (1 + 2\gamma^2 + \gamma^2\beta^2),\end{aligned} \quad (5.15)$$

where $\mu = \hat{\mathbf{p}} \cdot (\mathbf{k} - \mathbf{p}) / |\mathbf{k} - \mathbf{p}|$, $\gamma = \hat{\mathbf{k}} \cdot \hat{\mathbf{p}}$, $\beta = \hat{\mathbf{k}} \cdot (\mathbf{k} - \mathbf{p}) / |\mathbf{k} - \mathbf{p}|$. These equations agree, within our Fourier convention, with previous results by [70, 72]. The analysis of scalar magnetic perturbations requires the Fourier power spectra of both Lorentz force and scalar anisotropic stress:

$$\begin{aligned}|L(k)|^2 &= \frac{1}{128\pi^2 a^8} \int d^3p P_B(\mathbf{p}) P_B(|\mathbf{k} - \mathbf{p}|) [1 + \mu^2 + 4\gamma\beta(\gamma\beta - \mu)], \\ |\sigma_B(k)|^2 &= \frac{1}{288\pi^2 a^8} \int d^3p P_B(p) P_B(|\mathbf{k} - \mathbf{p}|) \times \\ &\quad [9(1 - \gamma^2)(1 - \beta^2) - 6(1 + \gamma\mu\beta - \gamma^2 - \beta^2)(1 + \mu^2)].\end{aligned} \quad (5.16)$$

Magnetic energy density, Lorentz force and scalar anisotropic stress are related by Eq. 4.13, hence it is necessary to compute only two of the three convolutions. We chose to compute the energy density and the Lorentz force deriving the anisotropic stress from Eq. 4.13.

5.2.1 PMF EMT spectrum integration technique

The convolutions for the PMF EMT components are rather complicated and require a particular integration technique. The worst complication is

caused by the sharp cut off at k_D in the PMF power spectrum. The sharp cut off imposes the following condition on the PMF power spectrum:

$$\begin{aligned} P_B(k) &= A k^{n_B} \quad \text{for } k \leq k_D \\ P_B(k) &= 0 \quad \text{for } k > k_D, \end{aligned}$$

where the condition must be verified independently on the power spectrum argument. In particular for the convolutions this leads to:

$$\begin{aligned} p &< k_D \\ |\mathbf{k} - \mathbf{p}| &< k_D, \end{aligned} \tag{5.17}$$

the second condition translates into:

$$\sqrt{k^2 + p^2 - 2kp\gamma} < k_D, \tag{5.18}$$

where we defined $\gamma = \cos\theta$. This condition is crucial, it imposes a condition on the angular integration and splits both the angular and the radial integration domains into multiple parts. We rescale the main variables k and p : $\tilde{k} = k/k_D$ and $\tilde{p} = p/k_D$ so that $0 < \tilde{p} < 1$. With the rescaling the condition of Eq. 5.18 translates in:

$$\gamma > \frac{\tilde{k}^2 + \tilde{p}^2 - 1}{2\tilde{k}\tilde{p}}. \tag{5.19}$$

We have to check the compatibility of the Eq. 5.18 condition with the natural integration bounds of the cosine function ($-1 < \gamma < 1$). First we check the lower bound:

$$\frac{\tilde{k}^2 + \tilde{p}^2 - 1}{2\tilde{k}\tilde{p}} > -1 \tag{5.20}$$

this condition is verified for $\tilde{p} > 1 - \tilde{k}$, therefore for $1 - \tilde{k} < \tilde{p} < 1$ the angular integration lower bound is: $\gamma > \frac{\tilde{k}^2 + \tilde{p}^2 - 1}{2\tilde{k}\tilde{p}}$, whereas for $0 < \tilde{p} < 1 - \tilde{k}$ it remains $\gamma > -1$. The upper bound condition then applies only to $1 - \tilde{k} < \tilde{p} < 1$:

$$\frac{\tilde{k}^2 + \tilde{p}^2 - 1}{2\tilde{k}\tilde{p}} < 1 \tag{5.21}$$

this condition is verified for every \tilde{p} for $0 < \tilde{k} < 1$, whereas in the interval $1 < \tilde{k} < 2$ is verified if $\tilde{k} - 1 < \tilde{p} < 1$. Since $\tilde{p} < 1$ we have that for $\tilde{k} > 2$ this

condition is never verified, therefore the angular integral collapses leading to a vanishing power spectrum. This demonstrates that EMT components are non zero only for $0 < \tilde{k} < 2$ and $0 < k < 2k_D$. Summarizing the integration scheme is:

$$\begin{aligned}
& 1) \quad 0 < \tilde{k} < 1 \\
& \quad \int_0^{1-\tilde{k}} dp \int_{-1}^1 d\gamma \cdots + \int_{1-\tilde{k}}^1 d\tilde{p} \int_{\frac{\tilde{k}^2+\tilde{p}^2-1}{2\tilde{k}\tilde{p}}}^1 d\gamma \\
& 2) \quad 1 < \tilde{k} < 2 \\
& \quad \int_{\tilde{k}-1}^1 d\tilde{p} \int_{\frac{\tilde{k}^2+\tilde{p}^2-1}{2\tilde{k}\tilde{p}}}^1 d\gamma. \tag{5.22}
\end{aligned}$$

Once performed the angular integrations the appearance of terms proportional to $|\tilde{k}-\tilde{p}|^{n_B}$ in the radial integrand functions makes necessary a further splitting of the radial integration domain. Before performing the radial integration it is necessary to solve the modulus and therefore to consider the sign of the term $\tilde{k}-\tilde{p}$. We start with the sector $0 < \tilde{k} < 1$:

$$\begin{aligned}
0 < \tilde{p} < 1 - \tilde{k} &\rightarrow \begin{cases} k < 1/2 & \begin{cases} 0 < \tilde{p} < k & \text{with } |\tilde{k}-\tilde{p}| = \tilde{k}-\tilde{p} \\ \tilde{k} < \tilde{p} < 1-\tilde{k} & \text{with } |\tilde{k}-\tilde{p}| = \tilde{p}-\tilde{k} \end{cases} \\ k > 1/2 & 0 < \tilde{p} < 1-\tilde{k} \quad \text{with } |\tilde{k}-\tilde{p}| = \tilde{k}-\tilde{p} \end{cases} \\
1 - \tilde{k} < \tilde{p} < 1 &\rightarrow \begin{cases} k < 1/2 & 1-\tilde{k} < \tilde{p} < 1 \quad \text{with } |\tilde{k}-\tilde{p}| = \tilde{p}-\tilde{k} \\ k > 1/2 & \begin{cases} 1-\tilde{k} < \tilde{p} < \tilde{k} & \text{with } |\tilde{k}-\tilde{p}| = \tilde{k}-\tilde{p} \\ k < \tilde{p} < 1 & \text{with } |\tilde{k}-\tilde{p}| = \tilde{p}-\tilde{k} \end{cases} \end{cases}
\end{aligned}$$

For the sector $1 < \tilde{k} < 2$ instead we have:

$$1 - \tilde{k} < \tilde{p} < 1 \rightarrow \begin{cases} 1 < k < 2 & 1 - \tilde{k} < \tilde{p} < 1 \quad \text{with } |\tilde{k}-\tilde{p}| = \tilde{k}-\tilde{p} \end{cases}$$

Using this integration technique we were able to solve analytically the EMT power spectrum convolutions as an original result of this thesis [83, 75].

5.2.2 PMF EMT power spectrum general behavior and comparison

Before going into details with the analytical results for the single components of the EMT, we wish to discuss some common features of the resulting spectra. Since the damping scale of PMFs is very small, the part of the EMT spectra which contributes to CMB anisotropies is the infrared part $k \ll k_D$. All the EMT components have similar infrared spectral behaviors which differ one from the other only by numerical factors. We consider as example the infrared limit of the energy density spectrum (for $n_B \neq -3/2$):

$$|\rho_B(\tilde{k})|_{k \ll k_D} = \frac{4}{3 + 2n_B} - \tilde{k} - \tilde{k}^{3+2n_B} \frac{2^{-(3+2n_B)}(3 + n_B(2 + n_B))\sqrt{\pi}\Gamma[2 + n_B]}{n_B^2(2 + n_B)\Gamma\left[\frac{5}{2} + n_B\right]}, \quad (5.23)$$

where Γ is the Gamma function [47]. We note that the main feature of the spectrum is the change of behavior with the spectral index. In particular, the spectrum is white noise dominated for indices greater than $n_B > -3/2$, whereas it becomes infrared dominated, as \tilde{k}^{3+2n_B} , for indices $-3 < n_B < -3/2$. This peculiar spectral behavior is crucial for the impact of PMFs on cosmological perturbations. We will show in the next chapter how CMB magnetic anisotropies depend on the shape of the EMT power spectra. In Fig. 5.1 we show the comparison of the different spectra for $n_B = 2$ and $n_B = -5/2$. We note how the dominant Fourier spectrum is the tensor one, Lorentz force and energy density are at the same level and the vector one is subdominant. We will show in the next chapter how the importance of the PMF contributions on CMB anisotropies does not reflect the amplitude of the EMT spectra. We note also the different spectral shape between the two spectral indices due to their completely different behaviors.

In the following sections we will show the analytical results for each EMT component.

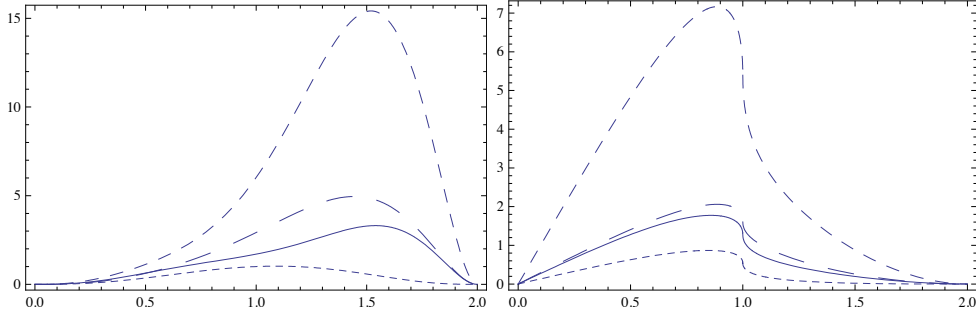


Figure 5.1: Comparison between the EMT component spectra for $n_B = 2$ left and $n_B = -5/2$ right. In the x-axis there is the rescaled wavenumber \tilde{k} whereas on the y-axis there are the EMT spectra (where we have considered only the solution of the convolutions without the $A^2 k_D^{2n_B+3}/(512 \text{ or } 256)\pi^4$ factors) multiplied for \tilde{k}^3 . Short dashed line is the tensor spectrum, solid line is the energy density spectrum, long dashed line is the Lorentz force spectrum, dotted line is the vector spectrum.

5.2.3 Magnetic energy density

In the following we show the analytical results for the magnetic energy density Fourier spectrum for several spectral indices:

$$|\rho_B(k)|_{n_B=3}^2 = \frac{A^2 k_D^9}{512\pi^4} \begin{cases} \frac{4}{9} - \tilde{k} + \frac{20\tilde{k}^2}{21} - \frac{5\tilde{k}^3}{12} + \frac{4\tilde{k}^4}{75} + \frac{4\tilde{k}^6}{315} - \frac{\tilde{k}^9}{1575} & \text{for } 0 \leq \tilde{k} \leq 1 \\ -\frac{4}{9} - \frac{88}{525\tilde{k}} + \frac{13\tilde{k}}{15} - \frac{20\tilde{k}^2}{21} + \frac{17\tilde{k}^3}{36} - \frac{4\tilde{k}^4}{75} - \frac{4\tilde{k}^6}{315} + \frac{\tilde{k}^9}{525} & \text{for } 1 \leq \tilde{k} \leq 2 \end{cases},$$

$$|\rho_B(k)|_{n_B=2}^2 = \frac{A^2 k_D^7}{512\pi^4} \left[4 - \tilde{k} + \frac{8\tilde{k}^2}{15} - \frac{\tilde{k}^5}{24} + \frac{11\tilde{k}^7}{2240} \right],$$

$$|\rho_B(k)|_{n_B=1}^2 = \frac{A^2 k_D^5}{512\pi^4} \begin{cases} \frac{4}{5} - \tilde{k} + \frac{\tilde{k}^3}{4} - \frac{4}{15}\tilde{k}^4 - \frac{\tilde{k}^5}{5} & \text{for } 0 \leq \tilde{k} \leq 1 \\ \frac{8}{15\tilde{k}} - \frac{4}{5} + \frac{\tilde{k}}{3} + \frac{\tilde{k}^3}{4} - \frac{4\tilde{k}^4}{15} + \frac{\tilde{k}^5}{15} & \text{for } 1 \leq \tilde{k} \leq 2 \end{cases},$$

$$|\rho_B(k)|_{n_B=0}^2 = \frac{A^2 k_D^3}{512\pi^4} \left[\frac{29}{24} - \frac{17\tilde{k}}{16} - \frac{7\tilde{k}^2}{8} + \frac{53\tilde{k}^3}{96} + \frac{\pi^2 \tilde{k}^3}{24} - \frac{\log|1-\tilde{k}|}{8\tilde{k}} + \frac{\tilde{k} \log|1-\tilde{k}|}{2} \right. \\ \left. - \frac{3\tilde{k}^3 \log|1-\tilde{k}|}{8} + \frac{\tilde{k}^3 \log|1-\tilde{k}| \log \tilde{k}}{2} - \frac{\tilde{k}^3 \log^2 \tilde{k}}{4} - \frac{\tilde{k}^3 \text{PolyLog} \left[2, \frac{-1+\tilde{k}}{\tilde{k}} \right]}{2} \right],$$

$$|\rho_B(k)|_{n_B=-1}^2 = \frac{A^2 k_D}{512\pi^4} \begin{cases} 4 - 5\tilde{k} + \frac{4\tilde{k}^2}{3} + \frac{\tilde{k}^3}{4} & \text{for } 0 \leq \tilde{k} \leq 1 \\ -4 + \frac{8}{3\tilde{k}} + 3\tilde{k} - \frac{4\tilde{k}^2}{3} + \frac{\tilde{k}^3}{4} & \text{for } 1 \leq \tilde{k} \leq 2 \end{cases},$$

$$|\rho_B(k)|_{n_B=-3/2}^2 = \frac{A^2}{512\pi^4} \begin{cases} \frac{232}{45\sqrt{1-\tilde{k}}} + \frac{88}{15\tilde{k}} - \frac{88}{15\sqrt{1-\tilde{k}\tilde{k}}} - 2\pi + \frac{4\tilde{k}}{3} - \frac{32\tilde{k}}{45\sqrt{1-\tilde{k}}} + \frac{64\tilde{k}^2}{45\sqrt{1-\tilde{k}}} \\ + \frac{\tilde{k}^3}{9} + 8 \log[1 + \sqrt{1-\tilde{k}}] - 4 \log \tilde{k} \\ \text{for } 0 \leq \tilde{k} \leq 1 \\ -\frac{232}{45\sqrt{-1+\tilde{k}}} + \frac{88}{15\tilde{k}} + \frac{88}{15\sqrt{-1+\tilde{k}\tilde{k}}} + \frac{4\tilde{k}}{3} + \frac{32\tilde{k}}{45\sqrt{-1+\tilde{k}}} - \frac{64\tilde{k}^2}{45\sqrt{-1+\tilde{k}}} \\ + \frac{\tilde{k}^3}{9} - 4 \arctan \left[\frac{1}{\sqrt{-1+\tilde{k}}} \right] + 4 \arctan \left[\sqrt{-1+\tilde{k}} \right] \\ \text{for } 1 \leq \tilde{k} \leq 2 \end{cases},$$

$$|\rho_B(k)|_{n_B=-5/2}^2 = \frac{A^2}{512\pi^4 k_D^2} \left[-\frac{32}{75\sqrt{|1-\tilde{k}|}} + \frac{272}{25\sqrt{|1-\tilde{k}|\tilde{k}^2}} + \frac{88}{15\tilde{k}} - \frac{848}{75\sqrt{|1-\tilde{k}|\tilde{k}}} \right. \\ \left. - \frac{4\tilde{k}}{5} + \frac{64\tilde{k}}{75\sqrt{|1-\tilde{k}|}} + \frac{\tilde{k}^3}{25} \right].$$

In Fig. 5.2 we show the comparison between the different spectral index results. We note that the amplitude of the spectra increases with the spectral index. We show also the comparison for the infrared limit $\tilde{k} \rightarrow 0$ and we note the change in the behavior of the spectra. We note how there is a minimum for $n_B = -3/2$ and that the shape changes, accordingly to the analytical spectrum, for redder spectral indices. The complete general solution is very

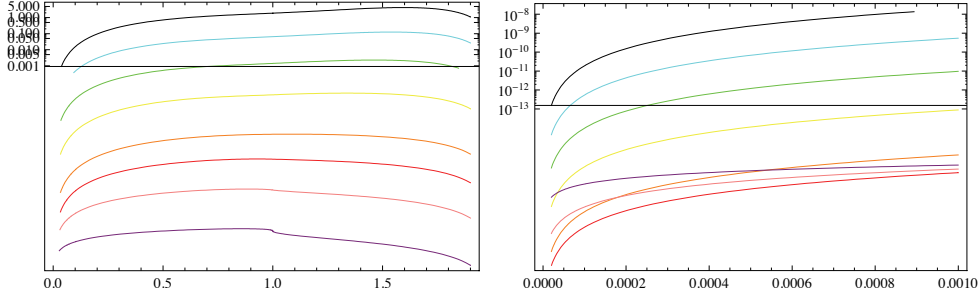


Figure 5.2: Comparison between the magnetic energy density spectra for different spectral indices: black $n_B = 3$, blue $n_B = 2$, green $n_B = 1$, yellow $n_B = 0$, orange $n_B = -1$, red $n_B = -3/2$, pink $n_B = -2$ and purple $n_B = -5/2$. On the x-axis we have the rescaled wavenumber \tilde{k} and on the y-axis we have the logarithm of the energy density (the complete expression for ρ_B which includes the n_B dependent factors $A^2 k_D^{2n_B+3}/(256\pi^4)$) multiplied for \tilde{k}^3 for $B_\lambda = 1$ nG, $\lambda = 1$ Mpc and $h = 0.706$. In the left panel we show the comparison in all the supported wavenumber range $0 < \tilde{k} < 2$ whereas on the right panel we show a focus on the infrared limit.

long, for brevity here we report only the region $0 < \tilde{k} < 1$:

$$\begin{aligned}
|\rho_B(k)|^2 = & \frac{A^2 k_D^{2n_B+3}}{512\pi^4} \left(\frac{2(1-\tilde{k})^{(3+n_B)} k^{n_B} (-1+n_B) {}_2F_1 \left[3+n_B, -n_B, 4+n_B, \frac{(-1+\tilde{k})}{\tilde{k}} \right]}{(n_B(2+n_B)(4+n_B))} \right. \\
& + \frac{2(1-\tilde{k})^{2+n_B} \tilde{k}^{n_B+1} (-1+n_B)(3+n_B) {}_2F_1 \left[2+n_B, -n_B, 3+n_B, \frac{-1+\tilde{k}}{\tilde{k}} \right]}{n_B(2+n_B)^2(4+n_B)} \\
& - \frac{1}{(n_B(1+n_B)(2+n_B)(4+n_B))} 2\tilde{k}^{n_B+2} (1-\tilde{k})^{1+n_B} \times \\
& \left({}_2F_1 \left[1+n_B, 1-n_B, 2+n_B, \frac{(-1+\tilde{k})}{\tilde{k}} \right] + (-1+n_B) \times \right. \\
& \left. {}_2F_1 \left[1+n_B, -n_B, 2+n_B, \frac{(-1+\tilde{k})}{\tilde{k}} \right] \right) \\
& + \frac{2\tilde{k}^{3+n_B} (1-\tilde{k})^{n_B} {}_2F_1 \left[n_B, -n_B, 1+n_B, \frac{-1+\tilde{k}}{\tilde{k}} \right]}{n_B^2(2+n_B)(4+n_B)} \\
& + \frac{1}{4\tilde{k}n_B^2(2+n_B)^2(4+n_B)} (-8(1-\tilde{k})^{n_B} \tilde{k}^3 n_B(2+n_B) \\
& - 8(-1+(1-\tilde{k})^{n_B}) n_B(1+n_B(4+n_B)) + 16(1-\tilde{k})^{n_B} \tilde{k} n_B(1+n_B(4+n_B)) \\
& + \tilde{k}^4(2+n_B)(8-8(1-\tilde{k})^{n_B} + n_B(6+n_B)) \\
& + 4\tilde{k}^2 n_B(-8-6n_B-n_B^2-2(1-\tilde{k})^{n_B}(-1+n_B(3+n_B)))) \\
& \left. - \frac{2^{-3-2n_B} \tilde{k}^{3+2n_B} (3+n_B(2+n_B)) \sqrt{\pi} \Gamma[2+n_B]}{n_B^2(2+n_B) \Gamma\left[\frac{5}{2}+n_B\right]} \right) \tag{5.24}
\end{aligned}$$

where ${}_2F_1$ is the hypergeometric function of second type [47]. We note how the expression for the general solution is very complex and not suitable for a numerical implementation. In order to have a simplified expression which can be used for the numerical implementation, we numerically fitted the leading infrared parts of the analytical spectra, the only relevant part for CMB anisotropies. In the dedicated section we will present the fits.

5.2.4 Lorentz force

In the following we show the analytical results for the Lorentz force Fourier spectrum for several spectral indices:

$$|L(k)|_{n_B=3}^2 = \frac{A^2 k_D^9}{512\pi^4} \begin{cases} \frac{44}{135} - \frac{2\tilde{k}}{3} + \frac{556\tilde{k}^2}{735} - \frac{4\tilde{k}^3}{9} + \frac{164\tilde{k}^4}{1575} + \frac{4\tilde{k}^6}{2079} - \frac{11\tilde{k}^9}{11025} \\ \text{for } 0 \leq \tilde{k} \leq 1 \\ -\frac{44}{135} + \frac{64}{24255\tilde{k}^5} - \frac{16}{945\tilde{k}^3} + \frac{88}{525\tilde{k}} + \frac{2\tilde{k}}{3} - \\ \frac{556\tilde{k}^2}{735} + \frac{4\tilde{k}^3}{9} - \frac{164\tilde{k}^4}{1575} - \frac{4\tilde{k}^6}{2079} + \frac{11\tilde{k}^9}{33075} \\ \text{for } 1 \leq \tilde{k} \leq 2 \end{cases} .$$

$$|L(k)|_{n_B=2}^2 = \frac{A^2 k_D^7}{512\pi^4} \left[\frac{44}{105} - \frac{2\tilde{k}}{3} + \frac{8\tilde{k}^2}{15} - \frac{\tilde{k}^3}{6} - \frac{\tilde{k}^5}{240} + \frac{13\tilde{k}^7}{6720} \right] .$$

$$|L(k)|_{n=1}^2 = \frac{A^2 k_D^5}{512\pi^4} \begin{cases} \frac{44}{75} - \frac{2\tilde{k}}{3} + \frac{32\tilde{k}^2}{105} + \frac{4\tilde{k}^4}{315} - \frac{\tilde{k}^5}{25} \\ \text{for } 0 \leq \tilde{k} \leq 1 \\ -\frac{44}{75} + \frac{64}{1575\tilde{k}^5} - \frac{16}{105\tilde{k}^3} + \frac{8}{15\tilde{k}} + \frac{2\tilde{k}}{3} - \frac{32\tilde{k}^2}{105} - \frac{4\tilde{k}^4}{315} + \frac{\tilde{k}^5}{75} \\ \text{for } 1 \leq \tilde{k} \leq 2 \end{cases} .$$

$$|L(k)|_{n_B=0}^2 = \frac{A^2 k_D^3}{512\pi^4} \left[\frac{43}{48} - \frac{1}{16\tilde{k}^4} - \frac{1}{32\tilde{k}^3} + \frac{7}{48\tilde{k}^2} + \frac{13}{192\tilde{k}} - \frac{67\tilde{k}}{96} + \frac{\tilde{k}^2}{48} + \frac{17\tilde{k}^3}{384} \right. \\ \left. - \frac{\log|1-k|}{16\tilde{k}^5} + \frac{\log|1-k|}{6\tilde{k}^3} - \frac{\log|1-k|}{8\tilde{k}} + \frac{\tilde{k}^3 \log|1-k|}{48} \right] .$$

$$|L(k)|_{n_B=-1}^2 = \frac{A^2 k_D}{512\pi^4} \begin{cases} \frac{44}{15} - 2\tilde{k} - \frac{4\tilde{k}^2}{105} & \text{for } 0 \leq \tilde{k} \leq 1 \\ -\frac{44}{15} - \frac{64}{105\tilde{k}^5} + \frac{16}{15\tilde{k}^3} + \frac{8}{3\tilde{k}} + \frac{2\tilde{k}}{3} + \frac{4\tilde{k}^2}{105} & \text{for } 1 \leq \tilde{k} \leq 2 \end{cases} .$$

$$|L(k)|_{n=-3/2}^2 = \frac{A^2}{512\pi^4} \left\{ \begin{array}{l} \frac{10616}{1755\sqrt{1-\tilde{k}}} - \frac{2048}{2925\tilde{k}^5} + \frac{2048}{2925\sqrt{1-\tilde{k}}\tilde{k}^5} - \frac{22\pi}{15} + \frac{128}{135\tilde{k}^3} \\ - \frac{9088}{8775\sqrt{1-\tilde{k}}\tilde{k}^3} + \frac{88}{15\tilde{k}} - \frac{10136}{1775\sqrt{1-\tilde{k}}\tilde{k}} + \frac{32\tilde{k}}{1755\sqrt{1-\tilde{k}}} \\ - \frac{64\tilde{k}^2}{1775\sqrt{1-\tilde{k}}} + \frac{88 \log[1+\sqrt{1-\tilde{k}}]}{15} - \frac{44 \log \tilde{k}}{15} \\ \text{for } 0 \leq \tilde{k} \leq 1 \\ - \frac{10616}{1755\sqrt{-1+\tilde{k}}} - \frac{2048}{2925\tilde{k}^5} - \frac{2048}{2925\sqrt{-1+\tilde{k}}\tilde{k}^5} \\ + \frac{1024}{2925\sqrt{-1+\tilde{k}}\tilde{k}^4} + \frac{128}{135\tilde{k}^3} + \frac{9088}{8775\sqrt{-1+\tilde{k}}\tilde{k}^3} \\ - \frac{3776}{8775\sqrt{-1+\tilde{k}}\tilde{k}^2} + \frac{88}{15\tilde{k}} + \frac{10136}{1755\sqrt{-1+\tilde{k}}\tilde{k}} \\ - \frac{32\tilde{k}}{1775\sqrt{-1+\tilde{k}}} + \frac{64\tilde{k}^2}{1775\sqrt{-1+\tilde{k}}} \\ - \frac{44 \arctan \left[\frac{1}{\sqrt{-1+\tilde{k}}} \right]}{15} + \frac{44 \arctan \left[\sqrt{-1+\tilde{k}} \right]}{15} \\ \text{for } 1 \leq \tilde{k} \leq 2 \end{array} \right.$$

$$|L(k)|_{n_B=-5/2}^2 = \frac{A^2}{512\pi^4 k_D^2} \left[- \frac{32}{1155\sqrt{|1-\tilde{k}|}} + \frac{2048}{1155\tilde{k}^5} - \frac{2048}{1155\sqrt{|1-\tilde{k}}\tilde{k}^5} + \right. \\ \left. \frac{1024}{1155\sqrt{|1-\tilde{k}}\tilde{k}^4} - \frac{128}{105\tilde{k}^3} + \frac{1664}{1155\sqrt{|1-\tilde{k}}\tilde{k}^3} + \frac{12976}{1155\sqrt{|1-\tilde{k}}\tilde{k}^2} + \right. \\ \left. \frac{88}{15\tilde{k}} - \frac{13648}{1155\sqrt{|1-\tilde{k}}\tilde{k}} + \frac{64\tilde{k}}{1155\sqrt{|1-\tilde{k}|}} \right]$$

In Fig. 5.3 we show the comparison between the results for the different spectral indices. We note how again the amplitude of the spectra increases with the spectral index. We note also that the Lorentz force shows the same infrared behavior of the energy density with a minimum for $n_B = -3/2$ and then a change in the behavior. Also for the Lorentz force the complete result for a generic n_B is rather long and we prefer to present it in the appendix A.1.

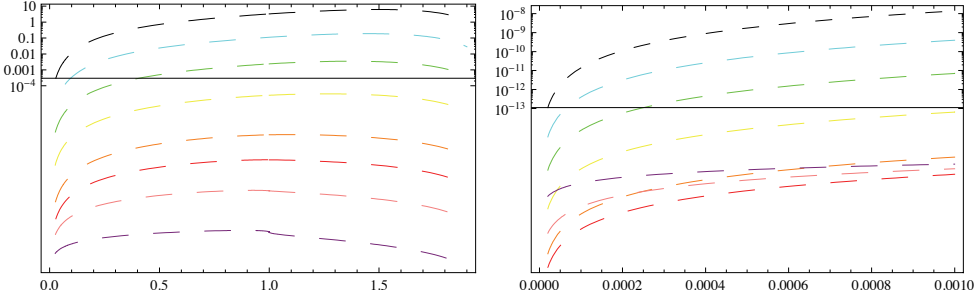


Figure 5.3: Comparison between the Lorentz force spectra for different spectral indices: black $n_B = 3$, blue $n_B = 2$, green $n_B = 1$, yellow $n_B = 0$, orange $n_B = -1$, red $n_B = -3/2$, pink $n_B = -2$ and purple $n_B = -5/2$. On the x-axis we have the rescaled wavenumber \tilde{k} and on the y-axis we have the logarithm of the Lorentz force (including the factors $A^2 k_D^{2n_B+3}/(256\pi^4)$) multiplied for \tilde{k}^3 for $B_\lambda = 1$ nG, $\lambda = 1$ Mpc and $h = 0.706$. In the left panel we show the comparison in all the supported wavenumber range $0 < \tilde{k} < 2$ whereas on the right panel we show a focus on the infrared limit.

5.2.5 Vector EMT spectrum

In the following we show the analytical results for the vector Fourier spectrum for various spectral indices:

$$|\Pi_B^{(V)}(k)|_{n_B=3}^2 = \frac{A^2 k_D^9}{256\pi^4} \begin{cases} \frac{28}{135} - \frac{5\tilde{k}}{12} + \frac{296\tilde{k}^2}{735} - \frac{2\tilde{k}^3}{9} + \frac{92\tilde{k}^4}{1575} - \frac{32\tilde{k}^6}{10395} + \frac{2\tilde{k}^9}{11025} \\ \text{for } 0 \leq \tilde{k} \leq 1 \\ -\frac{28}{135} - \frac{32}{24255\tilde{k}^5} + \frac{4}{945\tilde{k}^3} \\ + \frac{44}{525\tilde{k}} + \frac{23\tilde{k}}{60} - \frac{296\tilde{k}^2}{735} + \frac{2\tilde{k}^3}{9} - \frac{92\tilde{k}^4}{1575} + \frac{32\tilde{k}^6}{10395} - \frac{2\tilde{k}^9}{33075} \\ \text{for } 1 \leq \tilde{k} \leq 2 \end{cases},$$

$$|\Pi_B^{(V)}(k)|_{n_B=2}^2 = \frac{A^2 k_D^7}{256\pi^4} \left[\frac{4}{15} - \frac{5\tilde{k}}{12} + \frac{4\tilde{k}^2}{15} - \frac{\tilde{k}^3}{12} + \frac{7\tilde{k}^5}{960} - \frac{\tilde{k}^7}{1920} \right],$$

$$|\Pi_B^{(V)}(k)|_{n_B=1}^2 = \frac{A^2 k_D^5}{256\pi^4} \begin{cases} \frac{28}{75} - \frac{5\tilde{k}}{12} + \frac{4\tilde{k}^2}{35} - \frac{8\tilde{k}^4}{315} + \frac{\tilde{k}^5}{50} \\ \text{for } 0 \leq \tilde{k} \leq 1 \\ -\frac{32}{1575\tilde{k}^5} + \frac{4}{105\tilde{k}^3} + \frac{4}{15\tilde{k}} - \frac{28}{75} + \frac{\tilde{k}}{4} - \frac{4\tilde{k}^2}{35} + \frac{8\tilde{k}^4}{315} - \frac{\tilde{k}^5}{150} \\ \text{for } 1 \leq \tilde{k} \leq 2 \end{cases},$$

$$|\Pi_B^{(V)}(k)|_{n_B=0}^2 = \frac{A^2 k_D^3}{256\pi^4} \left[\frac{53}{96} + \frac{1}{32\tilde{k}^4} + \frac{1}{64\tilde{k}} - \frac{1}{32\tilde{k}^2} - \frac{5}{384\tilde{k}} - \frac{29\tilde{k}}{64} - \frac{5\tilde{k}^2}{96} + \frac{55\tilde{k}^3}{768} \right. \\ \left. + \frac{\log|1-\tilde{k}|}{32\tilde{k}^5} - \frac{\log|1-\tilde{k}|}{24\tilde{k}^3} - \frac{\log|1-\tilde{k}|}{16\tilde{k}} + \frac{\tilde{k}\log|1-\tilde{k}|}{8} - \frac{5\tilde{k}\log|1-\tilde{k}|}{96} \right],$$

$$|\Pi_B^{(V)}(k)|_{n_B=-1}^2 = \frac{A^2 k_D}{256\pi^4} \begin{cases} \frac{28}{15} - \frac{7\tilde{k}}{4} + \frac{16\tilde{k}^2}{105} & \text{for } 0 \leq \tilde{k} \leq 1 \\ -\frac{28}{15} + \frac{32}{105\tilde{k}^5} - \frac{4}{15\tilde{k}^3} + \frac{4}{3\tilde{k}} + \frac{11\tilde{k}}{12} - \frac{16\tilde{k}^2}{105} & \text{for } 1 \leq \tilde{k} \leq 2 \end{cases},$$

$$|\Pi_B^{(V)}(k)|_{n_B=-3/2}^2 = \frac{A^2}{256\pi^4} \begin{cases} \left(\frac{4936}{1755\sqrt{1-\tilde{k}}} + \frac{1024}{2925\tilde{k}^5} - \frac{1024}{2925\sqrt{1-\tilde{k}}\tilde{k}^5} - \frac{14\pi}{15} \right. \\ \left. + \frac{512}{2925\sqrt{1-\tilde{k}}\tilde{k}^4} - \frac{32}{135\tilde{k}^3} + \frac{2464}{8775\sqrt{1-\tilde{k}}\tilde{k}^3} \right. \\ \left. - \frac{848}{8775\sqrt{1-\tilde{k}}\tilde{k}^2} + \frac{44}{15\tilde{k}} - \frac{5176}{1755\sqrt{1-\tilde{k}}\tilde{k}} + \frac{\tilde{k}}{3} \right. \\ \left. - \frac{224\tilde{k}}{1755\sqrt{1-\tilde{k}}} + \frac{448\tilde{k}^2}{1755\sqrt{1-\tilde{k}}} + \frac{56\log[1+\sqrt{1-\tilde{k}}]}{15} - \frac{28\log\tilde{k}}{15} \right) \\ \text{for } 0 \leq \tilde{k} \leq 1 \\ \left(-\frac{4936}{1755\sqrt{-1+\tilde{k}}} + \frac{1024}{2925\tilde{k}^5} + \frac{1024}{2925\sqrt{-1+\tilde{k}}\tilde{k}^5} \right. \\ \left. - \frac{512}{2925\sqrt{-1+\tilde{k}}\tilde{k}^4} - \frac{32}{135\tilde{k}^3} - \frac{2464}{8775\sqrt{-1+\tilde{k}}\tilde{k}^3} + \frac{848}{8775\sqrt{-1+\tilde{k}}\tilde{k}^2} \right. \\ \left. + \frac{44}{15\tilde{k}} + \frac{5176}{1755\sqrt{-1+\tilde{k}}\tilde{k}} + \frac{\tilde{k}}{3} \right. \\ \left. + \frac{224\tilde{k}}{1755\sqrt{-1+\tilde{k}}} - \frac{448\tilde{k}^2}{1755\sqrt{-1+\tilde{k}}} - \frac{28\arctan\left[\frac{1}{\sqrt{-1+\tilde{k}}}\right]}{15} \right. \\ \left. + \frac{28\arctan\left[\sqrt{-1+\tilde{k}}\right]}{15} \right) \\ \text{for } 1 \leq \tilde{k} \leq 2 \end{cases},$$

$$|\Pi_B^{(V)}(k)|_{n_B=-5/2}^2 = \frac{A^2}{256\pi^4 k_D^2} \left[-\frac{32}{231\sqrt{|1-\tilde{k}|}} - \frac{1024}{1155\tilde{k}^5} + \frac{1024}{1155\sqrt{|1-\tilde{k}|}\tilde{k}^5} \right. \\ \left. - \frac{512}{1155\sqrt{|1-\tilde{k}|}\tilde{k}^4} + \frac{32}{105\tilde{k}^3} - \frac{32}{77\sqrt{|1-\tilde{k}|}\tilde{k}^3} + \frac{896}{165\sqrt{|1-\tilde{k}|}\tilde{k}^2} + \frac{44}{15\tilde{k}} \right. \\ \left. - \frac{6464}{1155\sqrt{|1-\tilde{k}|}\tilde{k}} - \frac{\tilde{k}}{5} + \frac{64\tilde{k}}{231\sqrt{|1-\tilde{k}|}} \right]$$

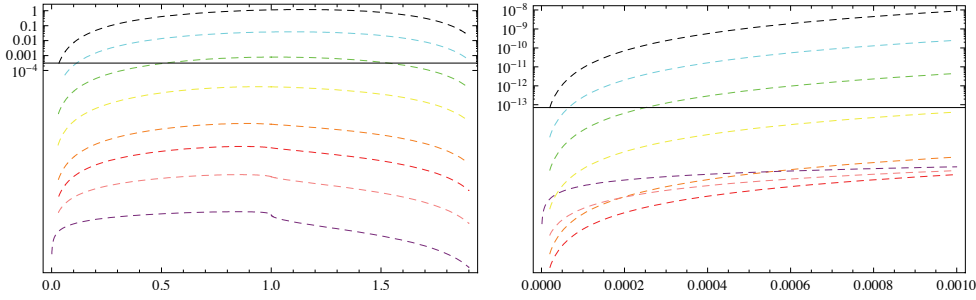


Figure 5.4: Comparison between the vector spectra for different spectral indices: black $n_B = 3$, blue $n_B = 2$, green $n_B = 1$, yellow $n_B = 0$, orange $n_B = -1$, red $n_B = -3/2$, pink $n_B = -2$ and purple $n_B = -5/2$. On the x-axis we have the rescaled wavenumber \tilde{k} and on the y-axis we have the logarithm of the vector spectrum (including the factors $A^2 k_D^{2n_B+3}/(512\pi^4)$) multiplied for \tilde{k}^3 . for $B_\lambda = 1$ nG, $\lambda = 1$ Mpc and $h = 0.706$. In the left panel we show the comparison in all the supported wavenumber range $0 < \tilde{k} < 2$ whereas on the right panel we show a focus on the infrared limit.

The solutions for generic spectral index for vector and also tensor Fourier spectra are longer and more complicated than the magnetic energy density and Lorentz force ones. Since they are not necessary to the purpose of our analysis for sake of brevity we omit them. In Fig. 5.4 we show the comparison between the results for different spectral indices. We note that the vector spectrum presents the same spectral behavior of the Lorentz force and magnetic energy density.

5.2.6 Tensor EMT spectrum

In the following we show the analytical results for the tensor Fourier spectrum for various spectral indices:

$$|\Pi_B^{(T)}(k)|_{n_B=3}^2 = \frac{A^2 k_D^9}{256\pi^4 k_*^6} \begin{cases} \frac{56}{135} - \frac{7\tilde{k}}{6} + \frac{1112\tilde{k}^2}{735} - \frac{127\tilde{k}^3}{144} \\ + \frac{296\tilde{k}^4}{1575} + \frac{104\tilde{k}^6}{10395} - \frac{29\tilde{k}^9}{11025} \\ \text{for } 0 \leq \tilde{k} \leq 1 \\ -\frac{56}{135} + \frac{16}{24255\tilde{k}^5} + \frac{8}{945\tilde{k}^3} + \frac{32}{525\tilde{k}} + \frac{37\tilde{k}}{30} \\ - \frac{1112\tilde{k}^2}{735} + \frac{43\tilde{k}^3}{48} - \frac{296\tilde{k}^4}{1575} - \frac{104\tilde{k}^6}{10395} + \frac{29\tilde{k}^9}{33075} \\ \text{for } 1 \leq \tilde{k} \leq 2 \end{cases} .$$

$$|\Pi_B^{(T)}(k)|_{n_B=2}^2 = \frac{A^2 k_D^7}{256\pi^4 k_*^4} \left[\frac{8}{15} - \frac{7\tilde{k}}{6} + \frac{16\tilde{k}^2}{15} - \frac{7\tilde{k}^3}{24} - \frac{13\tilde{k}^5}{480} + \frac{11\tilde{k}^7}{1920} \right] .$$

$$|\Pi_B^{(T)}(k)|_{n_B=1}^2 = \frac{A^2 k_D^5}{256\pi^4 k_*^2} \begin{cases} \frac{56}{75} - \frac{7\tilde{k}}{6} + \frac{64\tilde{k}^2}{105} - \frac{\tilde{k}^3}{16} + \frac{8\tilde{k}^4}{63} - \frac{4\tilde{k}^5}{25} \\ \text{for } 0 \leq \tilde{k} \leq 1 \\ \frac{16}{1575\tilde{k}^5} + \frac{8}{105\tilde{k}^3} - \frac{56}{75} + \frac{3\tilde{k}}{2} - \frac{64\tilde{k}^2}{105} + \frac{\tilde{k}^3}{16} - \frac{8\tilde{k}^4}{63} - \frac{4\tilde{k}^5}{75} \\ \text{for } 1 \leq \tilde{k} \leq 2 \end{cases} .$$

$$|\Pi_B^{(T)}(k)|_{n_B=0}^2 = \frac{A^2 k_D^3}{256\pi^4} \left[\frac{293}{192} - \frac{1}{64\tilde{k}^4} - \frac{1}{128\tilde{k}} - \frac{17}{192\tilde{k}^2} - \frac{35}{768\tilde{k}} - \frac{397\tilde{k}}{384} - \frac{17\tilde{k}^2}{192} \right. \\ + \frac{181\tilde{k}^3}{1536} + \frac{\pi^2\tilde{k}^3}{96} - \frac{\log|1-\tilde{k}|}{64\tilde{k}^5} - \frac{\log|1-\tilde{k}|}{12\tilde{k}^3} + \frac{5\log|1-\tilde{k}|}{16\tilde{k}} \\ - \frac{\tilde{k}\log|1-\tilde{k}|}{4} + \frac{7\tilde{k}^3\log|1-\tilde{k}|}{192} + \frac{\tilde{k}^3\log|1-\tilde{k}|\log\tilde{k}}{8} - \frac{\tilde{k}^3\log^2\tilde{k}}{16} \\ \left. - \frac{\tilde{k}^3 \text{PolyLog}[2, \frac{-1+\tilde{k}}{\tilde{k}}]}{8} \right] .$$

$$|\Pi_B^{(T)}(k)|_{n_B=-1}^2 = \frac{A^2 k_D k_*^2}{256\pi^4} \begin{cases} \frac{56}{15} - \frac{5\tilde{k}}{2} - \frac{8\tilde{k}^2}{105} + \frac{\tilde{k}^3}{16} \\ \text{for } 0 \leq \tilde{k} \leq 1 \\ -\frac{56}{15} - \frac{16}{105\tilde{k}^5} - \frac{8}{15\tilde{k}^3} + \frac{16}{3\tilde{k}} + \frac{\tilde{k}}{6} + \frac{8\tilde{k}^2}{105} + \frac{\tilde{k}^3}{16} \\ \text{for } 1 \leq \tilde{k} \leq 2 \end{cases} .$$

$$\begin{aligned}
|\Pi_B^{(T)}(k)|_{n_B=-3/2}^2 &= \frac{A^2 k_*^3}{256\pi^4} \left\{ \begin{array}{l}
\frac{16304}{1755\sqrt{1-\tilde{k}}} - \frac{512}{2925\tilde{k}^5} + \frac{512}{2925\sqrt{1-\tilde{k}}\tilde{k}^5} - \frac{28\pi}{15} - \frac{256}{2925\sqrt{1-\tilde{k}}\tilde{k}^4} \\
- \frac{64}{135\tilde{k}^3} + \frac{3968}{8775\sqrt{1-\tilde{k}}\tilde{k}^3} - \frac{2176}{8775\sqrt{1-\tilde{k}}\tilde{k}^2} + \frac{28}{3\tilde{k}} - \frac{16496}{1755\sqrt{1-\tilde{k}}\tilde{k}} - \frac{2\tilde{k}}{3} \\
+ \frac{64\tilde{k}}{351\sqrt{1-\tilde{k}}} - \frac{128\tilde{k}^2}{351\sqrt{1-\tilde{k}}} + \frac{\tilde{k}^3}{36} + \\
\frac{112 \log[1+\sqrt{1-\tilde{k}}]}{15} - \frac{56 \log \tilde{k}}{15} \\
\text{for } 0 \leq \tilde{k} \leq 1 \\
- \frac{16304}{1755\sqrt{-1+\tilde{k}}} - \frac{512}{2925\tilde{k}^5} - \frac{512}{2925\sqrt{-1+\tilde{k}}\tilde{k}^5} + \frac{256}{2925\sqrt{-1+\tilde{k}}\tilde{k}^4} - \frac{64}{135\tilde{k}^3} \\
- \frac{3968}{8775\sqrt{-1+\tilde{k}}\tilde{k}^3} + \frac{2176}{8775\sqrt{-1+\tilde{k}}\tilde{k}^2} + \frac{28}{3\tilde{k}} + \frac{16496}{1755\sqrt{-1+\tilde{k}}\tilde{k}} \\
- \frac{2\tilde{k}}{3} - \frac{64\tilde{k}}{351\sqrt{-1+\tilde{k}}} + \frac{128\tilde{k}^2}{351\sqrt{-1+\tilde{k}}} + \frac{\tilde{k}^3}{36} - \frac{56 \arctan\left[\frac{1}{\sqrt{-1+\tilde{k}}}\right]}{15} \\
+ \frac{56 \arctan\left[\sqrt{-1+\tilde{k}}\right]}{15} \\
\text{for } 1 \leq \tilde{k} \leq 2
\end{array} \right. . \\
|\Pi_B^{(T)}(k)|_{n_B=-5/2}^2 &= \frac{A^2 k_*^5}{256\pi^4 k_D^2} \left[\frac{1984}{5775\sqrt{|1-\tilde{k}|}} + \frac{512}{1155\tilde{k}^5} - \frac{512}{1155\sqrt{|1-\tilde{k}}\tilde{k}^5} + \right. \\
&\quad \frac{256}{1155\sqrt{|1-\tilde{k}}\tilde{k}^4} + \frac{64}{105\tilde{k}^3} - \frac{128}{231\sqrt{|1-\tilde{k}}\tilde{k}^3} + \frac{117728}{5775\sqrt{|1-\tilde{k}}\tilde{k}^2} \\
&\quad \left. + \frac{28}{3\tilde{k}} - \frac{37088}{1925\sqrt{|1-\tilde{k}}\tilde{k}}} + \frac{2\tilde{k}}{5} - \frac{3968\tilde{k}}{5775\sqrt{|1-\tilde{k}|}} + \frac{\tilde{k}^3}{100} \right]
\end{aligned}$$

In Fig. 5.5 we show the comparison between results for the different spectral indices. We note that the tensor spectrum presents the same behavior of the magnetic energy density, Lorentz force and vector spectrum: the amplitude of the spectrum increases with the spectral index, whereas the infrared limit reaches the minimum amplitude for $n_B = -3/2$ and then increases for redder indices.

5.2.7 PMF EMT spectral fits

The complexity of the analytical solutions for generic spectral index of the EMT Fourier spectra makes impossible the implementation of the exact spectra into the numerical code we used to study the evolution of magnetic

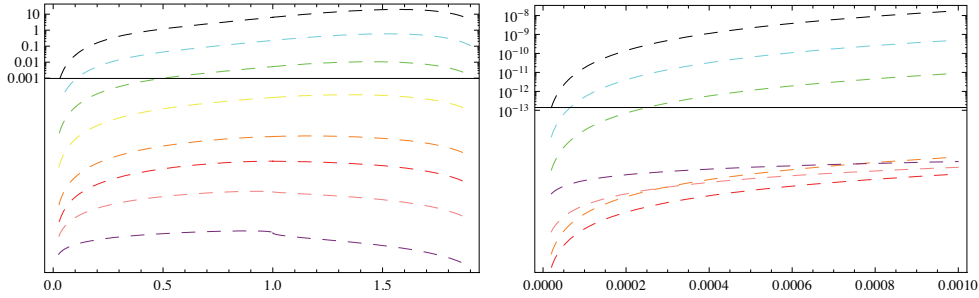


Figure 5.5: Comparison between the tensor spectra for different spectral indices: black $n_B = 3$, blue $n_B = 2$, green $n_B = 1$, yellow $n_B = 0$, orange $n_B = -1$, red $n_B = -3/2$, pink $n_B = -2$ and purple $n_B = -5/2$. On the x-axis we have the rescaled wavenumber \tilde{k} and on the y-axis we have the logarithm of the tensor spectrum (including the factors dependent on the spectral index $A^2 k_D^{2n_B+3}/(526\pi^4)$) multiplied for \tilde{k}^3 for $B_\lambda = 1$ nG, $\lambda = 1$ Mpc and $h = 0.706$. In the left panel we show the comparison in all the supported wavenumber range $0 < \tilde{k} < 2$ whereas on the right panel we show a focus on the infrared limit.

perturbations. To solve this problem we computed numerical fits of the exact spectra [84]. We fitted only the infrared part because it is the only one which contributes to CMB anisotropies. In the next chapter we will show that the magnetic tensor contribution to CMB anisotropies is strongly subdominant with respect to scalar and vector ones, therefore the numerical fits are limited to scalar and vector components.

In order to have the best fit possible we divided the fits in ranges of spectral indices. The first range derives naturally from the change in the infrared behavior between indices greater and smaller than $n_B = -3/2$. The second range derives from numerical reasons and is between positive and negative spectral indices. The leading terms of the fits are simply the infrared leading terms of the exact solutions, whereas higher orders depend on the index.

Scalar Spectra

$$n_B > 0$$

$$|\rho_B(k, n_B)|_{fit}^2 = \frac{A^2 k_D^{2n_B+3}}{512\pi^4 k_*^{2n_B}} \left(\frac{4}{2n_B+3} - \tilde{k} + \sum_{i=1}^3 A_i \tilde{k}^{i+1} + A_4 \tilde{k}^{(2n_B+3)} \right) \quad (5.25)$$

$$-3/2 < n_B < 0$$

$$|\rho_B(k, n_B)|_{fit}^2 = \frac{A^2 k_D^{2n_B+3}}{512\pi^4 k_*^{2n_B}} \left(\frac{4}{2n_B+3} - \tilde{k} + \sum_{i=1}^3 B_i \tilde{k}^{i+1} + B_4 \tilde{k}^{(2n_B+3)} \right) \quad (5.26)$$

$$-2.9 < n_B < -3/2$$

$$|\rho_B(k, n_B)|_{fit}^2 = \frac{A^2 k_D^{2n+3}}{512\pi^4 k_*^{2n_B}} \left(\frac{4}{2n_B+3} - \tilde{k} + C_1 \tilde{k}^{(2n_B+3)} \right) \quad (5.27)$$

Coefficients

For positive spectral indices:

$$A_1 = -0.8998 - \frac{0.03926}{n_B} + 1.419n_B - 0.695n_B^2 + 0.2642n_B^3 - 0.05418n_B^4 + 0.004595n_B^5$$

$$A_2 = 0.3265 + \frac{0.0008383}{n_B} + 0.01671n_B - 0.1016n_B^2 + 0.00989n_B^3 - 0.002607n_B^4 + 0.0002657n_B^5$$

$$A_3 = 11.3 - \frac{1.631}{n_B} - 21.8n_B + 19.66n_B^2 - 9.243n_B^3 + 2.184n_B^4 - 0.2041n_B^5$$

$$A_4 = 0.3919 + \frac{0.3111}{n_B} - 5.899n_B + 9.607n_B^2 - 6.21n_B^3 + 1.79n_B^4 - 0.1918n_B^5$$

for the negative spectral indices we have:

$$B_1 = \frac{1}{5}(-825 - 2848n_B - 3980n_B^2 - 2490n_B^3 - 580n_B^4) - \frac{57}{5n_B}$$

$$B_2 = \frac{1}{50}(15 - 4n_B^2)$$

$$B_3 = \frac{1}{25}(-5 - 11n_B - 8n_B^2 - 3n_B^3)$$

$$B_4 = \frac{171}{25n_B} + \frac{1}{50}(4673 + 12900n_B + 11500n_B^2 + 1950n_B^3 - 1155n_B^4)$$

for strongly infrared:

$$C_1 = -\frac{10527877}{200n_B} + \frac{-126773640 - 114087370n_B - 39615180n_B^2 + 4157430n_B^3}{1000} + \frac{7369110n_B^4 + 2081486n_B^5 + 198571n_B^6}{1000} \quad (5.28)$$

Lorentz Force Spectra

$$n_B > 0$$

$$|L(k, n_B)|_{fit}^2 = \frac{A^2 k_D^{2n_B+3}}{512\pi^4 k_*^{2n_B}} \left(A_1^L - \frac{2}{3}\tilde{k} + A_2^L \tilde{k}^2 + A_3^L \tilde{k}^{2n_B+3} \right) \quad (5.29)$$

$$-3/2 < n_B < 0$$

$$|L(k, n_B)|_{fit}^2 = \frac{A^2 k_D^{2n_B+3}}{512\pi^4 k_*^{2n_B}} \left(B_1^L - \frac{2}{3}\tilde{k} + B_2^L \tilde{k}^{2n_B+3} \right) \quad (5.30)$$

$$-2.9 < n_B < -3/2$$

$$|L(k, n_B)|_{fit}^2 = \frac{A^2 k_D^{2n_B+3}}{512\pi^4 k_*^{2n_B}} \left(C_1^L - \frac{2}{3}\tilde{k} + C_2^L \tilde{k}^{2n_B+3} \right) \quad (5.31)$$

Coefficients

For positive spectral indices:

$$\begin{aligned} A_1^L &= 0.933635 + \frac{0.00460612}{n_B} - 0.505278n_B + 0.183487n_B^2 \\ &\quad - 0.0238037n_B^3 - 0.00985191n_B^4 + 0.00437658n_B^5 - 0.000504247n_B^6 \\ A_2^L &= 0.22309 - \frac{0.021189}{n_B} - 0.152155n_B + 0.427087n_B^2 - 0.184484n_B^3 \\ &\quad - 0.0111374n_B^4 + 0.0292611n_B^5 - 0.00571069n_B^6 \\ A_3^L &= 1.84015 - \frac{0.319013}{n_B} - 3.60452n_B + 2.88574n_B^2 - 0.797507n_B^3 \\ &\quad - 0.145007n_B^4 + 0.116527n_B^5 - 0.0163659n_B^6 \end{aligned}$$

for the negative spectral indices we have:

$$\begin{aligned} B_1^L &= \frac{1}{100}(1630 + 4240n_B + 3360n_B^2 - 2080n_B^3 - 1960n_B^4 + 1970n_B^5 + 1559n_B^6) + \frac{41}{25n_B} \\ B_2^L &= \frac{1}{100}(-854 - 2838n_B - 2710n_B^2 + 1390n_B^3 + 1705n_B^4 - 1530n_B^5 - 1340n_B^6) - \frac{4}{5n_B} \end{aligned}$$

for strongly infrared:

$$\begin{aligned} C_1^L &= \frac{1}{50}(1327860 + 1077425n_B + 321980n_B^2 - 50935n_B^3 - 60380n_B^4 - 15115n_B^5 - 1302n_B^6) \\ &\quad + \frac{60569}{5n_B} \\ C_2^L &= -\frac{241194}{5n_B} + \frac{(-117123100 - 106256700n_B - 37275000n_B^2 + 3787200n_B^3}{1000} \\ &\quad + \frac{6930290n_B^4 + 1971640n_B^5 + 189111n_B^6}{1000} \end{aligned}$$

Vector Spectra

$$n_B > 0$$

$$|\Pi^{(V)}(k, n_B)|_{fit}^2 = \frac{A^2 k_D^{2n_B+3}}{256\pi^4 k_*^{2n_B}} \left(A_1^V - \frac{5}{12} \tilde{k} + A_2^V + A_3^V \tilde{k}^{2n_B+3} \right) \quad (5.32)$$

$$-3/2 < n_B < 0$$

$$|\Pi^{(V)}(k, n_B)|_{fit}^2 = \frac{A^2 k_D^{2n_B+3}}{256\pi^4 k_*^{2n_B}} \left(B_1^V - \frac{5}{12} \tilde{k} + B_2^V \tilde{k}^2 + B_3^V \tilde{k}^{2n_B+3} \right) \quad (5.33)$$

$$-2.9 < n_B < -3/2$$

$$|\Pi^{(V)}(k, n_B)|_{fit}^2 = \frac{A^2 k_D^{2n_B+3}}{256\pi^4 k_*^{2n_B}} \left(C_1^V - \frac{5}{12} \tilde{k} + C_2^V \tilde{k}^{2n_B+3} \right) \quad (5.34)$$

Coefficients

For positive spectral indices:

$$A_1^V = \frac{29500 - 16100n_B + 5850n_B^2 - 765n_B^3 - 314n_B^4 + 140n_B^5 - 16n_B^6}{50000}$$

$$A_2^V = \frac{-845 + 2600n_B - 690n_B^2 + 124n_B^3}{10000}$$

$$A_3^V = \frac{1}{500}(-280 + 545n_B - 425n_B^2 + 112n_B^3)$$

for the negative spectral indices we have:

$$B_1^V = \frac{26}{25n_B} + \frac{1}{100}(1040 + 2698n_B + 2140n_B^2 - 1327n_B^3 - 1249n_B^4 + 1255n_B^5 + 992n_B^6)$$

$$B_2^V = \frac{1}{100}(-2192 - 4681n_B - 2132n_B^2 + 2235n_B^3 + 908n_B^4 - 1464n_B^5 - 744n_B^6) - \frac{53}{20n_B}$$

$$B_3^V = \frac{73}{50n_B} + \frac{1}{100}(1078 + 1616n_B - 243n_B^2 - 735n_B^3 + 471n_B^4 + 59n_B^5 - 342n_B^6)$$

for strongly infrared:

$$C_1^V = \frac{445985}{500n_B} + \frac{(19923100 + 16525360n_B + 5113265n_B^2 - 742742n_B^3 - 956890n_B^4 - 246837n_B^5 - 21843n_B^6)}{1000}$$

$$C_2^V = \frac{-29003653 - 25196700n_B - 8371900n_B^2 + 995460n_B^3}{1000} + \frac{1561850n_B^4 + 429404n_B^5 + 40254n_B^6}{1000} - \frac{124807}{10n_B}$$

All the fits are accurate to more than 1% level.

5.2.8 Cross correlation between energy density and Lorentz force

The PMF contribution to scalar perturbations is given by the magnetic energy density, Lorentz force and anisotropic stress. We showed how these three quantities are not independent one from the other and that the anisotropic stress can be expressed as a function of the other two. Since both Lorentz force and energy density source magnetic scalar perturbations it is necessary to consider their mutual relation. Their cross correlation is given by [80, 81]:

$$\begin{aligned} \langle \rho_B(\mathbf{k}) L_B(\mathbf{k}') \rangle &= \frac{\delta(\mathbf{k} - \mathbf{k}')}{1024\pi^5} \int d\mathbf{p} P_B(p) P_B(|\mathbf{k} - \mathbf{p}|) \\ &\quad \times (1 - 1(\gamma^2 + \beta^2) + 2\gamma\beta\mu - \mu^2). \end{aligned} \quad (5.35)$$

With the same integration technique we developed for the EMT components, it is possible to analytically solve the convolution. The result for $n_B = 2$ is [84]:

$$\langle \rho_B(k) L_B(k) \rangle|_{n_B=2} = \frac{A^2 k_D^7}{1024\pi^5 a^8} \left[-\frac{4}{21} + \frac{\tilde{k}}{2} - \frac{8\tilde{k}^2}{15} + \frac{\tilde{k}^3}{6} + \frac{\tilde{k}^5}{96} - \frac{3\tilde{k}^7}{1120} \right], \quad (5.36)$$

and for $n_B = -5/2$ [84]:

$$\begin{aligned} \langle \rho_B(k) L_B(k) \rangle|_{n_B=-5/2} &= \frac{A^2}{1024\pi^5 a^8 k_D^2} \left[\frac{16(4 - 65\tilde{k} + 59\tilde{k}^2 - 2\tilde{k}^3 + 4\tilde{k}^4)}{(105\sqrt{|1 - \tilde{k}|\tilde{k}^3})} \right. \\ &\quad \left. - \frac{64 + 448\tilde{k}^2 + 42\tilde{k}^4}{105\tilde{k}^3} \right]. \end{aligned} \quad (5.37)$$

The two cross-correlators $\langle \rho_B(k) L_B(k) \rangle$ are shown in Fig. 5.6, where are compared with the magnetic energy density and the Lorentz force [84]. We note that the cross-correlation is negative in the whole range of scales. To study the general behavior of the cross correlation we derived the infrared limit [84]:

$$\begin{aligned} \langle \rho_B(k) L_B(k) \rangle &= -\frac{1}{3} |\rho_B(k)|^2 \text{ for } n_B \geq -3/2 \\ \langle \rho_B(k) L_B(k) \rangle &= -C |\rho_B(k)|^2 \text{ for } n_B < -3/2 \end{aligned}$$

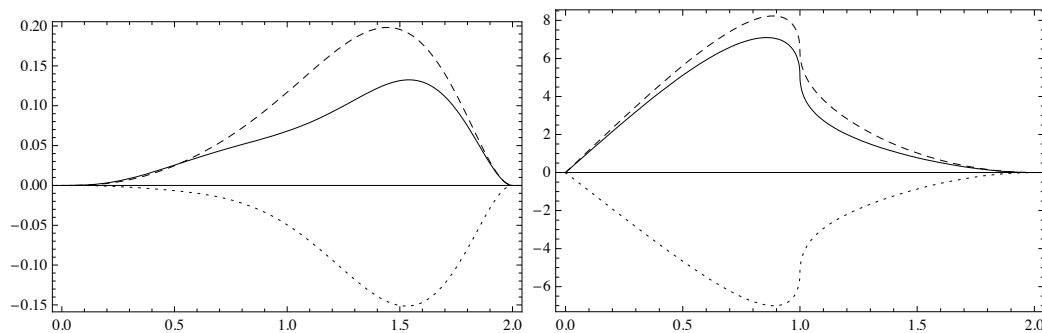


Figure 5.6: The cross-correlator $k^3\langle\rho_B(k)L_B(k)\rangle$ (dotted line) for $n_B = 2$ and $n_B = -5/2$ is plotted versus k/k_D in comparison with $k^3|\rho_B(k)|^2$ (solid line) and $k^3|L_B(k)|^2/U$ (dashed line). The spectrum of the energy density, Lorentz force and of the cross-correlation do not include the n_B dependent prefactors.

where $C \sim \mathcal{O}(1)$. For sake of simplicity for the numerical implementation we chose to approximate Lorentz force and magnetic energy density as fully anticorrelated $\text{sign}[L_B] = -\text{sign}[\rho_B]$. We will show how this approximation does not have a strong impact on CMB anisotropies and in particular it does not affect the constraints on PMFs.

Chapter 6

Magnetized Cosmological Perturbations

PMFs source all types of metric perturbations: scalar, vector and tensor. This section will be dedicated to the analysis of each type of magnetized cosmological perturbations and their contributions to the angular power spectrum of CMB anisotropies in temperature and polarization.

There have been several studies on the subject, some are limited to the study of magnetized scalar perturbations: [69, 73, 74, 76, 85, 86, 88, 90, 94, 101, 102]; other are dedicated to the study of magnetized vector and tensor perturbations: [70, 71, 82, 72, 77, 105, 116, 118]; and the ones which include the treatment of all magnetized perturbations and the derivation of PMF constraints: [79, 80, 81, 87, 89, 91, 92, 93, 95, 96, 97, 99, 100, 103, 104]. The best improvement of our analysis, with respect to the other ones, is the treatment of PMF EMT components and initial conditions. In fact, the exact solutions for the PMF EMT Fourier spectra we have derived, presented in the previous chapter, allowed us to have the first and only exact treatment of magnetized perturbations.

6.1 The scalar sector of magnetized cosmological perturbations

We will begin our analysis with the investigation of magnetized scalar perturbations. Their treatment involves an higher number of variables and equations with respect to vector and tensor ones, therefore the magnetized scalar perturbations analysis is the most complex of the three we will present.

Scalar magnetized perturbations are sourced by the magnetic energy density $\rho_B(k) = -\tau_0^0$ and the scalar magnetic anisotropic stress $\sigma_B(k) = (\hat{k}^i \hat{k}_j - \frac{1}{3} \delta_j^i) \Sigma_j^{i PMF}$, where $\Sigma_j^{i PMF}$ is the transverse and traceless part of PMF EMT.

PMFs gravitate at the level of perturbations and therefore indirectly affect all the components of the cosmological fluid: radiation, neutrinos, dark matter and baryons. Since ionized baryons carry electrical charge they are also directly affected by PMFs. In fact, PMFs induce a Lorentz force on baryons, modifying their velocity. The Lorentz force has an indirect effect also on photons because, prior to the decoupling, baryons are coupled with photons by Compton scattering. During this coupling period, the so-called "tight coupling regime", the two species behave like a single coupled fluid, therefore Lorentz force indirectly acts also on photon velocity. This indirect Lorentz force effect disappears when the tight coupling ends.

6.1.1 Magnetized metric perturbation equations

The evolution of metric perturbations is governed by the perturbed Einstein equations. PMF contribution is represented by the introduction of the PMF EMT as additional source term in the equations:

$$G_{\mu\nu} = 8\pi(T_{\mu\nu}^{Fluid} + \tau_{\mu\nu}), \quad (6.1)$$

where $G_{\mu\nu}$ is the perturbed Einstein tensor and $T_{\mu\nu}^{Fluid}$ is the energy momentum tensor of the fluid. In the synchronous gauge, with the notation of [66],

the metric perturbation equations are:

$$\begin{aligned}
 k^2\eta - \frac{1}{2}\mathcal{H}\dot{\eta} &= -4\pi Ga^2(\Sigma_i\rho_i\delta_i + \rho_B), \\
 k^2\dot{\eta} &= 4\pi Ga^2\Sigma_i(\rho_i + P_i)\theta_i, \\
 \ddot{h} + 2\mathcal{H}\dot{h} - 2k^2\eta &= -8\pi Ga^2\Sigma_i\left(c_{s_i}^2\rho_i\delta_i + \frac{\rho_B}{3}\right), \\
 \ddot{h} + 6\dot{\eta} + 2\mathcal{H}(\dot{h} + 6\dot{\eta}) - 2k^2\eta &= -24\pi Ga^2[\Sigma_i(\bar{\rho}_i + \bar{P}_i)\sigma_i + \sigma_B], \quad (6.2)
 \end{aligned}$$

where i runs over the various plasma species: cold dark matter c , baryons b , photons γ , neutrinos ν .

6.1.2 Fluid equations

The fluid equations for all the components are not affected by PMFs, except for the ionized baryon ones. Carrying electric charge, the conservation equations for baryons in presence of PMFs, require the introduction of an electromagnetic source term:

$$\nabla_\mu T_\nu^\mu = F_\nu^\mu J_\mu,$$

In the infinite conductivity limit $F_0^\mu = 0$, therefore the energy conservation equation is not affected by PMFs and the evolution of the baryon density perturbations is unchanged. The momentum constraint instead becomes:

$$\partial_\mu \delta T_i^\mu + \delta \Gamma_{\alpha\beta}^\alpha T_i^\beta + \Gamma_{\alpha\beta}^\alpha \delta T_i^\beta - \delta \Gamma_{i\beta}^\alpha T_\alpha^\beta - \Gamma_{i\beta}^\alpha \delta T_\alpha^\beta = F_i^j J_j.$$

Substituting the values for the connection coefficients and the components of the baryon EMT we obtain:

$$\dot{w}\rho v_i - 2(1+w)^2\rho v_i + (\rho + P)\dot{v}_i + ik_i\delta P + ik_j\Sigma_i^j + 4\mathcal{H}(\rho + P)v_i = F_i^j J_j, \quad (6.3)$$

where $w = P_b/\rho_b$, v_i is the baryon velocity. Multiplying for ik^i , substituting $\delta P = c_{s_b}^2\delta_b$ and $k^i k_j \Sigma_i^j = k^2\sigma_b$, defining $\theta = ik^i v_i$ and the Lorentz force as $k^2 L_B = k^i F_i^j J_j$ we obtain:

$$\dot{\theta}_b = -(1 - 3w)\mathcal{H}\theta_b - \frac{\dot{w}_b}{(1 + w_b)}\theta_b + \frac{k^2 c_{s_b}^2}{(1 + w_b)}\delta_b - k^2\sigma_b - \frac{k^2 L_B}{\rho_b(1 + w_b)}, \quad (6.4)$$

since baryon pressure and anisotropic stress are negligible, we can fix: $w_b = 0$ and $\sigma_b = 0$:

$$\dot{\theta}_b = -\mathcal{H}\theta_b + k^2 c_s^2 \delta_b - k^2 \frac{L_B}{\rho_b}. \quad (6.5)$$

We note the appearance of the new term $-k^2 \frac{L_B}{\rho_b}$. This term is the contribution of the Lorentz force, which decreases with time as $1/a(\tau)$.

6.1.3 Tight Coupling

The Euler equation for baryons with PMF contribution, prior to the decoupling, is:

$$\dot{\theta}_b = -\mathcal{H}\theta_b + c_s^2 k^2 \delta_b + R\tau_{opt}(\theta_\gamma - \theta_b) - \frac{k^2 L}{\rho_b}, \quad (6.6)$$

where we have included the interaction term with photons. The photon equation instead does not have PMF direct contribution:

$$\dot{\theta}_\gamma = k^2 \left(\frac{\delta_\gamma}{4} - \sigma_\gamma \right) + \tau_{opt}(\theta_b - \theta_\gamma), \quad (6.7)$$

where $R = 4\rho_\gamma/\rho_b$ and τ_{opt} is the optical depth. The tight coupling approximation has been originally introduced for a numerical reason. The optical depth prior to the recombination has a very high value and can create issues for solving numerically the fluid equation system. To avoid this numerical problem, it is assumed that during this regime baryons and photons behave like a single coupled fluid [66]. Summing photon Euler equation, multiplied for R , to baryon one, then adding and subtracting the term $R\dot{\theta}_b k$, we obtain:

$$\dot{\theta}_b = \frac{\left(-\mathcal{H}\theta_b + c_s^2 k^2 \delta_b + k^2 R \left(\frac{\delta_\gamma}{4} - \sigma_\gamma \right) + R(\dot{\theta}_\gamma - \dot{\theta}_b - \frac{k^2 L}{\rho_b}) \right)}{(1 + R)}. \quad (6.8)$$

Differentiating the equation for the velocity difference, $\theta_b - \theta_\gamma$, we have:

$$\begin{aligned} \dot{\theta}_b - \dot{\theta}_\gamma &= \frac{2R}{(1 + R)} \mathcal{H}(\theta_b - \theta_\gamma) + \frac{\tau}{(1 + R)} \\ &\left(-\frac{\ddot{a}}{a} \theta_b - \mathcal{H} k^2 \frac{1}{2} \delta_\gamma + k^2 \left(c_s^2 \dot{\delta}_b - \frac{1}{4} \dot{\delta}_\gamma \right) - k^2 \left(\frac{L}{\rho_b} \right) \right). \end{aligned}$$

The term $-k^2 \left(\frac{L}{\rho_b} \right) \dot{}$ can be written as $k^2 \frac{L_0}{\rho_{b0}} \frac{\mathcal{H}}{a}$:

$$\dot{\theta}_\gamma = \dot{\theta}_b = -R^{-1} \left(\dot{\theta}_b + \mathcal{H}\theta_b - c_s^2 k^2 \delta_b + k^2 \frac{L}{\rho_b} \right) + k^2 \left(\frac{1}{4} \delta_\gamma - \sigma_\gamma \right), \quad (6.9)$$

which is the photon velocity equation in tight coupling approximation. We note the appearance of a Lorentz force contribution $-R^{-1} \left(k^2 \frac{L}{\rho_b} \right)$ given by the interaction with baryons. When the tight coupling ends the Lorentz term, like every baryon contribution, disappears. This is consistent with the fact that free charges recombine in neutral atoms.

6.1.4 Initial conditions

The initial conditions with the inclusion of PMF contributions are necessary to study the evolution of magnetized cosmological perturbations. Initial conditions are the solutions, on long wavelengths and at early times, of the coupled Einstein-Boltzmann equation system. We can expand the metric and fluid perturbations in series of $k\tau \ll 1$. There is not a unique solution to the system but several possible modes. Through initial conditions is possible to select the mode which we wish to evolve. In particular we are interested in regular modes, i.e. series which are non-singular at early times in the radiation era. These modes are the ones that significantly contribute to CMB anisotropies, we will not consider any decaying mode (see however the decaying mode in absence of magnetic fields).

Our ansatz for a regular mode is:

$$\begin{aligned}
h &= C_1 (k\tau)^2 \\
\eta &= A + A_2(k\tau)^2 \\
\delta_\gamma &= \delta_\nu = B_\gamma + B_{2\gamma}(k\tau)^2 \\
\delta_c &= B_c + B_{2c}(k\tau)^2 \\
\delta_b &= B_b + B_{2b}(k\tau)^2 \\
\theta_\gamma &= D_\gamma k\tau + D_{2\gamma}(k\tau)^3 \\
\theta_b &= \theta_\gamma \\
\theta_c &= 0 \\
\theta_\nu &= D_\nu k\tau + D_{2\nu}(k\tau)^3 \\
\sigma_\nu &= F + F_1(k\tau)^2 \\
F_{3\nu} &= G_1 k\tau .
\end{aligned} \tag{6.10}$$

Since perturbations are initialized deep in the radiation era, the cosmological fluid can be considered dominated by radiation components: photons, neutrinos and PMFs. We can therefore rewrite the Einstein equations as:

$$k^2\eta - \frac{1}{2}\mathcal{H}\dot{h} = -\frac{3}{2}\mathcal{H}^2 [(1 - R_\nu)\delta_\gamma + R_\nu\delta_\nu + \Omega_B] , \tag{6.11}$$

$$k^2\dot{\eta} = 2\mathcal{H}^2 [(1 - R_\nu)\theta_\gamma + R_\nu\theta_\nu] , \tag{6.12}$$

$$\ddot{h} + 2\mathcal{H}\dot{h} - 2k^2\eta = -3\mathcal{H}^2 [(1 - R_\nu)\delta_\gamma + R_\nu\delta_\nu + \Omega_B] , \tag{6.13}$$

$$\ddot{h} + 6\ddot{\eta} + 2\mathcal{H}(\dot{h} + 6\dot{\eta}) - 2k^2\eta = -9\mathcal{H}\left(\frac{4}{3}R_\nu\delta_\nu + \frac{\Omega_B}{3} + \frac{L}{\rho}\right) , \tag{6.14}$$

where $R_\nu = \rho_\nu/(\rho_\nu + \rho_\gamma)$ is the neutrino density, relative to the radiation content of the fluid, and $\Omega_B = \rho_B/(\rho_\gamma + \rho_\nu)$ is the time independent ratio between magnetic and radiation energy densities.

Since perturbations are initialized prior to the decoupling, we can assume the tight coupling approximation. In this approximation photon anisotropic stress and higher order photon moments are negligible, and we can consider a single velocity for the coupled photon-baryon fluid. With this approximations

the fluid equations reduce to:

$$\begin{aligned}
 \dot{\delta}_\gamma &= -\frac{4}{3}\theta_\gamma - \frac{2}{3}\dot{h}, \\
 \dot{\theta}_{\gamma b} &= (1+R)^{-1} \left[-\mathcal{H}\theta_{\gamma b} + \frac{k^2\delta_\gamma R}{4} + \frac{3}{4} \frac{RL_B k^2}{(1-R_\nu)} + k^2 c_s^2 \delta_b \right], \\
 \dot{\delta}_\nu &= -\frac{4}{3}\theta_\nu - \frac{2}{3}\dot{h}, \\
 \dot{\theta}_\nu &= k^2 \left(\frac{1}{4}\delta_\nu - \sigma_\nu \right), \\
 \dot{\sigma}_\nu &= \frac{4}{15}\theta_\nu + \frac{2}{15}\dot{h} + \frac{4}{5}\dot{\eta} - \frac{3}{5}kF_{3\nu}, \\
 \dot{F}_{3\nu} &= \frac{6}{7}\sigma_\nu, \\
 \dot{\delta}_b &= -\theta_b - \frac{1}{2}\dot{h}, \\
 \dot{\delta}_c &= -\frac{1}{2}\dot{h},
 \end{aligned} \tag{6.15}$$

where we defined $L_B = L_B/(\rho_\nu + \rho_\gamma)$. Deep in the radiation era $\rho_\gamma \gg \rho_b$, therefore $R \gg 1$:

$$\dot{\theta}_{\gamma b} = \frac{3}{4} \frac{L_B k^2}{(1-R_\nu)} + k^2 \frac{\delta_\gamma}{4}, \tag{6.16}$$

Inserting the expansions of Eqs. 6.10 and solving the coupled system we

obtained [75]:

$$\begin{aligned}
h &= C_1 k^2 \tau^2 - \frac{C_1(5 + 4R_\nu)}{36(15 + 4R_\nu)} k^4 \tau^4 + \left[-\frac{55L_B}{336(15 + 4R_\nu)} + \frac{(-55 + 28R_\nu)\Omega_B}{1008(15 + 4R_\nu)} \right] k^4 \tau^4 \\
\eta &= 2C_1 - \frac{5 + 4R_\nu}{6(15 + 4R_\nu)} C_1 k^2 \tau^2 + \left[\frac{\Omega_B(-55 + 28R_\nu)}{168(15 + 4R_\nu)} - \frac{55L_B}{56(15 + 4R_\nu)} \right] k^2 \tau^2 \\
\delta_\gamma &= -\Omega_B - \frac{2}{3} C_1 k^2 \tau^2 + \left[\frac{\Omega_B}{6} + \frac{L_B}{2(1 - R_\nu)} \right] k^2 \tau^2 \\
\delta_\nu &= -\Omega_B - \frac{2}{3} C_1 k^2 \tau^2 - \left[\frac{\Omega_B(1 - R_\nu)}{6R_\nu} + \frac{L_B}{2R_\nu} \right] k^2 \tau^2 \\
\delta_b &= -\frac{3}{4} \Omega_B - \frac{C_1}{2} k^2 \tau^2 + \left[\frac{\Omega_B}{8} + \frac{3L_B}{8(1 - R_\nu)} \right] k^2 \tau^2 \\
\delta_c &= -\frac{3}{4} \Omega_B - \frac{C_1}{2} k^2 \tau^2 \\
\theta_\gamma &= -\frac{C_1}{18} k^4 \tau^3 - \left[\frac{\Omega_B}{4} + \frac{3}{4} \frac{L_B}{(1 - R_\nu)} \right] k^2 \tau + \left[\frac{\Omega_B}{72} + \frac{L_B}{24(1 - R_\nu)} \right] k^4 \tau^3 \\
\theta_b &= \theta_\gamma \\
\theta_c &= 0 \\
\theta_\nu &= -\frac{(23 + 4R_\nu)}{18(15 + 4R_\nu)} C_1 k^4 \tau^3 + \left[\frac{\Omega_B(1 - R_\nu)}{4R_\nu} + \frac{3}{4} \frac{L_B}{R_\nu} \right] k^2 \tau \\
&\quad - \left[\frac{(135 + 14R_\nu)L_B}{84R_\nu(15 + 4R_\nu)} - \frac{(-270 + 161R_\nu + 28R_\nu^2)\Omega_B}{504R_\nu(15 + 4R_\nu)} \right] k^4 \tau^3 \\
\sigma_\nu &= \frac{4C_1}{3(15 + 4R_\nu)} k^2 \tau^2 - \frac{\Omega_B}{4R_\nu} - \frac{3}{4} \frac{L_B}{R_\nu} + \left[\frac{-\Omega_B(-55 + 28R_\nu)}{56R_\nu(15 + 4R_\nu)} + \frac{165L_B}{56R_\nu(15 + 4R_\nu)} \right] k^2 \tau^2 \\
F_{3\nu} &= -\frac{6}{7} \left[\frac{\Omega_B}{4R_\nu} + \frac{3}{4} \frac{L_B}{R_\nu} \right] k\tau. \tag{6.17}
\end{aligned}$$

We note that the terms proportional to C_1 are the growing regular adiabatic mode of Λ CDM, non magnetized, cosmological model [66]. Together with the non magnetized mode, we note the appearance of fully magnetic terms proportional to Ω_B and L_B . These terms are a new inhomogeneous solution to the Einstein-Boltzmann system which is fully sourced by PMFs. PMFs generate an independent fully magnetized mode and this is an original result of this thesis.

The fully magnetized mode is created by the contribution of PMFs to

the Einstein equation system. The introduction of the magnetic source term makes the system no longer homogeneous, therefore its solution is given by the sum of two contributions. The first is the homogeneous solution, the one of the system without PMF contributions. This solution can be the growing adiabatic mode, like we chose, or any other curvature or isocurvature mode. The second contribution is a particular solution of the inhomogeneous system fully sourced by PMFs. This particular solution is a fully magnetized mode. The correlation between the fully magnetized mode and the inflationary ones is strictly related to the generation mechanism of the fields. Since it is beyond the purpose of this work to investigate this correlation, we will make the most conservative assumption of a magnetized mode fully uncorrelated with any other inflationary one.

In the magnetized mode initial conditions of Eqs. 6.17 we note many cancellations and compensations, like the lack of magnetic contributions at the leading order in the metric perturbations and the compensations between the magnetic velocity terms. These peculiarities are caused by the absence of an homogeneous component in PMFs modelled as a stochastic background. To compensate the lack of magnetic terms at the homogeneous level some cancellations must occur to solve the system. In order to characterize the above solution we give the value of the gauge invariant curvature perturbation [36] from Eq. 2.40:

$$\zeta = \frac{k^2 \tau^2 (6 + k^2 \tau^2) (165 L_B + (55 - 28 R_\nu) \Omega_B)}{1008 (15 + 4 R_\nu)}, \quad (6.18)$$

therefore the magnetized mode is a mode with zero curvature on long wavelengths in the radiation era.

We computed the magnetized initial conditions in the approximation of a universe completely dominated by radiation. This approximation is almost correct since initial conditions are computed deep in the radiation era, where photons and neutrinos dominate over the other species. But even if very

subdominant the matter content is not negligible. The matter contribution in the initial condition computation is supposed to introduce only higher order corrections to the radiation dominated results. It was argued in [79] that the matter presence could instead give a dominant contribution to the magnetized initial conditions, and completely modify the PMF impact on CMB anisotropies.

The matter contribution enters only in the Einstein equations. In particular it is necessary to consider also matter components in the source term and the second order terms in the evolution of the scale factor and of the Hubble parameter. In particular the scale factor can be written as [67]:

$$\begin{aligned} a(\tau) &= \frac{\Omega_m H_0^2}{\omega^2} \left(\omega\tau + \frac{1}{4}\omega^2\tau^2 \right), \\ \omega &= \frac{\Omega_m H_0}{\sqrt{\Omega_\nu + \Omega_\gamma}}, \\ R_c &= \frac{\Omega_c}{\Omega_m} \equiv \frac{\Omega_c}{\Omega_b + \Omega_c}. \end{aligned} \quad (6.19)$$

The Hubble parameter is expanded as $\mathcal{H} \propto \frac{1}{\tau} + \frac{\omega}{4}$. The Einstein equations become:

$$k^2\eta - \frac{1}{2}\mathcal{H}\dot{\eta} = -4\pi G a^2 [\rho_\gamma\delta_\gamma + \rho_\nu\delta_\nu + \rho_b\delta_b + \rho_c\delta_c + (\rho_\nu + \rho_\gamma)\Omega_B], \quad (6.20)$$

$$k^2\dot{\eta} = 4\pi G a^2 \left[\frac{4}{3}\rho_\gamma\theta_\gamma + \frac{4}{3}\rho_\nu\theta_\nu + \rho_b\theta_b \right], \quad (6.21)$$

$$\ddot{h} + 2\mathcal{H}\dot{h} - 2k^2\eta = -8\pi G a^2 \left[\frac{1}{3}\rho_\gamma\delta_\gamma + \frac{1}{3}\rho_\nu\delta_\nu + \frac{1}{3}(\rho_\gamma + \rho_\nu)\Omega_B \right], \quad (6.22)$$

$$\ddot{h} + 6\ddot{\eta} + 2\mathcal{H}(\dot{h} + 6\dot{\eta}) - 2k^2\eta = -24\pi G a^2 \left[\frac{4}{3}\rho_\nu\delta_\nu + (\rho_\nu + \rho_\gamma) \left(\frac{\Omega_B}{3} + L_B \right) \right], \quad (6.23)$$

The initial conditions with PMFs which include the matter corrections are

[84]:

$$\begin{aligned}
 h(k, \tau) &= -\frac{3}{4}\Omega_B\omega\tau + \frac{9}{32}\Omega_B\omega^2\tau^2 \\
 \eta(k, \tau) &= \frac{1}{8}\Omega_B\omega\tau - \frac{3\Omega_B\omega^2\tau^2}{64} + \frac{(-165L_B - 55\Omega_B + 28R_\nu\Omega_B)}{168(15 + 4R_\nu)}k^2\tau^2 \\
 \delta_\gamma(k, \tau) &= -\Omega_B + \frac{\Omega_B\omega\tau}{2} - \frac{3\Omega_B\omega^2\tau^2}{16} - \frac{(3L_B + \Omega_B - R_\nu\Omega_B)}{6(-1 + R_\nu)}k^2\tau^2 \\
 \delta_\nu(k, \tau) &= -\Omega_B + \frac{\Omega_B\omega\tau}{2} - \frac{3\Omega_B\omega^2\tau^2}{16} - \frac{(3L_B + \Omega_B - R_\nu\Omega_B)}{6R_\nu}k^2\tau^2 \\
 \delta_b(k, \tau) &= -3\frac{\Omega_B}{4} + \frac{3\Omega_B\omega\tau}{8} + \frac{1}{8}k^2\tau^2\Omega_B - \frac{9}{64}\Omega_B\omega^2\tau^2\omega^2 - \frac{3L_Bk^2\tau^2}{8(-1 + R_\nu)} \\
 \delta_c(k, \tau) &= -\frac{3\Omega_B}{4} + \frac{3\Omega_B\omega\tau}{8} - \frac{9}{64}\Omega_B\omega^2\tau^2 \\
 \theta_\gamma(k, \tau) &= \frac{3L_Bk^2\tau}{4(-1 + R_\nu)} - \frac{\Omega_B}{4}k^2\tau + k^2\tau^2 \left[-\frac{9L_B(-1 + R_c)\omega}{16(-1 + R_\nu)^2} + \frac{(-4 + R_\nu + 3R_c)\omega\Omega_B}{16(-1 + R_\nu)} \right] \\
 \theta_\nu(k, \tau) &= \frac{3L_Bk^2\tau}{4R_\nu} - \frac{k^2(-1 + R_\nu)\Omega_B\tau}{4R_\nu} + \frac{1}{16}k^2\tau^2\omega\Omega_B \\
 \theta_b(k, \tau) &= \frac{3L_Bk^2\tau}{4(-1 + R_\nu)} - \frac{1}{4}\Omega_Bk^2\tau + k^2\tau^2 \left[-\frac{9L_B(-1 + R_c)\omega}{16(-1 + R_\nu)^2} + \frac{(-4 + R_\nu + 3R_c)\omega\Omega_B}{16(-1 + R_\nu)} \right] \\
 \theta_c(k, \tau) &= 0 \\
 \sigma_\nu(k, \tau) &= -\frac{3L_B + \Omega_B}{4R_\nu} + \frac{\Omega_Bk^2(55 - 28R_\nu)\tau^2}{56R_\nu(15 + 4R_\nu)} + \frac{165L_Bk^2\tau^2}{56R_\nu(15 + 4R_\nu)} \\
 F_3(k, \tau) &= -\frac{3k\tau(3L_B + \Omega_B)}{14R_\nu} + \frac{165L_B + 55\Omega_B - 28R_\nu\Omega_B}{7(430R_\nu + 112R_\nu^2)}. \tag{6.24}
 \end{aligned}$$

We note how our results are in agreement with the one presented in [80, 81], and that both are in disagreement with the ones presented in [79]. As expected, the introduction of matter corrections leads to the appearance of next to leading terms, which depend on the matter content of the fluid. We demonstrated how the inclusion of the matter corrections does not produce any appreciable change in the results, contrary to what claimed in [79]. In fact, the relative difference between the temperature anisotropy angular power spectrum computed with and without matter corrections are of the order of $\mathcal{O}(10^{-5})$, which is the numerical noise level. The gauge invariant

curvature perturbation with matter corrections is given by:

$$\begin{aligned} \zeta = & \frac{k^2 \tau^2 (6 + k^2 \tau^2) (165 L_B + (55 - 28 R_\nu) \Omega_B)}{1008 (15 + 4 R_\nu)} \\ & - \frac{1}{48} \tau \omega (9 + k^2 \tau^2) \Omega_B + \frac{1}{128} \tau^2 \omega^2 (12 + k^2 \tau^2) \Omega_B. \end{aligned} \quad (6.25)$$

The initial conditions we presented are computed after neutrino decoupling when numerical codes start to evolve the perturbations. We have derived the initial conditions prior to this epoch, when the neutrino anisotropic stress is negligible. In this case we have the appearance of a logarithmic mode in the initial conditions for the metric perturbations:

$$\begin{aligned} h(k, \tau) &= -\frac{1}{8} (\Omega_B + 4 L_B) k^2 \tau^2 \\ \eta(k, \tau) &= -\frac{1}{2} (\Omega_B + 3 L_B) \log(k \tau) \\ \delta_\gamma(k, \tau) &= -\Omega_B + \frac{1}{12} \left[\frac{3 L_B (1 + R_\nu)}{(1 - R_\nu)} + \Omega_B \right] k^2 \tau^2 \\ \delta_\nu(k, \tau) &= -\Omega_B + \frac{1}{12} (-3 L_B + \Omega_B) k^2 \tau^2 \\ \theta_\gamma(k, \tau) &= -k^2 \tau \left[\frac{3 L_B}{4(1 - R_\nu)} + \frac{\Omega_B}{4} \right] \\ \theta_\nu(k, \tau) &= -\frac{1}{4} \Omega_B k^2 \tau. \end{aligned} \quad (6.26)$$

A detailed study of the neutrino decoupling in presence of PMFs is necessary to investigate the behavior of this logarithmic mode in the post decoupling epoch, but this study would be very complex and out of the purpose of this work. However we have verified that the leading magnetized mode after neutrino decoupling is the one we have presented before, therefore we can affirm that whatever happens to this mode during neutrino decoupling it should be subleading in the post-decoupling epoch.

6.2 The vector sector of magnetized cosmological perturbations

Metric vector perturbations are sourced by the vector anisotropic stress in the plasma. In absence of PMFs the only sources of anisotropic stress are photons and neutrinos. Photon anisotropic stress, prior to the decoupling, is strongly suppressed by the photon-baryon interaction, and therefore can be considered negligible. Neutrino vector anisotropic stress sources vector metric perturbations, but it has been shown that neutrino vector mode is decaying and has a negligible contribution to CMB anisotropies [82].

PMF carrying vector anisotropic stress are a source of vector perturbations and generates a fully magnetized vector mode. The vector metric perturbation is described by the vector:

$$h_{ij}^V = \partial_i h_j + \partial_j h_i, \quad (6.27)$$

which satisfies the divergenceless condition:

$$\partial_i h_i = 0. \quad (6.28)$$

The divergenceless condition assures that vector mode does not support density perturbations. The Einstein equations for the vector metric perturbation are sourced by magnetic anisotropic stress:

$$\dot{h}^V + 2\mathcal{H}h^V = -\frac{16\pi G a^2}{k}(\Pi_\nu^V + \Pi_\gamma^V + \Pi_B^V). \quad (6.29)$$

The neutrino and photon anisotropic stresses, which appear in the equation, are sourced themselves by PMFs.

6.2.1 Lorentz force

Also in vector perturbations baryons are affected by the Lorentz force, in fact even if vector perturbations do not support density perturbations,

they support baryon velocity. The vector PMF conservation equations give a relation between Lorentz force and the anisotropic stress:

$$-\nabla_i P^B + \nabla_j \Pi_{ij}^{(V,B)} = L_i^B, \quad (6.30)$$

which is the vector correspondent of the relation between anisotropic stress, Lorentz force and energy density of scalar perturbations. Since a stochastic background of PMFs does not carry pressure at the homogeneous level, in the Fourier space Lorentz force is directly related to the anisotropic stress:

$$L_i^B = k \Pi_i^{(V,B)}. \quad (6.31)$$

Therefore magnetized vector perturbations require the computation of the Fourier spectra only for the anisotropic stress, since Lorentz force can be obtained from Eq. 6.31.

The baryon velocity equation is:

$$\dot{\theta}_b + \mathcal{H}\theta_b = -\frac{\rho_\gamma}{\rho_b} \left[\frac{4}{3} n_e a \sigma_T (\theta_b - \theta_\gamma) - \frac{L_B^V}{\rho_\gamma} \right], \quad (6.32)$$

where we have neglected the baryon homogeneous pressure ($p_b/\rho_b \ll 1$).

6.3 The tensor sector of magnetized cosmological perturbations

Tensor perturbations are a key prediction of the inflationary model. The observational search of their signature in CMB anisotropies is one of the most active fields of observational cosmology. Tensor perturbations are sourced by tensor anisotropic stress; in particular the main source of anisotropic stress in the primordial plasma are neutrinos. Neutrinos slightly damp the tensor perturbations during their reentry in the Hubble radius [98]. PMFs carry tensor anisotropic pressure and therefore source a pure magnetized tensor mode.

The evolution of the tensor metric perturbation is described by the Einstein equations where PMF contribution is again an additional source term, given by PMF tensor anisotropic stress:

$$\ddot{h}_{ij} + 2\mathcal{H}\dot{h}_{ij} + k^2 h_{ij} = 16\pi G a^2 (\rho_\nu \pi_{ij}^\nu + \Pi_{ij}^{(T,B)}). \quad (6.33)$$

The source term is composed by the sum of the two contributions: PMFs and neutrinos. The two contributions have opposite signs and compensate each other in the so-called magnetized compensated mode.

The fluid equations for tensor perturbations are the given by the Boltzmann hierarchy for neutrinos. Since we are interested also in the next to leading order for the tensor initial conditions, we truncate the neutrino hierarchy at the moment $J_4 = 0$. Assuming the hierarchy truncated at J_4 , the neutrino equations are:

$$\begin{aligned} \dot{\sigma}_\nu^{(T)} &= -\frac{4}{15}\dot{h}_k - \frac{k}{3}J_3, \\ J_3 &= \frac{3}{7}k\sigma_\nu^{(T)}. \end{aligned} \quad (6.34)$$

6.3.1 Initial conditions

Tensor initial conditions are large scale solutions of the coupled system of the Einstein and neutrino equation system in the radiation era. We can expand the metric and fluid perturbations in powers of $k\tau$ and solve the simplified system. The tensor magnetized initial conditions are given by :

$$\begin{aligned} h_k &= A \left[1 - \frac{5(k\tau)^2}{2(15 + 4R_\nu)} \right] + \frac{15(1 - R_\nu)\tilde{\Pi}_B^{(T)}(k\tau)^2}{14(15 + 4R_\nu)}, \\ \sigma_\nu^{(T)} &= -\frac{(1 - R_\nu)}{R_\nu}\tilde{\Pi}_B^{(T)} \left[1 - \frac{15(k\tau)^2}{14(15 + 4R_\nu)} \right] + A \frac{2(k\tau)^2}{3(15 + 4R_\nu)}, \end{aligned} \quad (6.35)$$

where $\tilde{\Pi}_B^{(T)}$ is the time independent ratio $\Pi^{(T,B)}/\rho_\nu$. The terms proportional to A are the initial conditions for inflationary tensor perturbations; whereas the ones proportional to $\tilde{\Pi}_B^{(T)}$ are the initial conditions for the fully magnetized tensor mode. We note that the fully magnetized mode is the leading

one for the neutrino anisotropic stress. PMFs are the source of neutrino anisotropic stress and in the Einstein equations neutrino stress compensates the effect of PMFs. This is the so-called compensation between neutrinos and PMFs, neutrinos are sourced by PMF but at the same time suppress PMF impact on perturbations, namely their own source.

The compensation between PMFs and neutrinos can take place only after neutrino decoupling since, prior to this epoch, neutrino anisotropic stress is suppressed. We note that Einstein-Boltzmann codes evolve cosmological perturbations after neutrino decoupling. A detailed analysis of the evolution of magnetized tensor perturbations during neutrino decoupling is extremely complex and beyond the purpose of this thesis.

6.4 Magnetized CMB anisotropies

In order to evolve magnetized perturbations and compute the magnetized CMB anisotropy angular power spectra in temperature and polarization we developed an extension of the Einstein-Boltzmann code CAMB. The original code includes only partially the contribution of PMFs. In particular the original CAMB includes the treatment of magnetized vector mode and magnetized tensor initial conditions. We extended the code with several modules which compute all the required PMF EMT Fourier spectra, using the analytical results where possible and the spectral fits elsewhere.

We used the original implementation, with minor modifications, of magnetized vector perturbations, we only substituted the original power spectrum of the vector anisotropic stress with our results.

We also maintained the original implementation of the tensor initial conditions, but we had to include in the perturbation evolution equations the PMF contribution, not considered in the original code.

Scalar magnetized perturbations are not included in the original code, therefore scalar mode required a major modification to include all the mag-

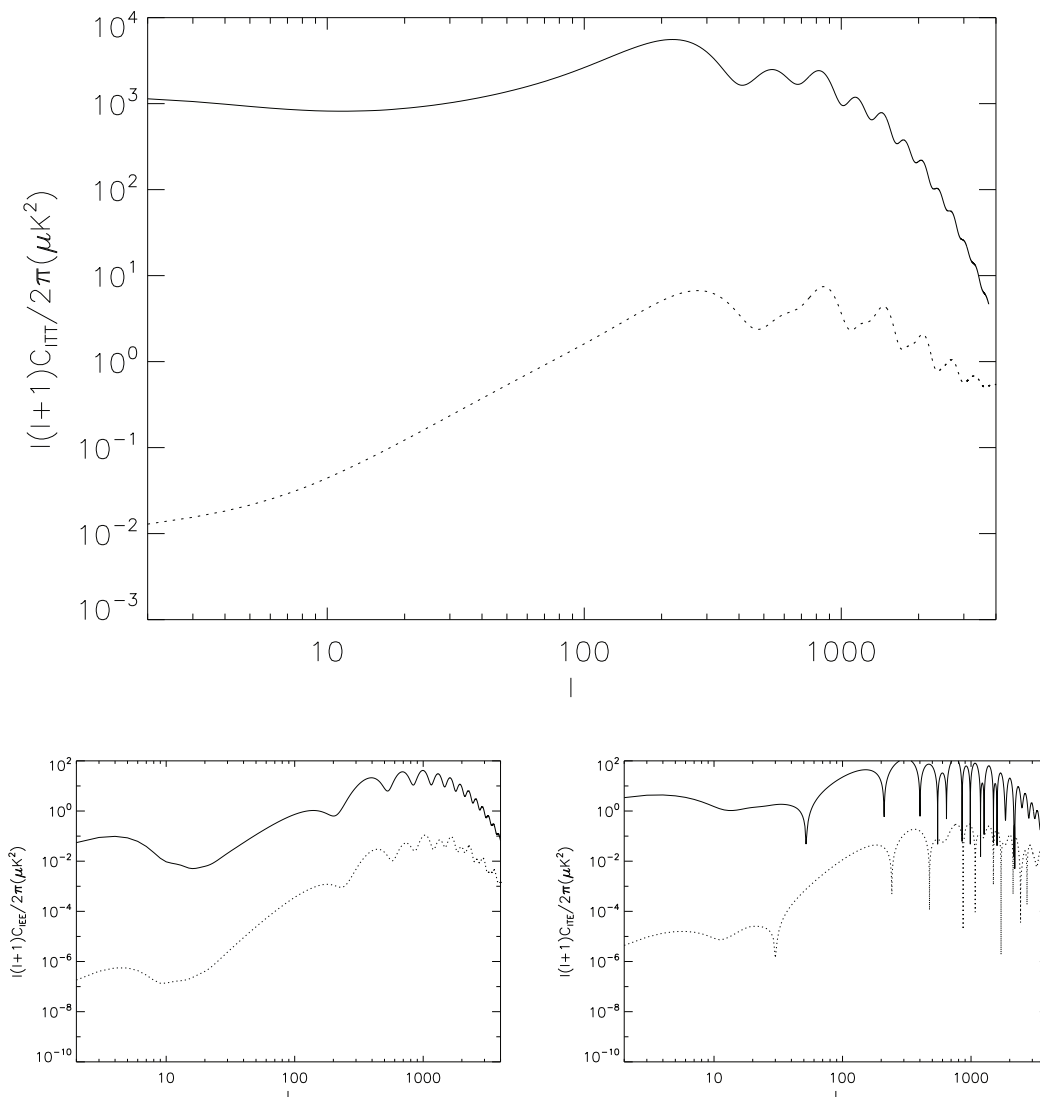


Figure 6.1: Temperature and polarization anisotropy angular power spectrum for the magnetized scalar mode with $n_B = -2.5$ and $B_{1\text{Mpc}} = 6 \text{ nG}$, dotted line is the magnetized scalar mode, for comparison in solid line we show the inflationary scalar mode. Upper panel: Temperature autocorrelation TT. Lower right panel: Cross correlation TE. Lower left panel: E-mode autocorrelation EE.

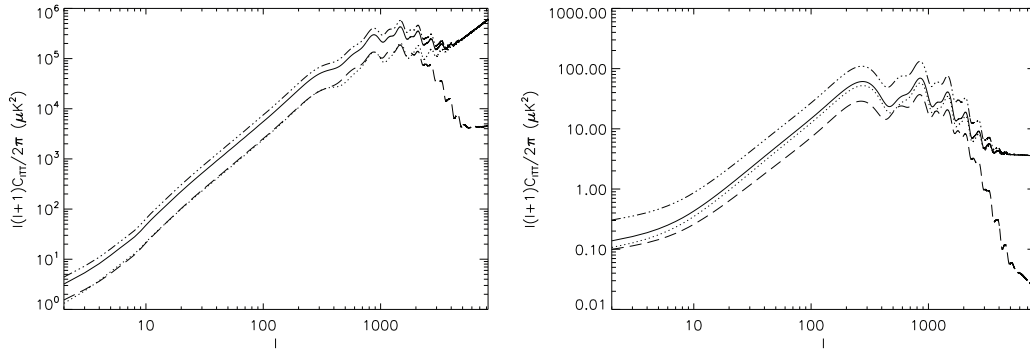


Figure 6.2: We computed the scalar power spectrum with the contribution of the Lorentz force-energy density cross correlation for $n_B = 2$ (left panel) and $n_B = -2.5$ (right panel). Solid line represents the correct assumption on the cross-correlation, the dotted line represents the result considering the Lorentz force and the energy density fully anti-correlated, triple dotted-dashed line represents the uncorrelated sum and the dashed line represents the result assuming full correlation.

netic contributions. We extended the initial conditions to the magnetized scalar mode and we modified the perturbation evolution equations to include PMF contribution. In the following sections we will show one by one the results we obtained on the magnetized CMB anisotropies with all kind of perturbations.

6.4.1 Magnetized scalar CMB anisotropies

We begin the review of the results on the anisotropies with the scalar magnetized mode. The angular power spectrum of CMB magnetized scalar anisotropies in temperature and polarization is shown in Fig. 6.1, we fixed the magnetic parameters to $n_B = -2.5$ and $B_{1\text{Mpc}} = 6 \text{ nG}$ [75]. The shape of the magnetized temperature anisotropies presents an increase on large scales and a series of acoustic peaks on the same scales as primary CMB. The contribution of scalar magnetized anisotropies is important on small scales. In fact on large scales the dominant contribution is given by the primary CMB,

but on small scales, while primary CMB is suppressed by the Silk damping, scalar magnetized mode is not and has a significant contribution.

Scalar polarization anisotropies are given only by EE and TE modes. PMFs do not have a strong impact on these polarizations, in fact, as shown in Fig. 6.1, scalar magnetized mode is strongly subdominant with respect to primary CMB.

In Fig. 6.2 we show the impact on magnetized temperature anisotropies of the assumptions on the cross-correlation between the magnetic energy density and the Lorentz force [84]. We note that our choice of considering the Lorentz force and the energy density as fully anti-correlated does not have a great impact on the power spectrum, with respect to the exact evaluation, especially for infrared indices. In particular we will show that this assumption does not modify the results on cosmological parameters, in fact the dominant contribution to the constraints is given by magnetized vector mode.

6.4.2 Magnetized vector CMB anisotropies

We will now show the results for vector anisotropies, as anticipated, the magnetized vector mode will be the dominant PMF contribution to the anisotropies. The angular power spectrum of magnetized vector anisotropies both in temperature and polarization is shown in Fig. 6.3 [75]. The shape is rapidly increasing and peaks around $\ell \sim 2000 - 3000$. The very different shape, with respect to scalar and tensor anisotropies, is given by the fact that vector perturbations are completely forced modes. The peak is in the region where primary CMB is suppressed by Silk damping, therefore magnetized vector anisotropies are the dominant contribution on small scales. For magnetized vector perturbations is very interesting the polarization. A characteristic of vector perturbations is that, like tensor ones, they produce a B-mode polarization signal.

Magnetized anisotropies remain subdominant for the EE mode and the

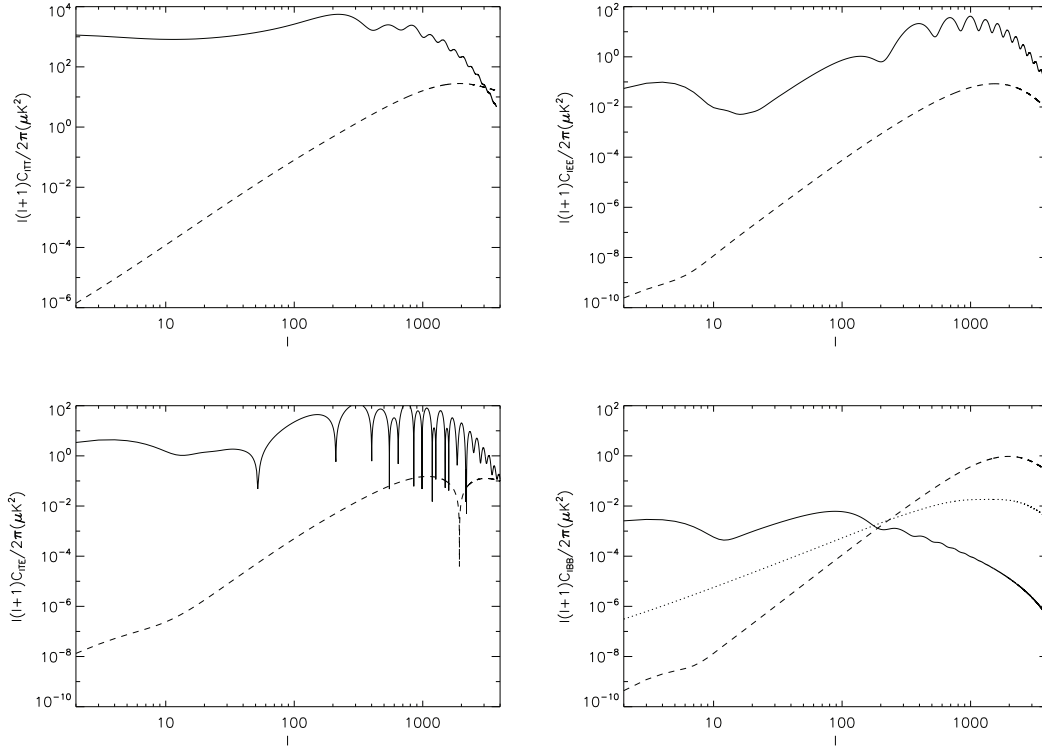


Figure 6.3: Temperature and polarization anisotropy angular power spectrum for the magnetized vector mode with $n_B = -2.5$ and $B_{1\text{Mpc}} = 6 \text{ nG}$, dashed line is the magnetized vector mode, for comparison in solid line we show the inflationary scalar mode. Upper left panel: Temperature autocorrelation TT. Upper right panel: E-mode polarization autocorrelation. Lower right panel: Cross correlation TE. Lower left panel: B-mode autocorrelation BB where for comparison we show in dotted the lensing curve and in solid the inflationary tensor mode with tensor to scalar ratio $r = 0.1$.

TE-mode, but the situation is different for the B mode. Magnetized vector anisotropy signature in B polarization is shown in the lower right panel of Fig. 6.3. We note how it has a shape similar to the temperature power spectrum, with a characteristic peak at $\ell \sim 2000 - 3000$. In particular its amplitude is greater than the lensing signal at the peak. The lensing B mode polarization represents a detection threshold below which is extremely difficult to reconstruct a cosmological signal, therefore the magnetic B mode characteristic signature and amplitude can be crucial for future CMB polarization dedicated experiments.

6.4.3 Magnetized tensor CMB anisotropies

The angular power spectra of magnetized tensor CMB anisotropies is shown in Fig. 6.4 for $B_{1\text{Mpc}} = 6 \text{ nG}$ and $r = 0.1$. We note how both in temperature and polarization magnetized tensor perturbations are strongly subdominant with respect to the primary CMB. In Fig. 6.4 for comparison we show, in B mode polarization, also an inflationary tensor mode with the same tensor to scalar ratio as the magnetized one [75]. We note how the magnetized tensor mode is strongly subdominant also with respect to inflationary tensor mode.

In Fig. 6.5 we show the impact of PMF and neutrino compensation. In particular we compare the magnetized mode generated with and without the contribution of neutrinos: note how the correct consideration of neutrino free-streaming after neutrino decoupling has a large impact on the tensor mode sourced by PMFs.

6.4.4 Magnetized CMB anisotropy dependence on the magnetic spectral index

As we anticipated in the previous chapter, magnetized CMB anisotropy power spectra strongly depend on the spectral behavior of the PMF EMT Fourier spectra.

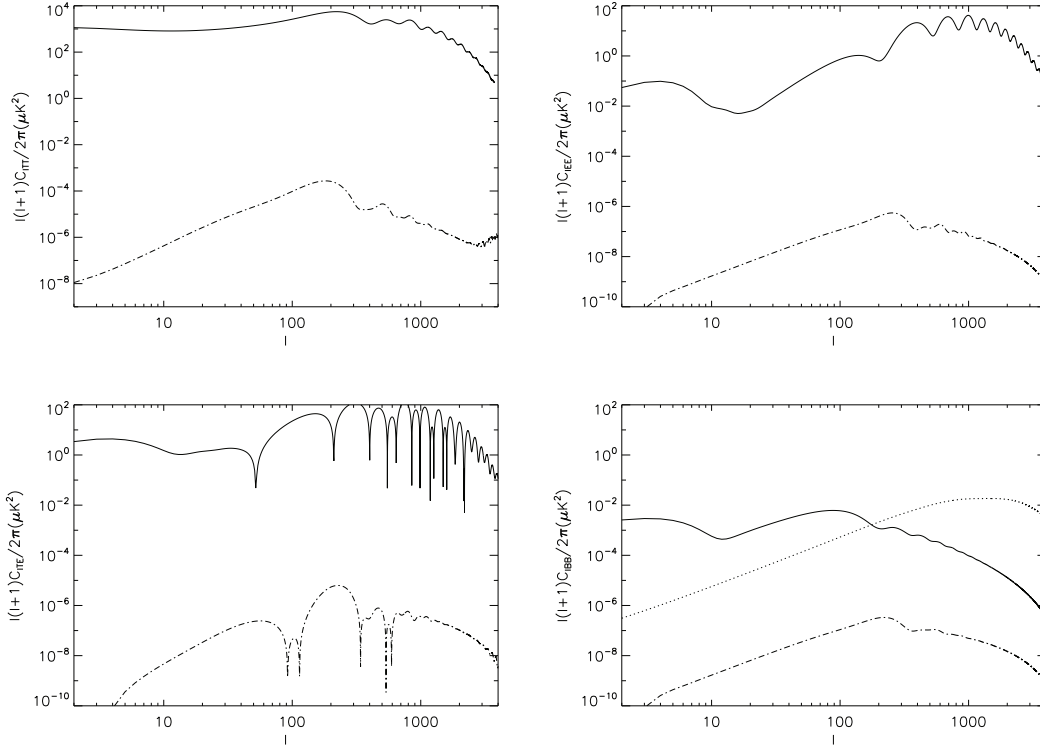


Figure 6.4: Temperature and polarization anisotropy angular power spectrum for the magnetized tensor mode with $n_B = -2.5$ and $B_{1\text{Mpc}} = 6 \text{ nG}$, dot-dashed line is the magnetized tensor mode, for comparison in solid line we show the inflationary scalar mode. Upper left panel: Temperature autocorrelation TT. Upper right panel: E-mode polarization autocorrelation. Lower right panel: Cross correlation TE. Lower left panel: B-mode autocorrelation BB where for comparison we show in dotted the lensing curve and in solid the inflationary tensor mode with tensor to scalar ratio $r = 0.1$.

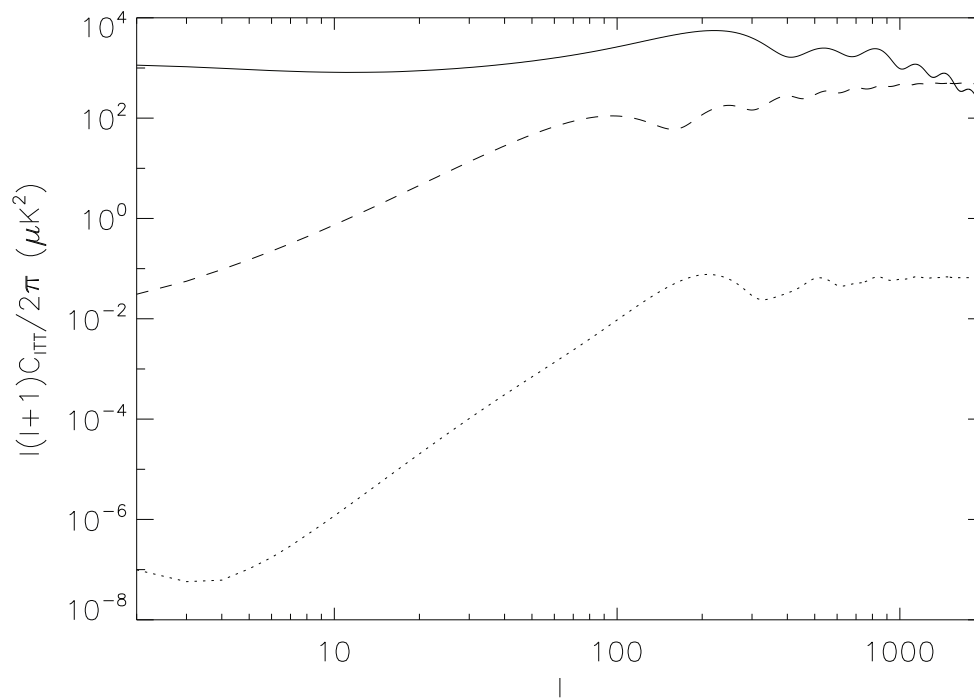


Figure 6.5: Comparison of the tensor magnetized mode temperature anisotropies with, dotted line, and without, dashed line, neutrino contribution. For comparison solid line represents the scalar adiabatic mode.

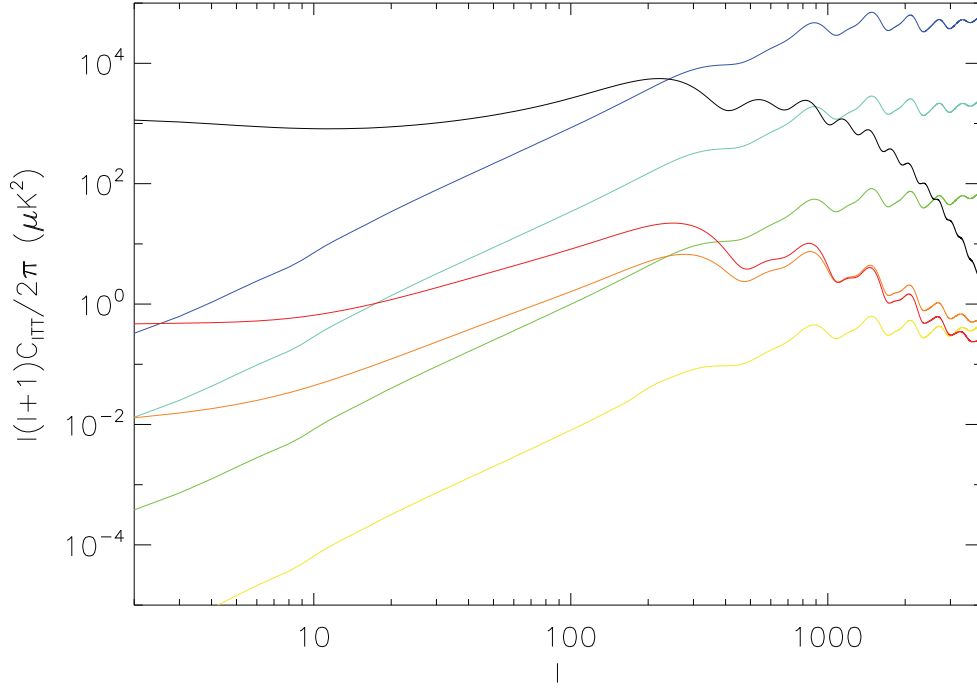


Figure 6.6: Temperature anisotropy angular power spectrum variation with the spectral index for the magnetized scalar mode the amplitude of PMFs is fixed at $B_{1\text{Mpc}} = 6 \text{ nG}$: black line is growing adiabatic mode, blue is $n_B = 2$, cyan is $n_B = 1$, green is $n_B = 0$, yellow is $n_B = -1.5$, orange is $n_B = -2.5$, red is $n_B = -2.9$

In particular in Fig. 6.6 and Fig. 6.7 we show, fixing $B_{1\text{Mpc}} = 6 \text{ nG}$, the dependence of the magnetized scalar and vector modes on the PMF spectral index n_B . For sake of simplicity, since it is subdominant, we do not show the results for magnetized tensor mode, but it shows the same behavior as vector and scalar ones.

The spectral behavior is similar for both scalar and vector anisotropies and presents peculiar characteristics. The amplitude increases with the spectral index for indices greater than $n_B > -1.5$. For $n_B = -1.5$ the behavior

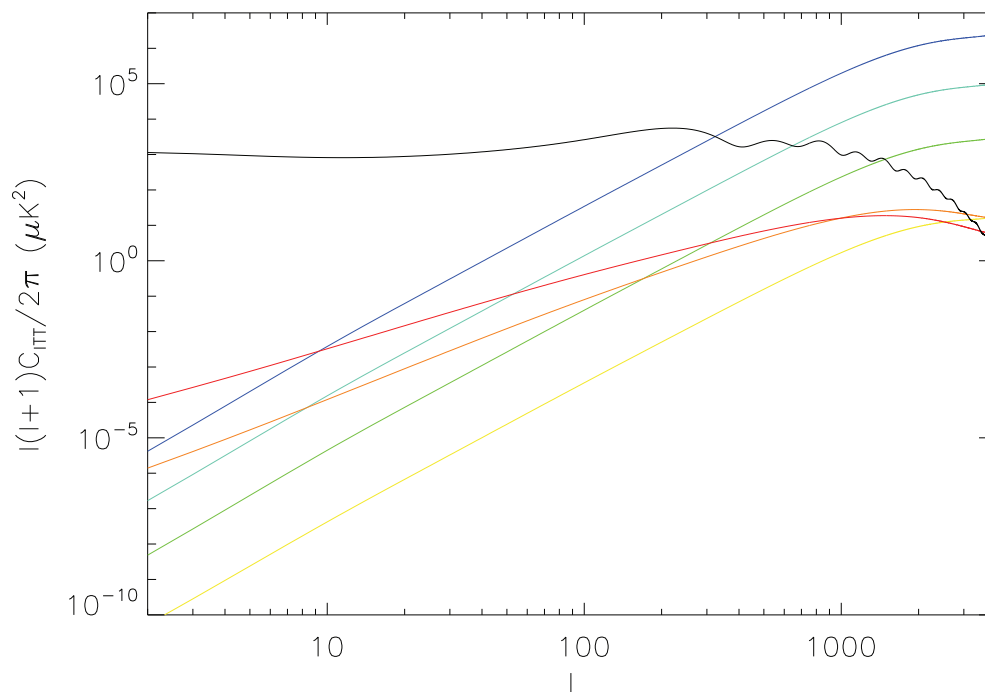


Figure 6.7: Temperature anisotropy angular power spectrum variation with the spectral index for the magnetized vector mode the amplitude of PMFs is fixed at $B_{1\text{Mpc}} \text{ nG}$: black line is growing adiabatic scalar mode plotted for comparison, blue is $n_B = 2$, cyan is $n_B = 1$, green is $n_B = 0$, yellow is $n_B = -1.5$, orange is $n_B = -2.5$, red is $n_B = -2.9$

changes, in fact for $-1.5 > n_B > -3$ the amplitude increases decreasing the spectral index. The minimum amplitude corresponds to $n_B = -1.5$. This behavior reflects, and is generated by, the infrared behavior of the EMT Fourier spectra. As shown in the previous chapter, the PMF EMT Fourier spectra change their infrared behavior for $n_B = -1.5$. In particular for indices $n_B > -1.5$ it is a white noise, whose amplitude grows with the spectral index, whereas for $n_B < -1.5$ it becomes infrared dominated and the amplitude increases decreasing the spectral index. The fact that the shape of the anisotropy angular power spectra reproduces the EMT spectral behavior is a natural consequence of the fact that magnetized perturbations are completely sourced by PMF.

In the next chapter we will present a semianalytical treatment of the magnetized Sachs-Wolfe effect which quantitatively shows the relation between PMF EMT and the angular power spectrum.

6.4.5 Comparison of magnetized modes

The comparison of the magnetic contributions to CMB anisotropies in temperature and polarization is shown in Fig. 6.8 and Fig. 6.9, respectively for $n_B = 2$ and $n_B = -2.5$. We note that the dominant magnetic contributions are the scalar and vector ones. The tensor contribution remains subdominant not only with respect to primary CMB, but also with respect to the other magnetized modes, both in temperature and polarization. On large scale the dominant magnetic contribution is given by the scalar mode, whereas the vector mode dominates on small scales around $\ell \sim 2000 - 3000$ where it peaks.

The major strength of magnetized modes is that, contrary to the primary CMB, they are not suppressed by the Silk damping. In fact we note how on large scales the leading contribution is the primary CMB, whereas on small scales, scalar and vector magnetized modes become important. In particular the dominant magnetic contribution are the vector perturbations, we will

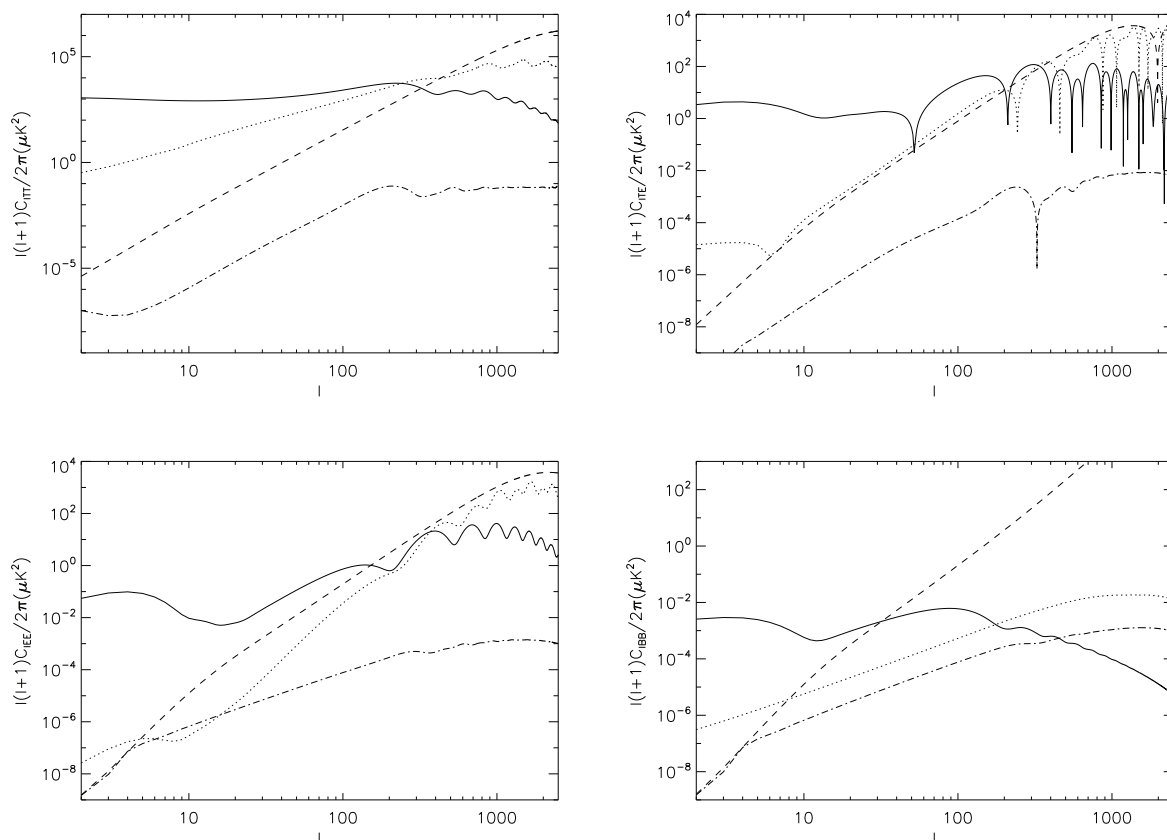


Figure 6.8: CMB anisotropies angular power spectrum for temperature , temperature-E polarization cross correlation , E polarization , B polarization. The solid line is the adiabatic scalar contribution in TT, TE, EE panels, whereas it is the tensor homogeneous contribution in the BB panel (for a tensor-to-scalar ratio $r = 0.1$); the dotted, dot-dashed, dashed are the scalar, vector and tensor contributions of a SB of PMF respectively for $B_{1\text{Mpc}} = 6$ nG, $n_B = 2$. The dotted line in the BB panel is the lensing contribution.

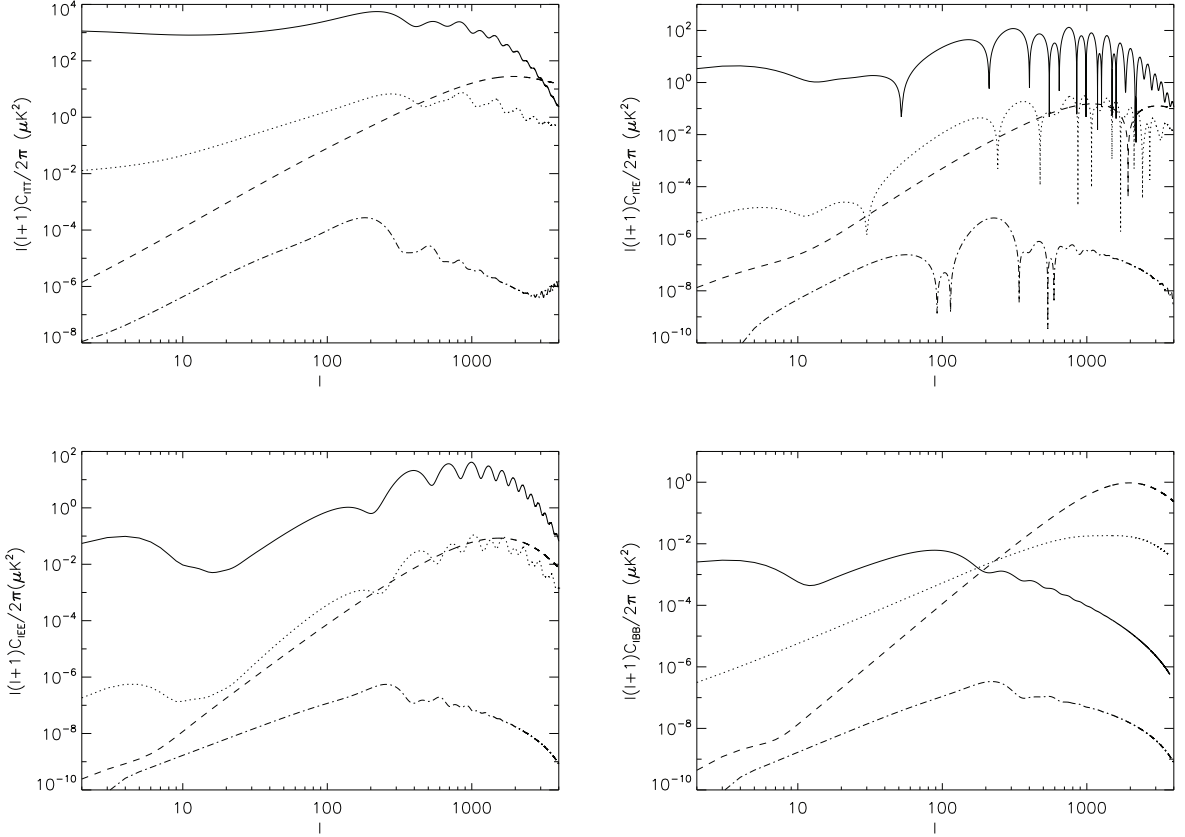


Figure 6.9: CMB angular power spectrum for TT (left top panel), TE (left top panel), EE (bottom left), BB (bottom right). The solid line is the adiabatic scalar contribution in TT, TE, EE panels, whereas it is the tensor homogeneous contribution in the BB panel (for a tensor-to-scalar ratio $r = 0.1$); the dotted, dot-dashed, dashed are the scalar, vector and tensor contributions of a SB of PMF respectively for $B_{1\text{Mpc}} = 6 \text{ nG}$, $n_B = -5/2$. The dotted line in the BB panel is the lensing contribution.

show in the next chapter how vector mode alone is enough to constrain PMFs with CMB data.

6.5 Magnetized matter power spectrum

PMFs affects the whole evolution of cosmological perturbations, therefore they do not affect only CMB but all the cosmological observables. In particular PMFs affect the thermal history of the universe and the matter power spectrum [106, 107, 108]. An accurate analysis of the impact of PMFs on the matter power spectrum would be extremely complex and it would require the application of non-linear physics and magnetohydrodynamics. We will limit our study only to the linear matter power spectrum that can be computed with our extension of the CAMB code.

In Fig. 6.10 we show the magnetized linear matter power spectrum generated by magnetized scalar perturbations in comparison with the correspondent matter power spectrum from the adiabatic scalar mode, for $B_{1\text{Mpc}} = 6 \text{ nG}$, $n_B = 2$ and $n_B = -2.5$ [83]. As for CMB anisotropies also on the matter power spectrum the greater impact of PMFs is on small scales. In particular we note the dominant feature PMFs introduce on small and intermediate scales. In the next chapter we will show how this feature will not have a strong impact on PMF constraints with present data.

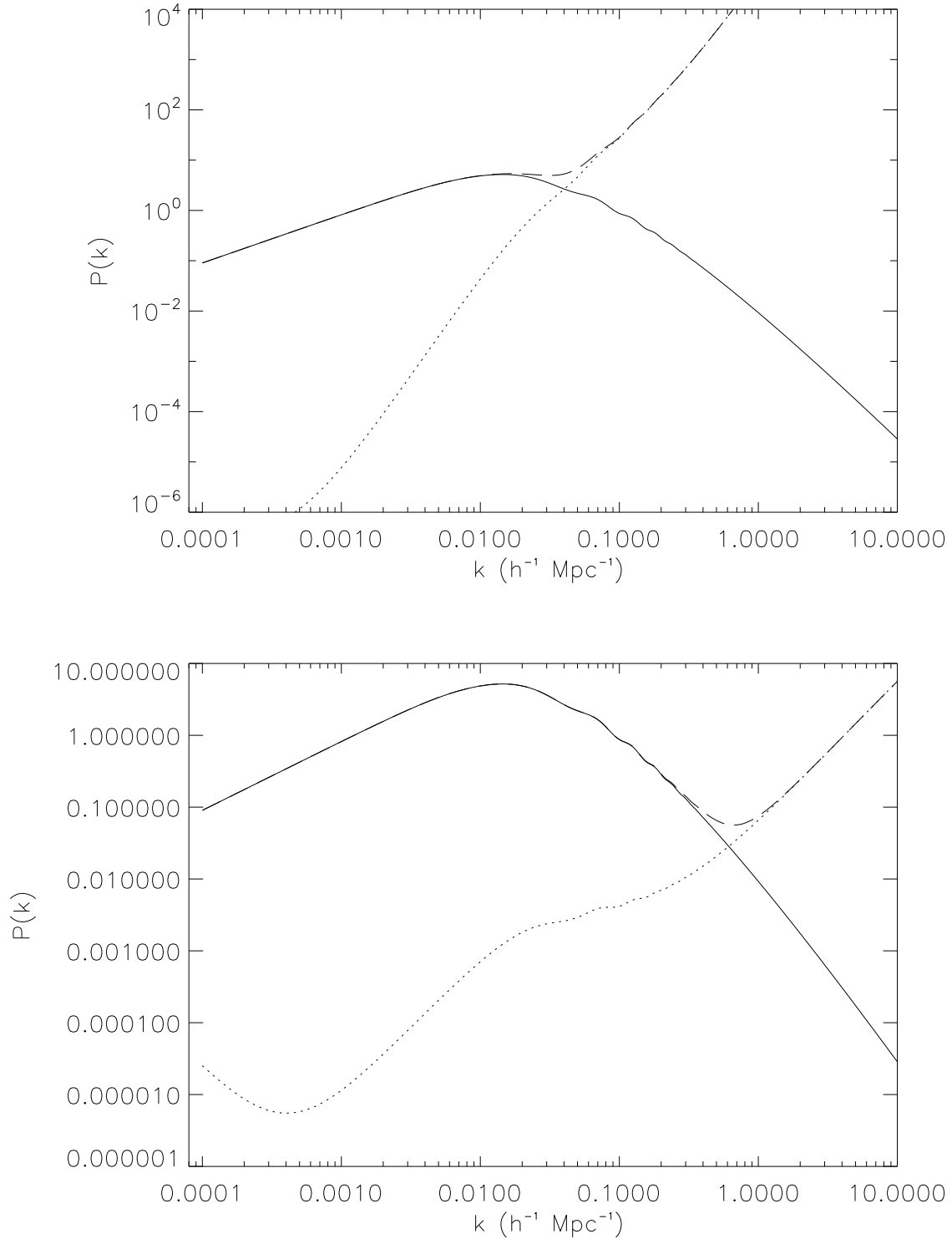


Figure 6.10: Matter power spectrum with PMF contribution. In solid we show the adiabatic power spectrum while in dotted is the magnetized matter power spectrum with $B_{1\text{Mpc}} = 6 \text{ nG}$ and respectively $n_B = 2$ for the upper panel and $n_B = -2.5$ for the lower one. Dashed line represents the uncorrelated sum of the adiabatic and magnetic contributions.

Chapter 7

Cosmological Parameters in Presence of PMFs

We developed an extension of the public Markov Chain MonteCarlo code CosmoMC in order to compute the Bayesian probability distribution of cosmological and magnetic parameters. In particular our extension is connected with our modified version of the CAMB code, which includes PMF contributions, and includes magnetic parameters. We excluded from the analysis the tensor magnetic contribution, since, as we have shown, it is always subdominant with respect to vector and scalar ones. We modified the code so that it computes together the angular power spectra of the standard CMB anisotropy and the magnetized scalar and vector ones both in temperature and polarization. The three sets (one for each component in temperature and polarization) of power spectra are then summed together in four single power spectra (TT, TE, EE, BB) which are used for the MCMC analysis. We vary the baryon density $\omega_b = \Omega_b h^2$, the cold dark matter density $\omega_c = \Omega_c h^2$ (with h being $H_0/100 \text{ km s}^{-1} \text{ Mpc}^{-1}$), the reionization optical depth τ_{opt} , the ratio of the sound horizon to the angular diameter distance at decoupling θ , $\log(10^{10} A_S)$, n_S and the magnetic parameters $B_{1\text{Mpc}}$ (in units of 10 nG) and n_B . As priors we use $[0, 10]$ for $B_{1\text{Mpc}}/(10 \text{ nG})$ and $[-2.9, 3]$ for n_B (> -3 in order to avoid infrared divergencies in the PMF EMT correlators). The

damping scale k_D is the one defined in Eq. 5.4 (in units of Mpc^{-1}). We assume a flat universe, a CMB temperature $T_{CMB} = 2.725$ K and we set the primordial Helium fraction to $y_{He} = 0.24$. We restrict our analysis to three massless neutrinos (a non-vanishing neutrino mass leads to a large scale enhancement in the power spectrum of CMB anisotropies in the presence of PMF [80, 81] and would not change our results). The pivot scale of the primordial scalar was set to $k_* = 0.05 \text{ Mpc}^{-1}$. We sample the posterior using the Metropolis-Hastings algorithm [119], generating four parallel chains and imposing a conservative Gelman-Rubin convergence criterion [120] of $R - 1 < 0.01$.

7.1 Constraints with Current CMB data

We performed an analysis of the WMAP 7 year [8], ACBAR [11], BICEP [14] and QUaD [13] CMB anisotropy data. In order to decrease the correlations between different data sets which cover the same region of the sky, we removed in the analysis the following CMB band powers: a) all the QUaD TT band powers since they overlap with data from the ‘CMB8’ region of ACBAR, b) the ACBAR band powers with $\ell < 910$ and $\ell > 1950$ to avoid overlap with WMAP (which is cosmic variance limited up to $\ell = 919$ [9, 10]) and contamination from foreground residuals, respectively, c) the QUaD TE band powers which overlap with WMAP ones, the QUaD EE band powers which overlap with BICEP, d) the BICEP TT, TE band powers (i.e., we use just EE and BB information from BICEP). In order to fit WMAP 7 years, ACBAR and QUaD data, we use the lensed CMB and matter power spectra and we follow the method implemented in CosmoMC consisting in varying a nuisance parameter A_{SZ} , which accounts for the unknown amplitude of the thermal Sunyaev-Zeldovich (SZ) contribution to the small-scale CMB data points assuming the model of [158].

In table 7.1 are reported the results of our analysis on current CMB data. For comparison we report both the results, obtained with the same datasets,

Parameter	Mean $B_\lambda = 0$	Mean
ω_b	$0.0222^{+0.0091}_{-0.00056}$	0.0222 ± 0.0010
ω_c	$0.109^{+0.007}_{-0.0077}$	0.112 ± 0.010
θ	$1.039^{+0.004}_{-0.003}$	$1.039^{+0.004}_{-0.005}$
τ_{opt}	$0.086^{+0.025}_{-0.022}$	$0.083^{+0.029}_{-0.030}$
$\log [10^{10} A_S]$	$3.05^{+0.06}_{-0.07}$	$3.06^{+0.07}_{-0.06}$
n_S	$0.955^{+0.024}_{-0.025}$	$0.955^{+0.025}_{-0.026}$
$B_{1\text{Mpc}}/\text{nG}$...	< 5.4
n_B	...	< -0.04
$H_0/\text{km s}^{-1}\text{Mpc}^{-1}$	$71.49^{+4.6}_{-4.3}$	$74.4^{+4.6}_{-5.4}$

Table 7.1: Mean parameter values and bounds of the central 95%-credible intervals without (left column) and with (right column) PMFs.

from the MCMC without PMFs contribution and the correspondent MCMC with PMF contribution. We note that neither the means nor the bounds of the cosmological parameters of the Λ CDM model with reionization are basically affected by the presence of PMF: this means that B_λ and n_B are not degenerate with the other six parameter of the concordance cosmological model.

In Figs. 7.1 and 7.2 we show the bidimensional and triangle plots of the MCMC with the magnetic parameters. We derived the following constraints on the amplitude and spectral index of PMF: $B_{1\text{Mpc}} < 5.4$ nG and $n_B < -0.04$ at 95% confidence level. Therefore, current and previous [81, 103] CMB data strongly disfavour positive n_B , putting pressure on causal mechanisms which produce a SB of PMFs with (comoving) amplitude of the order of nG. In order to derive the constraints with current data on this kind of PMFs, we performed a MCMC analysis, with all the four datasets, limited to PMFs with positive spectral indices.

In Figs. 7.3 and 7.4 we show the bidimensional and triangle plots of the results of the MCMC analysis on CMB anisotropy data for PMFs with spectral index limited to positive values: $n_B > 0$. We derived the following

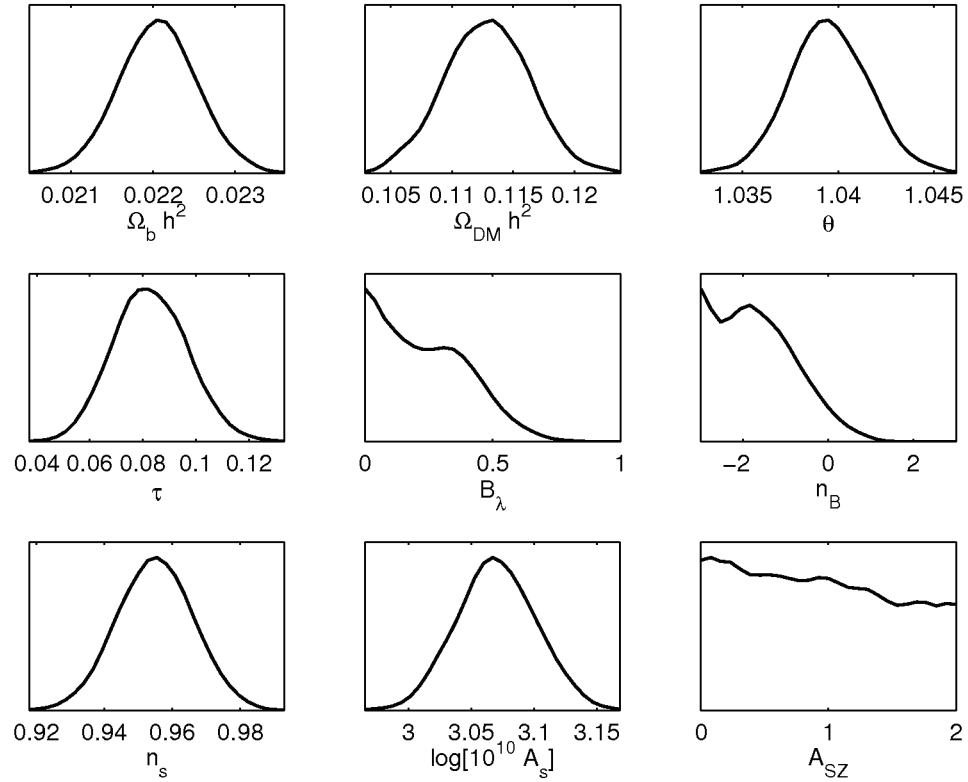


Figure 7.1: Results of the MCMC constrained with WMAP 7 years, ACBAR, BICEP and QUaD. Note that B_λ (with $\lambda = 1$ Mpc) is in 10 nG units.

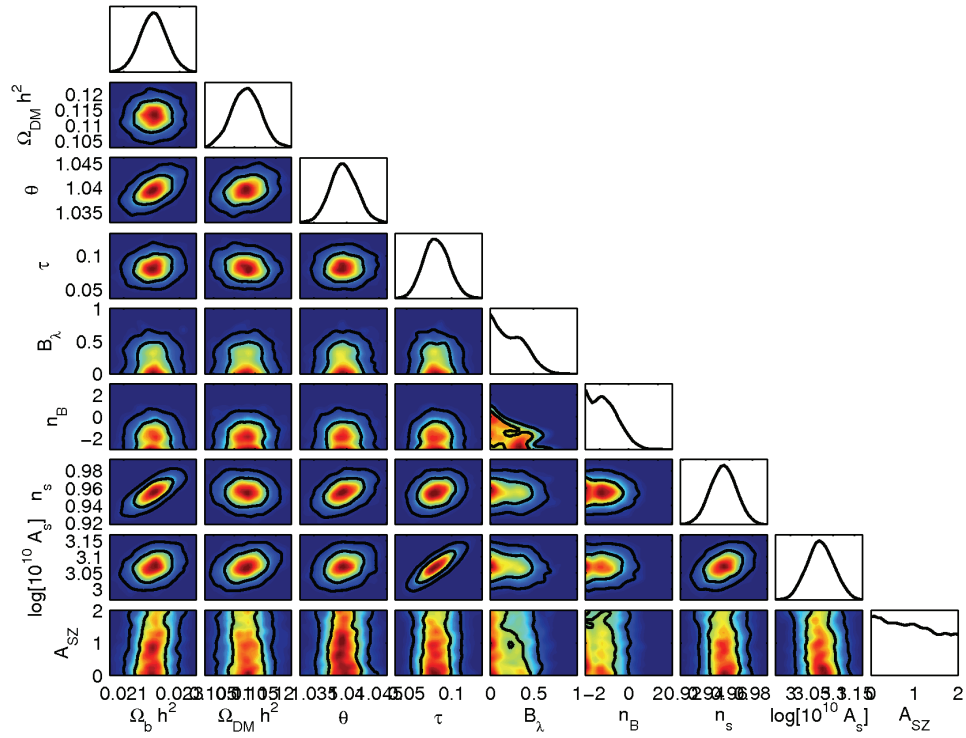


Figure 7.2: Results of the MCMC constrained with WMAP 7 years, ACBAR, BICEP and QUaD. Curves are the 68% and 95% confidence level. Note that B_λ (with $\lambda = 1$ Mpc) is in 10 nG units.

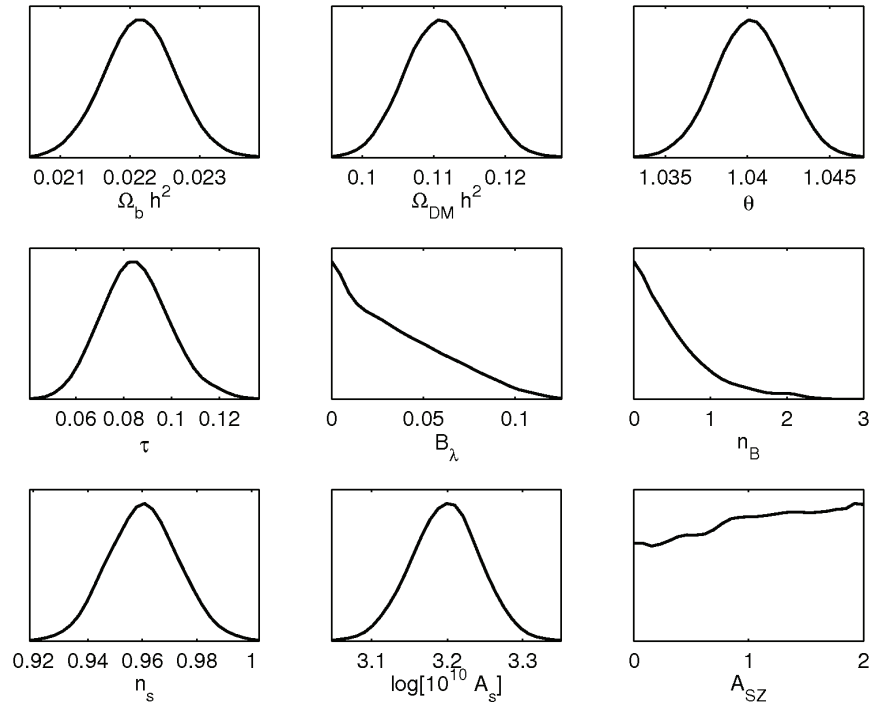


Figure 7.3: Results of the MCMC with PMFs only positive spectral index $n_B > 0$, constrained with WMAP 7 years, ACBAR, BICEP and QUaD. Note that B_λ (with $\lambda = 1$ Mpc) is in 10 nG units.

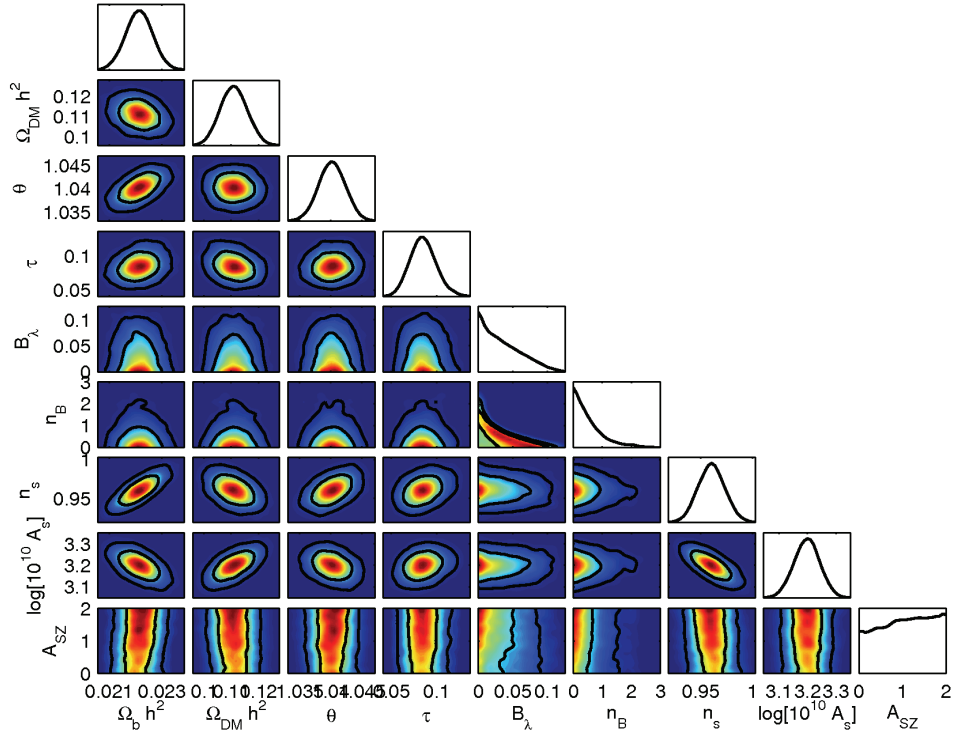


Figure 7.4: Triangle plot of the results of the MCMC with PMFs only positive spectral index $n_B > 0$, constrained with WMAP 7 years, ACBAR, BICEP and QUaD. Curves are the 68% and 95% confidence level. Note that B_λ (with $\lambda = 1$ Mpc) is in 10 nG units.

Parameter	Mean	Input value
ω_b	$0.0221^{+0.0002}_{-0.0003}$	0.022
ω_c	$0.111^{+0.002}_{-0.002}$	0.112
θ	$1.039^{+0.001}_{-0.0004}$	1.039
τ_{opt}	$0.0898^{+0.007}_{-0.0069}$	0.089
$\log [10^{10} A_S]$	$3.07^{+0.01}_{-0.02}$	3.07
n_S	$0.963^{+0.006}_{-0.007}$	0.96
$B_{1\text{Mpc}}/\text{nG}$...	< 2.8
n_B	...	< -0.17

Table 7.2: Mean parameter values and bounds of the central 95%-credible intervals for *Planck* simulated data, in the right column we show the input values for the cosmological model.

constraints on the amplitude and spectral index of PMFs: $B_{1\text{Mpc}} < 0.88$ nG and $n_B < 1.5$ at 95% confidence level. We note how even current CMB data with a positive prior for n_B do not favour causal mechanisms for the production of PMFs, which predict n_B even ≥ 2 [116].

7.2 Forecasts for *Planck*

We performed an analysis of *Planck* simulated mock data. We generated the mock data assuming *Planck* nominal 14 month plus 1 year approved extension mission performances (table 3.1). In order to test the *Planck* capability to constrain magnetic parameters, the mock data have been generated without PMF contribution. The input parameters of the cosmological model are reported in table 7.2.

In table 7.2 are reported the results of our MCMC analysis with simulated *Planck* data. We note how the code perfectly recovers the input parameters for the cosmological model. The constraints we obtained with *Planck* simulated data on the amplitude and spectral index of PMFs are: $B_{1\text{Mpc}} < 2.8$ nG and $n_B < -0.17$ at 95% confidence level.

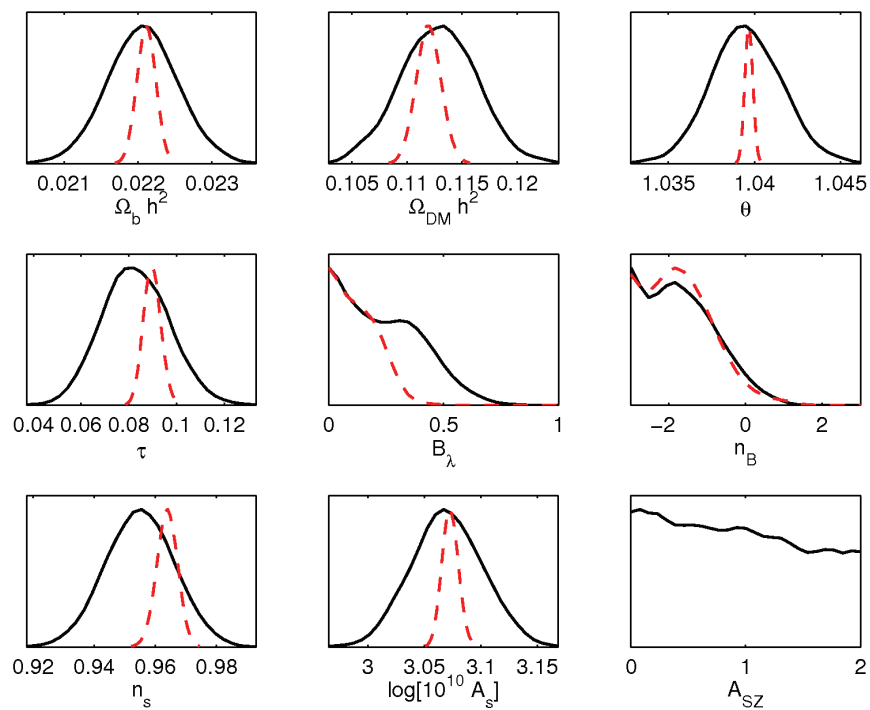


Figure 7.5: Results of the comparison between the MCMC constrained with WMAP 7 years, ACBAR, BICEP and QUAJ data (black) and the one with *Planck* simulated data (red). Note that B_λ (with $\lambda = 1$ Mpc) is in 10 nG units.

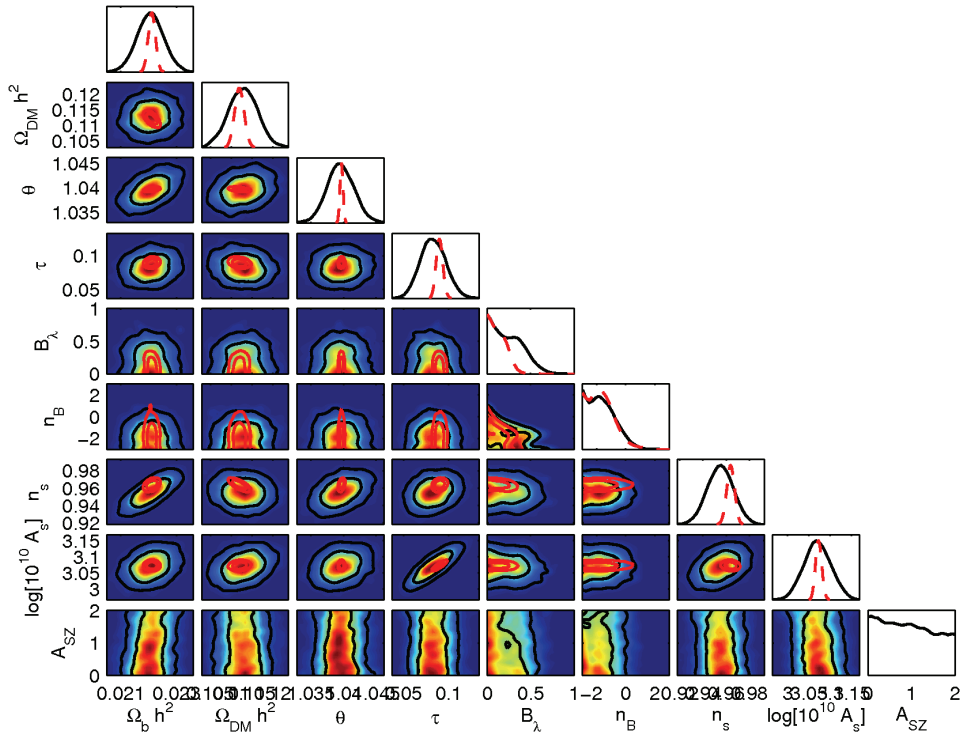


Figure 7.6: Triangle plot of the results of the comparison between the MCMC constrained with WMAP 7 years, ACBAR, BICEP and QUAED (black) and the one with *Planck* simulated data (red). Curves are the 68% and 95% confidence level. Note that B_λ (with $\lambda = 1$ Mpc) is in 10 nG units.

In Figs. 7.5 and 7.6 we show the bidimensional and triangle plots of the comparison between the MCMC with real current data and *Planck* simulated ones. We note how *Planck* data alone will improve the constraints on the PMF amplitude by a factor of two with respect to present data.

In the previous chapters we showed how the dominant contribution of PMFs is given by magnetized vector perturbations on small scales, the same happens for the constraints on cosmological and magnetic parameters. In particular in Figs. 7.7 and 7.8 we show the comparison of two MCMC analysis performed with *Planck* simulated data, one considers both scalar and vector magnetic contributions whereas the other considers only the vector one. We note how there are only minor differences between the two results. This confirms that the dominant contribution of PMFs to CMB anisotropies is given by magnetized vector perturbations.

7.3 Forecasts for CORE

Planck represents the present status of CMB observations, but the projects for the next generation of CMB dedicated experiments are already on their way. In particular we are interested in the project of the CORE (Cosmic ORigin Explorer) satellite [44]. The purpose of the CORE project is to perform a cosmic variance limited measurement of the EE mode. We investigated the capability to constrain magnetic parameters of a mission with an high resolution and sensitivity. We considered an average resolution of 5 arcmin and a noise level of the same order as the lensing signal in B-mode polarization. In Fig. 7.9 we show the noise level, beam convolved (in green), for temperature and B-mode polarization anisotropies, together with primary CMB we show also the contribution of magnetized scalar and vector CMB anisotropies. We created a simulated CORE dataset with the aforementioned characteristics and, as for the *Planck* case, without PMF contribution.

In table 7.3 we report the results of the MCMC analysis with CORE

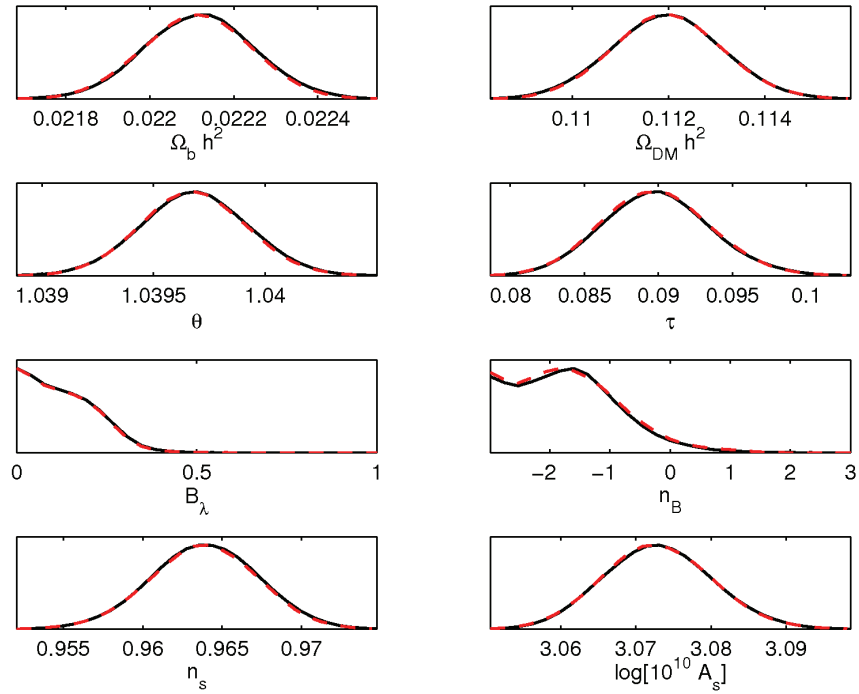


Figure 7.7: Results of the MCMC with PMF scalar and vector contributions (black) compared with vector only (red), constrained with *Planck* simulated data. Note that B_λ (with $\lambda = 1$ Mpc) is in 10 nG units.

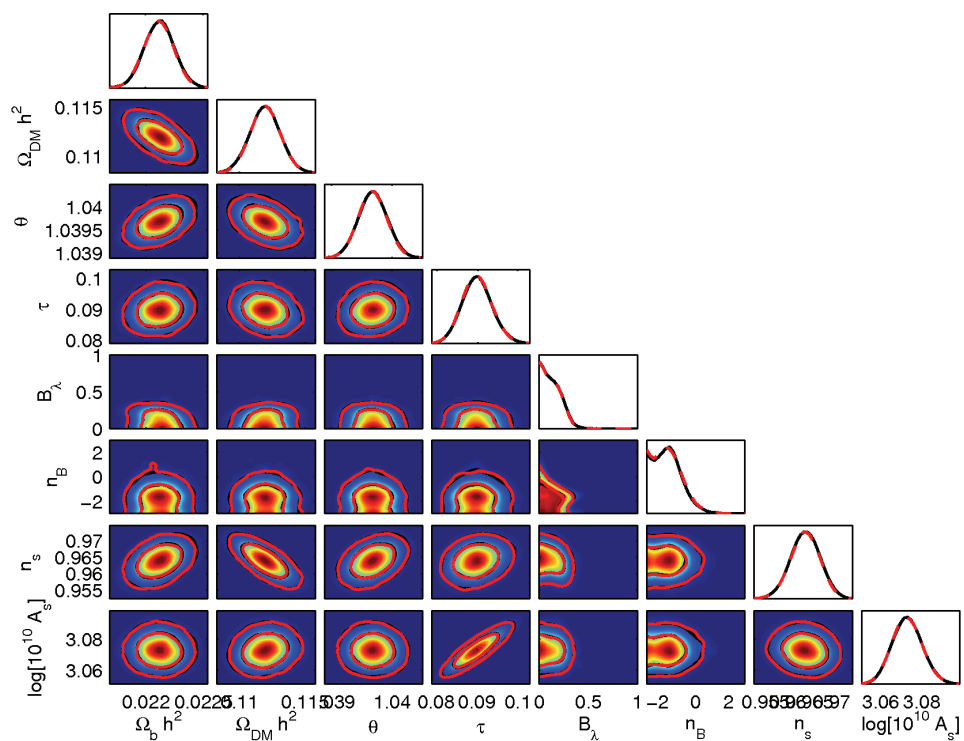


Figure 7.8: Results of the MCMC with PMF scalar and vector contributions (black) compared with vector only (red), constrained with *Planck* simulated data. Curves are the 68% and 95% confidence level. Note that B_λ (with $\lambda = 1$ Mpc) is in 10 nG units.

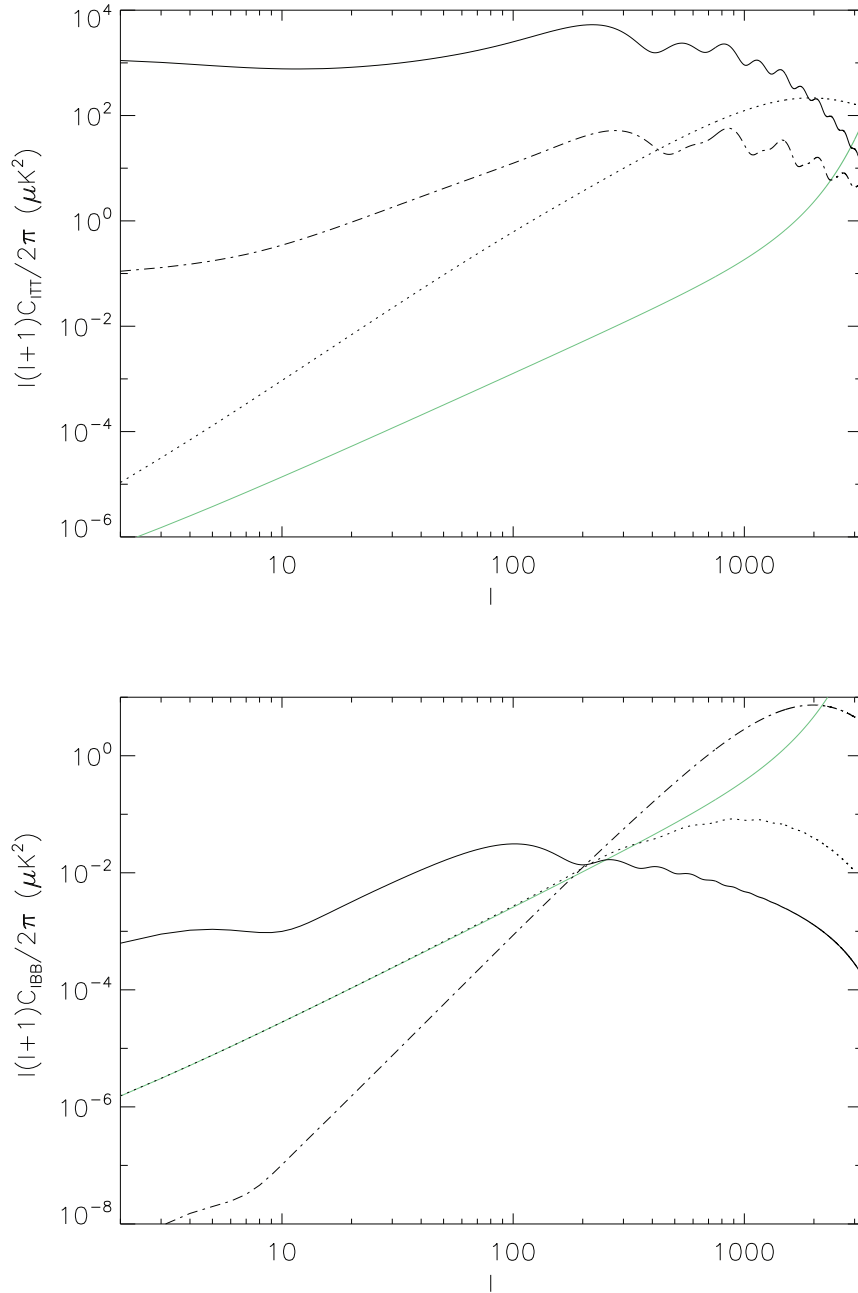


Figure 7.9: The noise level, beam convolved, for a 5' (green) CORE mission for temperature (upper panel) and B-mode polarization (lower panel), compared with primary CMB (black solid), magnetized vector mode (dot-dashed) and magnetized scalar mode (dotted) or lensing (in the right panel) with $B_\lambda = 6\text{nG}$ (with $\lambda = 1$ Mpc) and $n_B = -2.5$.

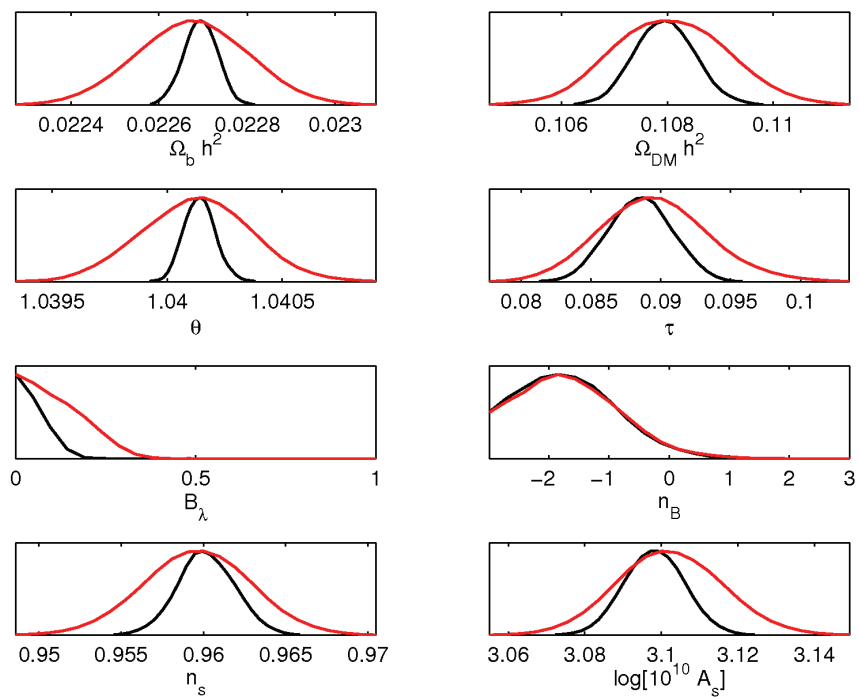


Figure 7.10: Results of the MCMC with PMF constrained with CORE simulated data (black) compared with *Planck* ones (red). Note that B_λ (with $\lambda = 1$ Mpc) is in 10 nG units.

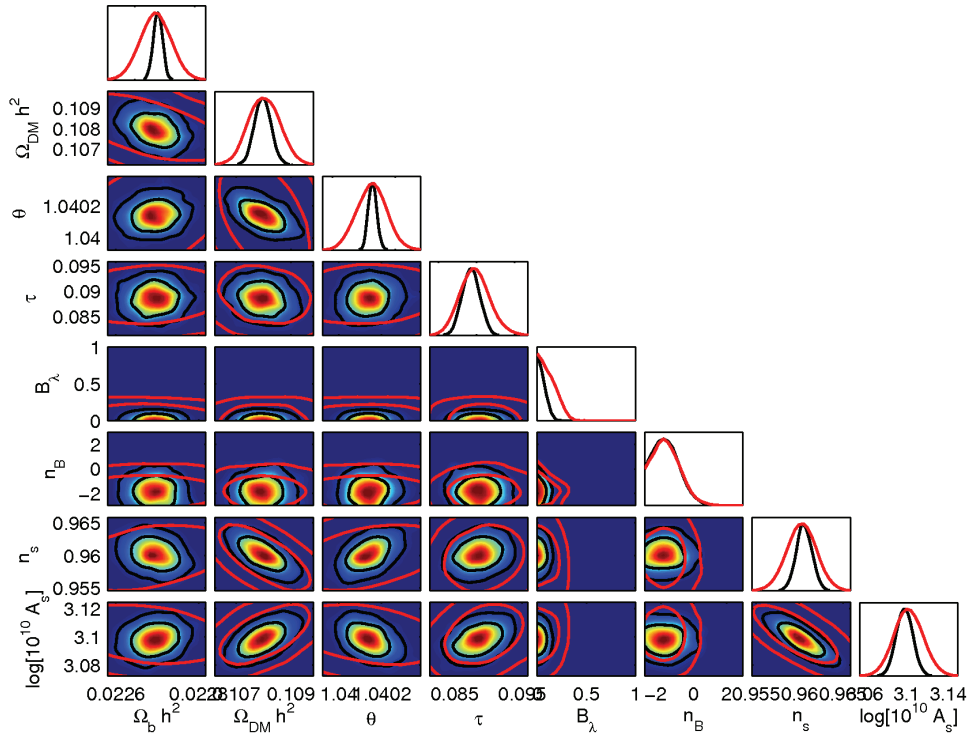


Figure 7.11: Results of the MCMC with PMF constrained with CORE simulated data (black) compared with *Planck* ones (red). Curves are the 68% and 95% confidence level. Note that B_λ (with $\lambda = 1$ Mpc) is in 10 nG units.

Parameter	Mean	Input value
ω_b	$0.0227 \pm 7 \times 10^{-5}$	0.0227
ω_c	0.107 ± 0.0011	0.108
θ	1.04 ± 0.0001	1.039
τ_{dec}	0.0898 ± 0.004	0.089
$\log [10^{10} A_S]$	3.07 ± 0.01	3.1
n_S	$0.960^{+0.001}_{-0.003}$	0.96
$B_{1\text{Mpc}}/\text{nG}$...	< 0.92
n_B	...	< -0.31

Table 7.3: Mean parameter values and bounds of the central 95%-credible intervals for CORE simulated data, in the right column we show the input values for the cosmological model, note that the input parameters are different from the *Planck* case.

simulated data. On the right column we show the input parameters of the cosmological model, which are different from the one used for the previous analysis with *Planck* data. We note the improvement in the constraints of magnetic parameters: $B_{1\text{Mpc}} < 0.92$ nG and $n_B < -0.31$ at 95% confidence level, and in particular how with CORE would be possible to constrain the PMF amplitude to values lower than nG.

In Figs. 7.10 and 7.11 we show the bidimensional and the triangle plots of the comparison of the results of the analysis with simulated CORE data with the *Planck* data one*. We note the improvement of CORE analysis with respect to *Planck* one for both cosmological and magnetic parameters.

7.4 CMB and large scale structure

In the previous chapter we have shown how PMFs have an impact also on the matter power spectrum. In order to investigate if this effect could im-

*We performed a different MCMC with *Planck* simulated data with the same input cosmological model as in the CORE simulated data.

Parameter	Mean	Input value
ω_b	0.0221 ± 0.0002	0.022
ω_c	0.112 ± 0.002	0.112
θ	$1.039_{0.0004}^{0.001}$	1.039
τ_{dec}	0.0898 ± 0.007	0.089
$\log [10^{10} A_S]$	3.07 ± 0.01	3.07
n_S	0.9634 ± 0.006	0.96
$B_{1\text{Mpc}}/\text{nG}$...	< 2.8
n_B	...	< -0.094

Table 7.4: Mean parameter values and bounds of the central 95%-credible intervals for *Planck* simulated data and SDSS LRG-DR4 matter power spectrum data, in the right column we show the input values for the cosmological model.

prove the cosmological parameter extraction, we performed a MCMC analysis with the large scale structure data of SDSS LRG DR4 [121], together with *Planck* simulated data for the CMB. In table 7.4 we show the results, with the addition of the SDSS data we obtained the following constraints on the amplitude and spectral index of PMF: $B_{1\text{Mpc}} < 2.8$ nG and $n_B < -0.094$ at 95% confidence level.

In Figs. 7.12 and 7.13 we show the bidimensional and triangle plot of the MCMC results compared with the case where the large scale structure data are not included. We note how the introduction of matter power spectrum does not change the constraints on PMFs. The apparent discrepancy between the important effect of PMFs on matter power spectrum and the unchanged constraints is related to the fact that matter power spectrum data do not reach small scales. As we have shown, the impact of PMFs on the matter power spectrum is on small scales, on large scales only PMFs with positive spectral index have an impact, but PMFs with blue spectral indices are already strongly constrained with CMB anisotropy data, for this reason

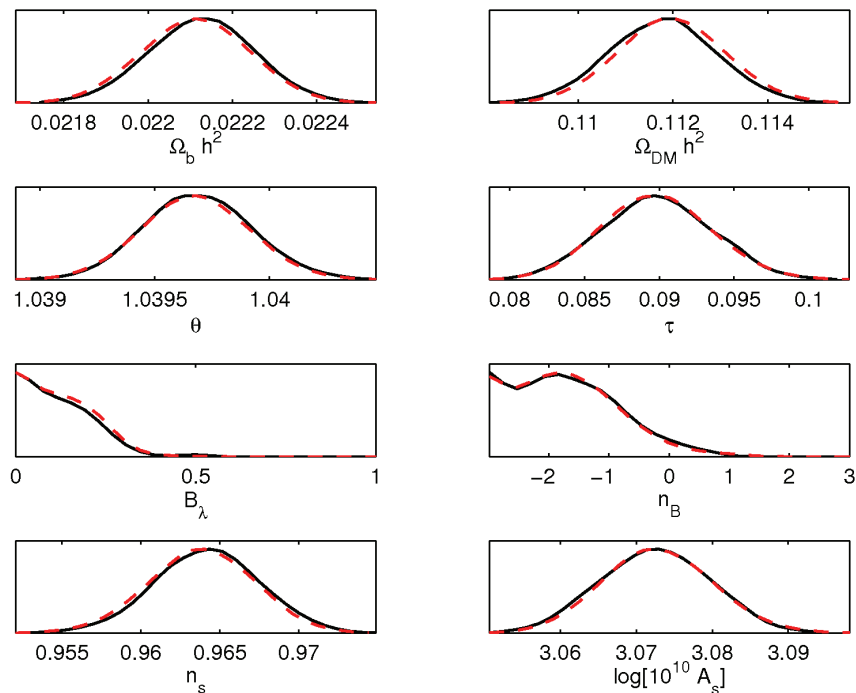


Figure 7.12: Comparison of the results of the MCMC with *Planck* simulated data and SDSS *LRGDR4* matter power spectrum data (black) with the ones with *Planck* simulated data alone (red). Note that B_λ (with $\lambda = 1$ Mpc) is in 10 nG units.

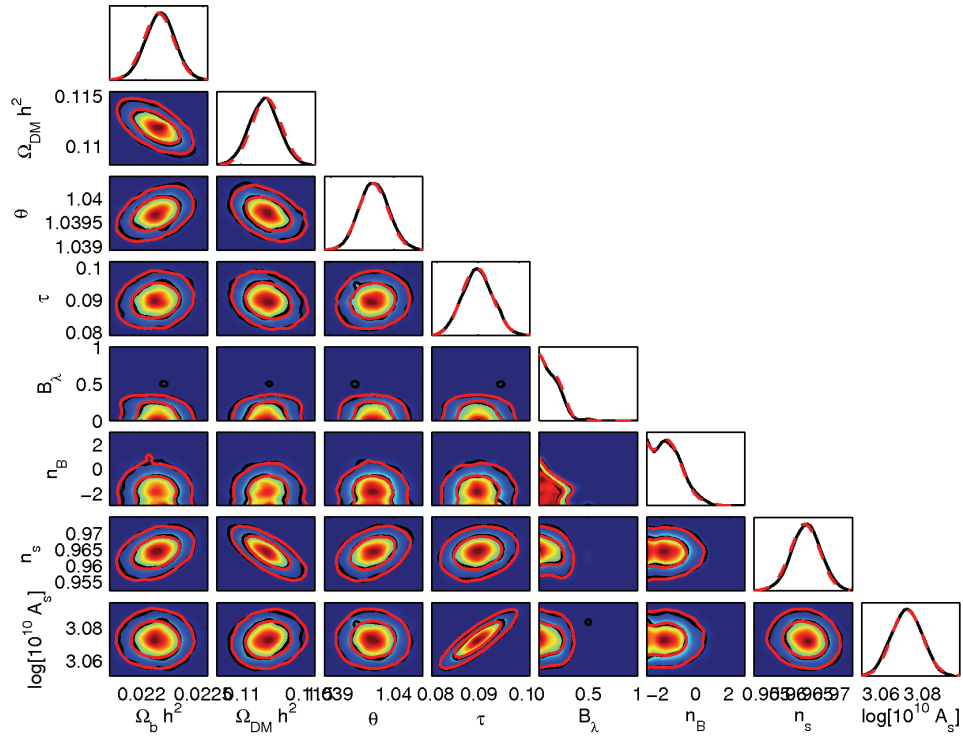


Figure 7.13: Comparison of the results of the MCMC with *Planck* simulated data and SDSS *LRGDR4* matter power spectrum data (black) with the ones with *Planck* simulated data alone (red). Note that B_λ (with $\lambda = 1 \text{ Mpc}$) is in 10 nG units.

the introduction of current matter power spectrum data does not add anything to the CMB data constraints.

We have shown the constraints on PMFs we obtained with current and simulated future CMB anisotropy data. We have shown how with present data the bounds on the amplitude are of the order of few nG and how with future ones it will be possible to constrain PMF amplitude to values lower than nG. Other possibilities to constrain PMFs have been proposed in recent years. In particular PMFs can be constrained with Faraday rotation. PMFs induce a Faraday rotation on CMB polarization, in particular PMFs rotate E-mode polarization into B-mode [149, 153, 151]. The present data on E-mode polarization and the bounds on B-mode one can be used to constrain PMF parameters [152, 150]: note however that in [152, 150] the vector contribution is not included and a full analysis is still lacking. Other possibilities to constrain PMFs are related with the modification of the TSZ effect induced by PMF [154] and the impact of PMFs on the universe thermal history [155, 156, 157].

The extension of CosmoMC+CAMB we have developed will be installed in the *Planck* LFI DPC.

PMFs not only have an impact on the CMB anisotropy angular power spectrum but they have a fully non-Gaussian contribution to CMB. In the next chapter we will investigate this contribution and we will show how PMFs can be constrained also with non-Gaussianity data.

Chapter 8

Non Gaussianities

The standard cosmological model with Gaussian cosmological perturbations is a very good fit to current cosmological data. This picture has recently received further confirmation by the WMAP seven year set of data [8]. The increasing accuracy of present and future CMB experiments opens the possibility to detect the non-linearities of the cosmological perturbations at the level of second- or higher-order perturbation theory. In particular the detection of these non-linearities through non-Gaussianities (NG) in the CMB, is one of the most important goals of experimental cosmology. A significant amount of NG is predicted by several models for the generation of cosmological perturbations. The detection of NG may represent a unique possibility to discriminate among different models, otherwise undistinguishable, and for this reason in recent years NG had attracted a lot of interest in cosmology.

Different models of perturbation generation predict the creation, either during or after inflation, of different amounts of NG with different characteristics. For example canonical single-field inflation models [122] predict a small amount of NG, the “curvaton-type” models [124, 125] instead predict a larger one. Models which generate perturbations at the end or after inflation [126], during pre [127] and reheating phase [128, 129, 130], predict the generation of NG dominated by the so-called “squeezed” configuration, where one of the momenta is much smaller than the other two. Models like DBI [131]

or ghost [132] inflation instead predict NG dominated by the “equilateral” configuration, in which the lengths of the three wavevectors in Fourier space are equal [133]. Present limits on NG are given by WMAP seven years data: $-5 < f_{NL}^{loc} < 59$, $-214 < f_{NL}^{equil} < 266$ and $-410 < f_{NL}^{ort} < 6$ at 95% CL.

Together with primordial origin, NG can be generated by other mechanisms and in particular, a stochastic background of PMFs has a fully non-Gaussian contribution to CMB anisotropies. PMFs, modelled as a fully inhomogeneous component, have an intrinsically non-Gaussian contribution to cosmological perturbations. In fact, as shown in previous chapter, the magnetic source terms in the perturbation equations are the PMF EMT and the Lorentz force, both are quadratic in PMFs and PMFs are randomly distributed. Therefore the magnetic source terms are χ -distributed, leading to a PMF contribution to CMB fully non-Gaussian. A non-Gaussian contribution translates in non-vanishing higher order statistical moments of the PMF EMT and the CMB anisotropies. In this chapter we will derive the large scale magnetic CMB bispectrum generated by scalar magnetized cosmological perturbations and the constraints on PMF parameters with current NG data.

8.1 CMB temperature spectrum at large angular scales

Before deriving the CMB magnetic bispectrum, we will derive an analytical expression for the large scale temperature anisotropies induced by magnetized scalar perturbations. Large scale CMB anisotropies are dominated by the Sachs-Wolfe term:

$$\frac{\Theta_\ell^{(0)}(\eta_0, \mathbf{k})}{2\ell + 1} = \left(\frac{1}{4} \delta_\gamma^{CG} + \psi \right) j_\ell(k(\eta_0 - \eta_{dec})), \quad (8.1)$$

where Φ and δ_γ^{CG} are respectively the newtonian potential and the photon density contrast in the Newtonian gauge, j_ℓ is the spherical Bessel function and η_0, η_{dec} denote conformal time respectively today and at decoupling.

Applying the gauge transformations, the newtonian potential can be written as a function of the two scalar metric perturbations of the synchronous gauge:

$$\psi(k, \tau) = \frac{\ddot{h}(k, \tau) + 6\ddot{\eta}(k, \tau)}{2k^2} + \mathcal{H}(\tau) \frac{\dot{h}(k, \tau) + 6\dot{\eta}(k, \tau)}{2k^2}, \quad (8.2)$$

while the relation between the density contrasts in the two gauges is:

$$\delta_\gamma^{CG}(k, \tau) = \delta_\gamma^{SG}(k, \tau) - 4\mathcal{H}(\tau) \frac{\dot{h}(k, \tau) + 6\dot{\eta}(k, \tau)}{2k^2} \quad (8.3)$$

Inserting Eqs. 8.2 and 8.3 in Eq. 8.1 we can express the temperature anisotropies on large scales in the synchronous gauge:

$$\frac{\Theta_\ell^{(0)}(\eta_0, \mathbf{k})}{2\ell + 1} = \left(\frac{1}{4} \delta_\gamma^{SG}(k, \tau) + \frac{\ddot{h}(k, \tau) + 6\ddot{\eta}(k, \tau)}{2k^2} \right) \quad (8.4)$$

Substituting the initial conditions for the magnetic scalar mode we obtain:

$$\frac{\Theta_\ell^{(0)}(\eta_0, \mathbf{k})}{2\ell + 1} = \frac{\alpha}{4} \Omega_B(\mathbf{k}) j_\ell(k(\eta_0 - \eta_{dec})), \quad (8.5)$$

where α is equal 1 in the radiation dominated era and accounts for possible corrections in the matter dominated one. The angular power spectrum of CMB anisotropies is given by:

$$C_\ell^B = \frac{2}{\pi} \int_0^\infty dk k^2 \frac{\langle \Theta_\ell^{(0)}(\eta_0, \mathbf{k}) \Theta_\ell^{(0)*}(\eta_0, \mathbf{k}) \rangle}{(2\ell + 1)^2} = \frac{\alpha^2}{8\pi} \int_0^\infty dk k^2 |\Omega_B(\mathbf{k})|^2 j_\ell^2(k(\eta_0 - \eta_{dec})). \quad (8.6)$$

Since we are interested in the large scale behavior of the angular power spectrum, we can use the infrared limit of the magnetic energy density Fourier spectrum:

$$\begin{aligned} |\rho_B(k)|^2 &\sim \frac{A^2 k_D^{2n_B+3}}{128\pi^4 (2n_B + 3)} \text{ for } n_B > -1.5 \\ |\rho_B(k)|^2 &\sim \frac{A^2 k_D^{2n_B+3}}{512\pi^4} \frac{3\pi^2}{4k} \text{ for } n_B \sim -2 \\ |\rho_B(k)|^2 &\sim \frac{A^2 k_D^{2n_B+3}}{128\pi^4} \frac{n_B}{(2n_B + 3)(n_B + 3)} \text{ for } n_B \sim -3, \end{aligned} \quad (8.7)$$

where in the $n_B \sim -3$ case, for simplicity, we used the results of [85]. Substituting the previous expressions in Eq. 8.6 we obtained:

$$\begin{aligned}
C_\ell^B &\simeq \frac{\alpha^2 A^2 k_D^{2n_B+6}}{1024\pi^4(2n_B+3)\rho_{rel}^2(k_D\eta_0)^3} \int_0^{k_D\eta_0} dx x^2 j_\ell^2(x) \\
&\simeq \frac{\alpha^2 \langle B^2 \rangle^2 (n_B+3)^2}{512\pi(2n_B+3)\rho_{rel}^2(k_D\eta_0)^2} \text{ for } n_B > -3/2 \\
C_\ell^B &\simeq \frac{3\alpha^2 A^2 k_D^{2n_B+5}}{16384\pi^3\rho_{rel}^2(k_D\eta_0)^2} \int_0^{k_D\eta_0} dx x j_\ell^2(x) \\
&\simeq \frac{3\pi\alpha^2 \langle B^2 \rangle^2 (n_B+3)^2}{8192\rho_{rel}^2(k_D\eta_0)^2} \log\left(\frac{k_D\eta_0}{l}\right) \text{ for } n_B = -2, \\
C_\ell^B &\simeq \frac{\alpha^2 A^2 k_D^{2n_B+3}}{1024\pi^5\rho_{rel}^2(k_D\eta_0)^{2n_B+6}} \frac{n_B}{(2n_B+3)(n_B+3)} \int_0^{k_D\eta_0} dx x^{2n_B+5} j_\ell^2(x) \\
&\simeq \frac{\alpha^2 \langle B^2 \rangle^2}{1024\sqrt{\pi}\rho_{rel}^2} \frac{n_B(n_B+3)}{(2n_B+3)} \frac{\Gamma[-n-2]}{\Gamma[-n-3/2]} \frac{1}{(k_D\eta_0)^{2n_B+6}} \ell^{2n_B+4} \text{ for } n_B < -2,
\end{aligned} \tag{8.8}$$

where $x = k\eta_0$, we have approximated $j_\ell(k(\eta_0 - \eta_{dec})) \simeq j_\ell(k\eta_0)$ and we integrate only up to the upper cutoff k_D . The approximated solutions of the bessel function integrals are described in the appendix. Expressing Eqs. 8.8 with smoothed PMFs we have:

$$\begin{aligned}
C_\ell^B &\simeq \frac{\alpha^2 \langle B_\lambda^2 \rangle^2 (k_D\lambda)^{2n_B+6}}{512\pi\Gamma^2\left(\frac{n_B+3}{2}\right)(2n_B+3)\rho_{rel}^2(k_D\eta_0)^2} \text{ for } n_B > -3/2 \\
C_\ell^B &\simeq \frac{3\pi\alpha^2 \langle B_\lambda^2 \rangle^2 (k_D\lambda)^{2n_B+6}}{8192\Gamma^2\left(\frac{n_B+3}{2}\right)\rho_{rel}^2(k_D\eta_0)^2} \log\left(\frac{k_D\eta_0}{l}\right) \text{ for } n_B = -2, \\
C_\ell^B &\simeq \frac{\alpha^2 \langle B_\lambda^2 \rangle^2 (k_D\lambda)^{2n_B+6}}{1024\sqrt{\pi}(n_B+3)\Gamma^2\left(\frac{n_B+3}{2}\right)\rho_{rel}^2} \frac{n_B}{(2n_B+3)} \frac{\Gamma[-n-2]}{\Gamma[-n-3/2]} \\
&\quad \frac{1}{(k_D\eta_0)^{2n_B+6}} \ell^{2n_B+4} \text{ for } n_B < -2,
\end{aligned} \tag{8.9}$$

The temperature anisotropies on large scale are proportional to the magnetic energy density, as a consequence the behavior of the angular power spectrum strongly depends on the Fourier spectrum of the PMF EMT. In the previous chapters we showed the numerical results on the dependence of the temperature anisotropy angular power spectrum on the magnetic spectral index. In

particular we showed how it has a strong dependence on the spectral index and follows the behavior of the PMF EMT. The magnetic Sachs-Wolfe effect we derived in Eq. 8.9 is the analytical counterpart of what we found numerically.

8.2 CMB temperature bispectrum at large angular scales

We wish to evaluate the CMB angular bispectrum of the temperature anisotropies due to the magnetic Sachs-Wolfe effect. The angular bispectrum is given by the three point correlation function of the a_{lm} ($\langle a_{\ell_1 m_1} a_{\ell_2 m_2} a_{\ell_3 m_3} \rangle$):

$$a_{\ell m}(\mathbf{x}) = \int d\Omega_{\hat{n}} Y_{\ell m}^*(\hat{n}; \hat{e}) \Theta^{(0)}(\mathbf{x}, \hat{n}), \quad (8.10)$$

where $Y_{\ell m}^*(\hat{n}; \hat{e})$ is the spherical harmonic with respect to a basis where \hat{e} is an arbitrary, but fixed, direction. The $\Theta^{(0)}(\mathbf{x}, \hat{n})$ is the scalar temperature perturbation at \mathbf{x} (\hat{n} is the direction of light propagation). Using the formalism developed in [134] we have:

$$\Theta^{(0)}(\mathbf{x}, \hat{n}) = \int \frac{d^3 k}{(2\pi)^3} \Sigma_{\ell} \Theta_{\ell}^{(0)}(\eta_0, \mathbf{k}) G_{\ell}^0, \quad (8.11)$$

$$G_{\ell}^0 = (-i)^{\ell} \sqrt{\frac{4\pi}{2\ell+1}} Y_{\ell 0}(\hat{n}; \hat{k}) e^{i\mathbf{k}\cdot\mathbf{x}}, \quad (8.12)$$

with respect to a basis where \hat{k} is fixed. Substituting the above expressions in Eq. 8.10, and changing basis accordingly [135], we found:

$$a_{\ell m}(\mathbf{x}) = \frac{4\pi(-i)^{\ell}}{2\ell+1} \int \frac{d^3 k}{(2\pi)^3} \Theta_{\ell}^{(0)}(\eta_0, \mathbf{k}) e^{i\mathbf{k}\cdot\mathbf{x}} Y_{\ell m}^*(\hat{k}; \hat{e}). \quad (8.13)$$

Therefore placing the observer in $\mathbf{x} = 0$, the angular bispectrum is given by:

$$\begin{aligned} \langle a_{\ell_1 m_1} a_{\ell_2 m_2} a_{\ell_3 m_3} \rangle &= \frac{(4\pi)^3 (-i)^{\ell_1 + \ell_2 + \ell_3}}{(2\ell_1 + 1)(2\ell_2 + 1)(2\ell_3 + 1)} \times \\ &\int \frac{d^3 k d^3 q d^3 p}{(2\pi)^9} Y_{\ell_1 m_1}^*(\hat{k}; \hat{e}) Y_{\ell_2 m_2}^*(\hat{q}; \hat{e}) Y_{\ell_3 m_3}^*(\hat{p}; \hat{e}) \\ &\times \langle \Theta_{\ell_1}^{(0)}(\eta_0, \mathbf{k}) \Theta_{\ell_2}^{(0)}(\eta_0, \mathbf{q}) \Theta_{\ell_3}^{(0)}(\eta_0, \mathbf{p}) \rangle. \end{aligned} \quad (8.14)$$

We note from Eq. 8.5 that the magnetic CMB bispectrum will depend on the bispectrum of the magnetic energy density $\langle \rho_B(\mathbf{k})\rho_B(\mathbf{q})\rho_B(\mathbf{p}) \rangle$.

8.3 Magnetic energy density bispectrum

The magnetic energy density bispectrum depends on the six point correlation function of the PMFs:

$$\begin{aligned} \langle \rho_B(\mathbf{k})\rho_B(\mathbf{q})\rho_B(\mathbf{p}) \rangle &= \frac{1}{(8\pi)^3} \int \frac{d^3\tilde{k} d^3\tilde{q} d^3\tilde{p}}{(2\pi)^9} \times \\ &\quad \langle B_i(\tilde{\mathbf{k}})B_i(\mathbf{k}-\tilde{\mathbf{k}})B_j(\tilde{\mathbf{q}})B_j(\mathbf{q}-\tilde{\mathbf{q}})B_l(\tilde{\mathbf{p}})B_l(\mathbf{p}-\tilde{\mathbf{p}}) \rangle. \end{aligned} \quad (8.15)$$

PMF are modelled as a Gaussian variable, therefore is possible to apply the Wick theorem to decompose the six point correlation function into products of the PMF power spectrum. We can also use the property $B_i^*(\mathbf{k}) = B_i(-\mathbf{k})$. The results of the decomposition with the Wick theorem is made by fifteen terms. Of these terms, seven disappear because they are proportional to $\delta(\mathbf{k})$, $\delta(\mathbf{q})$ or $\delta(\mathbf{p})$. The remaining eight terms are:

$$\begin{aligned} \langle B_i(\tilde{\mathbf{k}})B_i(\mathbf{k}-\tilde{\mathbf{k}}) B_j(\tilde{\mathbf{q}})B_j(\mathbf{q}-\tilde{\mathbf{q}})B_l(\tilde{\mathbf{p}})B_l(\mathbf{p}-\tilde{\mathbf{p}}) \rangle &= \\ &\quad \langle B_i(\tilde{\mathbf{q}})B_j(\tilde{\mathbf{k}}) \rangle \langle B_i(\mathbf{q}-\tilde{\mathbf{q}})B_l(\tilde{\mathbf{p}}) \rangle \langle B_j(\mathbf{k}-\tilde{\mathbf{k}})B_l(\mathbf{p}-\tilde{\mathbf{p}}) \rangle + \\ &\quad \langle B_i(\tilde{\mathbf{q}})B_j(\tilde{\mathbf{k}}) \rangle \langle B_i(\mathbf{q}-\tilde{\mathbf{q}})B_l(\mathbf{p}-\tilde{\mathbf{p}}) \rangle \langle B_j(\mathbf{k}-\tilde{\mathbf{k}})B_l(\mathbf{p}) \rangle + \\ &\quad \langle B_i(\tilde{\mathbf{q}})B_j(\mathbf{k}-\tilde{\mathbf{k}}) \rangle \langle B_i(\mathbf{q}-\tilde{\mathbf{q}})B_l(\tilde{\mathbf{p}}) \rangle \langle B_j(\tilde{\mathbf{k}})B_l(\mathbf{p}-\tilde{\mathbf{p}}) \rangle + \\ &\quad \langle B_i(\tilde{\mathbf{q}})B_j(\mathbf{k}-\tilde{\mathbf{k}}) \rangle \langle B_i(\mathbf{q}-\tilde{\mathbf{q}})B_l(\mathbf{p}-\tilde{\mathbf{p}}) \rangle \langle B_j(\tilde{\mathbf{k}})B_l(\tilde{\mathbf{p}}) \rangle + \\ &\quad \langle B_i(\tilde{\mathbf{q}})B_l(\tilde{\mathbf{p}}) \rangle \langle B_i(\mathbf{q}-\tilde{\mathbf{q}})B_j(\tilde{\mathbf{k}}) \rangle \langle B_j(\mathbf{k}-\tilde{\mathbf{k}})B_l(\mathbf{p}-\tilde{\mathbf{p}}) \rangle + \\ &\quad \langle B_i(\tilde{\mathbf{q}})B_l(\tilde{\mathbf{p}}) \rangle \langle B_i(\mathbf{q}-\tilde{\mathbf{q}})B_j(\mathbf{k}-\tilde{\mathbf{k}}) \rangle \langle B_j(\tilde{\mathbf{k}})B_l(\mathbf{p}-\tilde{\mathbf{p}}) \rangle + \\ &\quad \langle B_i(\tilde{\mathbf{q}})B_l(\mathbf{p}-\tilde{\mathbf{p}}) \rangle \langle B_i(\mathbf{q}-\tilde{\mathbf{q}})B_j(\tilde{\mathbf{k}}) \rangle \langle B_l(\tilde{\mathbf{p}})B_j(\mathbf{k}-\tilde{\mathbf{k}}) \rangle + \\ &\quad \langle B_i(\tilde{\mathbf{q}})B_l(\mathbf{p}-\tilde{\mathbf{p}}) \rangle \langle B_i(\mathbf{q}-\tilde{\mathbf{q}})B_j(\mathbf{k}-\tilde{\mathbf{k}}) \rangle \langle B_j(\tilde{\mathbf{k}})B_l(\tilde{\mathbf{p}}) \rangle, \end{aligned} \quad (8.16)$$

where $\langle B_i(\mathbf{k})B_j^*(\mathbf{p}) \rangle = (2\pi)^3\delta(\mathbf{k}-\mathbf{p})P_{ij}(\mathbf{k})$ and $P_{ij}(\mathbf{k}) = P_B(k)(\delta_{ij} - \hat{k}_i\hat{k}_j)$. Using $B_i^*(\mathbf{k}) = B_i(-\mathbf{k})$ we have: $\langle B_i(\mathbf{k})B_j^*(\mathbf{p}) \rangle = (2\pi)^3\delta(\mathbf{k}+\mathbf{p})P_{ij}(\mathbf{k})$. Sub-

stituting we obtain:

$$\begin{aligned}
& \langle B_i(\tilde{\mathbf{k}})B_i(\mathbf{k} - \tilde{\mathbf{k}})B_j(\tilde{\mathbf{q}})B_j(\mathbf{q} - \tilde{\mathbf{q}})B_l(\tilde{\mathbf{p}})B_l(\mathbf{p} - \tilde{\mathbf{p}}) \rangle = \\
& P_{ij}(\tilde{\mathbf{q}})P_{il}(\mathbf{q} - \tilde{\mathbf{q}})P_{jl}(\mathbf{k} - \tilde{\mathbf{k}})\delta(\tilde{\mathbf{k}} + \tilde{\mathbf{q}})\delta(\mathbf{q} - \tilde{\mathbf{q}} + \tilde{\mathbf{p}})\delta(\mathbf{k} - \tilde{\mathbf{k}} + \mathbf{p} - \tilde{\mathbf{p}}) + \\
& P_{ij}(\tilde{\mathbf{q}})P_{il}(\mathbf{q} - \tilde{\mathbf{q}})P_{jl}(\mathbf{k} - \tilde{\mathbf{k}})\delta(\tilde{\mathbf{k}} + \tilde{\mathbf{q}})\delta(\mathbf{q} - \tilde{\mathbf{q}} + \mathbf{p} - \tilde{\mathbf{p}})\delta(\mathbf{k} - \tilde{\mathbf{k}} + \tilde{\mathbf{p}}) + \\
& P_{ij}(\tilde{\mathbf{q}})P_{il}(\mathbf{q} - \tilde{\mathbf{q}})P_{jl}(\tilde{\mathbf{k}})\delta(\mathbf{k} - \tilde{\mathbf{k}} + \tilde{\mathbf{q}})\delta(\mathbf{q} - \tilde{\mathbf{q}} + \tilde{\mathbf{p}})\delta(\tilde{\mathbf{k}} + \mathbf{p} - \tilde{\mathbf{p}}) + \\
& P_{ij}(\tilde{\mathbf{q}})P_{il}(\mathbf{q} - \tilde{\mathbf{q}})P_{jl}(\tilde{\mathbf{k}})\delta(\mathbf{k} - \tilde{\mathbf{k}} + \tilde{\mathbf{q}})\delta(\mathbf{q} - \tilde{\mathbf{q}} + \mathbf{p} + \tilde{\mathbf{p}})\delta(\tilde{\mathbf{k}} + \tilde{\mathbf{p}}) + \\
& P_{il}(\tilde{\mathbf{q}})P_{ij}(\mathbf{q} - \tilde{\mathbf{q}})P_{jl}(\tilde{\mathbf{k}})\delta(\tilde{\mathbf{p}} + \tilde{\mathbf{q}})\delta(\mathbf{q} - \tilde{\mathbf{q}} + \mathbf{k} + \tilde{\mathbf{k}})\delta(\tilde{\mathbf{k}} + \mathbf{p} - \tilde{\mathbf{p}}) + \\
& P_{il}(\tilde{\mathbf{q}})P_{ij}(\mathbf{q} - \tilde{\mathbf{q}})P_{jl}(\mathbf{k} - \tilde{\mathbf{k}})\delta(\tilde{\mathbf{p}} + \tilde{\mathbf{q}})\delta(\mathbf{q} - \tilde{\mathbf{q}} + \tilde{\mathbf{k}})\delta(\mathbf{k} - \tilde{\mathbf{k}} + \mathbf{p} - \tilde{\mathbf{p}}) + \\
& P_{il}(\tilde{\mathbf{q}})P_{ij}(\mathbf{q} - \tilde{\mathbf{q}})P_{jl}(\mathbf{k} - \tilde{\mathbf{k}})\delta(\tilde{\mathbf{q}} + \mathbf{p} - \tilde{\mathbf{p}})\delta(\mathbf{q} - \tilde{\mathbf{q}} + \tilde{\mathbf{k}})\delta(\mathbf{k} - \tilde{\mathbf{k}} + \tilde{\mathbf{p}}) + \\
& P_{il}(\tilde{\mathbf{q}})P_{ij}(\mathbf{q} - \tilde{\mathbf{q}})P_{jl}(\tilde{\mathbf{k}})\delta(\mathbf{p} - \tilde{\mathbf{p}} + \tilde{\mathbf{q}})\delta(\mathbf{q} - \tilde{\mathbf{q}} + \mathbf{k} + \tilde{\mathbf{k}})\delta(\tilde{\mathbf{k}} + \tilde{\mathbf{p}}). \quad (8.17)
\end{aligned}$$

Each of the terms contains the product of three delta functions, we can integrate two of the three and the remaining one represents the homogeneity condition: $\delta(\mathbf{k} + \mathbf{q} + \mathbf{p})$. The right hand side of Eq. 8.15 apparently is not symmetric under the exchange of \mathbf{k} , \mathbf{q} and \mathbf{p} , contrary to the left hand side. The lack of explicit symmetry is the reason why the results depend on which of the variables we decide to integrate. In particular performing the integration in $d^3\tilde{p}$ and $d^3\tilde{q}$, leaving out $d^3\tilde{k}$, the result is:

$$\langle \rho_B(\mathbf{k})\rho_B(\mathbf{q})\rho_B(\mathbf{p}) \rangle = \frac{1}{128\pi^3}\delta(\mathbf{k}+\mathbf{p}+\mathbf{q}) \int d^3\tilde{k} P_{ij}(\tilde{\mathbf{k}})P_{jl}(\mathbf{k}-\tilde{\mathbf{k}})[P_{il}(\mathbf{q}+\tilde{\mathbf{k}})+P_{il}(\mathbf{p}+\tilde{\mathbf{k}})], \quad (8.18)$$

while integrating out $d^3\tilde{k}$ and $d^3\tilde{p}$ the result is:

$$\langle \rho_B(\mathbf{k})\rho_B(\mathbf{q})\rho_B(\mathbf{p}) \rangle = \frac{1}{128\pi^3}\delta(\mathbf{k}+\mathbf{p}+\mathbf{q}) \int d^3\tilde{q} P_{ij}(\tilde{\mathbf{q}})P_{jl}(\mathbf{q}-\tilde{\mathbf{q}})[P_{il}(\mathbf{k}+\tilde{\mathbf{q}})+P_{il}(\mathbf{p}+\tilde{\mathbf{q}})], \quad (8.19)$$

finally integrating out $d^3\tilde{q}$ and $d^3\tilde{k}$:

$$\langle \rho_B(\mathbf{k})\rho_B(\mathbf{q})\rho_B(\mathbf{p}) \rangle = \frac{1}{128\pi^3}\delta(\mathbf{k}+\mathbf{p}+\mathbf{q}) \int d^3\tilde{p} P_{ij}(\tilde{\mathbf{p}})P_{jl}(\mathbf{p}-\tilde{\mathbf{p}})[P_{il}(\mathbf{k}+\tilde{\mathbf{p}})+P_{il}(\mathbf{q}+\tilde{\mathbf{p}})]. \quad (8.20)$$

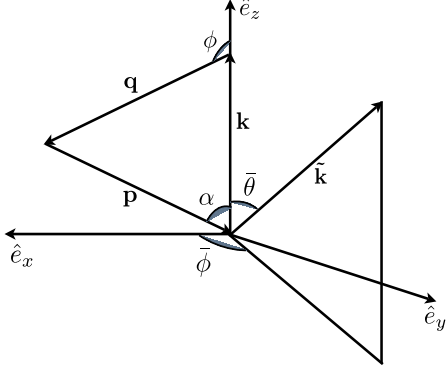


Figure 8.1: The geometrical configuration used to perform the integration: \mathbf{k} , \mathbf{q} and \mathbf{p} are free, while $\tilde{\mathbf{k}}$ is the integration wave-vector [141].

Since the final result has to be symmetric, we set:

$$\begin{aligned}
 \langle \rho_B(\mathbf{k}) \rho_B(\mathbf{q}) \rho_B(\mathbf{p}) \rangle &= \frac{\delta(\mathbf{k} + \mathbf{p} + \mathbf{q})}{384\pi^3} \times \\
 &\left\{ \int d^3\tilde{\mathbf{k}} P_{ij}(\tilde{\mathbf{k}}) P_{jl}(\mathbf{k} - \tilde{\mathbf{k}}) [P_{il}(\mathbf{q} + \tilde{\mathbf{k}}) + P_{il}(\mathbf{p} + \tilde{\mathbf{k}})] \right. \\
 &+ \int d^3\tilde{\mathbf{k}} P_{ij}(\tilde{\mathbf{k}}) P_{jl}(\mathbf{q} - \tilde{\mathbf{k}}) [P_{il}(\mathbf{k} + \tilde{\mathbf{k}}) + P_{il}(\mathbf{p} + \tilde{\mathbf{k}})] \\
 &\left. + \int d^3\tilde{\mathbf{k}} P_{ij}(\tilde{\mathbf{k}}) P_{jl}(\mathbf{p} - \tilde{\mathbf{k}}) [P_{il}(\mathbf{q} + \tilde{\mathbf{k}}) + P_{il}(\mathbf{k} + \tilde{\mathbf{k}})] \right\}, \tag{8.21}
 \end{aligned}$$

where the product of the projectors P_{ij} is given by:

$$\begin{aligned}
 P_{ij}(\mathbf{k}) P_{jl}(\mathbf{q}) P_{il}(\mathbf{p}) &= A^3 k^{n_B} p^{n_B} q^{n_B} \times \\
 &[(\hat{k} \cdot \hat{q})^2 + (\hat{k} \cdot \hat{p})^2 + (\hat{q} \cdot \hat{p})^2 - (\hat{k} \cdot \hat{q})(\hat{k} \cdot \hat{p})(\hat{q} \cdot \hat{p})] \\
 &\text{if } k \leq k_D, q \leq k_D, p \leq k_D, \tag{8.22}
 \end{aligned}$$

and zero else.

We want to derive an expression for the magnetic energy density bispectrum, Eq. 8.21, valid in every geometrical configuration of the vectors.

Unfortunately the complexity of the angular integration avoids the derivation of the exact expression. Anyway, since the angular integration always gives a finite contribution, as first approximation we can neglect the angular part:

$$\langle \rho_B(\mathbf{k})\rho_B(\mathbf{q})\rho_B(\mathbf{p}) \rangle \simeq \frac{\delta(\mathbf{k} + \mathbf{p} + \mathbf{q})}{384\pi^3} A^3 \left\{ \int d^3\tilde{k} \tilde{k}^n |\mathbf{k} - \tilde{\mathbf{k}}|^{n_B} \left[|\mathbf{q} + \tilde{\mathbf{k}}|^{n_B} + |\mathbf{p} + \tilde{\mathbf{k}}|^{n_B} \right] + perm.s \right\}. \quad (8.23)$$

To perform the integration, following [141], we choose a basis with $\hat{e}_z \parallel \mathbf{k}$ and where the triangle formed by \mathbf{k} , \mathbf{q} , \mathbf{p} lies in the plane perpendicular to \hat{e}_y , in $y = 0$, see Fig. 8.1. We call ϕ the angle between \mathbf{k} and \mathbf{q} , $\cos \phi = \hat{k} \cdot \hat{q}$, and α the angle between \mathbf{k} and $-\mathbf{p}$, $\cos(\pi - \alpha) = \hat{k} \cdot \hat{p}$. The angle $\bar{\theta}$ is the one between $\tilde{\mathbf{k}}$ and $\hat{e}_z \parallel \mathbf{k}$, whereas $\bar{\phi}$ is the one formed by $\tilde{\mathbf{k}}$ with the plane identified by the triangle formed by \mathbf{k} , \mathbf{q} , \mathbf{p} . The angle between $\tilde{\mathbf{k}}$ and \mathbf{q} is given by:

$$\hat{k} \cdot \hat{q} = \sin \bar{\theta} \cos \bar{\phi} \sin \phi + \cos \bar{\theta} \cos \phi, \quad (8.24)$$

and the one between $\tilde{\mathbf{k}}$ and \mathbf{p} is

$$\hat{k} \cdot \hat{p} = -(\sin \bar{\theta} \cos \bar{\phi} \sin \alpha + \cos \bar{\theta} \cos \alpha). \quad (8.25)$$

The sharp cut off in the PMF power spectrum imposes: $\tilde{k} \leq k_D$, $|\mathbf{k} - \tilde{\mathbf{k}}| \leq k_D$, $|\mathbf{q} + \tilde{\mathbf{k}}| \leq k_D$.

In the first integral of Eq. 8.23 we note that for negative spectral indices we have integrable divergences for $\tilde{\mathbf{k}} \rightarrow \mathbf{k}$ and for $\tilde{\mathbf{k}} \rightarrow -\mathbf{q}$. Therefore these two angular configurations are the dominant ones for negative spectral indices. We can consider the two configurations at least representative of the total result for positive spectral indices and therefore approximate the total result with only these two configurations. The integral becomes:

$$\int d^3\tilde{k} \tilde{k}^{n_B} |\mathbf{k} - \tilde{\mathbf{k}}|^{n_B} |\mathbf{q} + \tilde{\mathbf{k}}|^{n_B} = \int_0^{k_D} d\tilde{k} \tilde{k}^{n_B+2} \int_{\bar{\Omega}} d\Omega \left[k^2 + \tilde{k}^2 - 2k\tilde{k} \cos \bar{\theta} \right]^{n_B/2} \left[q^2 + \tilde{k}^2 + 2q\tilde{k}(\sin \bar{\theta} \cos \bar{\phi} \sin \phi + \cos \bar{\theta} \cos \phi) \right]^{n_B/2}$$

$$\simeq 2\pi \int_0^{k_D} d\tilde{k} \tilde{k}^{n_B+2} \times \left[|k - \tilde{k}|^{n_B} (q^2 + \tilde{k}^2 + 2q\tilde{k} \cos \phi)^{n_B/2} + (k^2 + \tilde{k}^2 + 2k\tilde{k} \cos \phi)^{n_B/2} |q - \tilde{k}|^{n_B} \right] \quad (8.26)$$

The first term of the second equality is the contribution of the angular configuration $\tilde{\mathbf{k}} \rightarrow \mathbf{k}$ where $\bar{\theta} = 0$; whereas the second one is the contribution of the angular configuration $\tilde{\mathbf{k}} \rightarrow -\mathbf{q}$, where $\bar{\theta} = \pi - \phi$ and $\bar{\phi} = \pi$. We have inserted the factor 2π to simulate the integration in $d\bar{\phi}$, which should be present at least in the first configuration. We repeat the same approximation scheme in each term of Eq. 8.23:

$$\begin{aligned} \langle \rho_B(\mathbf{k}) \rho_B(\mathbf{q}) \rho_B(\mathbf{p}) \rangle &\simeq \frac{\delta(\mathbf{k} + \mathbf{p} + \mathbf{q})}{96\pi^2} A^3 \times \\ &\left\{ \int_0^{k_D} d\tilde{k} \tilde{k}^{n_B+2} \left[|k - \tilde{k}|^{n_B} (q^2 + \tilde{k}^2 + 2q\tilde{k} \cos \phi)^{n_B/2} + \right. \right. \\ &\quad \left. \left. (k^2 + \tilde{k}^2 + 2k\tilde{k} \cos \phi)^{n_B/2} |q - \tilde{k}|^{n_B} \right] \right. \\ &+ \int_0^{k_D} d\tilde{k} \tilde{k}^{n_B+2} \left[|k - \tilde{k}|^{n_B} (p^2 + \tilde{k}^2 - 2p\tilde{k} \cos \alpha)^{n_B/2} + \right. \\ &\quad \left. (k^2 + \tilde{k}^2 - 2k\tilde{k} \cos \alpha)^{n_B/2} |p - \tilde{k}|^{n_B} \right] \\ &+ \int_0^{k_D} d\tilde{k} \tilde{k}^{n_B+2} \left[|q - \tilde{k}|^{n_B} (p^2 + \tilde{k}^2 - 2p\tilde{k} \cos(\phi - \alpha))^{n_B/2} + \right. \\ &\quad \left. (q^2 + \tilde{k}^2 - 2q\tilde{k} \cos(\phi - \alpha))^{n_B/2} |p - \tilde{k}|^{n_B} \right] \left. \right\}. \end{aligned} \quad (8.27)$$

It is possible to evaluate the above integrals. Assuming $k < q < k_D$, we approximate the first integral with:

$$\begin{aligned} \int_0^{k_D} d\tilde{k} \tilde{k}^{n_B+2} \left[|k - \tilde{k}|^{n_B} (q^2 + \tilde{k}^2 + 2q\tilde{k} \cos \phi)^{n_B/2} + (k^2 + \tilde{k}^2 + 2k\tilde{k} \cos \phi)^{n_B/2} |q - \tilde{k}|^{n_B} \right] &\simeq \\ &2 \left(q^{n_B} k^{n_B} \int_0^k d\tilde{k} \tilde{k}^{n_B+2} + q^{n_B} \int_k^q d\tilde{k} \tilde{k}^{2n_B+2} + \int_q^{k_D} d\tilde{k} \tilde{k}^{3n_B+2} \right). \end{aligned} \quad (8.28)$$

The disappearance of the angular dependence on the angles between the

three vectors is a natural consequence of our approximation scheme and is not true in general for PMFs.

Applying the same technique for each integral in Eq. 8.27, for the combination $k \leq q \leq p \leq k_D$ we found:

$$\begin{aligned} \langle \rho_B(\mathbf{k})\rho_B(\mathbf{q})\rho_B(\mathbf{p}) \rangle &\simeq \frac{\delta(\mathbf{k} + \mathbf{p} + \mathbf{q})}{48\pi^2} A^3 \times & (8.29) \\ &\left\{ \frac{n_B}{(n_B + 3)(2n_B + 3)} q^{n_B} k^{2n_B+3} + \frac{n_B}{(3n_B + 3)(2n_B + 3)} q^{3n_B+3} + \frac{k_D^{3n_B+3}}{3n_B + 3} \right. \\ &+ \frac{n_B}{(n_B + 3)(2n_B + 3)} p^{n_B} k^{2n_B+3} + \frac{n_B}{(3n_B + 3)(2n_B + 3)} p^{3n_B+3} + \frac{k_D^{3n_B+3}}{3n_B + 3} \\ &\left. + \frac{n_B}{(n_B + 3)(2n_B + 3)} p^{n_B} q^{2n_B+3} + \frac{n_B}{(3n_B + 3)(2n_B + 3)} p^{3n_B+3} + \frac{k_D^{3n_B+3}}{3n_B + 3} \right\} \\ &\text{for } k \leq q \leq p \leq k_D. \end{aligned}$$

For $q \leq k \leq p$ we have to exchange k and q in the above expression, and so on with all the ordered permutations of the wave-numbers. We focus on the main contribution to the CMB bispectrum on large scales, which is given by the infrared limit of the bispectrum. As it happens for the magnetic energy density Fourier spectrum, also the bispectrum presents two different regimes depending on the spectral index. For flat and blue spectral indices, $n_B > -1$, the infrared limit of the bispectrum is white noise; Eq. 8.29 is in fact dominated by the constant terms $k_D^{3n_B+3}/(3n_B+3)$. For red magnetic field indices, $n_B < -1$, the bispectrum diverges as k^{2n_B+3} or as k^{3n_B+3} , depending on the wave-vector configuration. The edge value of the spectral index between the two regimes of the magnetic energy density bispectrum is $n_B = -1$, whereas for the spectrum it was $n_B = -1.5$. As happens for the spectrum which presents a logarithmic divergence for $n_B = -1.5$, the bispectrum for $n_B = -1$ diverges logarithmically. Also for the bispectrum the analysis of the integration domains shows that the bispectrum is supported only in $k < 2k_D$ and is zero elsewhere. Eq. 8.29 is a general approximation to the magnetic field energy density bispectrum, in the infrared limit, independent on the geometrical configuration. We will now investigate the results for specified configuration and compare them with the general expression Eq. 8.29. The

three configurations (equilateral, colinear and squeezed) give a comparable white noise contribution for $n_B > -1$, whereas for $n_B < -1$ they show different divergences. In particular the colinear and equilateral configurations diverge as k^{3n_B+3} , whereas the squeezed one diverges as k^{2n_B+3} .

8.3.1 Colinear configuration

In the colinear configuration two of the three wave-vectors are equal and the third has a double modulus and points in the opposite direction of the other two: for example, $\mathbf{p} = \mathbf{q}$ and $\mathbf{k} = -2\mathbf{q}$. The colinear is the only geometrical configuration in which is possible to evaluate the bispectrum exactly. The symmetric expression which considers all the permutations is given by:

$$\begin{aligned} & \langle \rho_B(\mathbf{k})\rho_B(\mathbf{q})\rho_B(\mathbf{p}) \rangle |_{colinear} = \\ & \frac{\delta(\mathbf{k} + \mathbf{p} + \mathbf{q})}{384\pi^3} \frac{2}{3} \int d^3\tilde{\mathbf{k}} P_{ij}(\tilde{\mathbf{k}}) \left\{ P_{jl} \left(\frac{\mathbf{k}}{2} + \tilde{\mathbf{k}} \right) \left[P_{il}(\mathbf{k} + \tilde{\mathbf{k}}) + P_{il} \left(\frac{\mathbf{k}}{2} - \tilde{\mathbf{k}} \right) \right] \right. \\ & \left. + P_{jl}(\mathbf{k} - \tilde{\mathbf{k}}) P_{il} \left(\frac{\mathbf{k}}{2} - \tilde{\mathbf{k}} \right) + \mathbf{k} \rightarrow \mathbf{p} + \mathbf{k} \rightarrow \mathbf{q} \right\}. \end{aligned} \quad (8.30)$$

Using Eq. 8.22 we obtained:

$$\begin{aligned} & \langle \rho_B(\mathbf{k})\rho_B(\mathbf{q})\rho_B(\mathbf{p}) \rangle |_{colinear} = \frac{\delta(\mathbf{k} + \mathbf{p} + \mathbf{q})}{576\pi^3} A^3 \times \\ & \left\{ 2 \int_{V_1} d^3\tilde{\mathbf{k}} \tilde{k}^{n_B} \left| \frac{\mathbf{k}}{2} + \tilde{\mathbf{k}} \right|^{n_B} \left| \mathbf{k} + \tilde{\mathbf{k}} \right|^{n_B} \times \right. \\ & \left[\frac{(\hat{k} \cdot \mathbf{k} + 2\tilde{k})^2}{4 \left| \frac{\mathbf{k}}{2} + \tilde{\mathbf{k}} \right|^2} + \frac{(\hat{k} \cdot \mathbf{k} + \tilde{k})^2}{\left| \mathbf{k} + \tilde{\mathbf{k}} \right|^2} + \frac{(k^2 + 3\tilde{\mathbf{k}} \cdot \mathbf{k} + 2\tilde{k}^2)(k^2 - (\hat{k} \cdot \mathbf{k})^2)}{4 \left| \frac{\mathbf{k}}{2} + \tilde{\mathbf{k}} \right|^2 \left| \mathbf{k} + \tilde{\mathbf{k}} \right|^2} \right] \\ & + \int_{V_2} d^3\tilde{\mathbf{k}} \tilde{k}^{n_B} \left| \frac{\mathbf{k}}{2} + \tilde{\mathbf{k}} \right|^{n_B} \left| \frac{\mathbf{k}}{2} - \tilde{\mathbf{k}} \right|^{n_B} \times \\ & \left[\frac{(\hat{k} \cdot \mathbf{k} + 2\tilde{k})^2}{4 \left| \frac{\mathbf{k}}{2} + \tilde{\mathbf{k}} \right|^2} + \frac{(\hat{k} \cdot \mathbf{k} - 2\tilde{k})^2}{4 \left| \frac{\mathbf{k}}{2} - \tilde{\mathbf{k}} \right|^2} + \frac{(k^2 - 4\tilde{k}^2)(k^2 - (\hat{k} \cdot \mathbf{k})^2)}{16 \left| \frac{\mathbf{k}}{2} + \tilde{\mathbf{k}} \right|^2 \left| \frac{\mathbf{k}}{2} - \tilde{\mathbf{k}} \right|^2} \right] \\ & \left. + \mathbf{k} \rightarrow \mathbf{p} + \mathbf{k} \rightarrow \mathbf{q} \right\}, \end{aligned} \quad (8.31)$$

where V_1 denotes the volume given by the three conditions:

$$\begin{aligned}\tilde{k} &\leq k_D \\ |\mathbf{k}/2 + \tilde{\mathbf{k}}| &\leq k_D \\ |\mathbf{k} + \tilde{\mathbf{k}}| &\leq k_D,\end{aligned}\tag{8.32}$$

and V_2 is given by the conditions:

$$\begin{aligned}\tilde{k} &\leq k_D \\ |\mathbf{k}/2 + \tilde{\mathbf{k}}| &\leq k_D \\ |\mathbf{k}/2 - \tilde{\mathbf{k}}| &\leq k_D.\end{aligned}\tag{8.33}$$

We computed the exact results of Eq. 8.31 for $n_B = 2$ and $n_B = -2$. The colinear case is simplified by the fact that for $\mathbf{p} = \mathbf{q}$ and $\mathbf{k} = -2\mathbf{q}$, the integrands in Eq. 8.31 depend only on $\cos\bar{\theta}$ and the boundaries given by V_1 and V_2 are trivial. The details of the calculation are given in the appendix, in Fig. 8.2 we show the results. For the case $n_B = 2$ we found the complete expression, whereas for the case $n_B = -2$ we evaluated only the infrared part, up to $k \leq k_D/2$, because of the complexity of the computation. The boundary conditions of V_1 , $|\mathbf{k} + \tilde{\mathbf{k}}| \leq k_D$, show what anticipated: the integral is non-zero only for $k < 2k_D$. With the exact results we have the possibility to test, at least for the colinear case, the goodness of the general approximation. Specifying the general result of Eq. 8.29 to the colinear configuration, we found:

$$\begin{aligned}\langle \rho_B(\mathbf{k})\rho_B(\mathbf{q})\rho_B(\mathbf{p}) \rangle|_{colinear} &\simeq \frac{\delta(\mathbf{k} + \mathbf{p} + \mathbf{q})}{144\pi^2} A^3 \times \\ &\left\{ \frac{n_B}{2^{3n_B+3}(2n_B+3)} \left(\frac{2^{n_B+1}+1}{n_B+3} + \frac{2^{3n_B+4}+1}{3n_B+3} \right) k^{3n_B+3} + \frac{k_D^{3n_B+3}}{n_B+1} \right. \\ &\left. + k \rightarrow p + k \rightarrow q \right\}.\end{aligned}\tag{8.34}$$

We note that for $n_B > -1$ the infrared limit is a white noise, whereas for $n_B < -1$ it diverges as k^{3n_B+3} . The case $n_B = -2$ diverges as k^{-3} , whereas the case $n_B = 2$ is regular. In Fig. 8.2 we compare the exact and the approximated results. In both cases, our approximation underestimates the

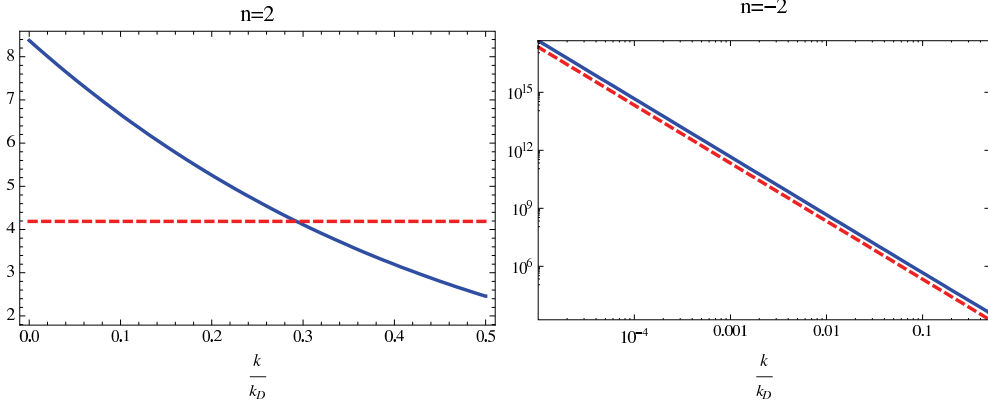


Figure 8.2: The magnetic field bispectrum in the collinear configuration $\mathbf{p} = \mathbf{q} = -\mathbf{k}/2$, normalised by the quantity $A^3 k_D^{3n_B+3}/(576\pi^3)$, as a function of k/k_D , for $n_B = 2$ (left plot) and $n_B = -2$ (right plot). We only show the infrared region $k \leq k_D/2$. The blue, solid line is the exact result, while the red, dashed line the approximation given in 8.34.

exact result by a factor of two. In particular for the case $n_B = 2$, the bispectrum is not pure white noise, but shows a mild dependence on k that our approximation does not capture. In Fig. 8.3, we show the comparison of the exact result for the bispectrum in the collinear configuration with the magnetic energy power spectrum to the power $3/2$, for $n_B = 2$ and $n_B = -2$ (both multiplied by the phase space density $(k/k_D)^3$). For $n_B = 2$, spectrum and bispectrum are of the same order of magnitude, for $n_B = -2$ instead the bispectrum goes as k^{3n_B+3} while the spectrum as k^{2n_B+3} .

8.3.2 Squeezed configuration

The squeezed configuration is characterized by one wave-vector null, and the other two equal with opposite direction. Considering the case $\mathbf{q} \simeq 0$,

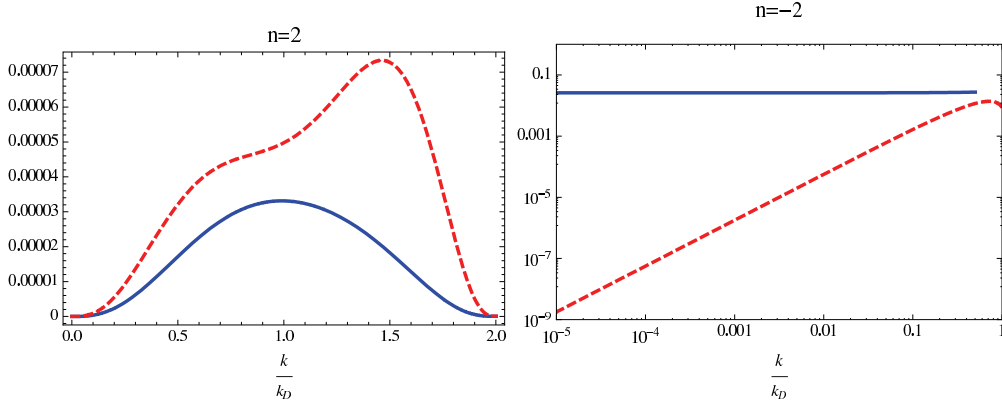


Figure 8.3: The magnetic field bispectrum in the collinear configuration $\mathbf{p} = \mathbf{q} = -\mathbf{k}/2$ (blue, solid) and the magnetic field spectrum to the 3/2 (red, dashed), both multiplied by the phase space density k^3 , as a function of k/k_D for $n_B = 2$ and $n_B = -2$. Note that in the $n_B = -2$ case, we only calculated the bispectrum up to $k = k_D/2$, while the spectrum is known up to $k = k_D$.

$\mathbf{k} = -\mathbf{p}$, the magnetic energy density bispectrum reduce to:

$$\begin{aligned}
 \langle \rho_B(\mathbf{k})\rho_B(\mathbf{q})\rho_B(\mathbf{p}) \rangle |_{squeezed} &= \frac{\delta(\mathbf{k} + \mathbf{p} + \mathbf{q})}{384\pi^3} \frac{1}{3} \times \\
 &\int d^3\tilde{\mathbf{k}} P_{ij}(\tilde{\mathbf{k}}) \left\{ P_{jl}(\mathbf{k} - \tilde{\mathbf{k}}) [P_{il}(\mathbf{q} + \tilde{\mathbf{k}}) + P_{il}(\mathbf{k} - \tilde{\mathbf{k}})] \right. \\
 &+ P_{jl}(\mathbf{q} - \tilde{\mathbf{k}}) [P_{il}(\mathbf{k} - \tilde{\mathbf{k}}) + P_{il}(\mathbf{k} + \tilde{\mathbf{k}})] \\
 &+ P_{jl}(\mathbf{k} + \tilde{\mathbf{k}}) [P_{il}(\mathbf{k} + \tilde{\mathbf{k}}) + P_{il}(\mathbf{q} + \tilde{\mathbf{k}})] \\
 &\left. + (\mathbf{q} \rightarrow \mathbf{p} \simeq 0, \mathbf{k} \rightarrow \mathbf{q}) + (\mathbf{q} \rightarrow \mathbf{k} \simeq 0, \mathbf{k} \rightarrow \mathbf{p}) \right\} .
 \end{aligned} \tag{8.35}$$

Expliciting and simplifying we obtain:

$$\begin{aligned}
\langle \rho_B(\mathbf{k}) \rho_B(\mathbf{q}) \rho_B(\mathbf{p}) \rangle|_{squeezed} &= \frac{\delta(\mathbf{k} + \mathbf{p} + \mathbf{q})}{384\pi^3} A^3 \times \tag{8.36} \\
\frac{2}{3} &\left\{ \int_{V_1} d^3 \tilde{k} \tilde{k}^{n_B} |\mathbf{k} - \tilde{\mathbf{k}}|^{n_B} |\mathbf{q} + \tilde{\mathbf{k}}|^{n_B} \right. \\
&\left[\frac{(\hat{k} \cdot \mathbf{k} - \tilde{k})^2}{|\mathbf{k} - \tilde{\mathbf{k}}|^2} + \frac{(\hat{k} \cdot \mathbf{q} + \tilde{k})^2}{|\mathbf{q} + \tilde{\mathbf{k}}|^2} + \frac{(\mathbf{k} \cdot \mathbf{q} - \mathbf{k} \cdot \tilde{\mathbf{k}} + \mathbf{q} \cdot \tilde{\mathbf{k}} - \tilde{k}^2)[\mathbf{k} \cdot \mathbf{q} - (\hat{k} \cdot \mathbf{k})(\hat{k} \cdot \mathbf{q})]}{|\mathbf{k} - \tilde{\mathbf{k}}|^2 |\mathbf{q} + \tilde{\mathbf{k}}|^2} \right] \\
&+ \int_{V_2} d^3 \tilde{k} \tilde{k}^{n_B} |\mathbf{k} - \tilde{\mathbf{k}}|^{2n_B} \left[2 \frac{(\hat{k} \cdot \mathbf{k} - \tilde{k})^2}{|\mathbf{k} - \tilde{\mathbf{k}}|^2} + \frac{(k^2 - 2\mathbf{k} \cdot \tilde{k} + \tilde{k}^2)[k^2 - (\hat{k} \cdot \mathbf{k})^2]}{|\mathbf{k} - \tilde{\mathbf{k}}|^4} \right] \\
&+ \int_{V_3} d^3 \tilde{k} \tilde{k}^{n_B} |\mathbf{q} - \tilde{\mathbf{k}}|^{n_B} |\mathbf{k} - \tilde{\mathbf{k}}|^{n_B} \times \\
&\left[\frac{(\hat{k} \cdot \mathbf{k} - \tilde{k})^2}{|\mathbf{k} - \tilde{\mathbf{k}}|^2} + \frac{(\hat{k} \cdot \mathbf{q} - \tilde{k})^2}{|\mathbf{q} - \tilde{\mathbf{k}}|^2} + \frac{(\mathbf{k} \cdot \mathbf{q} - \mathbf{k} \cdot \tilde{\mathbf{k}} - \mathbf{q} \cdot \tilde{\mathbf{k}} + \tilde{k}^2)[\mathbf{k} \cdot \mathbf{q} - (\hat{k} \cdot \mathbf{k})(\hat{k} \cdot \mathbf{q})]}{|\mathbf{k} - \tilde{\mathbf{k}}|^2 |\mathbf{q} - \tilde{\mathbf{k}}|^2} \right] \\
&+ (\mathbf{q} \rightarrow \mathbf{p} \simeq 0, \mathbf{k} \rightarrow \mathbf{q}) + (\mathbf{q} \rightarrow \mathbf{k} \simeq 0, \mathbf{k} \rightarrow \mathbf{p}) \} ,
\end{aligned}$$

where V_1 is given by the conditions:

$$\begin{aligned}
\tilde{k} &\leq k_D \\
|\mathbf{k} - \tilde{\mathbf{k}}| &\leq k_D \\
|\mathbf{q} + \tilde{\mathbf{k}}| &\leq k_D , \tag{8.37}
\end{aligned}$$

V_2 by the conditions:

$$\begin{aligned}
\tilde{k} &\leq k_D \\
|\mathbf{k} - \tilde{\mathbf{k}}| &\leq k_D , \tag{8.38}
\end{aligned}$$

and V_3 by the conditions:

$$\begin{aligned}
\tilde{k} &\leq k_D \\
|\mathbf{q} - \tilde{\mathbf{k}}| &\leq k_D \\
|\mathbf{k} - \tilde{\mathbf{k}}| &\leq k_D . \tag{8.39}
\end{aligned}$$

The conditions imposed on the volumes ensure that again the bispectrum goes to zero for $k > 2k_D$. In the squeezed configuration the angular integration is not trivial. For example let us consider the configuration $\mathbf{q} \simeq 0$, $\mathbf{k} = -\mathbf{p}$. In this configuration we have $\phi \rightarrow \pi/2$, which leads to terms like $(q^2 + \tilde{k}^2 + 2\tilde{k}q \sin \bar{\theta} \cos \bar{\phi})^{n/2}$; in this case it is therefore impossible to disentangle the integration boundary over $\bar{\theta}$ and $\bar{\phi}$ given by V_1 . Therefore for the squeezed configuration we used our approximation of Eq. 8.29, without computing the exact expression. Eq. 8.29 in the squeezed configuration reduce to:

$$\begin{aligned} \langle \rho_B(\mathbf{k}) \rho_B(\mathbf{q}) \rho_B(\mathbf{p}) \rangle |_{squeezed} \simeq & \frac{\delta(\mathbf{k} + \mathbf{p} + \mathbf{q})}{144\pi^2} A^3 \times \\ & \left\{ \frac{2n_B}{(n_B + 3)(2n_B + 3)} q^{2n_B+3} k^{n_B} + \frac{6n_B(n_B + 2)}{(3n_B + 3)(2n_B + 3)(n_B + 3)} k^{3n_B+3} \right. \\ & \left. + \frac{k_D^{3n_B+3}}{n_B + 1} + (q \rightarrow p \simeq 0, k \rightarrow q) + (q \rightarrow k \simeq 0, k \rightarrow p) \right\}. \end{aligned} \quad (8.40)$$

For $n_B > -1$, the white noise has the same amplitude as in the colinear case, whereas the behavior for $n_B < -1$ of the squeezed configuration differs from the colinear one. In particular the squeezed configuration diverges for $q \rightarrow 0$ as q^{2n_B+3} and not as q^{3n_B+3} like in the colinear case. Therefore the squeezed configuration presents a weaker divergence, only in the limit $k \rightarrow q \rightarrow 0$ it reaches the colinear behaviour: q^{3n_B+3} .

8.3.3 Equilateral configuration

The equilateral configuration is characterize by the three wave-vectors in an equilateral triangle. The magnetic energy density bispectrum in this

configuration (with $\mathbf{q} = k\hat{q}$, and $\mathbf{p} = k\hat{p}$) is:

$$\begin{aligned} \langle \rho_B(\mathbf{k})\rho_B(\mathbf{q})\rho_B(\mathbf{p}) \rangle|_{equilateral} &= \frac{\delta(\mathbf{k} + \mathbf{p} + \mathbf{q})}{384\pi^3} \frac{2}{3} \\ &\int d^3\tilde{k} P_{ij}(\tilde{\mathbf{k}}) \left\{ P_{jl}(\mathbf{k} - \tilde{\mathbf{k}}) [P_{il}(k\hat{q} + \tilde{\mathbf{k}}) + P_{il}(k\hat{p} + \tilde{\mathbf{k}})] \right. \\ &+ P_{jl}(k\hat{q} - \tilde{\mathbf{k}}) P_{il}(k\hat{p} + \tilde{\mathbf{k}}) + \left(\mathbf{k} \rightarrow \mathbf{q}, k\hat{q} \rightarrow q\hat{k}, k\hat{p} \rightarrow q\hat{p} \right) + \\ &\left. \left(\mathbf{k} \rightarrow \mathbf{p}, k\hat{q} \rightarrow p\hat{q}, k\hat{p} \rightarrow p\hat{k} \right) \right\}. \end{aligned} \quad (8.41)$$

It becomes:

$$\begin{aligned} \langle \rho_B(\mathbf{k})\rho_B(\mathbf{q})\rho_B(\mathbf{p}) \rangle|_{equilateral} &= \frac{\delta(\mathbf{k} + \mathbf{p} + \mathbf{q})}{384\pi^3} A^3 \times \quad (8.42) \\ &\frac{2}{3} \left\{ \int_{V_1} d^3\tilde{k} \tilde{k}^{n_B} \left| \mathbf{k} - \tilde{\mathbf{k}} \right|^{n_B} \left| k\hat{q} + \tilde{\mathbf{k}} \right|^{n_B} \times \right. \\ &\left[\frac{(\hat{k} \cdot \mathbf{k} - \tilde{k})^2}{\left| \mathbf{k} - \tilde{\mathbf{k}} \right|^2} + \frac{(\hat{k} \cdot k\hat{q} + \tilde{k})^2}{\left| k\hat{q} + \tilde{\mathbf{k}} \right|^2} + \frac{(\mathbf{k} \cdot k\hat{q} - \mathbf{k} \cdot \tilde{\mathbf{k}} + k\hat{q} \cdot \tilde{\mathbf{k}} - \tilde{k}^2)[\mathbf{k} \cdot k\hat{q} - (\hat{k} \cdot \mathbf{k})(\hat{k} \cdot k\hat{q})]}{\left| \mathbf{k} - \tilde{\mathbf{k}} \right|^2 \left| k\hat{q} + \tilde{\mathbf{k}} \right|^2} \right] \\ &+ \int_{V_2} d^3\tilde{k} \tilde{k}^{n_B} \left| \mathbf{k} - \tilde{\mathbf{k}} \right|^{n_B} \left| k\hat{p} + \tilde{\mathbf{k}} \right|^{n_B} \times \\ &\left[\frac{(\hat{k} \cdot \mathbf{k} - \tilde{k})^2}{\left| \mathbf{k} - \tilde{\mathbf{k}} \right|^2} + \frac{(\hat{k} \cdot k\hat{p} + \tilde{k})^2}{\left| k\hat{p} + \tilde{\mathbf{k}} \right|^2} + \frac{(\mathbf{k} \cdot k\hat{p} - \mathbf{k} \cdot \tilde{\mathbf{k}} + k\hat{p} \cdot \tilde{\mathbf{k}} - \tilde{k}^2)[\mathbf{k} \cdot k\hat{p} - (\hat{k} \cdot \mathbf{k})(\hat{k} \cdot k\hat{p})]}{\left| \mathbf{k} - \tilde{\mathbf{k}} \right|^2 \left| k\hat{p} + \tilde{\mathbf{k}} \right|^2} \right] \\ &+ \int_{V_3} d^3\tilde{k} \tilde{k}^{n_B} \left| k\hat{q} - \tilde{\mathbf{k}} \right|^{n_B} \left| k\hat{p} + \tilde{\mathbf{k}} \right|^{n_B} \times \\ &\left[\frac{(\hat{k} \cdot k\hat{q} - \tilde{k})^2}{\left| k\hat{q} - \tilde{\mathbf{k}} \right|^2} + \frac{(\hat{k} \cdot k\hat{p} + \tilde{k})^2}{\left| k\hat{p} + \tilde{\mathbf{k}} \right|^2} + \frac{(k\hat{q} \cdot k\hat{p} - k\hat{q} \cdot \tilde{\mathbf{k}} + k\hat{p} \cdot \tilde{\mathbf{k}} - \tilde{k}^2)[k\hat{q} \cdot k\hat{p} - (\hat{k} \cdot k\hat{q})(\hat{k} \cdot k\hat{p})]}{\left| k\hat{q} - \tilde{\mathbf{k}} \right|^2 \left| k\hat{p} + \tilde{\mathbf{k}} \right|^2} \right] \\ &+ \left(\mathbf{k} \rightarrow \mathbf{q}, k\hat{q} \rightarrow q\hat{k}, k\hat{p} \rightarrow q\hat{p} \right) + \left(\mathbf{k} \rightarrow \mathbf{p}, k\hat{q} \rightarrow p\hat{q}, k\hat{p} \rightarrow p\hat{k} \right) \left. \right\}, \quad (8.43) \end{aligned}$$

where again V_1 is given by the conditions:

$$\begin{aligned} \tilde{k} &\leq k_D \\ \left| \mathbf{k} - \tilde{\mathbf{k}} \right| &\leq k_D \\ \left| k\hat{q} + \tilde{\mathbf{k}} \right| &\leq k_D, \end{aligned} \quad (8.44)$$

and similarly for V_2 and V_3 . Like in the squeezed configuration, the angular integration in $d\bar{\phi}$ is non-trivial, since $\phi = 2\pi/3$ and it contains terms like $(k^2 + \tilde{k}^2 + 2\tilde{k}k(\frac{1}{2}\sin\bar{\theta}\cos\bar{\phi} - \frac{1}{2}\cos\bar{\theta}))^{n/2}$. We used again only the approximated expression in Eq. 8.29, which reduces to:

$$\langle \rho_B(\mathbf{k})\rho_B(\mathbf{q})\rho_B(\mathbf{p}) \rangle|_{equilateral} \simeq \frac{\delta(\mathbf{k} + \mathbf{p} + \mathbf{q})}{144\pi^2} A^3 \left\{ \frac{6n_B}{(n_B + 3)(3n_B + 3)} k^{3n_B+3} + \frac{k_D^{3n_B+3}}{n_B + 1} + (k \rightarrow q) + (k \rightarrow p) \right\}. \quad (8.45)$$

For $n_B > -1$ the infrared limit is always white noise, with an amplitude comparable with the ones of colinear and squeezed configurations. For $n_B < -1$ instead it divergences, for $k \rightarrow 0$, like the colinear case. In the equilateral configuration the infrared divergence occurs for $k = q = p \rightarrow 0$. In this limit we have that $\tilde{\mathbf{k}} \rightarrow \mathbf{k}$ and $\tilde{\mathbf{k}} \rightarrow -\mathbf{q}$ are no longer distinct. Therefore we expect a divergence like k^{3n_B+3} , which is the equivalent of what we found in the colinear and in the squeezed configurations (where for the squeezed $q \rightarrow k \rightarrow 0$ Eq. 8.40).

After having analyzed the single configurations we can affirm that our approximated magnetic energy density bispectrum correctly reproduces the behavior of the exact solutions. The approximation of neglecting the angular integration introduces anyway uncertainties. In particular we showed how our approximated bispectrum is underestimate of a factor of two in the colinear case. But the greater uncertainty is the weight the different configurations have in the total result, which is not possible to know with our approximation. Even if with a certain degree of uncertainties, our approximated bispectrum gives at least a good representation of the real one.

8.4 The CMB magnetic bispectrum

We have derived the magnetic energy density bispectrum $\langle \rho_B(\mathbf{k})\rho_B(\mathbf{q})\rho_B(\mathbf{p}) \rangle$, we will now compute the CMB magnetic bispectrum. We will use the approximated expression for the magnetic energy density bispectrum of Eq.

8.29:

$$\begin{aligned}
\langle \rho_B(\mathbf{k}) \rho_B(\mathbf{q}) \rho_B(\mathbf{p}) \rangle &\simeq \delta(\mathbf{k} + \mathbf{p} + \mathbf{q}) \frac{A^3 k_D^{3n_B+3}}{48\pi^2} \mathcal{I}(K, Q, P) & (8.46) \\
\mathcal{I}(K, Q, P) &= \frac{n_B}{(n_B+3)(2n_B+3)} Q^n K^{2n_B+3} + \frac{n_B}{(3n_B+3)(2n_B+3)} Q^{3n_B+3} + \\
&\frac{n_B}{(n_B+3)(2n_B+3)} P^{n_B} K^{2n_B+3} + \frac{n_B}{(3n_B+3)(2n_B+3)} P^{3n_B+3} + \\
&\frac{n_B}{(n_B+3)(2n_B+3)} P^{n_B} Q^{2n_B+3} + \frac{n_B}{(3n_B+3)(2n_B+3)} P^{3n_B+3} \\
&+ \frac{1}{n_B+1} \quad \text{for } K \leq Q \leq P \leq 1,
\end{aligned}$$

where $K = k/k_D$, and so on, denote normalized wave-numbers. We want to estimate the reduced bispectrum $b_{\ell_1 \ell_2 \ell_3}$ introduced in [136]:

$$\langle a_{\ell_1 m_1} a_{\ell_2 m_2} a_{\ell_3 m_3} \rangle = \mathcal{G}_{\ell_1 \ell_2 \ell_3}^{m_1 m_2 m_3} b_{\ell_1 \ell_2 \ell_3}, \quad (8.47)$$

where $\mathcal{G}_{\ell_1 \ell_2 \ell_3}^{m_1 m_2 m_3}$ is the Gaunt integral. We used the procedure described in [137]: substituting in Eq. 8.14 the result in Eq. 8.5, and using Eq. 8.46 for the source, we have:

$$\begin{aligned}
b_{\ell_1 \ell_2 \ell_3} &= \frac{\pi \alpha^3 A^3 k_D^{3n_B+9}}{6 \rho_{rel}^3} \int_0^\infty dx x^2 \int_0^1 dK K^2 \int_0^1 dQ Q^2 \\
&\int_0^1 dP P^2 j_{\ell_1}(Ky) j_{\ell_1}(Kx) j_{\ell_2}(Qy) \\
&j_{\ell_2}(Qx) j_{\ell_3}(Py) j_{\ell_3}(Px) \mathcal{I}(K, Q, P), & (8.48)
\end{aligned}$$

where $y = k_D \eta_0$, $x = k_D r$, and r comes from the decomposition of the delta function in Eq. 8.46. Substituting Eq. 8.46, the above equation becomes:

$$\begin{aligned}
b_{\ell_1 \ell_2 \ell_3} &= \frac{\pi \alpha^3 A^3 k_D^{3n_B+9}}{36 \rho_{rel}^3} \int_0^\infty dx x^2 \int_0^1 dK K^2 j_{\ell_1}(Ky) j_{\ell_1}(Kx) \\
&\int_0^K dQ Q^2 j_{\ell_2}(Qy) j_{\ell_2}(Qx) \int_0^Q dP P^2 j_{\ell_3}(Py) j_{\ell_3}(Px) \\
&\times \{ a(n_B) [K^{n_B} Q^{2n_B+3} + K^{n_B} P^{2n_B+3} + Q^{n_B} P^{2n_B+3}] \\
&\quad + b(n_B) [2K^{3n_B+3} + Q^{3n_B+3}] + c(n_B) \} \\
&+ \text{permutations}, & (8.49)
\end{aligned}$$

where $a(n_B) = n_B/(n_B + 3)/(2n_B + 3)$, $b(n_B) = n_B/(3n_B + 3)/(2n_B + 3)$, $c(n_B) = 1/(n_B + 1)$, plus the six ordered permutations of K , Q and P , which represents the permutations of ℓ_1 , ℓ_2 , ℓ_3 .

Since the Bessel functions $j_\ell(Py)$ peak at $P \simeq \ell/y$ and $y \gg 1$, we substituted the upper integration bounds with 1. Following [138], for each of these integrals we used the approximation given in Eq. 6.512 of [139]:

$$\int_0^1 dP P^2 j_{\ell_3}(Py) j_{\ell_3}(Px) \sim \frac{1}{4} \frac{\delta(y-x)}{x^2}. \quad (8.50)$$

Solving the integral in dx , using the delta function, we obtained for the first term:

$$\frac{a(n)}{4} \int_0^1 dK K^{n_B+2} j_{\ell_1}^2(Ky) \int_0^1 dQ Q^{2n_B+5} j_{\ell_2}^2(Qy), \quad (8.51)$$

and so on for the others. We leave to the appendix the description of the approximation we used for these integrals. For the case $n_B > -1$, in Eq. 8.49 we considered only the dominant white noise term $c(n_B)$. In this case all permutations give the same result:

$$b_{\ell_1 \ell_2 \ell_3} \simeq \frac{\pi^7 \alpha^3 \langle B^2 \rangle^3}{96} \frac{(n_B + 3)^3}{n_B + 1} \frac{1}{\rho_{rel}^3} \frac{1}{(k_D \eta_0)^4}, \quad \text{for } n_B > -1. \quad (8.52)$$

For $n_B < -1$, considered the complexity of the general solution, we computed explicit expressions only for two values of the spectral index: $n_B = -2$, and $n_B \rightarrow -3$. For the case $n_B = -2$ we found:

$$b_{\ell_1 \ell_2 \ell_3} \simeq \frac{\pi^8 \alpha^3 \langle B^2 \rangle^3}{288} \frac{1}{\rho_{rel}^3} \frac{1}{(k_D \eta_0)^3} \times \left\{ \frac{1}{\ell_1} \left[\log \left(\frac{k_D \eta_0}{\sqrt{\ell_2} \sqrt{\ell_3}} \right) - \frac{2k_D \eta_0}{3\pi} \frac{1}{\ell_1} \right] + \frac{1}{\ell_2} \left[\frac{1}{2} \log \left(\frac{k_D \eta_0}{\ell_3} \right) - \frac{k_D \eta_0}{3\pi} \frac{1}{\ell_2} \right] \right\} + \text{permutations}, \quad \text{for } n_B = -2. \quad (8.53)$$

We remark that, since this expression has been derived from the wave-number configuration $P \leq Q \leq K$, the squeezed limit must be taken with $\ell_3 \ll \ell_2 \simeq \ell_1$. For this spectral index the dominant term in the bispectrum goes as $\log(k_D \eta_0 / \ell_3)$, which corresponds to the dominant term in wave-number

space, P^{2n_B+3} . The permutations must be treated accordingly: for example, for $Q \leq P \leq K$ the corresponding is $\ell_2 \ll \ell_1 \simeq \ell_3$.

For $n \rightarrow -3$ we used the approximation Eq. A.4 with $m = -1$, and we found

$$b_{\ell_1 \ell_2 \ell_3} \simeq \frac{\pi^7 \alpha^3 n_B (n_B + 3)^2 \langle B^2 \rangle^3}{288 \frac{2n+3}{\rho_{rel}^3}} \times \left[\left(\frac{1}{\ell_1^2 \ell_2^2} + \frac{1}{\ell_1^2 \ell_3^2} + \frac{1}{\ell_2^2 \ell_3^2} \right) + \frac{\pi n_B + 3}{16 n_B + 1} k_D \eta_0 \left(\frac{1}{\ell_1^5} + \frac{1}{2\ell_2^5} \right) \right] + \text{permutations}, \quad \text{for } n_B \approx -3, \quad (8.54)$$

where the same considerations as above apply for the squeezed limit. The Eq. 8.54 is valid only for $n_B \rightarrow -3$ so the denominator is always finite. The apparent divergence for $n_B = -3/2$ is just an artefact due to our approximation, Eq. 5.2.3: $n_B = -3/2$ corresponds to a threshold value for which $|\rho_B(k)|^2$ diverges logarithmically for $k \rightarrow 0$. The Eq. 8.54 is composed by two terms. The second one comes from the term proportional to $b(n_B)$ in Eq. 8.49, it is sub-leading since the $a(n_B)$ terms contains $(n_B + 3)^{-1}$. The leading term of Eq. 8.54, specified to the squeezed and equilateral configurations, gives the same result as found in [142] (Eq. (17) and (18) and discussion thereafter, we remind that we use $\alpha = 0.1$).

8.5 PMF constraints with current NG data

We will now use the results we obtained on the CMB magnetic bispectrum on large scale to derive the constraints on PMFs with the current NG data from WMAP5 [7]. NG data are typically quantified in terms of the parameter f_{NL} , which is related to non-linearities in the gravitational potential of primordial perturbations. Since magnetic NG are quantified by the bispectrum, to use NG data it is necessary to derive a effective magnetic f_{NL} from the bispectrum. Before going into details of the derivation we will present an easier derivation of the constraints on PMFs from NG data.

8.5.1 Constraints from the bispectrum

An easy approach to derive the constraints on PMFs from NG data is the one presented in [142], which compares the bispectrum directly with the f_{NL} . The comparison is given by [142]:

$$\ell_1(\ell_1 + 1)\ell_3(\ell_3 + 1)b_{\ell_1\ell_2\ell_3} \sim 4 \times 10^{-22} f_{NL}. \quad (8.55)$$

We evaluated the constraints for the most infrared spectral index $n_B \rightarrow -3 \sim -2.9$. From the expression for the bispectrum of Eq. 8.54 we obtained:

$$\ell_1(\ell_1 + 1)\ell_3(\ell_3 + 1)b_{\ell_1\ell_2\ell_3} \sim \frac{\pi^7 \alpha^3 n_B (n_B + 3)^2 \langle B^2 \rangle^3}{288 (2n_B + 3) \rho_{rel}^3} < 4 \times 10^{-18} f_{NL}, \quad (8.56)$$

assuming an $f_{NL} \leq 111$ from WMAP5 [7] and a correction factor of $\alpha = 0.1$ we obtained:

$$\ell_1(\ell_1 + 1)\ell_3(\ell_3 + 1)b_{\ell_1\ell_2\ell_3} \sim 10^{-21} \langle B_{nG}^2 \rangle^3 < 4 \times 10^{-18} f_{NL}, \quad (8.57)$$

which gives:

$$\sqrt{\langle B^2 \rangle} < 7.95 \text{ nG} \quad (8.58)$$

We obtained a different result with respect to the constraints derived in [142], the difference is due to two main factors. The first is that [142] use a different correction factor: $\alpha \sim 0.03$, the second is related to the different analytical approximations done in the two works, which give different amplitudes of the bispectrum.

8.5.2 Constraints from f_{NL}^{loc}

The signal-to-noise ratios (S/N) is a function of the maximum multipole a given experiment can reach, since $\ell_{max} \gg 1$, we can use the flat-sky approximation [143, 144]. Within this approximation, and with the following notation, the reduced bispectrum coincides with the bispectrum:

$$\langle a(\vec{\ell}_1)a(\vec{\ell}_2)a(\vec{\ell}_3) \rangle = (2\pi)^2 \delta^{(2)}(\vec{\ell}_{123}) B(\ell_1, \ell_2, \ell_3), \quad (8.59)$$

where $\vec{\ell}_{123} = \vec{\ell}_1 + \vec{\ell}_2 + \vec{\ell}_3$. In order to use present NG data we need to quantify the NG signal coming from PMFs, the simpler way to do it is to estimate an effective f_{NL} . The WMAP5 search for non-Gaussianities is optimised to search for local primordial contribution, therefore its bounds are given in terms of $-9 < f_{NL}^{loc} < 111$. But since PMFs non-Gaussian signature may be different from the local type this method cannot be directly applied. Therefore we proceeded in a different way. First, we defined the Fisher matrix (see, for example, [136])

$$F_{ij} = \frac{f_{sky}}{(2\pi)^2\pi} \int d^2\ell_1 d^2\ell_2 d^2\ell_3 \delta^{(2)}(\vec{\ell}_{123}) \frac{B_i(\ell_1, \ell_2, \ell_3) B_j(\ell_1, \ell_2, \ell_3)}{6 C(\ell_1) C(\ell_2) C(\ell_3)}, \quad (8.60)$$

where f_{sky} is the portion of the observed-sky in a given experiment and i (or j) = (*mag*, *loc*). The first entry $F_{mag,mag}$ of the Fisher matrix corresponds to the signal-to-noise ratio $(S/N)^2$ provided by the PMFs to the NG. We have defined the power spectrum in the flat-sky approximation by $\langle a(\vec{\ell}_1) a(\vec{\ell}_2) \rangle = (2\pi)^2 \delta^{(2)}(\vec{\ell}_{12}) C(\ell_1)$, with $\ell^2 C(\ell) = \mathcal{A}/\pi$ and $\mathcal{A} \simeq 17.46 \times 10^{-9}$ is the amplitude of the primordial gravitational potential power spectrum computed at first-order. In other words, we assume that the two-point correlation function is dominated by the usual adiabatic contribution from inflation. The local bispectrum is given by [143]:

$$B_{loc}(\ell_1, \ell_2, \ell_3) = \frac{2 f_{NL}^{loc} \mathcal{A}^2}{\pi^2} \left(\frac{1}{\ell_1^2 \ell_2^2} + cycl. \right), \quad (8.61)$$

all these expressions are obtained in the Sachs-Wolfe approximation.

We defined an effective f_{NL}^{eff} which minimises the χ^2 as

$$\chi^2 = \int d^2\ell_1 d^2\ell_2 d^2\ell_3 \delta^{(2)}(\vec{\ell}_{123}) \frac{\left(f_{NL}^{eff} B_{loc}(\ell_1, \ell_2, \ell_3) \Big|_{f_{NL}^{loc}=1} - B_{mag}(\ell_1, \ell_2, \ell_3) \right)^2}{6 C(\ell_1) C(\ell_2) C(\ell_3)},$$

and found:

$$f_{NL}^{eff} = \frac{F_{mag,loc}}{F_{loc,loc}} \Big|_{f_{NL}^{loc}=1}. \quad (8.62)$$

The signal-to-noise ratio for the primordial local case has already been computed in the flat-sky approximation in [143]. The result is that $F_{loc,loc} \simeq$

$(4/\pi^2)f_{sky}\mathcal{A}(f_{NL}^{loc})^2\ell_{max}^2\log(\ell_{max}/\ell_{min})$. The logarithm is typical of scale invariant power spectra and ℓ_{min} is the minimum multipole compatible with the flat-sky approximation. The physical meaning of f_{NL}^{eff} is that it is the value of the local f_{NL}^{loc} which best mimics the bispectrum from PMFs. With this definition we can apply to this value the current observational limits.

We start with the simplest case $n_B \approx -3$. Indeed, for n close to -3 , the leading term of the bispectrum is of the same form of the local primordial bispectrum Eq. 8.61 in the squeezed limit $\ell_3 \ll \ell_1 \simeq \ell_2$ and we found

$$f_{NL}^{eff} \simeq \frac{3\pi^9 \alpha^3 n_B(n_B+3)^2 \langle B^2 \rangle^3}{288 \mathcal{A}^2 2n_B+3 \rho_{rel}^3} \simeq 10^{-2} (n_B+3)^2 \left(\frac{\langle B^2 \rangle}{(10^{-9}\text{G})^2} \right)^3, \quad \text{for } n_B \approx -3. \quad (8.63)$$

For the case $n_B > -1$ we found

$$f_{NL}^{eff} \simeq \frac{\pi^9 \alpha^3 (n_B+3)^3 \langle B^2 \rangle^3}{2304 \mathcal{A}^2 n_B+1 \rho_{rel}^3} \left(\frac{\ell_{max}}{\ell_D} \right)^4 \frac{1}{\log(\ell_{max}/\ell_{min})} \simeq 6 \times 10^{-7} \frac{(n_B+3)^3}{n_B+1} \left(\frac{\langle B^2 \rangle}{(10^{-9}\text{G})^2} \right)^3, \quad \text{for } n_B > -1. \quad (8.64)$$

For the case $n = -2$:

$$f_{NL}^{eff} \simeq \frac{5\pi^{10} \alpha^3 \langle B^2 \rangle^3}{2304 \mathcal{A}^2 \rho_{rel}^3} \left(\frac{\ell_{max}}{\ell_D} \right)^3 \frac{\log(\ell_D/\ell_{max})}{\log(\ell_{max}/\ell_{min})} \simeq 5 \times 10^{-5} \left(\frac{\langle B^2 \rangle}{(10^{-9}\text{G})^2} \right)^3, \quad \text{for } n_B = -2. \quad (8.65)$$

In all numerical estimates we have taken $\ell_D = k_D \eta_0 \simeq 3000$, $\ell_{max} \sim 750$, $\ell_{min} \sim 10$, $\alpha \simeq 0.1$. We see that the effective value of NG f_{NL}^{eff} is smaller than the present upper bound of $\mathcal{O}(10^2)$ on f_{NL}^{loc} from WMAP5 [7], for PMFs $\mathcal{O}(10) \cdot 10^{-9}$ G for $n_B \approx -3$ and $\mathcal{O}(20) \cdot 10^{-9}$ G for the other cases *. Sub-

*We have obtained similar estimates repeating the same procedure to define an effective non-Gaussianity parameter starting from a primordial equilateral configuration for which WMAP5 limits exist. In such a case the primordial equilateral configuration is peaked for $\ell_1 \sim \ell_2 \sim \ell_3$ and the effective non-Gaussianity parameter scales with ℓ_{max} with one power less than the corresponding one obtained from a local primordial bispectrum.

stituting the expression of the damping scale k_D , we obtained

$$\begin{aligned}\sqrt{\langle B^2 \rangle} &\leq 9\text{nG} && \text{for } n_B = -2.9 \\ \sqrt{\langle B^2 \rangle} &\leq 25\text{nG} && \text{for } n_B = -2 \\ \sqrt{\langle B^2 \rangle} &\leq 20\text{nG} && \text{for } n_B = 2,\end{aligned}\tag{8.66}$$

and

$$\begin{aligned}\sqrt{\langle B_\lambda^2 \rangle}|_{\lambda=0.1\text{Mpc}} &\leq 9 \text{ nG} && \text{for } n_B = -2.9 \\ \sqrt{\langle B_\lambda^2 \rangle}|_{\lambda=0.1\text{Mpc}} &\leq 26 \text{ nG} && \text{for } n_B = -2 \\ \sqrt{\langle B_\lambda^2 \rangle}|_{\lambda=0.1\text{Mpc}} &\leq 2 \mu\text{G} && \text{for } n_B = 2.\end{aligned}\tag{8.67}$$

The very large bound for blue spectral indices is the consequence of the fact that the procedure of using an effective f_{NL} returns a bound on the integrated PMF spectrum, and therefore for very blue spectra the constraints on large scales are irrelevant.

8.6 Preliminary study of the magnetized source term on intermediate scales

We derived the CMB magnetic bispectrum on large scales and used it to estimate the constraints on PMFs with NG data. In the previous chapters we showed that the main contribution of magnetized scalar perturbations is on small scales, therefore from the small scale magnetic bispectrum we expect to have much stronger constraints. For this reason we are extending our treatment also to these scales [148]. The treatment of small scale magnetized CMB anisotropies is more complex with respect to large scale ones, in particular in this section we will study the source of temperature anisotropies induced by PMFs on small scales. The temperature anisotropy according to Eq. 79 of [134] can be written as (neglecting the integrated Sachs Wolfe and

the polarisation terms):

$$\frac{\Theta_\ell^{(0)}(\tau_0, \mathbf{k})}{2\ell + 1} = \int_0^{\tau_0} d\tau g(\tau) \left[\left(\frac{\delta_\gamma}{4} + \psi \right) j_\ell(k(\tau_0 - \tau)) - \frac{v_b}{k} \dot{j}_\ell(k(\tau_0 - \tau)) + \frac{\pi_\gamma}{48} j_\ell(k(\tau_0 - \tau)) + \frac{\pi_\gamma}{16k^2} \ddot{j}_\ell(k(\tau_0 - \tau)) \right], \quad (8.68)$$

where $\dot{\tau}_{opt} e^{-\tau_{opt}} = g(\tau)$. Integrating by parts and setting the boundary terms to zero, we have:

$$\frac{\Theta_\ell^{(0)}(\tau_0, \mathbf{k})}{2\ell + 1} = \int_0^{\tau_0} d\tau j_\ell(k(\tau_0 - \tau)) \left[g(\tau) \left(\frac{\delta_\gamma}{4} + \psi + \frac{\dot{v}_b}{k} + \frac{\pi_\gamma}{48} + \frac{\ddot{\pi}_\gamma}{16k^2} \right) + \dot{g}(\tau) \left(\frac{v_b}{k} + \frac{\dot{\pi}_\gamma}{8k^2} \right) + \ddot{g}(\tau) \frac{\pi_\gamma}{16k^2} \right]. \quad (8.69)$$

This expression agrees with Eq. 12b of [146] setting their $\Pi = \pi_\gamma/12$ (a part from the term $\dot{g} \dot{\pi}_\gamma/8k^2$, which should be divided by two to get exactly the result of [146]). We passed to the synchronous gauge in agreement with our conventions, defining $\alpha = (\dot{h} + 6\dot{\eta})/2k^2$:

$$\begin{aligned} \psi &= \dot{\alpha} + \mathcal{H}\alpha \\ \phi &= \bar{\eta} - \mathcal{H}\alpha \\ \delta_\gamma &= \delta_\gamma^{sync} - 4\mathcal{H}\alpha \\ v_b &= \frac{\theta_b}{k} + k\alpha \\ \pi_\gamma &= 6\sigma_\gamma. \end{aligned} \quad (8.70)$$

The source term in the synchronous gauge becomes:

$$\begin{aligned} \frac{\Theta_\ell^{(0)}(\tau_0, \mathbf{k})}{2\ell + 1} &= \int_0^{\tau_0} d\tau j_\ell(k(\tau_0 - \tau)) \times \\ &\left[g(\tau) \left(\frac{\delta_\gamma^{sync}}{4} - \mathcal{H}\alpha + \dot{\alpha} + \mathcal{H}\alpha + \frac{\dot{\theta}_b}{k^2} + \dot{\alpha} + \frac{\sigma_\gamma}{8} + \frac{3\ddot{\sigma}_\gamma}{8k^2} \right) \right. \\ &+ \dot{g}(\tau) \left(\frac{\theta_b}{k^2} + \alpha + \frac{3\dot{\sigma}_\gamma}{4k^2} \right) \\ &\left. + \ddot{g}(\tau) \frac{3\sigma_\gamma}{8k^2} \right]. \end{aligned} \quad (8.71)$$

Chapter 9

Foregrounds, Secondary Anisotropies and Their Residuals on Small Scales

Small scale CMB anisotropies are a fundamental tool to test the standard cosmological model and its extensions. In particular in the previous part we have shown the importance of these scales for the cosmological model which includes the contribution of primordial magnetic fields.

Recent years have seen a great improvement in observational instrumentation for microwaves and the blossoming of observations of smaller and smaller scale CMB anisotropies. These observational data improvements make necessary the creation of more and more accurate data analysis tools. Of particular importance are the tools for the removal of foreground contamination and the marginalization over foreground residuals. In fact the microwave sky is a puzzle of different emissions of which the CMB is just a piece. All the non-CMB emissions are called foregrounds. In order to have the most accurate CMB data is necessary to remove the better as possible the foreground contamination and to take into account the effect of possible residuals in the data analysis. We can identify two great families of foreground contributions: large scale or diffuse foregrounds and small scale ones, mainly

associated to extragalactic sources. At small scales it is necessary to consider also the contribution of secondary anisotropies, which are larger than primary anisotropies in the Silk damping regime. Secondary anisotropies are generated during the propagation of CMB photons from the last scattering surface to the observer and are caused by different mechanisms of interactions and distortions of the primary CMB. In the following sections we will give an overview of foregrounds and secondary anisotropies with particular attention to small scales. Our analysis is restricted to anisotropies and foregrounds in temperature only and it is optimized for the *Planck* mission.

9.1 Diffuse foregrounds

Diffuse foregrounds are mainly produced by the Galactic emission, composed by synchrotron radiation, free-free and thermal dust emission. Due to their spectral behaviors, the three components dominate different frequency regimes: synchrotron emission is the dominant contribution for frequencies lower than 40 GHz, free-free becomes important at intermediate frequencies, while the higher ones are dominated by thermal dust emission. In the 70 GHz region, where the different contributions are comparable, Galactic foregrounds are minimum. In Fig. 9.1 the spectra of Galactic foregrounds and the *Planck* frequency bands are shown.

Synchrotron emission is due to the cosmic rays accelerated by the Galactic magnetic field. It dominates frequencies below 40 GHz. Its antenna temperature spectrum is well approximated by a power law:

$$T_B^{Sy}(\nu) = \nu^{-\alpha_s} . \tag{9.1}$$

The intensity of the synchrotron emission depends on the spectrum of the electronic component of cosmic rays, on the intensity of the magnetic field and also on the spatial distribution of the electrons. The spectral index has an average value between $\alpha \sim 2.6 - 3.4$ but it depends on the propagation

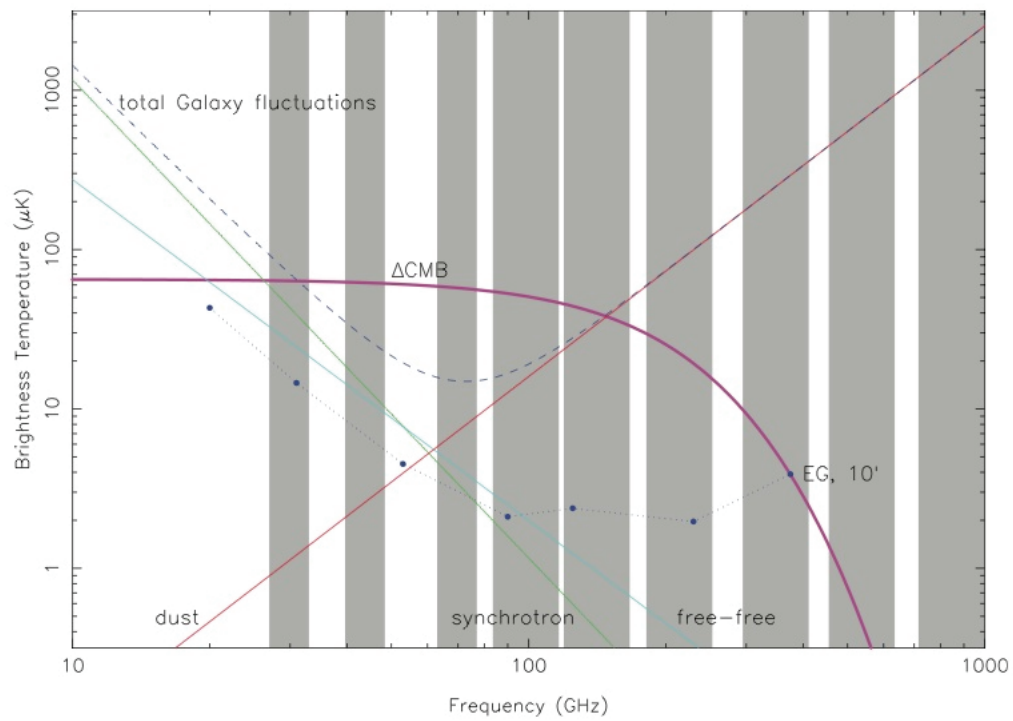


Figure 9.1: Spectrum of CMB and galactic emissions. Dust, synchrotron and free-free levels corresponds to the WMAP Kp2 levels (85% of the sky)[6]

effects of cosmic ray electrons and therefore varies with the frequency and depends on the position on the sky.

The bremsstrahlung or free-free emission is due to the collisions of thermalized electrons and ions in regions where there is hot ionized gas with temperatures of the order of 10^6 K. The spectrum of the free-free emission can be described again with a power law:

$$T_B^{FF}(\nu) = \nu^{-\alpha_{FF}}, \quad (9.2)$$

where the index α_{FF} is determined by the physics of the collisions and is typically $\sim 2 - 2.15$. Since free-free emission is characteristic of regions with highly ionized gas it represents a tracer of star formation.

Thermal dust emission dominates the higher frequencies and the information available on this component mainly comes from Galactic observations at infrared and ultraviolet wavelenghts. It is composed by grains of various sizes, from few nm up to several hundreds of nm and it is made of PAHs (Polycyclic Aromatic Hydrocarbon molecules), silicate and carbonate compounds. The thermal dust emission can be modelled as a grey body:

$$I_{dust}(\nu, T_{dust}) = \nu^{\alpha_{dust}} B_{BB}(\nu, T_{dust}) \sim \nu^{\alpha_{dust}+2}, \quad (9.3)$$

and therefore has a very steep frequency behavior with a spectral index of $\alpha \sim 3.5 - 4$. With such an α the dust emission is the dominant one for frequencies larger than 200 GHz.

Thanks to its high frequency channels, *Planck* will provide an high resolution full sky map of Galactic dust emission, which will be useful to investigate the dust properties. In Fig. 9.2 the first year full sky *Planck* map (obtained by the combination of the nine frequencies) is shown. We note the prominent Galactic dust contribution coming from the higher frequency channels. A zoom of the dust structure of the Galaxy, obtained combining the two higher *Planck* frequencies, is shown in Fig. 9.3.

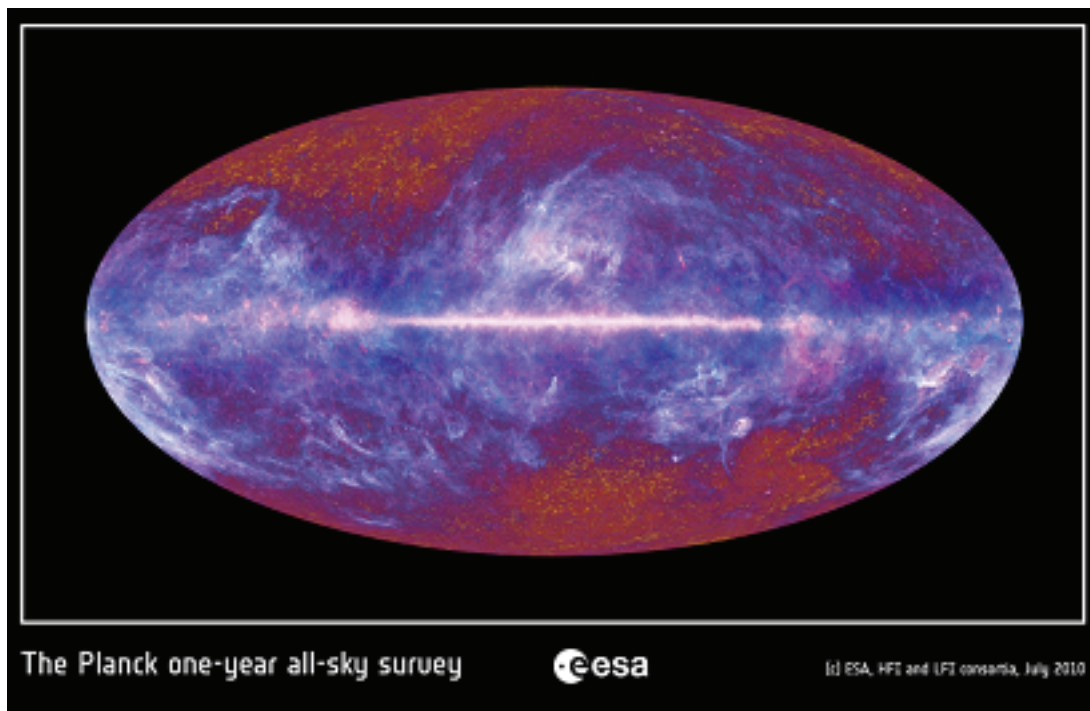


Figure 9.2: Full sky map done by Planck, all the nine frequencies are overposed (copyright: ESA)



Figure 9.3: Focus of the cold dust structures of the Milky way done by Planck, overposition of the 545 and 857 frequencies (copyright: ESA, HFI consortium)

Dust have a small effect also on low frequency channels. The low frequency observations of WMAP showed the existence of an anomalous component. In particular the 23 GHz frequency is supposed to be dominated by synchrotron emission, but its map shows a correlation with the intensity map of the Galaxy at $100\ \mu\text{m}$ [179], wavelength dominated by dust emission and it presents an excess with respect to the extrapolation from 1.4 GHz [182]. Also component separation evidences the presence of this emission in WMAP data [183]. This dust-correlated emission at low frequencies could be produced by another population of dust grains [184]. These smaller grains of dust that can be excited into rotational mode and emit for electric dipole may be responsible for this anomalous emission [185], relevant at few tens of GHz, and of uncertain polarization degree. This component has been called spinning dust.

The WMAP observations evidenced the presence of an excess of diffuse microwave emission around the Galactic center region (within 20 degrees), with an approximate radial symmetry [180]. This emission is called “Haze” emission, it is not compatible with free-free and standard synchrotron emissions, its origin is still unknown [179] but one mechanism proposed for this excess is the annihilation of Dark Matter [181].

In the diffuse foregrounds there is also a contribution from an emission in the Solar system: the zodiacal light. The zodiacal light is an emission produced by a population of dust particles diffuse between the Sun and the asteroid belt. These particles have sizes from micron to millimeters, temperatures of the order of 260 K and emit in the far-IR. In particular the zodiacal light peaks at $10\ \mu\text{m}$ and its contribution is strongly subdominant with respect to the Galactic one for all but the highest *Planck* frequency channel (857 GHz) [187]. The zodiacal light emission COBE model [186] has been exploited in simulations for the Planck mission [187].

Another contribution, called the Kuiper Light Emission (KLE), by cold IDPs (50 K) located in the collisional debris disk in the Kuiper band at 30-50 AU [188] could exist. From current estimates, KLE is between 0.1 and

10 in the sub-mm [188, 189]. At frequencies < 250 GHz, KLE should be dominant over the zodiacal light, possibly contributing [190, 191] to large angular scale CMB anomalies observed by WMAP [192].

Large scale foregrounds are removed through component separation. For component separation we refer in general to a number of techniques which aim to separate and isolate each component of the microwave sky. The basic idea, which is developed with different algorithms and different techniques, is to use the frequency dependence of the various signals combining as many frequency maps as possible. In particular CMB black body spectrum is the same at all frequencies in thermodynamic equivalent temperature. Foregrounds instead have different frequency dependences, like power laws with different spectral indices. The combination of different frequency maps allows to isolate each foreground and possibly to derive their emission properties. The combination can be done both assuming or not a priori knowledge of the foreground components, the former methods are called non-blind techniques, whereas the latter are called blind techniques. For small scales CMB anisotropies it is not necessary to pass through the component separation process to get rid of diffuse foregrounds but, for many cases of interest, is sufficient the application of Galactic masks which cut out the brighter part of Galactic emission.

9.2 Small scale foregrounds

Great part of the small scale foregrounds has an extragalactic origin and is due to point source emission. Because of its angular resolution, an experiment like *Planck* is not optimized for point source detection, as instead are dedicated experiments like *HERSCHEL* and ground based radio telescopes. However, *Planck* thanks to its full sky coverage, will detect a large number of sources, although it will miss faint sources. The capability of an instrument to detect the sources is quantified by the detection threshold flux. The detec-

<i>Channels</i>	70GHz	100GHz	143GHz	217GHz	353GHz
$S_{max}(J_y)$	0.57	0.41	0.32	0.24	0.28

Table 9.1: Planck detection threshold fluxes for 14 months mission [196, 159].

tion threshold flux is the flux limit below which a source is not distinguished as a point source. It depends on the optical properties of the instrument on the global fluctuation level of the sky at the considered frequencies (mainly the angular resolution) and on the algorithm used to extract the sources from the maps. Typically, a confidence level equal or greater than 5σ for the detection is assumed. In Table 9.1 we report the detection threshold fluxes for *Planck* channels [159].

In the frequency range covered by Planck we have the contribution of different populations of extragalactic point sources. These sources can be divided into two major categories: radio and infrared galaxies. The former dominate at low frequencies while the latter at high frequencies. Together with these two populations there is a contribution from anomalous objects like Gigahertz Peaked Spectrum (GPS), starforming, Advection Dominated Accretion Flows/Adiabatic Inflow Outflow Solution (ADAF/ADIOS) and radio afterglows of Gamma Ray Burst (GRB)[160, 161, 162, 163].

Radio galaxies, typically BL LACs and Flat Spectrum Radio Quasars (FSRQ) present a flat spectrum $S_\nu \propto \nu^\alpha$ with $\alpha \sim -0.3 - 0.7$ [164] given by the dominant synchrotron emission. Radio galaxies have also a contribution from steep spectra radio sources which typically have fluxes $S_\nu \propto \nu^\alpha$ with $\alpha \sim -0.7 - (-1)$. Infrared galaxies are instead dominated by dust emission and present a steep spectra $S_\nu \propto \nu^{3.5}$. The point source emission is minimal at the intersection of these two main contributions which takes place at wavelenghts of the order of few mm.

We now briefly summarize the anomalous population. In particular GHz Peaked Spectrum (GPS) present a convex spectrum which peaks around few GHz and are believed to be young and compact radio sources with a self

absorbed synchrotron emission. Their contribution due to their small number and flat counts is almost negligible at the arcmin scale [161]. Advection Dominated Accretion Flows (ADAF) and Adiabatic Inflow Outflow Solution (ADIOS) are objects, typically early type galaxies, in which the central engine emits in the late stages of evolution and the accretion efficiency of the central black hole is very diminished. This causes the emission to be mainly in the cm and mm ranges but due to the low radio power their contribution is almost negligible [162]. Starforming galaxies are either late type or starburst galaxies at low redshift, dominated by synchrotron and free free emission, or high redshift protospheroid with active star formation. They are numerous and there is a lot of information on their population of sources coming from different surveys [162]. Radio afterglows of Gamma Ray Burst are rare, their synchrotron emission in radio has a flux which scales as $S_\nu \propto \nu^{1/3}$ up to a peak frequency which decreases with time [162].

The most updated model of extragalactic sources which includes all the aforementioned populations is presented in [163]; for the project we will present we referred to this model that has been based and validated by numerous radio and infrared data.

The contribution of detected source is simply removed masking them in the maps, however, it is not possible to remove the contribution of unresolved point sources. The contribution of unresolved point sources acts like an unavoidable noise and has an impact on the angular power spectrum and the cosmological information contained in it. Since it is not possible to remove this residual contribution, the only possibility is to model it and include its contribution in the data analysis. In the following we will describe the contributions of unresolved point sources to CMB anisotropy angular power spectrum, as it will be detected by *Planck*. This study is crucial for *Planck*, since its measurements of CMB primary anisotropies on small scales are limited by the capability in subtracting astrophysical foregrounds rather than noise/angular resolution.

9.2.1 Poissonian contribution

All types of sources, both radio and infrared, produce an important contribution which is given by their random distribution in the sky. The coefficients of spherical harmonics of a Poissonian distribution of a population of sources in the sky with flux S are [165]:

$$\langle a_{lm} \rangle = \begin{cases} \sqrt{4\pi\bar{n}}S & \text{for } \ell = 0 \\ 0 & \text{for } \ell \neq 0, \forall m \end{cases}$$

where $\bar{n} = N/4\pi$ is the mean number of sources per steradian with flux S . The angular power spectrum is given by:

$$C_l = \langle |a_{lm}|^2 \rangle - |\langle a_{lm} \rangle|^2 = \bar{n}S^2, \quad (9.4)$$

which can be generalized to $C_l = \sum_i \bar{n}_i S_i^2$ if we consider sources with different fluxes. Extrapolating the continuum limit in flux up to the detection threshold, above which the source contribution is removed, we have that the angular power spectrum for a Poissonian distribution of sources in sky is given by a flat C_l :

$$C_l^{PSP} = \int_0^{S_{max}} \frac{dN(S)}{dS} S^2 dS, \quad (9.5)$$

where S_{max} is the detection threshold flux and $\frac{dN(S)}{dS}$ are the source number counts. Eq. 9.5 can be converted from $\frac{\text{Jy}^2}{\text{sr}}$ (the flux S is in measured Jy) in μK^2 , applying the conversion to antenna temperature and then to thermodynamic temperature:

$$C_l^{PSP} = \frac{c^4}{4K_B^2\nu^4} \frac{(e^x - 1)^4}{x^4 e^{2x}} \int_0^{S_{max}} \frac{dN(S)}{dS} S^2 dS, \quad (9.6)$$

where $x = \frac{h\nu}{K_B T_0} = \frac{\nu}{56.78\text{GHz}}$. In order to compute the expected values of the Poissonian contribution is necessary to model the source number counts. The Poissonian contribution is dominated by the sources which are just below the detection threshold.

9.2.2 Clustering contribution

Radio source contribution is described by a Poissonian term, in fact radiogalaxies at Planck frequencies have a clustering negligible with respect to the Poissonian term, at least for the detection thresholds in the range of that achievable by *Planck*. Only at much lower frequencies, the clustering of radio sources starts to become important but these frequencies are well outside the CMB observational frequency range. The situation is different for infrared sources, galaxies, which are strongly clustered and therefore it is necessary to model a clustering contribution in addition to the Poissonian one.

Infrared source clustering

The clustering term is not trivial and depends on the cosmological model, on the galaxy models, on the redshift and on the frequency. In particular the clustering term increases with the frequency becoming the dominant one already at 353 GHz. Contrary to what happens for the Poissonian term, the clustering one is dominated by faint sources well below the detection threshold and therefore channels with lower detection thresholds suffer a greater contribution from clustering. Because of this important contribution by faint sources, a very accurate model of infrared sources at all fluxes is necessary to model the clustering term. We shall review the basic points of the clustering contribution to fluctuation modelling.

The Cosmic Infrared Background (CIB) is composed by different emissions [167]. Its galaxy contribution is mainly given by starburst galaxies, Luminous InfraRed Galaxies (LIRGs, $10^{11}L_{\odot} < L_{IR} < 10^{12}L_{\odot}$) and Ultra Luminous InfraRed Galaxies (ULIRGs, $L_{IR} > 10^{12}L_{\odot}$), (plus a little contribution by AGN) [167, 168, 169]. One of the greater complexity related to CIB is that infrared emission collects contributions from very different populations at different redshifts. In particular, for the two main CIB contributions we have that LIRGs dominate at low and intermediate redshifts $0.5 < z < 1.5$, whereas ULIRGs dominate at higher redshifts $2 < z < 3$

[169]. While ULIRGs and LIRGs can be modelled with a passive evolution involving only a weak variation with redshift, starburst galaxies present a strong evolution of the Spectral Energy Distribution (SED) which has to be considered. The total intensity of the CIB is given by:

$$\bar{I}_{CIB} = \int_0^{S_{max}} dS \frac{dN}{dS} S, \quad (9.7)$$

A flattening of the number counts at low fluxes $\frac{dN}{dS}|_{S < S_*} = const$ is necessary to have a finite CIB intensity. The clustering power spectrum is given by [171, 169]:

$$C_l^{Clustering} = \int \frac{dz dr}{r^2} a^2(z) \bar{j}_d^2(\nu, z) b^2(k, \nu, z) P_M(k)|_{k=l/r} G^2(z), \quad (9.8)$$

where r is the proper distance, $k = l/r$ derives from the Limber approximation, the $\frac{dz dr}{r^2} a^2(z)$ term takes into account all geometrical effects and depends on the cosmological model adopted, $\bar{j}_d^2(\nu, z)$ is the mean galaxy emissivity per unit of comoving volume, $b^2(k, \nu, z)$ is the bias, P_M is the matter power spectrum today and $G^2(z)$ is the linear theory growing factor. The emissivity of infrared galaxies can be written as [169]:

$$j_d^2(\nu, z) = (1+z) \int_{L_b} L_{\nu'=(1+z)\nu} \frac{dN}{dln(L_b)} dln(L_b), \quad (9.9)$$

where the subscript b stands for bolometric, $\frac{dN}{dln(L_b)}$ is the comoving luminosity function and ν is the observed frequency. Eq. 9.8 contains a great number of dependences and uncertainties. It strongly depends on the cosmological model through the geometrical factor, and through the linear perturbation theory for the growth factor. Another complication comes from the fact that the luminosity function strongly depends on the assumptions on the galaxy Spectral Energy Distribution (SED), as shown in [171, 169]. In particular, different assumptions lead to very different overall results. The last, but not least in term of complexity, uncertainty is the bias. The bias describes the relation between the infrared galaxies and the dark matter distribution underneath them. The bias of optical and radio galaxies is well know thanks to

a great amount of data available, on the contrary the knowledge of the infrared one is still very poor. The infrared bias depends on the wavenumber, on the frequency and also on the redshift since different populations with different SEDs might have different spatial distributions. A full theoretical treatment of the bias term which includes all the exact dependences is still lacking and the present simulations of the CIB typically use a constant bias approximation. The complexity of the clustering term makes almost impossible to extrapolate a simplified theoretical model without using drastic approximations which would not allow reliable results. For this reason, we use a complete empirical approach to this problem, presented in the next chapter.

9.3 Secondary anisotropies

Secondary anisotropies are induced by interactions of the primary CMB photons occurred with particles or the gravitational field during the propagation from the last scattering surface to the observer. They involve various and different processes and the main ones are (see [172] for a review):

- Integrated Sachs Wolfe effect
- Rees Sciama effect
- Lensing
- Reionization
- Ostriker Vishniac effect
- Sunyaev Zeldovich effect.

In the following we will briefly review for completeness these secondary anisotropies but we will focus on the Sunyaev Zeldovich effect which strongly affects small scale CMB anisotropies.

As previously mentioned the main contribution to anisotropies on large scales, generated by the blueshifts and redshifts of the CMB photons due to the gravitational perturbations on the last scattering surface, is called Sachs Wolfe term [173]. As the name suggests, the Integrated Sachs Wolfe effect (ISW) has a similar origin; it is caused by the blueshifts and redshifts created by gravitational potentials but after the last scattering. During the propagation from last scattering surface to the observer CMB photons pass through numerous potential wells and hills generated by evolving cosmological perturbations and structure formation. In a static situation, the resulting effect of this crossing would be null due to compensation, but the universe and perturbations evolve. Therefore the gravitational potential crossed by photons changes during the path from last scattering surface to present time and causes a net blueshift or redshift. This effect is an Integrated Sachs Wolfe effect (ISW). In particular the temperature anisotropy produced by the ISW depends on the integral of the time variation of the potential:

$$\frac{\Delta T}{T} = 2 \int \dot{\Phi} d\tau. \quad (9.10)$$

We can distinguish two different contributions to the ISW.

The early ISW takes place just after the decoupling epoch when the cosmological fluid is matter dominated, but a not negligible radiation density modifies the gravitational potential.

The second is called late time ISW, which instead takes place at low redshift when the universe is dominated by dark energy. For a standard matter dominated universe the late ISW is zero. Dark energy instead causes a decrease of gravitational potential on large scales and therefore induces an ISW effect. This late ISW term, intrinsically related to dark energy properties, is a powerful tool to constrain dark energy models, however, being important only at low multipoles is blurred by cosmic variance.

The ISW effects take into account only linear effects: when considering also non-linearities in the time dependence of the gravitational potential the effect takes the name of Rees-Sciama [174]. This is a very small effect for all

the scales of interest and is smaller than the linear ISW.

The lensing effect term is due to the gravitational lensing induced on the CMB photons by structures and gravitational potentials, encountered during the propagation from the last scattering surface. Lensing conserves the surface brightness and therefore its effect can be observed only in an anisotropic photon distribution. In particular in an anisotropic distribution (as is the CMB) the dispersion of the deflection angles of near photons induces an intrinsic modification of the anisotropies. Lensing acts on all scales but induces a transfer of power from large to small scales, then its effect is larger on small scales. On these scales primary CMB is affected by the Silk damping and the transferred power from large scale is more visible. The publicly available Einstein-Boltzmann codes already include the computation of the predicted lensing contribution, therefore we refer to [175].

After the recombination epoch the universe was reionized by the emission of stars and AGNs. Observations of quasar spectra show that the universe was fully ionized at redshift $z = 6$, therefore reionization must have occurred at some time between the recombination and that epoch. The reionization induces a Thompson scattering of the CMB photons, with optical depth τ , and therefore modifies the CMB anisotropies. In particular it causes a damping of the primary anisotropies in temperature and polarization and the production/amplification of polarization anisotropies at large angular scales: i.e. the characteristic reionization bump. During the reionization phase the bulk motions of the reionized patches can produce very small scale anisotropies with the same mechanism of the kinetic Sunyaev Zeldovich and the Ostriker Vishniac effects.

The Ostriker Vishniac effect is also called kinetic Sunyaev Zeldovich effect from large scale structure [176]. The effect is in fact due to the modulation of the second order Doppler effect from the motion along the line of sight of

DM halos. As the standard kinetic Sunyaev Zeldovich effect, it is very small and negligible for the angular scales of interest in this project.

9.3.1 Sunyaev Zeldovich effect

The Sunyaev Zeldovich (SZ) effect is given by the interactions of CMB photons with cluster of galaxies encountered during the propagation from the last scattering surface. In particular we can distinguish two contributions, the thermal and the kinetic SZ effects.

Thermal SZ effect

The thermal SZ effect (TSZ) is generated by the inverse Compton interaction of the CMB photons with the electrons of the hot gas in galaxy clusters [177]. The interaction shifts photons toward higher energies creating a local spectral distortion of the CMB.

The TSZ effect strongly depends on the cluster properties. It has a strong dependence on the mass of the clusters with a major contribution coming from the rare but massive clusters. The correlation between halos instead is almost negligible and therefore is possible to use the 1-halo model to describe the DM halo properties. Together with the dependence on the mass of the clusters, the TSZ depends also on the characteristics of the gas inside them. It depends on the projected gas pressure profile and in particular the major contribution comes from the more external and extended regions of the gas distribution.

For the study of the TSZ induced on the single cluster, it is possible to collect independent information on the cluster gas properties from X-ray observations. In fact, the gas has a very high temperature, of the order of 10^6 K, and emits for free-free in the X-ray. The emission flux at high energies depends on the square of the electronic density and its measure can represent an important tool to estimate the expected TSZ effect of the single cluster, but also to study in a more general manner the cluster gas properties.

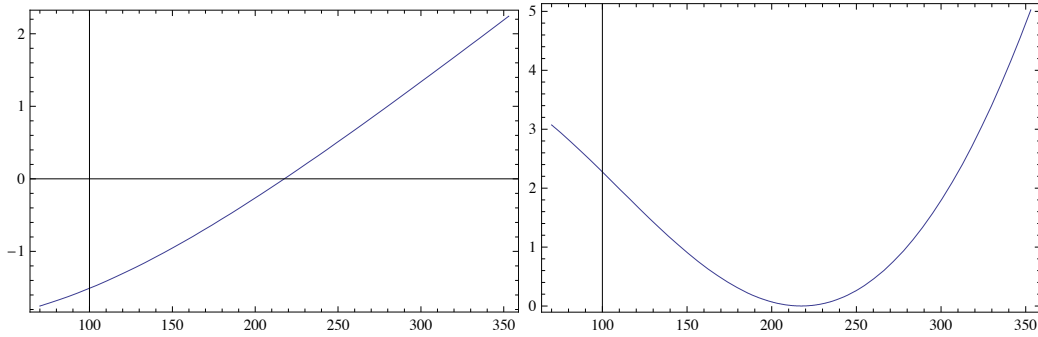


Figure 9.4: TSZ frequency dependence $g(\nu)$ (left panel) and its square $g^2(\nu)$ (on the right), on the x-axes is the frequency in GHz

For the case of CMB anisotropies it is necessary to estimate the angular power spectrum of the expected TSZ which will come from the integrated effect of all the clusters encountered by CMB photons. In the following we will describe it mainly following [158]. The angular power spectrum of the TSZ effect is given by:

$$C_l^{SZ} = g^2(\nu) \int_0^{z_{max}} dz \frac{dV}{dz} \int_{M_{min}}^{M_{max}} dM \frac{dn(M, z)}{dM} |\tilde{y}_l(M, z)|^2, \quad (9.11)$$

where $g(\nu) = -\left(\frac{\nu}{56.78\text{GHz}} \frac{e^{\frac{\nu}{56.78\text{GHz}} + 1}}{e^{\frac{\nu}{56.78\text{GHz}} - 1}} - 4\right)$ is the analytical frequency dependence, $\frac{dn(M, z)}{dM}$ is the DM halo mass function, $\tilde{y}_l(M, z)$ is the projected 2D Fourier transform of the Compton parameter and $V(z)$ is the comoving volume. In Fig. 9.4 we show the behavior of the frequency dependence $g(\nu)$ and its square, we note how it changes behavior, from decreasing to increasing at 217 GHz where the effect vanishes ($g(\nu)|_{217\text{GHz}} = 0$). To have the convergence of the integral it is necessary to specify the integration bounds: $M_{max} = 5 \times 10^{15} h^{-1} M_\odot$, $M_{min} = 5 \times 10^{12} h^{-1} M_\odot$, $z_{max} \sim 10$, once specified it is demonstrated that the integral converge at all scales. There are two options for the choice of the halo mass function. The first is to assume a standard Press-Schechter function [193] (in alternative it is used also the Sheth and Tormen function [194]):

$$n(M)dM = \frac{\alpha \bar{\rho}}{\sqrt{2\pi}} \left(\frac{M}{M_*}\right)^{\alpha/2} \exp\left[-\frac{1}{2} \left(\frac{M}{M_*}\right)^\alpha\right] dM, \quad (9.12)$$

where $\bar{\rho}$ is the mean density of the cosmic matter, M_* is the non-linear mass scale ($\sim 10^{13}M_\odot$) and α is related to the dark matter power spectrum slope. The second possibility is to derive more accurately the halo mass function from large scale structure numerical simulations [158]. The results of the simulations are given as a function of the parameter M_δ which is the mass inside a radius which contains δ times the average matter density, with a typical choice of $\delta \sim (180 - 200)\Omega_m$. The mass function expressed with the virial mass is connected with the one from simulations through:

$$\frac{dn(M, z)}{dM} = \frac{dM_\delta}{dM} \frac{dn(M_\delta, z)}{dM_\delta}, \quad (9.13)$$

where the coefficient $\frac{dM_\delta}{dM}$ is given by numerical simulations. The mass function resulting from simulations is:

$$\frac{dn(M_\delta, z)}{dM_\delta} = \Omega_m|_0 \frac{\rho_c|_0}{M_\delta} \frac{d \log \sigma^{-1}}{dM_\delta} 0.301 e^{-|\log \sigma^{-1} + 0.64|^{3.82}}, \quad (9.14)$$

where $\sigma(M_\delta, z)$ is the variance of the mass distribution at the scale M_δ and redshift z and $\rho_c|_0 = 2.775 \times 10^{11} h^2 M_\odot \text{Mpc}^{-3}$.

The cluster gas physics is represented by the projection of the Compton parameter:

$$\tilde{y}_l(M, z) = \frac{4\pi r_s}{l_s^2} \int_0^\infty dx x^2 y_{3D}(x) \frac{\sin(l_x/l_s)}{l_x/l_s}, \quad (9.15)$$

where r_s is a scale radius, $x = r/r_s$ and $l_s = d_A/r_s$. The term $y_{3D}(x)$ is the three dimensional gas profile of the cluster and depends on the model assumed for the gas pressure profile. The pressure profile depends on the temperature and density profiles of the gas:

$$P_{gas} \propto \rho_{gas}(x) T_{gas}(x) \frac{K_B}{m_p}. \quad (9.16)$$

The gas temperature is generally assumed to be isothermal and equal to the virial one. There are two different models for the gas density profile. The first is the β -profile:

$$\rho_{gas}(x) = \rho_{central} \left(1 + \left(\frac{x}{x_c} \right)^2 \right)^{-3\beta/2}, \quad (9.17)$$

where $x_c = r/r_c$. The second possibility is to assume hydrostatic equilibrium between gas and DM and a constant polytropic $P_{gas} = \rho_{gas}^\gamma$ [158]:

$$\rho_{gas}(x) = \rho_{gas|0} \left[1 - A \left(1 - \frac{\log(1+x)}{x} \right) \right]^{1/(1-\gamma)} \quad (9.18)$$

where A is a function of γ and the concentration.

Great part of the brighter clusters is removed with the application of masks in the maps but residuals due to unresolved clusters remain and must be considered in the data analysis. In particular the strong dependence of the TSZ from the cluster properties and the uncertainties on the knowledge about them is the reason why in a residual marginalization context the use of the physical model can introduce biases on the cosmological parameters. In the next chapter we will show that the best physical parametrization for the TSZ does not introduce biases.

Kinetic SZ effect

The Kinetic SZ effect (KSZ) is the Doppler effect caused by the motion of galaxy clusters along the line of sight [178]. If the electron bulk is not static with respect to the CMB, in the cluster reference frame the CMB appears anisotropic. The Comptonization of the electronic component in the gas and the CMB photons isotropizes the distribution. But the isotropization takes place only in the cluster reference frame, hence it creates a Planckian distortion of the CMB photons in the observer reference frame. The temperature anisotropies generated depend on the baryon velocity:

$$\frac{\Delta T}{T}(\vec{n}) = \frac{\sigma_T}{c} \int dr n_e(\vec{n}, r) v_{gas}(\vec{n}, r) \quad (9.19)$$

where \vec{n} is the photon propagation direction and v_{gas} is the baryon velocity. Since the KSZ depends on the component along the line of sight of the baryon velocity is a second order effect and is an order of magnitude lower than the TSZ. It is dominated by the correlation terms between halos and therefore it becomes important at very small scales.

We have made a brief review of the main small scale foreground and secondary anisotropy contributions to CMB anisotropy data. We have shown how the dominant ones for Planck frequencies, on small scales, are the point sources contribution, both Poissonian and clustering, and the TSZ effect. In the next chapters we will show the simple parametrizations we derived for these residuals and their marginalization for cosmological parameters.

Chapter 10

Multifrequency Approach to Small Scale Residual Marginalization

Small scale foreground and secondary anisotropy residuals have an important impact on CMB anisotropies on small angular scales and may induce bias in the estimate of cosmological parameters. Therefore, it is necessary to properly take into account the contribution of such residuals and try to minimize it. Our approach consists in minimizing their impact on cosmological parameters modelling their contributions on the angular power spectrum and marginalizing over them. In the following part of the work we will present a multifrequency approach to the marginalization on foreground and secondary anisotropy residuals that we elaborated in the perspective of the *Planck* satellite mission.

10.1 Basic concepts

Our approach aims in taking the maximum advantage from the *Planck* frequency coverage and angular resolution for the marginalization over residuals. The frequencies we considered are: 70, 100, 143, 217, 353 GHz but our

technique can be easily extended to other frequencies. Since we are interested in small scale residuals, we can use the maps at these frequency channels with conservative masks for the galaxy and the point sources (including clusters). From cutted single frequency maps we can derive single frequency angular power spectra. The single frequency spectra can be combined, with different methods that will be explained later, to obtain a single power spectrum that can be used for the extraction of cosmological parameters.

Once defined the method to build the datasets from single frequency data the second step is the parametrization of foreground and secondary anisotropy residuals.

The conservative approach, which is the one typically applied, is a blind approach which does not assume almost any a priori knowledge on residual contributions and where are applied the most general as possible parametrizations for each signal. The typical conservative approach considers for each frequency a different set of parameters to characterize the residuals [196, 197]. For example we would have a different amplitude for each frequency for the point source poissonian contribution, a different amplitude for the SZ effect and for the clustering of infrared sources. The most general parametrizations consider also different shapes for each frequency for non-trivial contributions like the SZ effect and the clustering term. Therefore, in the conservative approach at the end we have to marginalize over a number of parameters which scales as the number of frequencies used multiplied for the number of the parameters which characterize each residual signal. If for example we consider a combination of all the cosmological *Planck* channels, even considering the minimal model for foreground and secondary anisotropy residuals which is a Poissonian term for each frequency, a clustering term for the 217, 353 GHz and the thermal SZ effect (which is null for the 217 GHz) we will have a total of 5 Poissonian amplitudes, 2 clustering amplitudes, 2 clustering shapes, 4 SZ amplitudes, 4 SZ shapes, for a total of 17 parameters only for the residual marginalization. Therefore the blind approach can be easily used for combi-

nations of few frequencies but for a high number of frequencies the increasing number of marginalization parameters complicate the situation and can create slow convergence issues. A similar approach has been developed in [197] including auto and cross spectra of 70, 100, 143, 217 GHz.

Since we are interested in using all the available frequencies we developed an approach which can be considered complementary to the conservative one. Instead of not assuming any knowledge on foreground and secondary anisotropy residuals, we chose to use all the possible theoretical and observational information available. In particular, instead of generic parametrizations, we employed hybrid parametrizations approach which consider both theoretical/empirical models and data and uses the frequency dependence of the foregrounds. An important point is that we parametrize also the frequency dependences of the residual contributions in addition to their amplitudes and angular power spectra. The parametrization of the frequency dependence allows an important decrease of the number of parameters for the marginalization. With the use of the information available on the residuals we created suitable parametrizations which can be considered as theoretical predictions of the signal expected at the considered frequencies. In our approach the minimum number of marginalization parameters can be considered as the amplitudes for each contribution. These minimal marginalization parameters represent in amplitude the deviation from the expected values. The entire method we will present is optimized for *Planck* data. In particular we considered only the three dominant foreground and secondary anisotropy residual contributions which for the frequency considered and the multipole range reachable by *Planck*, $\ell_{max} \sim 2500$, are represented by: thermal SZ effect, point source residuals deriving from Poissonian and clustering terms.

10.2 Foreground and secondary anisotropy residuals parametrizations

In the following we will present in details the parametrizations we have derived for each contribution.

10.2.1 Unresolved thermal Sunyaev Zeldovich effect

The thermal SZ effect can be parametrized in three different ways [199]. The first is to consider directly the full physical model for the power spectrum [172]:

$$C_l^{SZ}(\nu) = G(x) \int_0^{z_{max}} \frac{dV(z)}{dz} \int_{M_{min}}^{M_{max}} \frac{dN(M, z)}{dM} (\hat{y}(z, M))^2 dM \quad (10.1)$$

where again $x = \frac{\nu}{56.78GHz}$ and $G(x) = -\left(x \frac{e^x+1}{e^x-1} - 4\right)$. The second parametrization is derived by [158]:

$$C_l^{SZ}(\nu) = G(x) \sigma_8^7 \Omega_b^2 h^2 \hat{C}_l \quad (10.2)$$

where \hat{C}_l is a spectral shape template. We note that this parametrization has a strong dependence on the σ_8 . The third parametrization is a simple semi-blind approach which consider a template for the spectral shape and a variable amplitude:

$$C_l^{SZ} = A_{SZ} \hat{C}_l. \quad (10.3)$$

In [198] is shown that the parametrization which best represents the TSZ contribution and at the same time introduces the minor bias on cosmological parameters is given by the second one, the one by [158]. The third parametrization is extremely generic and is not the best representative for the TSZ signal, the first one is strongly dependent on the cluster physics. Cluster physics still includes a lot of uncertainties and in [198] it is shown how these uncertainties may strongly bias cosmological parameters. Therefore a parametrization of this kind is too dangerous for the present status

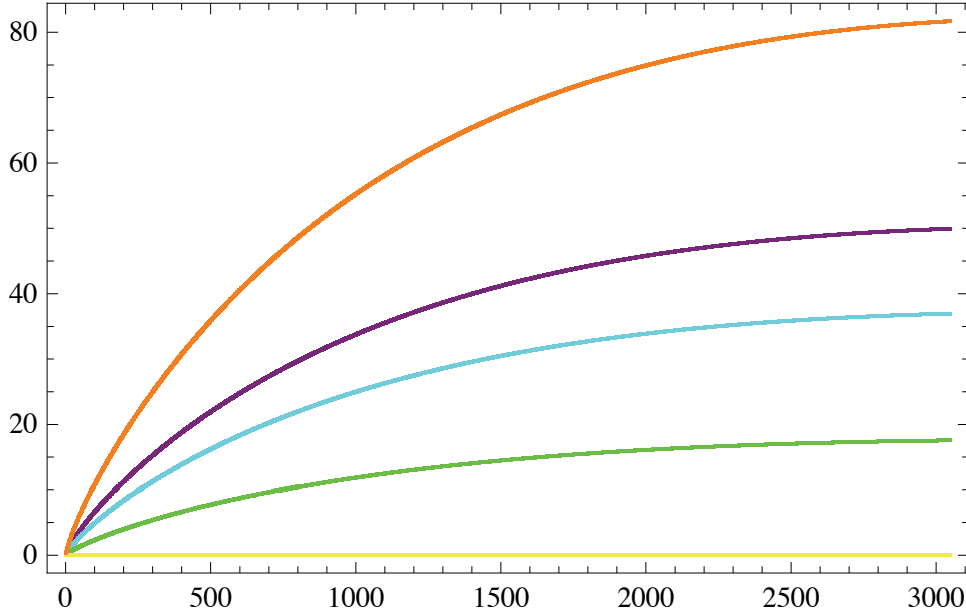


Figure 10.1: SZ effect angular power spectra for the frequency channels considered. Colors: Purple 70 GHz, Cyan 100 GHz, Green 143 GHz, Yellow 217 GHz, orange 353 GHz

of cluster physics knowledge. According to this results we chose to use the intermediate parametrization:

$$C_l^{SZ}(\nu) = A_{SZ}G(x)\sigma_8^7\Omega_b^2h^2\hat{C}_l \quad (10.4)$$

where A_{SZ} accounts for the possible deviations of the real signal from this approximation. For the TSZ effect the extrapolation of the frequency dependence is trivial since it is given by the analytical function $G(x)$. In Fig. 10.1 we show the TSZ spectra computed with this parametrization for all frequencies we are interested in. Let us end this section noticing that the WMAP Science Team has always marginalized on TSZ residuals by using the third option. It is not clear why the WMAP Science Team has decided to marginalize only on the TSZ contribution at frequencies lower than 100 GHz.

10.2.2 Unresolved point sources

We considered both the Poissonian and the clustering contribution for residual point sources. While Poissonian term has to be considered for every frequency the clustering term is negligible for the lowest ones where the dominant point source contribution is given by radio sources. At the selected *Planck* frequencies we considered the following contributions from point sources:

- 70 GHz → Poisson
- 100 GHz → Poisson + IR Clustering
- 143 GHz → Poisson + IR Clustering
- 217 GHz → Poisson + IR Clustering
- 353 GHz → Poisson + IR Clustering.

Poissonian contribution

The Poissonian contribution, as previously shown, is characterized by a flat spectrum whose amplitude is given by:

$$C_l^{PSP} = \int_0^{S_{max}} S^2 \frac{dN(S)}{dS} dS, \quad (10.5)$$

where S_{max} is the detection threshold flux, which depends on the instrument properties on the global sky confusion noise at fluctuation level and the algorithm used to extract the point sources from the maps, and $\frac{dN(S)}{dS}$ are the differential number counts (the conversion function from Jy^2/sr to μK^2 is $c^4(e^x - 1)^4 / (4K^2\nu^4 x^4 e^{2x})$ with $x = \frac{h\nu}{KT_0}$).

The flat spectral shape of the Poissonian contribution needs only a very simple parametrization in terms of a simple amplitude. The structure of the Poissonian term makes impossible to extrapolate a frequency dependence. The origin of this relies on the dependence of the spectrum on the detection threshold flux S_{max} , which is not an astrophysical parameter. It is not possible to derive an analytical function for the frequency dependence of

the signal, but the detection threshold is known. Therefore, we were able to compute the expected Poissonian contribution value for each frequency. In particular, to compute this value is necessary to have a representative function for the number counts. We empirically fitted the number counts predicted by the model of [162, 163] at each frequency. Each fit is composed by the weighted sum of three different components which represent the number counts for low, intermediate, and high fluxes. The first step to create the fits has been the empirical study of the functional dependence of the number counts on the flux, then for each fit we have tuned the exponents and the coefficients for each of the three curves. The final step has been to manually tune the coefficients of the sum of the three pieces for each frequency. In the following we present the results for each frequency. Note that our fit is limited at fluxes below 1Jy which is a value higher than any of the *Planck* detection thresholds and is particularly accurate for the sources with higher fluxes which dominate the Poissonian term. The differential number counts are normalized to the Euclidean ones ($\frac{dN(S)}{dS} \propto S^{-2.5}$).

70 GHz

$$\begin{aligned}
 F_{70}^{Low} &= S^{-2.5} \frac{dN(S)}{dS} \Big|_{70LOW} = \frac{8.05838 S^{0.45}}{(1 + 10^{14} S^{2.5})} \\
 F_{70}^{Med} &= S^{-2.5} \frac{dN(S)}{dS} \Big|_{70MED} = \frac{306.984 S^{0.75}}{(1 + 20408 S^2)} \\
 F_{70}^{HIGH} &= S^{-2.5} \frac{dN(S)}{dS} \Big|_{70HIGH} = \frac{55.9996 S^{0.72}}{(1 + 0.683569 S^{1.45})} \\
 S^{-2.5} \frac{dN(S)}{dS} \Big|_{70TOT} &= \frac{F_{70}^{Low}}{4.4} + \frac{F_{70}^{Med}}{2.3} + \frac{F_{70}^{HIGH}}{1.03}
 \end{aligned} \tag{10.6}$$

100 GHz

$$\begin{aligned}
 F_{100}^{Low} &= S^{-2.5} \frac{dN(S)}{dS} \Big|_{100LOW} = \frac{7.75538S^{0.45}}{(1 + 10^{14}S^{2.5})} \\
 F_{100}^{Med} &= S^{-2.5} \frac{dN(S)}{dS} \Big|_{100MED} = \frac{224.988S^{0.74}}{(1 + 40000S^2)} \\
 F_{100}^{HIGH} &= S^{-2.5} \frac{dN(S)}{dS} \Big|_{100HIGH} = \frac{55.6811S^{0.74}}{(1 + 0.767692S^{1.45})} \\
 S^{-2.5} \frac{dN(S)}{dS} \Big|_{100TOT} &= \frac{F_{100}^{Low}}{4.9} + \frac{F_{100}^{Med}}{2.5} + \frac{F_{100}^{HIGH}}{1.03} \tag{10.7}
 \end{aligned}$$

143 GHz

$$\begin{aligned}
 F_{143}^{Low} &= S^{-2.5} \frac{dN(S)}{dS} \Big|_{143LOW} = \frac{7.4763S^{0.45}}{(1 + 10^{14}S^{2.5})} \\
 F_{143}^{Med} &= S^{-2.5} \frac{dN(S)}{dS} \Big|_{143MED} = \frac{241.081S^{0.75}}{(1 + 111111S^2)} \\
 F_{143}^{HIGH} &= S^{-2.5} \frac{dN(S)}{dS} \Big|_{143HIGH} = \frac{55.9236S^{0.76}}{(1 + 0.870925S^{1.45})} \\
 S^{-2.5} \frac{dN(S)}{dS} \Big|_{143TOT} &= \frac{F_{143}^{Low}}{4.2} + \frac{F_{143}^{Med}}{2.7} + \frac{F_{143}^{HIGH}}{1.03} \tag{10.8}
 \end{aligned}$$

217 GHz

$$\begin{aligned}
 F_{217}^{Low} &= S^{-2.5} \frac{dN(S)}{dS} \Big|_{217LOW} = \frac{7.1636S^{0.45}}{(1 + 10^{14}S^{2.5})} \\
 F_{217}^{Med} &= S^{-2.5} \frac{dN(S)}{dS} \Big|_{217MED} = \frac{203.688S^{0.73}}{(1 + 308642S^2)} \\
 F_{217}^{HIGH} &= S^{-2.5} \frac{dN(S)}{dS} \Big|_{217HIGH} = \frac{52.8062S^{0.75}}{(1 + 0.869266S^{1.47})} \\
 S^{-2.5} \frac{dN(S)}{dS} \Big|_{217TOT} &= \frac{F_{217}^{Low}}{4.2} + \frac{F_{217}^{Med}}{3.2} + \frac{F_{217}^{HIGH}}{1.03} \tag{10.9}
 \end{aligned}$$

353 GHz

$$\begin{aligned}
 F_{353}^{Low} &= S^{-2.5} \frac{dN(S)}{dS} \Big|_{353LOW} = \frac{6.81276 S^{0.45}}{(1 + 10^{14} S^{2.5})} \\
 F_{353}^{Med} &= S^{-2.5} \frac{dN(S)}{dS} \Big|_{353MED} = \frac{165.845 S^{0.7}}{(1 + 501187 S^{1.9})} \\
 F_{353}^{HIGH} &= S^{-2.5} \frac{dN(S)}{dS} \Big|_{353HIGH} = \frac{51.1698 S^{0.75}}{(1 + 0.929429 S^{1.5})} \\
 S^{-2.5} \frac{dN(S)}{dS} \Big|_{353TOT} &= \frac{F_{353}^{Low}}{4.5} + \frac{F_{353}^{Med}}{3.8} + \frac{F_{353}^{HIGH}}{1.03} \quad (10.10)
 \end{aligned}$$

In Fig. 10.2 we show the comparison between the fits and the real number counts while in Fig. 10.3 we show a zoom of the most interesting region just below the flux threshold. The resulting power spectra are:

$$\begin{aligned}
 C_{170\text{ GHz}}^{PSP} &= 1.9784 S_{max}^{0.95} 2F1[0.339286, 1, 1.33929, -10^{14} S_{max}^{2.5}] + \\
 &\quad 104.262 S_{max}^{1.25} 2F1[0.64, 1., 1.64, -20408.2 S_{max}^2] + \\
 &\quad 44.5644 S_{max}^{1.22} 2F1[0.841379, 1., 1.84138, -0.683569 S_{max}^{1.45}] \\
 C_{100\text{ GHz}}^{PSP} &= 1.66603 S_{max}^{0.95} 2F1[0.339286, 1, 1.33929, -10^{14} S_{max}^{2.5}] + \\
 &\quad 72.5767 S_{max}^{1.24} 2F1[0.62, 1., 1.62, -400000 S_{max}^2] + \\
 &\quad 43.5962 S_{max}^{1.24} 2F1[0.855173, 1., 1.85517, -0.767692 S_{max}^{1.45}]
 \end{aligned}$$

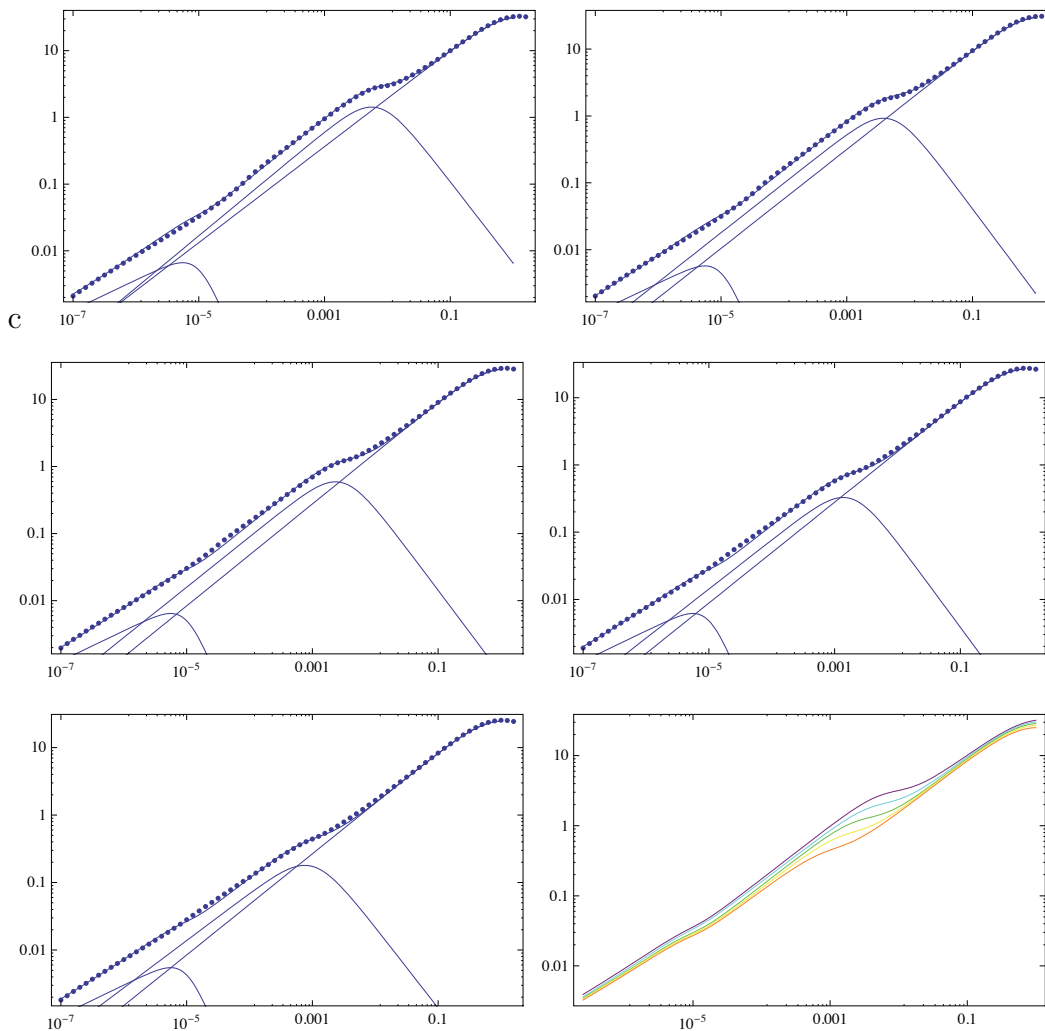


Figure 10.2: Comparison of the De Zotti et al. model (dotted line) with our fit (black solid line) where the three lower curves represent the three contributions. From top left to right: 70 GHz, 100 GHz, 143 GHz, 217 GHz, 353 GHz. Bottom right is the comparison of the fits for the different frequencies: 70 GHz is purple, 100 GHz is cyan, 143 GHz is green, 217 GHz is yellow, 353 GHz is orange.

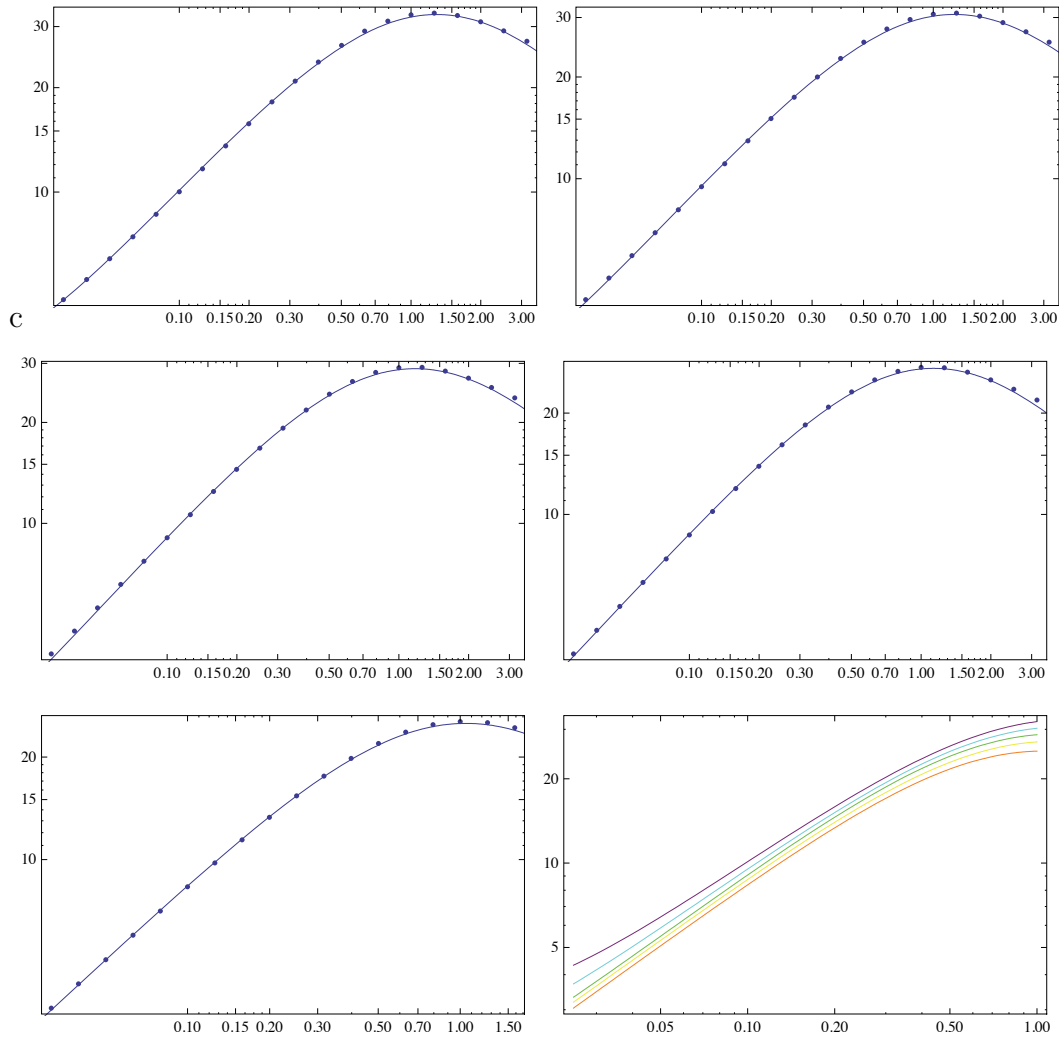


Figure 10.3: Comparison of the De Zotti et al. model (dotted line) with our fit (black solid line) where the three lower curves represent the three contributions. From top left to right: 70 GHz, 100 GHz, 143 GHz, 217 GHz, 353 GHz. Bottom right is a focus on the comparison of the fits for the different frequencies: 70 GHz is purple, 100 GHz is cyan, 143 GHz is green, 217 GHz is yellow, 353GHz is orange.

Channels	$S_{max}(J_y)$	$C_l^{PSP}(\mu K^2)$
70	0.57	1.14873×10^{-3}
100	0.41	2.35549×10^{-4}
143	0.32	6.69299×10^{-5}
217	0.24	2.83675×10^{-5}
353	0.28	8.72182×10^{-5}

Table 10.1: Amplitude for the Poissonian terms.

$$\begin{aligned}
 C_{l143\text{ GHz}}^{PSP} &= 1.87376 S_{max}^{0.95} 2F1[0.339286, 1, 1.33929, -10^{14} S_{max}^{2.5}] + \\
 &\quad 71.4315 S_{max}^{1.25} 2F1[0.625, 1., 1.625, -111111 S_{max}^2] + \\
 &\quad 43.09 S_{max}^{1.26} 2F1[0.868966, 1., 1.86897, -0.870925 S_{max}^{1.45}] \\
 C_{l217\text{ GHz}}^{PSP} &= 1.79539 S_{max}^{0.95} 2F1[0.339286, 1, 1.33929, -10^{14} S_{max}^{2.5}] + \\
 &\quad 51.7501 S_{max}^{1.23} 2F1[0.615, 1., 1.615, -309642 S_{max}^2] + \\
 &\quad 41.0145 S_{max}^{1.25} 2F1[0.85034, 1., 1.85034, -0.869266 S_{max}^{1.47}] \\
 C_{l353\text{ GHz}}^{PSP} &= 1.59363 S_{max}^{0.95} 2F1[0.339286, 1, 1.33929, -10^{14} S_{max}^{2.5}] + \\
 &\quad 36.3695 S_{max}^{1.25} 2F1[0.631579, 1., 1.63158, -501187 S_{max}^{1.9}] + \\
 &\quad 39.7435 S_{max}^{1.25} 2F1[0.833333, 1., 1.833333, -0.929429 S_{max}^{1.47}]
 \end{aligned} \tag{10.11}$$

where $2F1$ are the *Hypergeometric* functions of second type [47]. In Fig. 10.4 we show the results for the Poissonian angular power spectra at the *Planck* frequencies. In Table 10.1 we report the values we obtained for the poissonian contribution for each channel.

Clustering of IR galaxies

The complexity of the clustering term for infrared galaxies shown in the previous chapter makes impossible to create a simple parametrization based only on the physical model. Since our purpose was to create the easier physical based parametrizations to characterize the residuals we chose to use an empirical approach. In particular we decided to rely on the empirical simula-

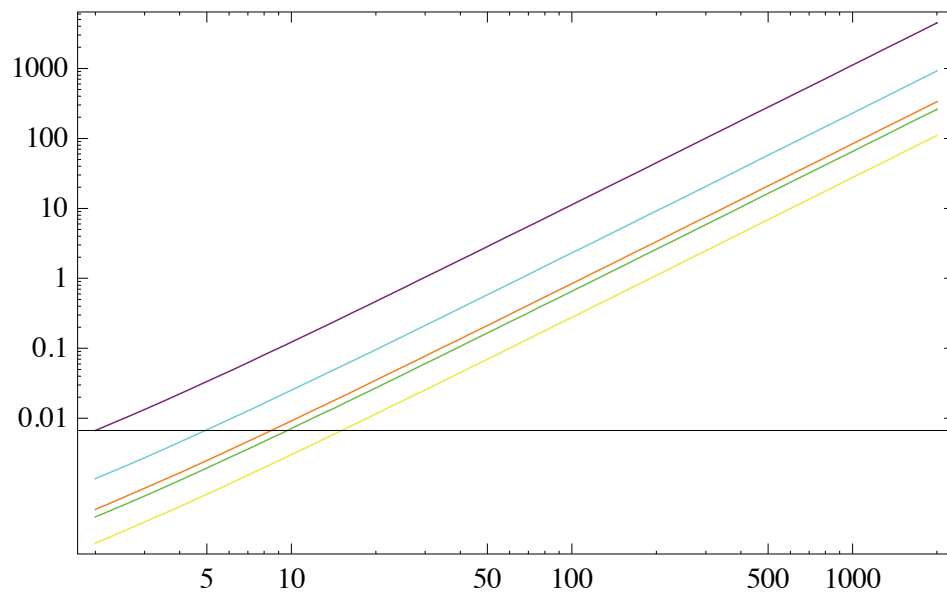


Figure 10.4: Power spectrum of Poissonian contribution ($\ell(\ell + 1)C_l/(2\pi)$ in μK^2) for the different frequencies: 70 GHz is purple, 100 GHz is cyan, 143 GHz is green, 217 GHz is yellow, 353 GHz is orange.

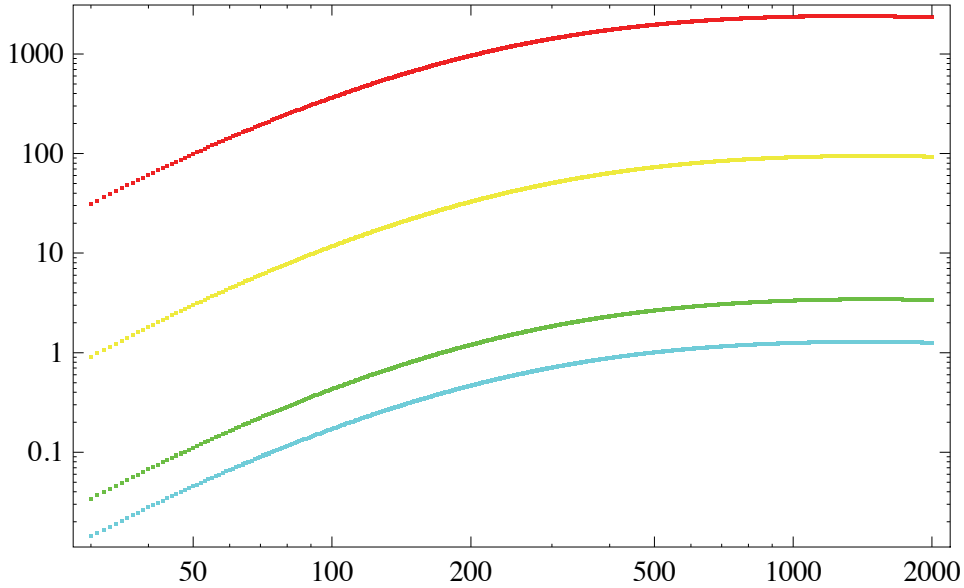


Figure 10.5: Infrared sources clustering spectra $(\ell(\ell + 1)C_l)/(2\pi)$ in μK^2 for the various frequency channels. Colors: Cyan 100 GHz, Green 143 GHz, Yellow 217 GHz, Red 353 GHz.

tions done by Lagache and collaborators of the Cosmic Infrared Background (CIB) which are based on the theoretical model [167, 168] and use the results of large scale structure simulations [169, 170]. In Fig. 10.6 we show the results of the empirical simulations of the clustering of the CIB for the *Planck* frequencies affected by this contribution. We chose to fit these results in order to obtain the best empirical parametrization. To derive the fit we proceeded by steps. The first step has been to find the a very good function of ℓ which could represent the clustering behaviour:

$$\frac{C_l^{\text{clustering}}}{2\pi} \propto \beta \frac{\log(l)^\alpha}{(190 + l)^{2.7}}. \quad (10.12)$$

The second step has been to find the coefficient β and exponent α which best fitted the real spectrum for each frequency. The final step has been to interpolate the results for the coefficient and the exponent in order to obtain a general frequency dependent fit for the CIB clustering. The resulting fit is

10.2 Foreground and secondary anisotropy residuals parametrization

accurate at least at the 2% level in all ℓ range, and at the 1% in great part, around 90%, of the range. It is given by:

$$\begin{aligned} \frac{C_l^{clustering}}{2\pi} &= \beta(\nu) \frac{\log(l)^{\alpha(\nu)}}{(190+l)^{2.7}} \\ \beta(\nu) &= -926.457 + 20.3332 \left(\frac{\nu}{\text{GHz}}\right) - 0.142687 \left(\frac{\nu}{\text{GHz}}\right)^2 + 0.000320917835 \left(\frac{\nu}{\text{GHz}}\right)^3 \\ \alpha(\nu) &= 2.09520083 + 0.011893432 \left(\frac{\nu}{\text{GHz}}\right) - 4.086 \times 10^{-5} \left(\frac{\nu}{\text{GHz}}\right)^2 \\ &\quad + 3.40535 \times 10^{-8} \left(\frac{\nu}{\text{GHz}}\right)^3, \end{aligned} \quad (10.13)$$

where the frequency is expressed in units of GHz. The fit of Eq. 10.13 is optimized for the frequency range 100 – 353 GHz. We realized also a more complex version of the fit which instead is optimized for highest frequency channels, up to 857 GHz:

$$\begin{aligned} \frac{C_l^{clusteringEx}}{2\pi} &= \beta_H(\nu) \frac{\log(l)^{\alpha_H(\nu)}}{(190+l)^{2.7}} \\ \beta_H(\nu) &= -1.34984 \times 10^8 + 3.38661 \times 10^6 \left(\frac{\nu}{\text{GHz}}\right) - 30137.2 \left(\frac{\nu}{\text{GHz}}\right)^2 \\ &\quad + 11.548 \left(\frac{\nu}{\text{GHz}}\right)^3 - 0.127558 \left(\frac{\nu}{\text{GHz}}\right)^4 - 1.36455 \times 10^{-4} \left(\frac{\nu}{\text{GHz}}\right)^5 \\ &\quad + 2.67097 \times 10^{-7} \left(\frac{\nu}{\text{GHz}}\right)^6 \\ \alpha_H(\nu) &= 2.18962 + 0.00946075 \left(\frac{\nu}{\text{GHz}}\right) - 0.0000180152 \left(\frac{\nu}{\text{GHz}}\right)^2 \\ &\quad - 6.23404 \times 10^{-8} \left(\frac{\nu}{\text{GHz}}\right)^3 + 1.7946 \times 10^{-10} \left(\frac{\nu}{\text{GHz}}\right)^4 \\ &\quad - 1.14717 \times 10^{-13} \left(\frac{\nu}{\text{GHz}}\right)^5 \end{aligned} \quad (10.14)$$

For simplicity we chose to use the lower frequency fit of Eq. 10.13. Therefore the parametrization of the clustering term is given by :

$$C_l^C = A_{PSIRC} C_l^{clustering}$$

where the amplitude, like for the SZ effect and the Poissonian terms, accounts for the deviations of the real signal from our empirical model.

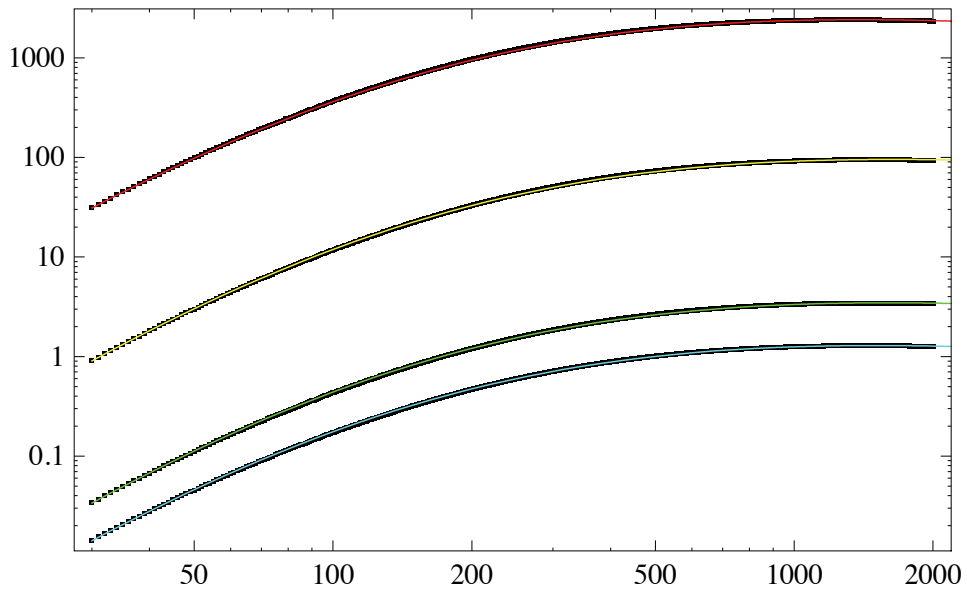


Figure 10.6: Infrared sources clustering fitted spectra (solid) compared with the simulation results (dotted) $(\ell(\ell + 1)C_l/(2\pi)$ in μK^2) for the various frequency channels. Colors: Cyan 100 GHz, Green 143 GHz, Yellow 217 GHz, Red 353 GHz.

10.3 CMB anistropies with foreground and secondary anisotropy residual contribution

We have shown how the residual signals have different impacts depending on the frequency channel. In Fig. 10.7 we show the comparison between the foreground residuals and the primary CMB for the five *Planck* frequencies of interest. In particular we note how, as anticipated, the higher frequency channels are completely dominated by the clustering term, whereas the lower ones are dominated by the Poissonian term. We note also that at small scales the TSZ remains subdominant with respect to the other residuals. In Fig. 10.8 we show the comparison between the sum of all foreground residual contributions with the primary CMB for all the frequencies. We note how the 353 GHz channel is the most contaminated due to the clustering contribution, while the cleanest channel is the 143 GHz thanks to the low contribution of both clustering and Poissonian term.

10.4 Frequency channel combination

We have derived the parametrizations for the foreground and secondary anisotropy residuals, now we need the combination of the angular power spectra of different frequency channels in a single power spectrum that can be used for the estimate of cosmological parameters. The combination is done with a weighted linear sum of single frequency power spectra:

$$C_l^{TOT} = \sum_i w_i(\ell) C_l^i$$

where the index i spans over the frequency. The optimal method, in noise dominated regimes, to combine channels is the inverse noise variance weighting scheme [196]. This weighting scheme is based on the instrumental properties of the frequency channels, it gives the larger weights to the channels with higher resolutions and lower noise levels. The noise is modelled as an

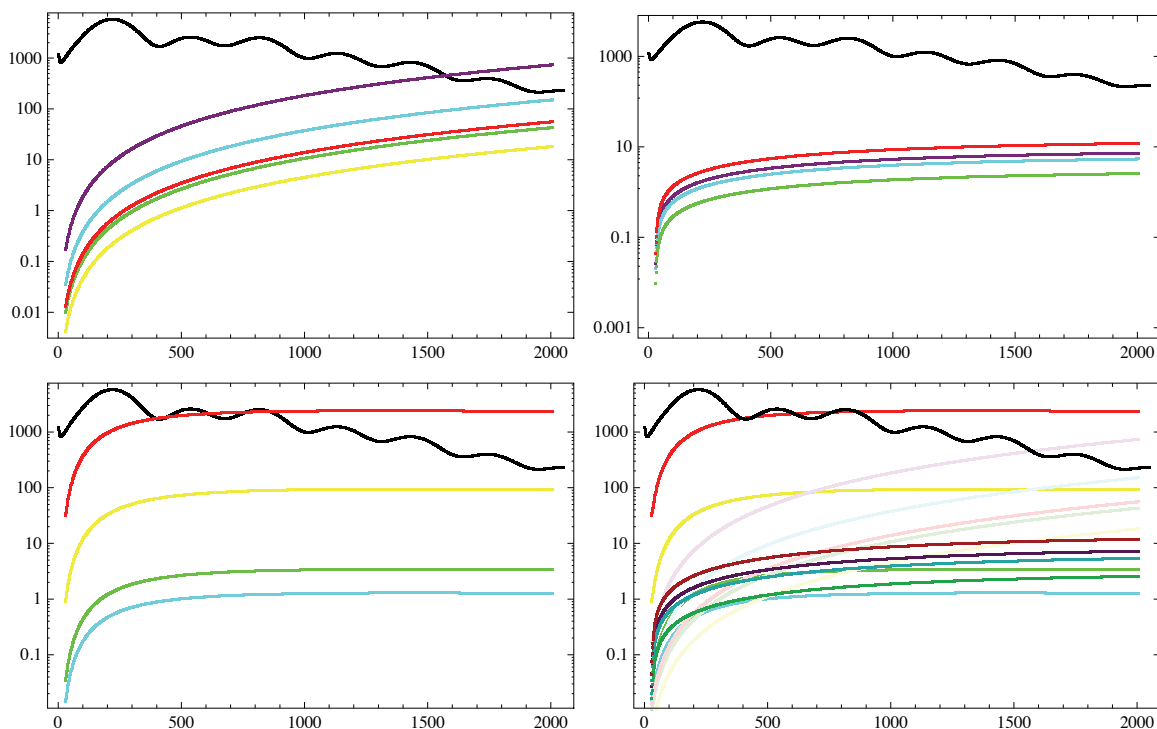


Figure 10.7: Comparison of the foreground and secondary anisotropy residuals with primary CMB for the different frequencies. The lines are: primary CMB (black), 70 GHz (purple), 100 GHz (cyan), 143 GHz (green), 217 GHz (yellow), 353 GHz (red). The upper left panel is the comparison of Poissonian term with CMB. The upper right panel is the comparison between SZ term and primary CMB. Lower left panel is the comparison of the clustering term with primary CMB. The lower right panel is the comparison of all residuals (lighter colors are the Poissonian term, darker ones the SZ term, the normal are the clustering term).

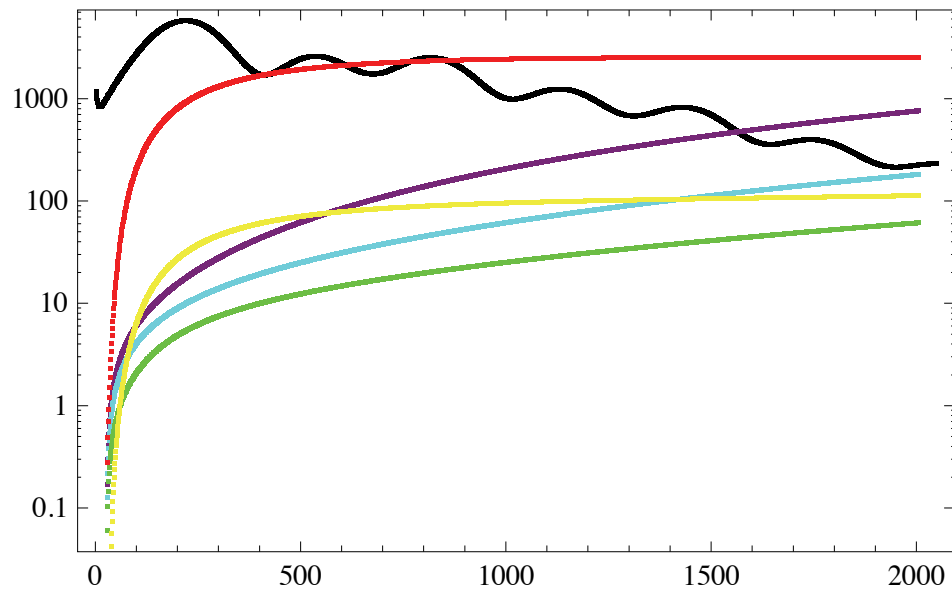


Figure 10.8: Comparison of the sum of all foreground and secondary anisotropy residuals with primary CMB for the different frequencies. The lines are: primary CMB (black), 70 GHz (purple), 100 GHz (cyan), 143 GHz (green), 217 GHz (yellow), 353 GHz (red).

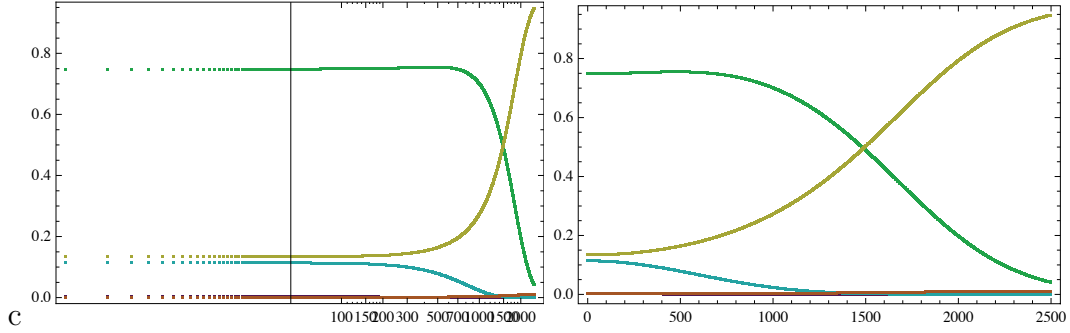


Figure 10.9: Inverse noise variance weights on large scales (left panel) and small scales (right panel): purple 70 GHz, dark cyan 100 GHz, dark green 143 GHz, dark yellow 217 GHz, dark orange 353 GHz.

isotropic Gaussian white noise with variance σ_N^2 on the total integration time. We start defining the beam function:

$$b_l^2 = e^{-\ell(\ell+1)(0.425 FWHM/60 \pi/180)^2}; \quad (10.15)$$

where $FWHM$ is the full width half maximum of the channel in arcminutes. We can define the noise function as:

$$N_l = \frac{(\sigma_N)^2 \Omega_{pix}}{b_l^2}, \quad (10.16)$$

where Ω_{pix} is the area corresponding to the pixel. With these definitions the weights for the single frequency spectrum is given by:

$$w_i(l) = \frac{\frac{1}{N_{l_i}^2}}{\sum_j \frac{1}{N_{l_j}^2}}, \quad (10.17)$$

where i stands for the specific channel while j runs over all channels. In Fig. 10.9 we show the weights for the *Planck* channels obtained using the inverse noise variance scheme. We note how the dominant contribution is given by the two channels at 143GHz and 217GHz which have higher resolution and lower noise level. In particular on small scales we have that the 217GHz is the dominant one due to the highest *Planck* angular resolution of 5'. The inverse noise variance weighting scheme is the optimal weighting for noise dominated

regimes which are typical of high multipoles region where the noise and the beam smearing start to dominate.

However *Planck* has been designed to be limited in probing the CMB primary anisotropy pattern in intensity by the ability in subtracting foreground contamination rather than instrumental noise. Therefore, there might be alternatives to the inverse noise variance weighting scheme. In particular, adopting the inverse noise variance weighting scheme, we showed how of the wide frequency coverage of *Planck* only two channels contribute on small scales. In fact, inverse noise variance scheme does not take into account the sky properties at the different frequencies. Weighting the channels only on the base of the instrumental properties, this scheme does not consider the information about which are the channels less affected by foreground and secondary anisotropy residuals and therefore more convenient to observe the CMB.

At the map level the multifrequency observations are applied to the foreground removal with the component separation, which improves with the number of frequencies observed. We tried to apply the same approach also at the power spectrum level on small scales. We created an alternative completely empirical weighting scheme: the inverse noise plus foreground weighting. The basic idea is the same as the inverse noise variance one but, instead of considering only instrumental noise to weight the channels, it considers also the foreground and secondary anisotropy residual contamination. Whereas inverse noise variance weighting considers the foreground and secondary anisotropy residuals as signal like the CMB, our method considers the predicted residuals also as noise. When the foreground and secondary anisotropy residual contributions become part of the noise, more the channel is contaminated less it weights. The major issue related to this approach is represented by the fact that foreground and secondary anisotropy residual signals are not known fixed quantities, like noise levels and beams, but are variables. To solve this issue as first approximation we used the nominal pre-

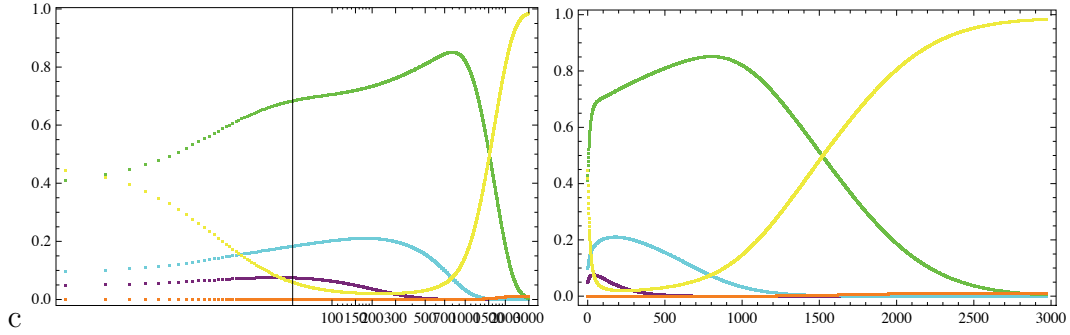


Figure 10.10: Noise plus foreground weights on large scales (left panel) and small scales (right panel): blue 70 GHz, cyan 100 GHz, green 143 GHz, yellow 217 GHz, orange 353 GHz.

dicted foregrounds (all amplitudes equal 1). Since we chose to adopt physical based parametrizations which want to best represent the real expected signal, the predicted ones are a good approximation to what we expect to be the real weights. Since we want to account the foreground contribution as noise we sum the expected signal to the noise convolved with the beam:

$$N_l^2 = \left(\frac{(\sigma_N)^2 \Omega_{pix}}{b_l^2} \right)^2 + (C_l^{FG})^2. \quad (10.18)$$

The structure of the weight remains unchanged:

$$w_i(l) = \frac{\frac{1}{N_{l_i}^2}}{\sum_j \frac{1}{N_{l_j}^2}}. \quad (10.19)$$

In Fig. 10.10 we show the weights obtained with our scheme. In Fig. 10.11 we show the comparison between standard inverse noise weights and our weights. In the following chapter we will show the results obtained for cosmological parameters with both weighting schemes.

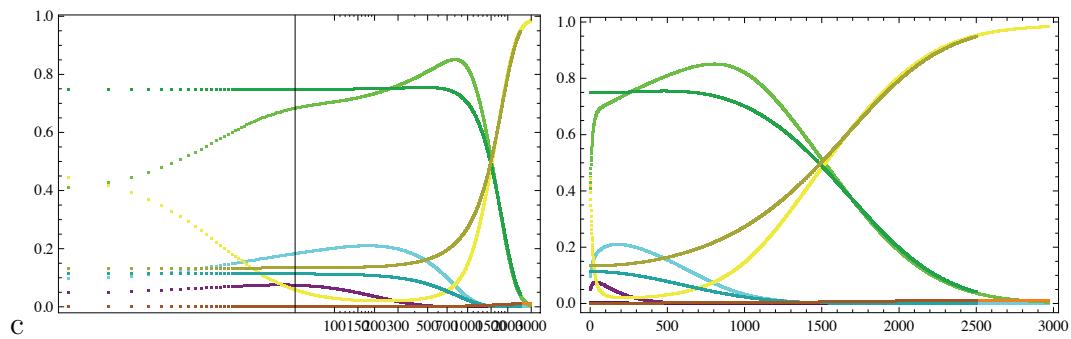


Figure 10.11: Noise plus foreground weights in lighter colors and inverse noise variance weights in darker colors lines on large scales (left panel) and small scales (right panel): purple and dark purple 70 GHz, cyan and dark cyan 100 GHz, green and dark green 143 GHz, yellow and dark yellow 217 GHz, orange and dark orange 353 GHz.

Chapter 11

Cosmological Parameters with Small Scale Foreground and Secondary Anisotropy Residual Marginalization

We developed an extension of the public CosmoMC code which includes the marginalization over foreground and secondary anisotropy residuals, computed in previous chapter. In particular we have considered the contribution of a Poissonian term, a clustering term and the term of TSZ. We marginalize over the minimal three parameters for the residuals: A_{SZ} , A_{PSP} , A_{PSIRC} . Our CosmoMC code is connected to a modified version of CAMB, that we have implemented. This modified CAMB code computes the standard CMB angular power spectra and for each frequency channel sums it with the foreground and secondary anisotropy residual contribution (i.e. from un-subtracted sources) predicted with our models. The CMB plus foregrounds power spectra at the different frequencies are combined in a single effective power spectrum in the CosmoMC code. We implemented two different versions of CosmoMC: one combines the single frequency power spectra using the inverse noise variance weighting, whereas the other version uses the em-

pirical frequency combination technique that we have developed to account for foreground contribution, illustrated in the previous chapter.

To test the codes we have used *Planck* simulated data. We simulated data for all the 5 frequencies, where the simulated signal includes the standard CMB and the predicted foreground and secondary anisotropy residual contaminations. In particular, since our purpose is to test the capability of the code to estimate unbiased cosmological parameters, with the foreground and secondary anisotropy residual marginalization, we generated the simulated data with the same model of residuals that we use for the marginalization: $A_{SZ}|_{SimulatedData} = 1$, $A_{PSP}|_{SimulatedData} = 1$, $A_{PSIRC}|_{SimulatedData} = 1$. The 5 frequency simulated data are combined in a single dataset using the same combination scheme of the code: in one dataset we used the inverse noise variance weighting and in the other our empirical technique.

We performed different tests of the codes. In particular, we first investigated the impact of the foreground and secondary anisotropy residual marginalization on the cosmological parameters for the standard, six parameters, and different extended parameter spaces. For this analysis we chose to use the inverse noise variance weighting combination of the four central frequency *Planck* channels 70, 100, 143, 217 GHz. We then investigated two aspects of the frequency channel combination. The first is the study of which is the best frequency combination, which are the best channels and how many channels it is necessary to use to have the best estimate of cosmological parameters. The second aspect concerns the study of the combination technique: we compared the results of the code which implements the inverse noise variance weighting with the ones of the code which implements the empirical technique we have developed. We will show in the following the results of the different tests of the codes.

We vary the baryon density $\omega_b = \Omega_b h^2$, the cold dark matter density $\omega_c = \Omega_c h^2$ (with h being $H_0/100\text{km s}^{-1}\text{Mpc}^{-1}$), the reionisation optical

depth τ_{opt} , the ratio of the sound horizon to the angular diameter distance at decoupling θ , $\log(10^{10}A_S)$, n_S and, where not otherwise indicated, the three foreground and secondary anisotropy residual uncertainty parameters A_{SZ} , A_{PSP} , A_{PSIRC} . As priors we use the range $[0, 2]$, if not otherwise indicated, for all the parameters of the foreground and secondary anisotropy residuals. We assume a flat universe, a CMB temperature $T_{CMB} = 2.725$ K and we set the primordial Helium fraction to $y_{He} = 0.24$, three massless neutrinos and set the pivot scale of the primordial scalar to $k_* = 0.05$ Mpc $^{-1}$. We sample the posterior using the Metropolis-Hastings algorithm [119], generating four parallel chains and imposing a conservative Gelman-Rubin convergence criterion [120] of $R - 1 < 0.01$.

11.1 Cosmological parameters with small scale foreground and secondary anisotropy residuals

We performed an analysis of *Planck* simulated mock data with the inclusion of foreground and secondary anisotropy residuals. We generated the mock data assuming *Planck* nominal 14 month plus 1 year approved extension mission performances (table 3.1). We combined the central 4 frequencies 70, 100, 143, 217 GHz.

The input parameters of the cosmological model are reported in table 11.1.

In table 11.1 are reported the results of our MCMC analysis with simulated *Planck* data with foreground and secondary anisotropy residual marginalization. We note how the code perfectly recovers the input parameters for the cosmological model. The residual parameters are recovered but we note a big uncertainty for the Poissonian term, and in particular also for the TSZ parameter.

In Figs. 11.1 and 11.2 we show the bidimensional and triangle plots of

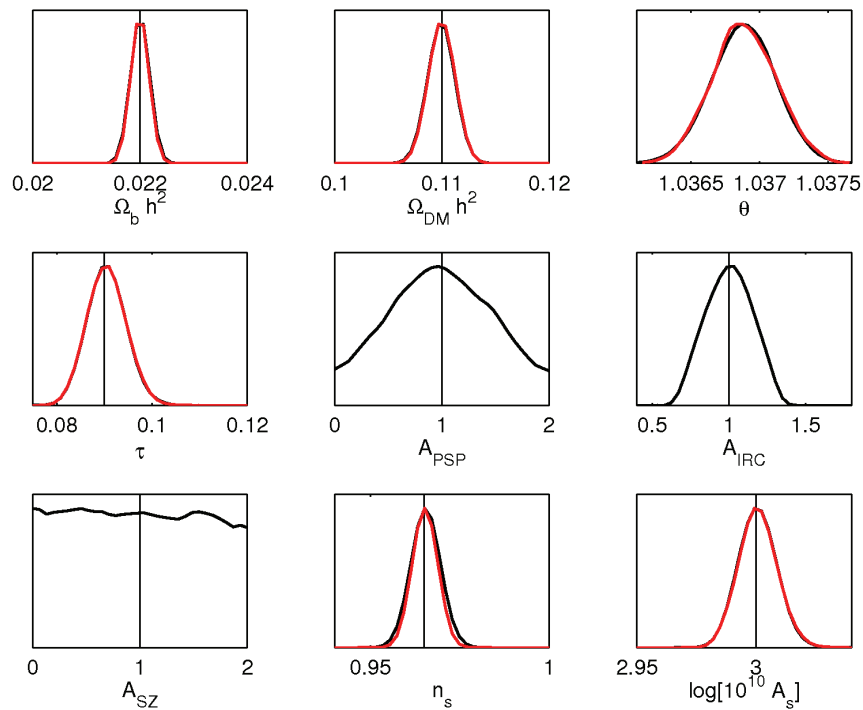


Figure 11.1: Results of the MCMC constrained with *Planck* simulated data with (black) and without (red) foreground and secondary anisotropy residual marginalization. Vertical bars are the input parameter.

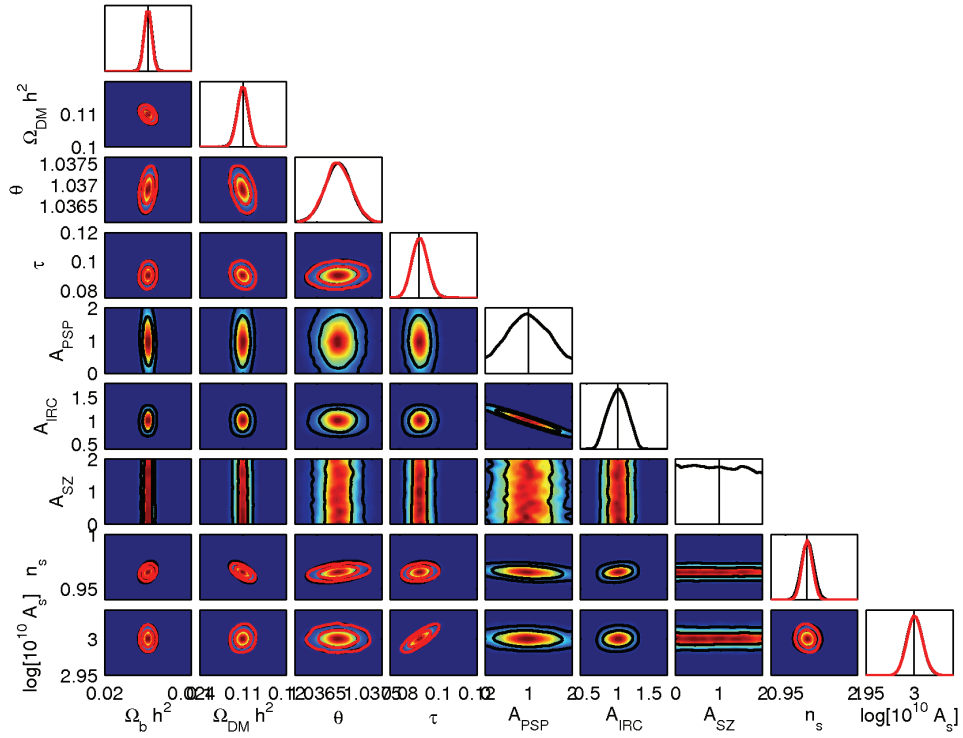


Figure 11.2: Results of the MCMC constrained with *Planck* simulated data with (black) and without (red) foreground and secondary anisotropy residual marginalization. Curves are the 68% and 95% confidence level, vertical bars are the input parameters.

Parameter	Mean	Input value
ω_b	0.022 ± 0.0002	0.022
ω_c	$0.11^{+0.002}_{-0.001}$	0.11
θ	1.037 ± 0.0004	1.038
τ_{opt}	0.09 ± 0.006	0.09
$\log [10^{10} A_S]$	3.0 ± 0.01	3.0
n_s	0.965 ± 0.006	0.965
A_{PSP}	$0.99^{+0.7}_{-0.9}$	1
A_{PSIRC}	1.0 ± 0.24	1
A_{SZ}	$0.98^{+1.02}_{-0.98}$	1

Table 11.1: Mean parameter values and bounds of the central 95%-credible intervals for *Planck* simulated data with foreground and secondary anisotropy residual marginalization, in the right column we show the input values for the cosmological model.

the comparison of the results of the MCMC with (black curve) and without (red curves) the foreground and secondary anisotropy residual marginalization. For both the MCMCs the input cosmological model is the same, table 11.1, but in the case without marginalization we have fixed the foreground residuals to the input models (all the amplitudes equal one) in the CosmoMC code. We note how the residual marginalization does not introduce biases in the cosmological parameters, its only effect is a minor widening of the posterior distribution of the scalar spectral index. We note also how the clustering and Poissonian terms are very well recovered whereas the TSZ remains unconstrained. As we have shown in the previous chapter, the TSZ term is strongly subdominant on small scales, with respect to the other two contributions, and therefore remains unconstrained. In Fig. 11.2 it is evident the presence of a strong degeneration between the clustering and the Poissonian terms.

In order to investigate the impact of the foreground and secondary anisotropy

residuals on the cosmological parameters, we performed three MCMC analysis with the same simulated data as the previous one (which include all the foreground residual models), but modifying the residual model inside the CAMB+CosmoMC code. We first study the impact of the clustering term hiding it in the data and performing a MCMC exploration with zero clustering term. In Fig. 11.3 we show the results of this MCMC analysis compared with the standard MCMC which considers all the three contributions to the residuals. We note how the absence of the clustering term in the code introduces strong biases on all cosmological parameters. The effect of the absence of the clustering term can be reduced widening the prior on the Poissonian term. As shown in Fig. 11.2, there is a strong degeneration between clustering and Poissonian terms, therefore the absence of the clustering can be compensated by a larger Poissonian contribution. In Fig. 11.4 we show the results of the MCMC analysis, without clustering contribution, but with a prior for the Poissonian term: $A_{PSP} \rightarrow [0, 10]$. We note how the the code strongly overestimates the Poissonian term, this overestimate compensate the absence of the clustering term and allows a better recovery of the cosmological parameters, reducing the biases.

The biases become much bigger when excluding also the Poissonian term from the analysis. In the third analysis we performed, we excluded in the code not only the clustering term but also the Poissonian one. The results are shown in Fig. 11.5. They clearly show how, if we do not consider the point source residual contribution in the data analysis, we may introduce large biases in the cosmological parameters, which would strongly affect the scientific results.

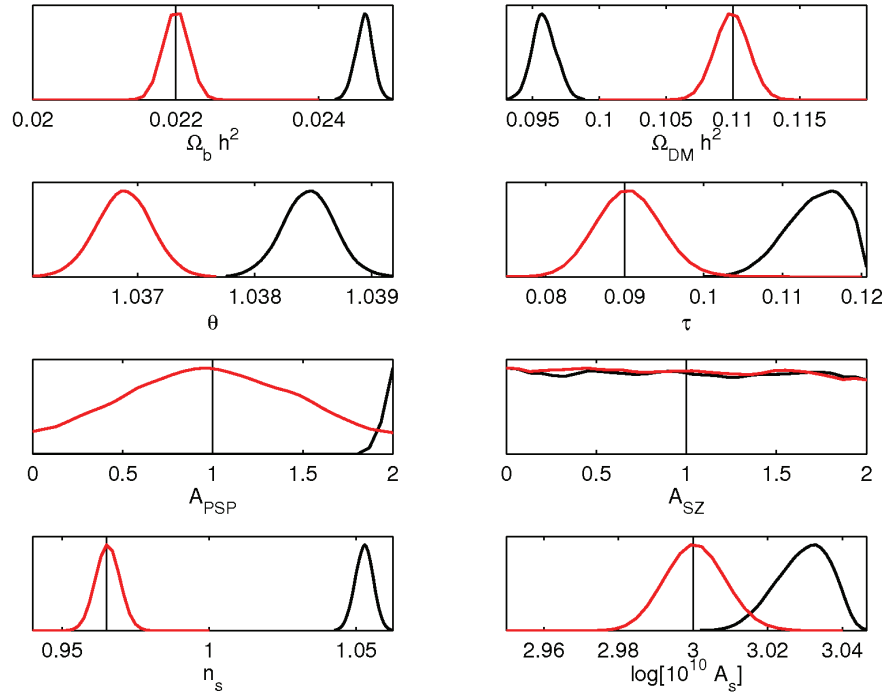


Figure 11.3: Comparison of the results of the MCMCs constrained with *Planck* simulated data with foreground and secondary anisotropy residual marginalization which considers or not the clustering term. Vertical bars are the input parameters. The black curves show the results of the MCMC which does not include the clustering contribution, whereas red curves consider all the three residuals.

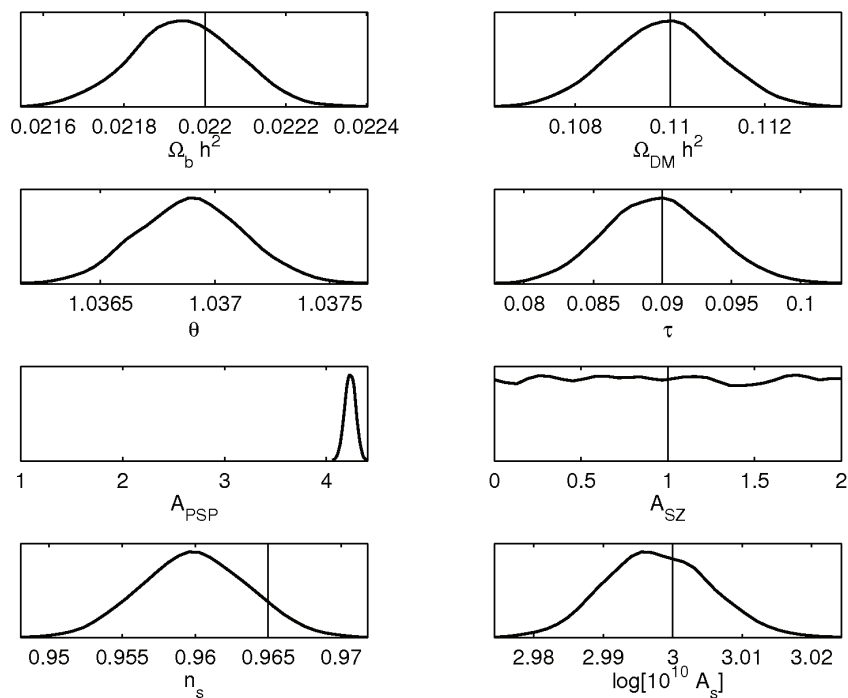


Figure 11.4: Comparison of the results of the MCMCs constrained with the *Planck* simulated data with foreground and secondary anisotropy residual marginalization which do not consider the clustering term. In this plot we show the results we obtained widening the prior of the Poissonian term to $[0 - 10]$. Vertical bars are the input parameters.

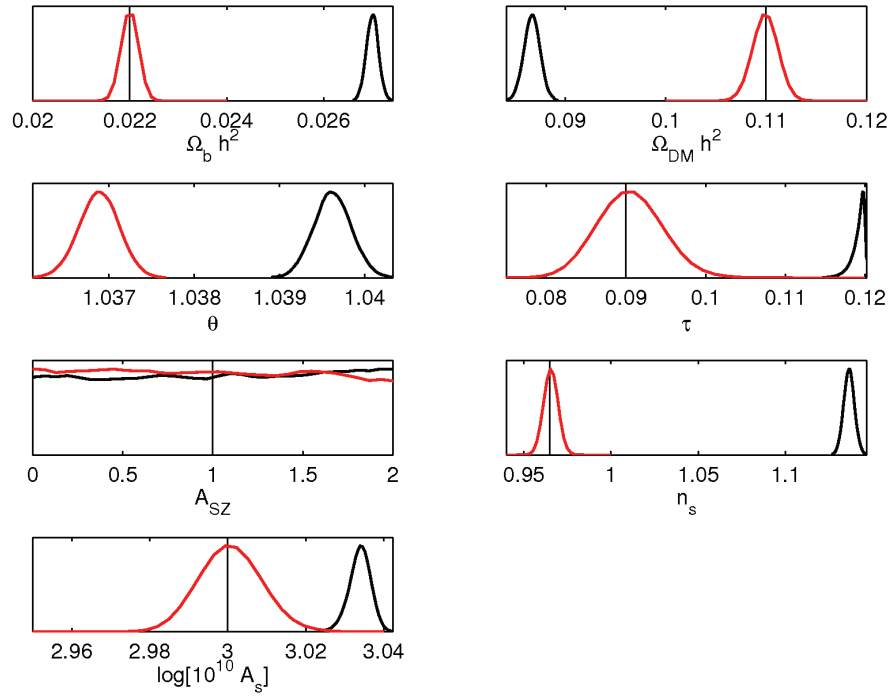


Figure 11.5: Comparison of the results of the MCMCs constrained with *Planck* simulated data with foreground and secondary anisotropy residual marginalization which considers or not the clustering and the Poissonian terms. Vertical bars are the input parameters. The black curves show the results of the MCMC which does not include the clustering and the Poissonian contributions, whereas red curves consider all the three residuals.

11.2 Foreground and secondary anisotropy residual marginalization with extended parameter space

We have shown the importance of small scale foreground and secondary anisotropy residuals for a standard, six parameters, cosmological model. We will now present some results we obtained with our CosmoMC version on three examples of extended parameter space.

The first model we consider is the one which, together with the standard six parameters, varies also the running of the spectral index n_{run} . The simulated data have been generated with zero running $n_{run} = 0$. In Figs. 11.6 and 11.7 we show the bidimensional and triangle plots of the comparison of the results of the MCMC which includes the running of the spectral index with (black curve) and without (red curves) the foreground and secondary anisotropy residual marginalization. We note how the marginalization introduces only minor changes in almost all the parameters but induces a widening of the posterior distributions of the scalar spectral index and the running of the spectral index.

A similar situation happens if we consider a model which includes tensor perturbations. In this case together with the standard six parameters we varied also the tensor to scalar ratio r . We generated the simulated data without the tensor contribution, therefore with $r = 0$. In Figs. 11.8 and 11.9 we show the bidimensional and triangle plots of the comparison of the results of the MCMC which includes the variation of the tensor to scalar ratio with (black curve) and without (red curves) the foreground and secondary anisotropy residual marginalization. We note how again the marginalization introduces only minor changes in almost all the parameters but induces again a noticeable widening of the posterior distributions of the scalar spectral index.

The last example of extended parameter space we present is the combination of the two previous ones. In this case together with the six standard

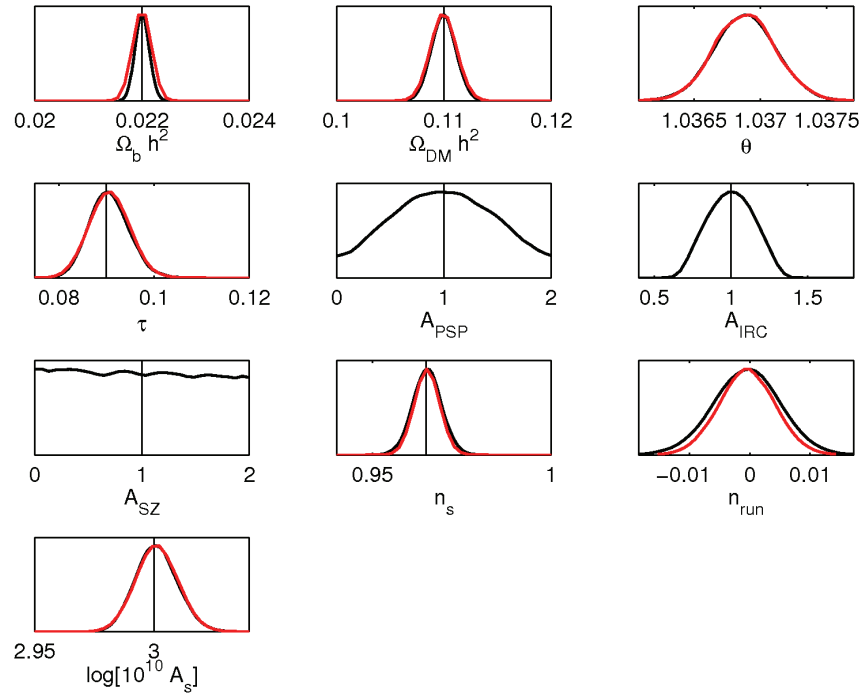


Figure 11.6: Comparison of the results of the MCMCs, including the running of the spectral index, constrained with *Planck* simulated data with (black curves) and without (red curves) foreground and secondary anisotropy residual marginalization. Vertical bars are the input parameters.

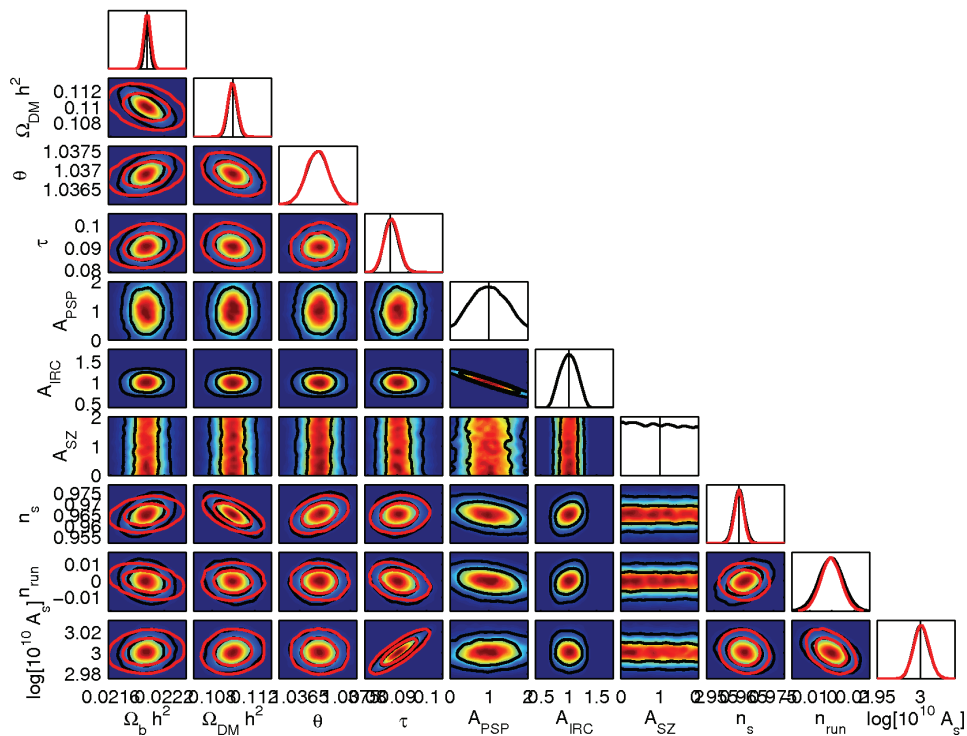


Figure 11.7: Comparison of the results of the MCMCs, including the running of the spectral index, constrained with *Planck* simulated data with (black curves) and without (red curves) foreground and secondary anisotropy residual marginalization. Curves are the 68% and 95% confidence level, vertical bars are the input parameters.

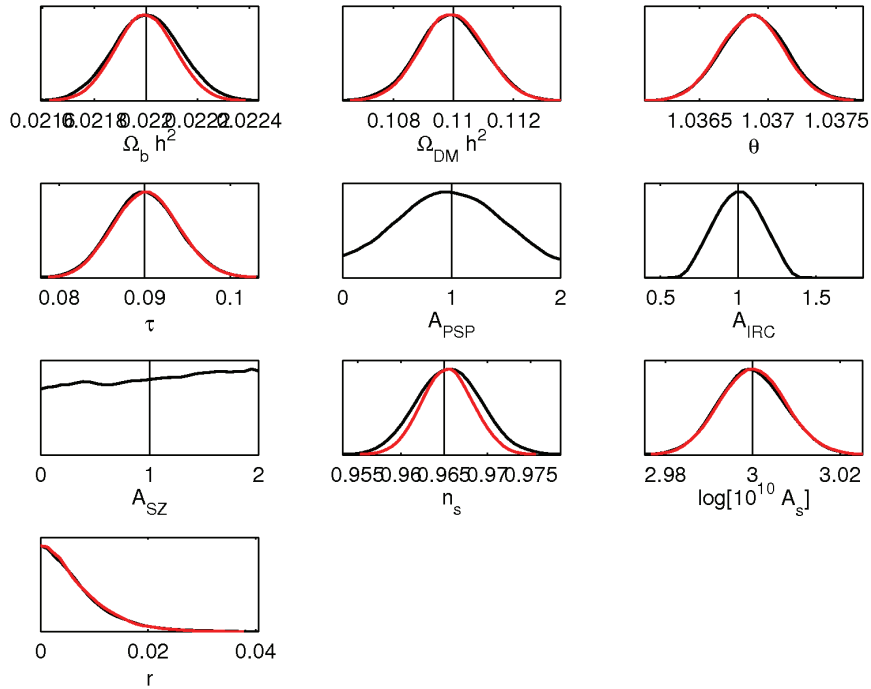


Figure 11.8: Comparison of the results of the MCMCs, including the variation of the tensor to scalar ratio, constrained with *Planck* simulated data with (black curves) and without (red curves) foreground and secondary anisotropy residual marginalization. Vertical bars are the input parameters.

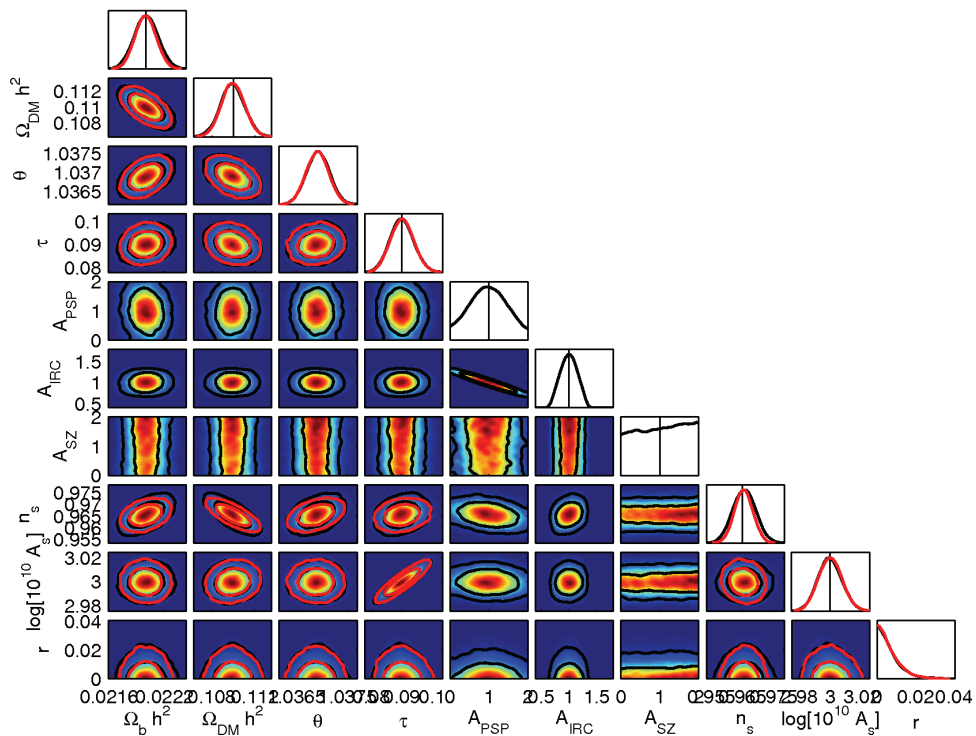


Figure 11.9: Comparison of the results of the MCMCs, including the variation of the tensor to scalar ratio, constrained with *Planck* simulated data with (black curves) and without (red curves) foreground and secondary anisotropy residual marginalization. Curves are the 68% and 95% confidence level, vertical bars are the input parameters.

parameters we varied both the tensor to scalar ratio and the running of the spectral index. Again we have generated the simulated data with both parameters set equal zero. We have considered the inflation consistency condition up to the second order [200]:

$$n_T = -\frac{A_s}{8} \left(2 - \frac{A_s}{8} - n_s \right). \quad (11.1)$$

In Figs. 11.10 and 11.11 we show the bidimensional and triangle plots of the comparison of the results of the MCMC which includes the variation of the tensor to scalar ratio and the running of the spectral index, with (black curve) and without (red curves) the foreground and secondary anisotropy residual marginalization. The marginalization induces again a widening of the posterior distribution of both the running of the spectral index and the scalar spectra index. In Fig. 11.12 we show the bidimensional plot of the scalar spectral index versus the running. We note how the introduction of the marginalization does not induce only a widening of the distribution, but also a degeneration between the two parameters which is not present without it.

11.3 Frequency channel combination

We have shown the results of different tests we performed with our modified version of CosmoMC and in particular we have shown the impact of foreground and secondary anisotropy residuals on the estimate of cosmological parameters. For simplicity we have considered the combination of the four cleanest channels, but for the multifrequency approach one of the crucial point is the determination of which and of how many frequency channels it is better to use in the data analysis. The second crucial point is the frequency channel combination. In particular, we have shown the results obtained using an inverse noise variance weighting scheme, but in the previous chapter we have presented also an alternative method. In this section we will address these two points, for simplicity, since it is subdominant, we excluded the TSZ

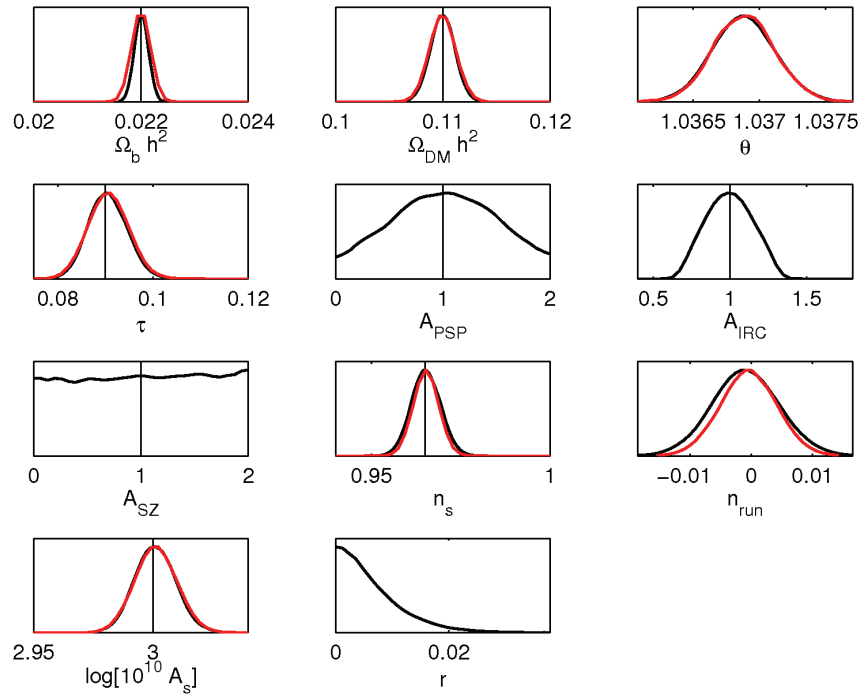


Figure 11.10: Comparison of the results of the MCMCs, including the variation of the tensor to scalar ratio and the running of the spectral index, constrained with *Planck* simulated data with (black curves) and without (red curves) foreground and secondary anisotropy residual marginalization. Vertical bars are the input parameters.

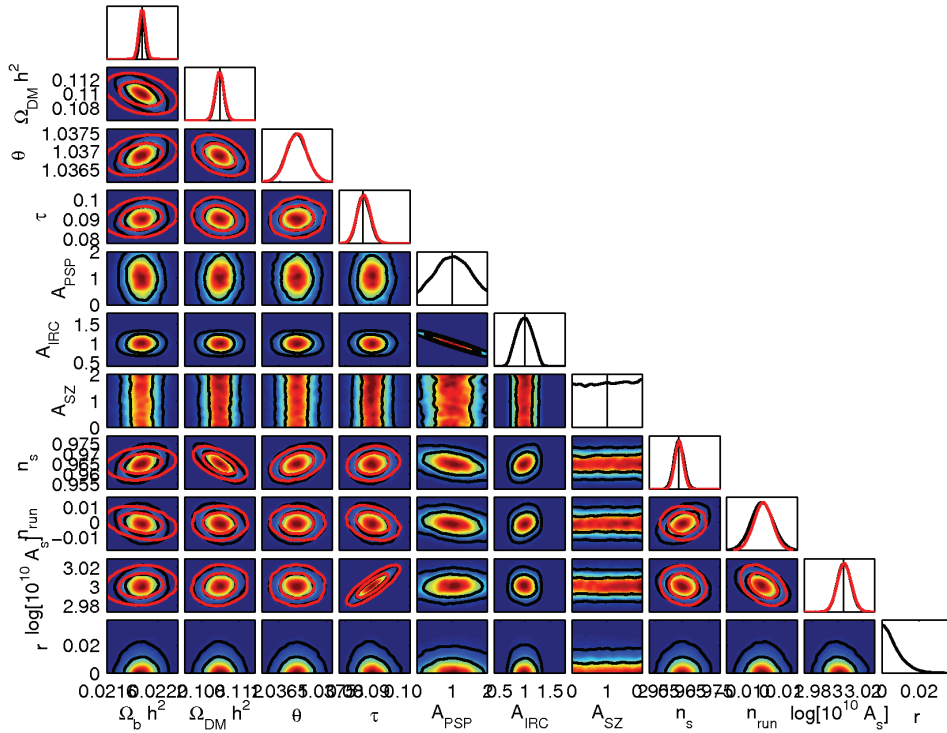


Figure 11.11: Comparison of the results of the MCMCs, including the variation of the tensor to scalar ratio and the running of the spectral index, constrained with *Planck* simulated data with (black curves) and without (red curves) foreground and secondary anisotropy residual marginalization. Curves are the 68% and 95% confidence level, vertical bars are the input parameters.

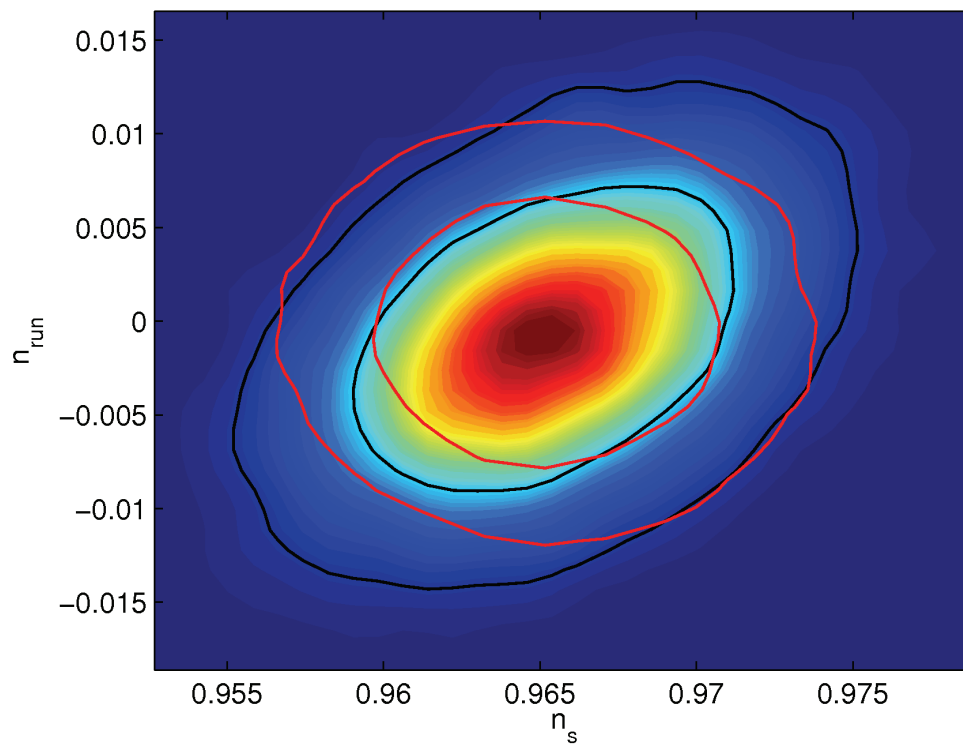


Figure 11.12: Comparison of the results of the MCMCs, including the variation of the tensor to scalar ratio and the running of the spectral index, constrained with *Planck* simulated data with (black curves) and without (red curves) foreground and secondary anisotropy residual marginalization. We show the comparison for the two analysis for the running of the spectral index and the scala spectral index. Curves are the 68% and 95% confidence level.

from the current analysis.

In order to determine which is the best frequency channel combination, we compared the results obtained with the best possible combinations. In particular, we performed four different MCMC analysis, with the foreground and secondary anisotropy residual marginalization, considering four different combinations: the easier, 143 – 217 GHz, which considers the two most sensible channels, as suggested in [196], the central ones, 100 – 217 GHz, and, 70 – 217 GHz, with respectively three and four channels, and the full five channel combination 70 – 353 GHz. In Fig. 11.13 we show the comparison of the results of the four MCMC performed with the inverse noise variance weighting scheme. We note how there is little improvement in the addition of channels with respect to the simple combination of 143 – 217 GHz for all parameters except for the clustering. The clustering term is much more sensitive than the other parameters to the number of frequencies used. In particular we note the great improvement we have with the addition of the 353 GHz channel. This demonstrates the relevance of the multifrequency approach. It uses the fact that the residuals have a different impacts on the different frequencies to better marginalize over them; the 353 GHz is completely dominated by the clustering term and therefore, even if strongly contaminated from the point of view of the CMB, it is the richest source of information on the clustering term and may strongly improve its marginalization.

We repeated the same analysis combining the frequencies with our empirical weighting scheme. In Fig. 11.14 we show the results. Again we note that there is little improvement in the addition of channels for the standard parameters, but with our combination technique we note that not only the clustering term is better constrained with the addition of frequencies but also the Poissonian one improves. Again the introduction of the the 353 GHz improves the marginalization over the foreground and secondary anisotropy residuals, but in this case also the 70 and the 100 GHz channels have an

impact for the Poissonian term. This difference between the two schemes is related to their intrinsic differences. The inverse noise variance weighting considers only instrumental properties to weight the channels and therefore only very sensitive and high resolution channels enter in the analysis, our technique instead considers also the cleanliness of the channels. Therefore channels which are less powerful from the point of view of resolution and sensitivity, like the 70 and the 100 GHz, have a greater weight in our method with respect to the inverse noise variance one because they are less contaminated by foreground and secondary anisotropy residuals. Increasing the weight of more frequencies our technique allows the multifrequency approach to take advantage of the information on the foreground and secondary anisotropy residual signal at these frequencies and therefore to better marginalize.

In Figs. 11.15, 11.16, 11.17, 11.18, we show the comparison of the MCMC analysis results of the four different frequency combinations (respectively 143–217, 100–217, 70–217, 70–353) with the inverse noise variance channel combination and our empirical technique. We note that both techniques have similar results, but in particular our technique improves a little the posterior distributions of the foreground parameters especially for the full five channel combination. With the standard six parameter cosmological model this demonstrates how our empirical weighting scheme can be a valuable alternative to the inverse noise variance one, and the differences between the two methods should be investigated for extended cosmological models.

The extension of the CosmoMC code which considers the foreground and secondary anisotropy residual marginalization that we have developed will be installed in the *Planck* LFI DPC.

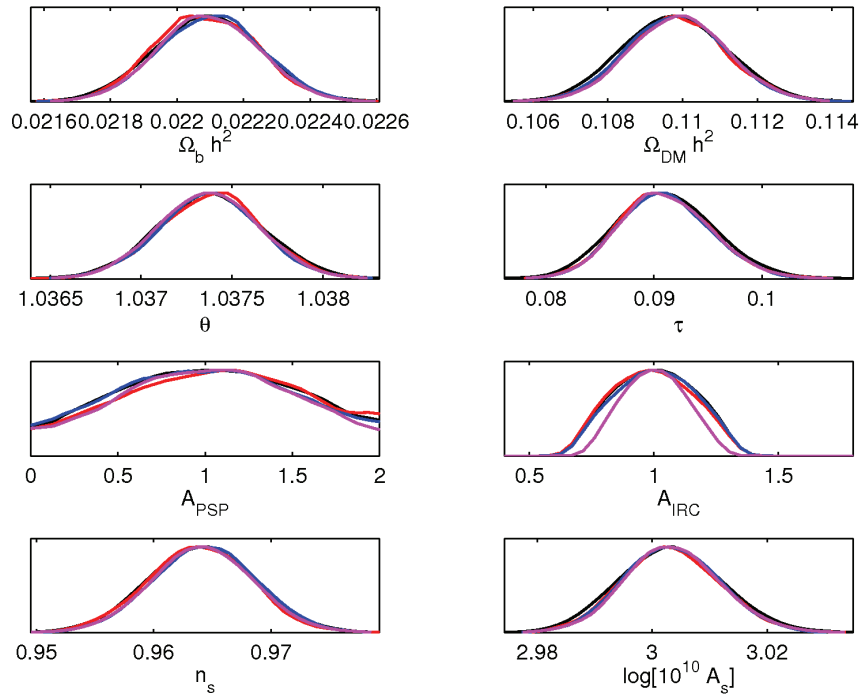


Figure 11.13: Comparison of the results of the MCMCs, with inverse noise variance weighting scheme, constrained with *Planck* simulated data with foreground and secondary anisotropy residual marginalization, for different frequency combinations. Black curve is 143 – 217 GHz, red curve is 100 – 217 GHz, blue curve is 70 – 217 GHz and pink curve is 70 – 353 GHz.

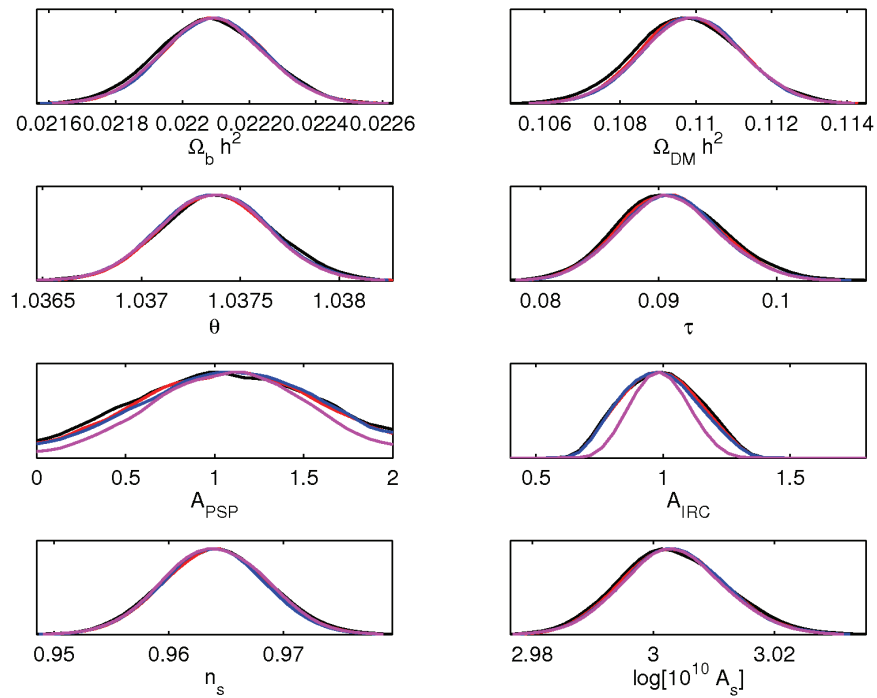


Figure 11.14: Comparison of the results of the MCMCs, with our empirical weighting scheme, constrained with *Planck* simulated data with foreground and secondary anisotropy residual marginalization, for different frequency combinations. Black curve is 143 – 217 GHz, red curve is 100 – 217 GHz, blue curve is 70 – 217 GHz and pink curve is 70 – 353 GHz.

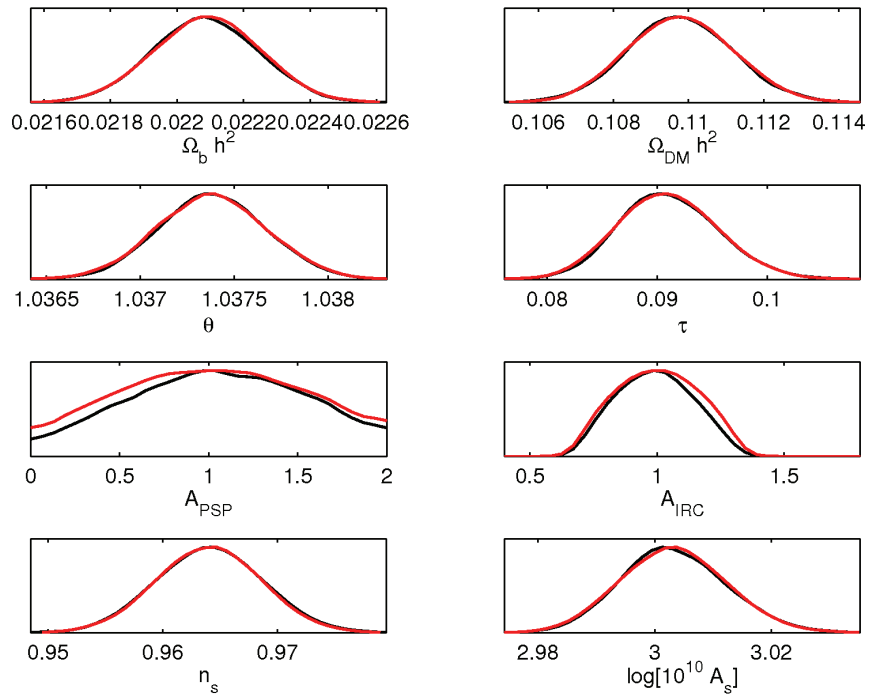


Figure 11.15: Comparison of the results of the MCMCs for the two weighting scheme: inverse noise variance weighting (red) and our empirical scheme (black), for the combination 143 – 217 GHz .

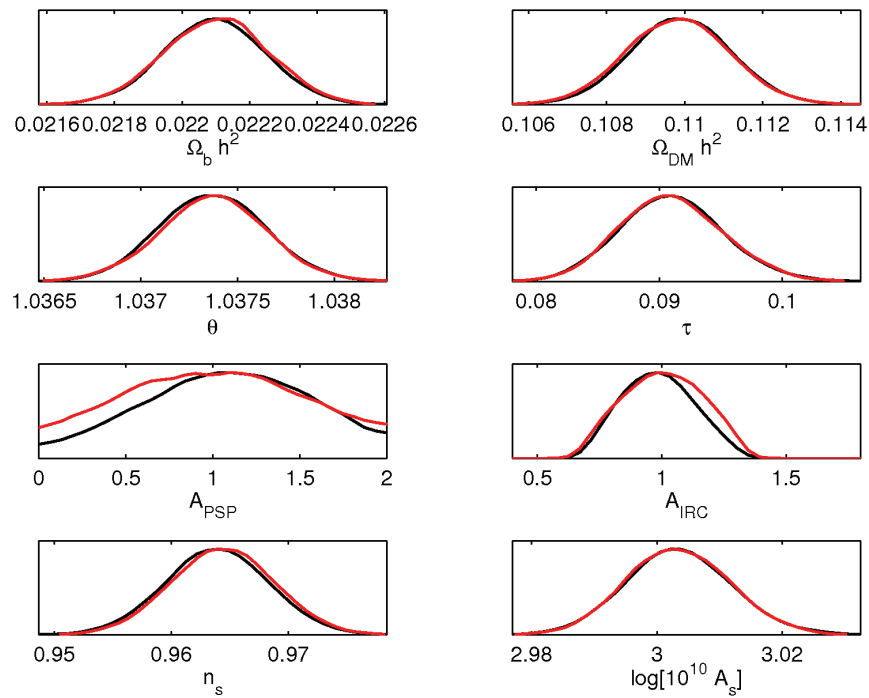


Figure 11.16: Comparison of the results of the MCMCs for the two weighting scheme: inverse noise variance weighting (red) and our empirical scheme (black), for the combination 100 – 217 GHz .

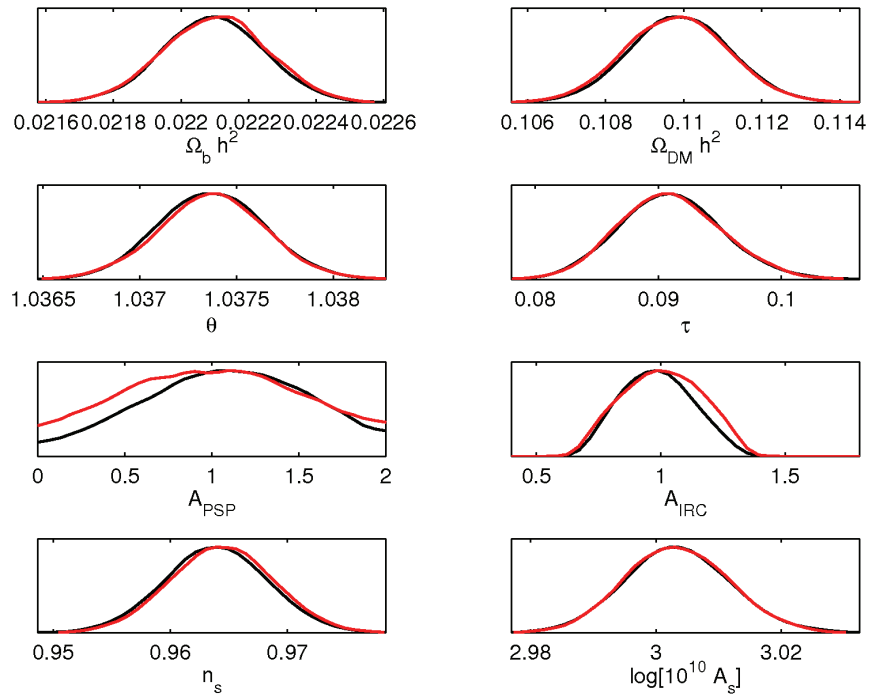


Figure 11.17: Comparison of the results of the MCMCs for the two weighting scheme: inverse noise variance weighting (red) and our empirical scheme (black), for the combination 70 – 217 GHz .

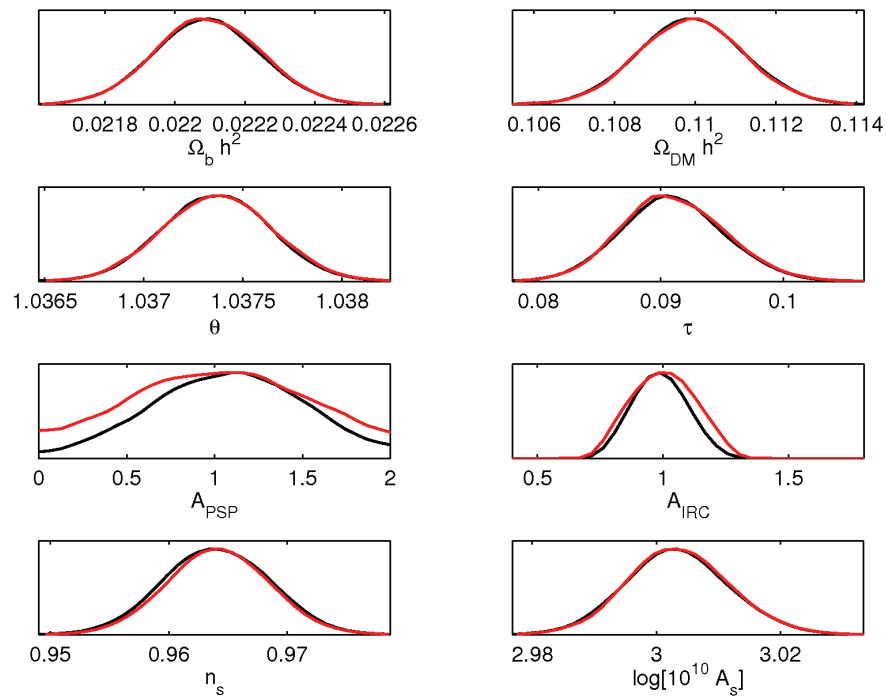


Figure 11.18: Comparison of the results of the MCMCs for the two weighting scheme: inverse noise variance weighting (red) and our empirical scheme (black), for the combination 70 – 353 GHz .

Conclusions

The CMB anisotropies are a fundamental tool to investigate the standard cosmological model and its extensions. In particular we have investigated the impact of a stochastic background of primordial magnetic fields (PMFs) and of foreground and secondary anisotropy residuals on small scales on the CMB anisotropy pattern.

The first part of this thesis was devoted to the characterization and the computation of CMB anisotropies in presence of PMFs, with the goal to constrain the PMF parameters by current CMB anisotropy data. An original result of this thesis is the computation of the exact expressions of the Fourier spectra of the relevant magnetic energy momentum tensor components, with the approximation of a sharp cut off at a comoving damping scale. The energy momentum tensor is quadratic in the fields and this implies that the Fourier transforms of its components are convolutions. In particular the solution of the convolutions is complicated by the presence of the sharp cut off which requires a splitting of both the angular and radial integration domains. We have identified these domains and performed both the radial and angular integrations [83, 75]. The behavior of the resulting spectra for large scales, $k \rightarrow 0$, is a white noise for spectral indices greater than $n_B > -3/2$ whereas for $-3 < n_B < -3/2$ is infrared dominated as k^{2n_B+3} . We have computed also the Fourier spectrum of the cross correlation between Lorentz force and magnetic energy density. The exact expressions of the PMF energy momentum tensor spectra allowed us to have an exact treatment of magnetic perturbations in the MHD limit.

Another original result of this thesis is the computation of the initial conditions for scalar magnetized perturbations both with the approximation of a universe dominated by radiation, with and without matter corrections. The results show that the introduction of matter corrections leads to the appearance of next to leading terms and that it does not modify substantially the results on CMB anisotropies [84].

In order to study the scalar, vector and tensor PMF contributions to the angular power spectrum of CMB anisotropies in temperature and polarization, we have developed an extension of the public Einstein-Boltzmann code CAMB including all the possible magnetic contributions. The results show that the impact of PMFs on CMB anisotropies is larger on small scales where the primary CMB is suppressed by the Silk damping. In particular the dominant contribution is given by vector perturbations on small scales and by the scalar ones on large scales, whereas the tensor contribution always remains subdominant with respect to the other two. The magnetized CMB anisotropies show a strong dependence on the PMF spectral index and in particular there is a strong correlation between the behavior of magnetized anisotropies and the one in the infrared limit of the Fourier spectra of the PMF energy momentum tensor components. PMFs have an impact also on the matter power spectrum, in particular we have shown that (considering only linear physics) PMFs strongly affect the small scales of the matter power spectrum.

In order to constrain PMFs with cosmological data, we have developed an extension of the public Markov Chain Monte Carlo code CosmoMC which includes the magnetic parameters in the parameter space and is connected with our modified version of CAMB. We performed a MCMC analysis with present CMB data: WMAP7 [8], ACBAR [11], QUaD [13] and BICEP [14] and analyzed the forecasts for the upcoming *Planck* satellite data and for the future generation CMB satellite CORE. The constraints on PMF amplitude with present CMB data are $B_\lambda < 5.4$ nG [84] and can be improved of a factor two by *Planck*, $B_\lambda < 2.7$ nG [84], and of a factor of five with the recent

proposal submitted to ESA CORE, $B_\lambda < 0.92$ nG (see the proposal in [44]). Current data strongly disfavour PMFs generated with causal mechanisms ($n_B \geq 2$).

PMFs do not only impact on CMB anisotropy angular power spectrum but also on the CMB bispectrum because of their non-Gaussian modelization. We have investigated the non-Gaussian contribution of magnetized scalar perturbations on large angular scales, and in particular an original result of this thesis is the derivation of the CMB magnetic bispectrum on large scales. The CMB magnetic bispectrum depends on the magnetic energy density bispectrum. We have derived an approximation of the magnetic energy density bispectrum which is valid for every geometrical configuration, and tested its goodness with the exact results we computed for the bispectrum in the colinear configuration. With the estimated expression of the magnetic CMB bispectrum it was possible to derive constraints on PMFs with present non-Gaussianity data of WMAP5: the results show that the bounds coming from non-Gaussianities, $B_\lambda < 7.95$ nG [140], are comparable with the ones coming from CMB spectrum. Tighter constraints from non-Gaussianities are expected on small scales, either from the scalar or the vector sector. A project on small scale non-Gaussianities in the scalar sector is already on-going [148].

Small scale CMB anisotropies are fundamental to constrain cosmological models. But small scale microwave sky contains a puzzle of contributions of which primary CMB is only a piece. It is therefore crucial to properly take into account all the possible foreground and secondary anisotropy contributions to small scale data, in particular now that these have been measured by ACT [16] and SPT [15]. Great part of extragalactic foreground contribution is removed by masking the detected point sources and clusters, but residuals due to unresolved sources remain and may introduce biases in the cosmological parameters. The second main subject of this thesis has been therefore the study of the impact of small scale foreground and secondary anisotropy

residuals on cosmological parameters. We have developed a multifrequency approach with the purpose to have a very good marginalization over foreground residuals in the cosmological parameter extraction with *Planck* data. An original result of this thesis has been the derivation of hybrid theoretical/empirical parametrizations for each foreground and secondary anisotropy residual signal on small scales relevant for *Planck* data [201]: residual point source Poissonian and clustering terms and the thermal Sunyaev Zeldovich effect. In order to reduce the number of parameters necessary to describe the residuals, the parametrizations consider both the theoretical spectral shape and frequency dependence of the signals.

The base of the multifrequency approach is to use different frequency channels to better marginalize over foreground residuals. The *Planck* frequencies considered are: 70, 100, 143, 217 and 353 GHz. We have addressed also the issue of the frequency channel combination. In particular the optimal method, in noise dominated regimes, is the inverse noise variance weighting [196]. One of the original results of this thesis is also the introduction of an alternative empirical combination scheme: the inverse noise plus foreground weighting.

We have developed an extension of the CosmoMC code which includes the marginalization over foreground and secondary anisotropy residuals with the multifrequency approach illustrated. We have investigated the impact of the marginalization on foreground and secondary anisotropy residuals on the cosmological parameters both in the standard six parameter and in extended cosmological models. The results show a widening of the posterior distribution on some of the cosmological parameters. We also observe a strong degeneration between the clustering and the Poissonian terms. We also studied the impact of the residuals on the parameters, in particular the impact of the clustering and the Poissonian terms. The results of the analysis show that the neglect either of only one or of both the terms induces strongly biases the cosmological parameters [201].

With the comparison of the results obtained with different frequency

channel combinations we demonstrated the importance of having a wide frequency coverage in the marginalization over foreground and secondary anisotropy residuals with a multifrequency approach .

We have compared the results obtained with the inverse noise variance weighting and the inverse noise plus foreground weighting technique [201]. The results are comparable for the standard six parameter cosmological models. The project on the investigation of their differences for extended models is on-going.

We plan to install both the extensions of the CosmoMC code, with PMF contributions and with the residual marginalization that have been described in this thesis in the *Planck* LFI DPC.

The two main projects of this thesis, the one on the impact of PMFs on CMB anisotropies and the one on the impact of small scale foreground and secondary anisotropy residuals, can be easily merged. In fact, we have shown that the impact of PMFs on CMB anisotropies is larger on small scales and therefore is with small scale CMB data that will be possible to derive the stronger constraints on PMFs. But we have shown how small scale CMB anisotropy data are strongly affected by foreground and secondary anisotropy residuals and how these can bias the cosmological parameters if not taken properly into account. Present experiments are already measuring very small scale CMB anisotropies, see ACT [16] and SPT [15], and to constrain PMFs with this new data it will be crucial to apply to the cosmological parameter extraction with PMF parameters, the technique of marginalization over the residuals that we have developed. The project to merge the main two topics of this thesis to constrain PMFs parameters with small scale data marginalizing over foreground and secondary anisotropy residuals is already on-going.

Appendix A

A.1 Lorentz force Fourier spectrum

In the following we present the result of the solution of the convolution for the Lorentz force Fourier spectrum, since the complete result is rather complicated and we will show the results only for the infrared part $0 < \tilde{k} < 1$:

$$\begin{aligned}
|L_B(k)|^2 = & \frac{A^2 k_D^{2n_B+3}}{512\pi^4} \left[2((1 - \tilde{k})\tilde{k})^{n_B} \left(\frac{\tilde{k}^3 {}_2F_1 \left[n_B, -n_B, 1 + n_B, \frac{-1+\tilde{k}}{\tilde{k}} \right]}{n_B(4 + n_B)(6 + n_B)(8 + n_B)} \right. \right. \\
& + (-1 + \tilde{k})\tilde{k}^2 \left(\frac{{}_2F_1 \left[1 + n_B, 1 - n_B, 2 + n_B, \frac{-1+\tilde{k}}{\tilde{k}} \right]}{(1 + n_B)(4 + n_B)(6 + n_B)(8 + n_B)} \right. \\
& \left. \left. + \frac{(-1 + n_B){}_2F_1 \left[1 + n_B, -n_B, 2 + n_B, \frac{-1+\tilde{k}}{\tilde{k}} \right]}{(1 + n_B)(4 + n_B)(6 + n_B)(8 + n_B)} \right) \right. \\
& + \frac{(-1 + \tilde{k})^2 \tilde{k} (134 + 69n_B + 12n_B^2 + n_B^3) {}_2F_1 \left[2 + n_B, -n_B, 3 + n_B, \frac{-1+\tilde{k}}{\tilde{k}} \right]}{(2 + n_B)^2 (4 + n_B)(6 + n_B)(8 + n_B)} \\
& - \frac{(-1 + \tilde{k})^3 (-192 - 38n_B + 9n_B^2 + 4n_B^3 + n_B^4) {}_2F_1 \left[3 + n_B, -n_B, 4 + n_B, \frac{-1+\tilde{k}}{\tilde{k}} \right]}{n_B(2 + n_B)(3 + n_B)(4 + n_B)(6 + n_B)(8 + n_B)} \\
& \left. - \frac{8(-1 + \tilde{k})^4 (90 + 55n_B + 15n_B^2 + 2n_B^3) {}_2F_1 \left[4 + n_B, -n_B, 5 + n_B, \frac{-1+\tilde{k}}{\tilde{k}} \right]}{kn_B(4 + n_B)^2 (2 + n_B)(6 + n_B)(8 + n_B)} \right]
\end{aligned}$$

$$\begin{aligned}
& + \frac{4(-1 + \tilde{k})^5(300 + 115n_B + 15n_B^2 + 2n_B^3)_2F_1\left[5 + n_B, -n_B, 6 + n_B, \frac{-1+\tilde{k}}{\tilde{k}}\right]}{k^2 n_B(2 + n_B)(4 + n_B)(5 + n_B)(6 + n_B)(8 + n_B)} \\
& - \frac{144(-1 + \tilde{k})^6(7 + 2n_B)_2F_1\left[6 + n_B, -n_B, 7 + n_B, \frac{-1+\tilde{k}}{\tilde{k}}\right]}{k^3 n_B(6 + n_B)^2(2 + n_B)(4 + n_B)(8 + n_B)} \\
& + \frac{48(-1 + \tilde{k})^7(7 + 2n_B)_2F_1\left[7 + n_B, -n_B, 8 + n_B, \frac{-1+\tilde{k}}{\tilde{k}}\right]}{k^4 n_B(2 + n_B)(4 + n_B)(6 + n_B)(7 + n_B)(8 + n_B)} \Big) \\
& - \frac{1}{(8\tilde{k}^5 n_B(2 + n_B)^2(4 + n_B)^2)} \times \\
& \left(- \frac{16(48(2 + n_B) + \tilde{k}^2(4 + n_B)(8 + n_B)(-4(2 + n_B) + \tilde{k}^2(6 + n_B)(1 + n_B(4 + n_B))))}{(6 + n_B)(8 + n_B)} \right. \\
& + \frac{1}{(6 + n_B)(8 + n_B)} 16(1 - \tilde{k})^{n_B}(48(2 + n_B) - 192\tilde{k}(2 + n_B) + \\
& \tilde{k}^8(2 + n_B)^2(4 + n_B) + \tilde{k}^7 n_B(2 + n_B)^2(4 + n_B) - 12\tilde{k}^3(2 + n_B)(80 + n_B(36 + 5n_B)) \\
& + 4\tilde{k}^2(2 + n_B)(136 + n_B(36 + 5n_B)) + \tilde{k}^6 n_B(4 + n_B)(138 + n_B(73 + n_B(13 + n_B))) \\
& - 2\tilde{k}^5(4 + n_B)(64 + n_B(194 + n_B(87 + n_B(14 + n_B)))) + \\
& \left. \left. \tilde{k}^4(1632 + n_B(2248 + n_B(1002 + n_B(193 + n_B(18 + n_B))))\right) \right) \\
& + \frac{4^{-n_B} \tilde{k}^8 (\tilde{k}^2)^{n_B} (2 + n_B)(4 + n_B)(1 + n_B(4 + n_B)) \sqrt{\pi} \Gamma[2 + n_B]}{\Gamma\left[\frac{5}{2} + n_B\right]} \Big) \Big]. \tag{A.1}
\end{aligned}$$

A.2 Integrals of Bessel functions

In order to evaluate both the magnetic field spectrum and bispectrum at large angular scales, it is necessary to evaluate integrals of Bessels functions:

$$\int_0^y dx x^m j_\ell^2(x) \tag{A.2}$$

with $y \gg 1$. This integral can be expressed generically in terms of hypergeometric functions [47]; however, we can find good approximations, which are much simpler. For $m = 2$, the integral can be performed exactly:

$$\int_0^y dx x^2 j_\ell^2(x) = \frac{\pi}{4} y^2 \left[J_{\ell+\frac{1}{2}}^2(y) - \frac{2}{y} \left(\ell + \frac{1}{2} \right) J_{\ell+\frac{1}{2}}(y) J_{\ell+\frac{3}{2}}(y) + J_{\ell+\frac{3}{2}}^2(y) \right] \simeq \frac{y}{2} \tag{A.3}$$

where since $y \gg \ell$ we used the expansion of the Bessel functions for large arguments.

For $m < 1$, the integral reaches a constant value for $y \gg \ell$, and can therefore be evaluated in the limit $y \rightarrow \infty$. We found:

$$\int_0^y dx x^m j_\ell^2(x) \simeq \frac{1}{4} \left[\frac{\sqrt{\pi} \Gamma(\frac{1-m}{2}) \Gamma(\ell + \frac{m+1}{2})}{\Gamma(1 - \frac{m}{2}) \Gamma(\ell + \frac{3-m}{2})} + y^{m-2} \left(\frac{2y}{m-1} + \sin(\pi\ell - 2y) \right) \right] \xrightarrow{\ell \gg 1} \frac{\sqrt{\pi} \Gamma(\frac{1-m}{2})}{4 \Gamma(1 - \frac{m}{2})} \ell^{m-1}$$

for $m < 1$, $y \gg \ell$. (A.4)

The case $m = 1$ is a bit more involved: the integral (A.2) grows logarithmically with y and cannot be evaluated with the same approximation as before. In this case we set

$$\int_0^y dx x j_\ell^2(x) \simeq \int_\ell^y \frac{dx}{x} \cos^2 \left(x - \frac{\pi}{2} \ell - \frac{\pi}{4} \right) \simeq \frac{1}{2} [\log(y) - \log(\ell)] \quad \text{for } y \gg \ell.$$

(A.5)

We are neglecting the subdominant contribution to the integral of the interval $[0, \ell]$, therefore this approximation is slightly underestimating the true result. However, it captures the correct behaviour in ℓ and y . These approximations are shown in Fig. A.1.

A.3 Bispectrum in colinear configuration

This section is dedicated the description of the technique used to compute the magnetic energy density bispectrum in the colinear configuration Eq.8.30.

Due to the complexity of the calculations we restrict the analytical solutions of the bispectrum to only two representative spectral indices: the case $n_B = 2$ and the case $n_B = -2$. The integral over the momenta in Eq.8.30 is given by the sum of the three basic integrals plus permutations: *

$$I(K) = \int d\tilde{K} \int dx (I_a(K, \tilde{K}) + I_b(K, \tilde{K}) + I_c(K, \tilde{K})), \quad (\text{A.6})$$

*For simplicity of notation in this appendix we use re-scaled variables: $K = k/k_D$, $Q = q/k_D$, $P = p/k_D$ and $\tilde{K} = \tilde{k}/k_D$

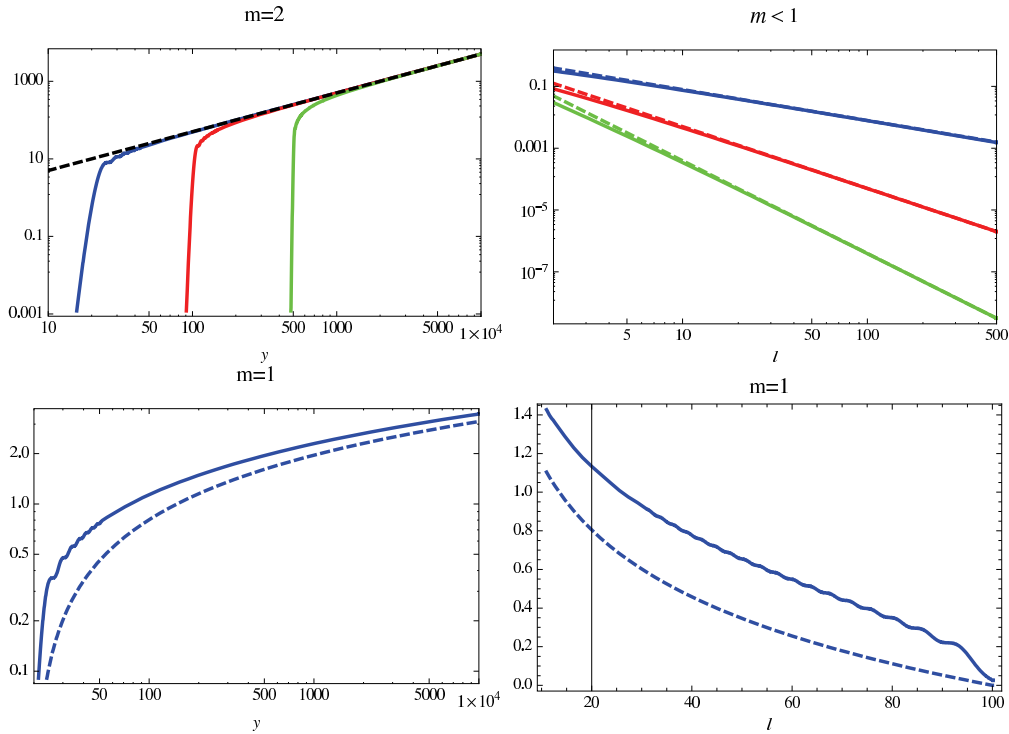


Figure A.1: The approximations for the integral in Eq.A.2. Upper left plot, for $m = 2$: the integral (solid) and the approximation $y/2$ (dashed) are shown for $\ell = 20$, $\ell = 100$, $\ell = 500$ as a function of y . Upper right plot, for $m < 1$: the approximations for $y \gg \ell$ (solid) and for $\ell \gg 1$ (dashed) given in Eq.A.4 are shown as a function of ℓ for $m = 0$, $m = -1$ and $m = -2$. Lower plots, for $m = 1$: the integral (solid) and the approximation in Eq.A.5 (dashed) are shown as a function of y for $\ell = 20$ (left plot) and as a function of ℓ for $y = 100$ (right plot).

where $x = \hat{K} \cdot \tilde{K}$. The functions $I_a(K, \tilde{K}), I_b(K, \tilde{K}), I_c(K, \tilde{K})$ are:

$$\begin{aligned}
I_a(K, \tilde{K}) &= \tilde{K}^{2+n} \left(\frac{K^2}{4} + \tilde{K}^2 + K\tilde{K}x \right)^{\frac{n}{2}} (K^2 + \tilde{K}^2 + 2K\tilde{K}x)^{-1+\frac{n}{2}} \\
&\quad \left(\frac{8\tilde{K}^4 + 24K\tilde{K}^3x + K^4(1+x^2) + 3K^3\tilde{K}x(3+x^2) + K^2\tilde{K}^2(7+19x^2)}{K^2 + 4\tilde{K}^2 + 4K\tilde{K}x} \right) \\
I_b(K, \tilde{K}) &= \tilde{K}^{2+n} \left(\frac{K^2}{4} + \tilde{K}^2 + K\tilde{K}x \right)^{n/2} \left(\tilde{K}^2 + \frac{1}{4}K(K - 4\tilde{K}x) \right)^{n/2} \\
&\quad \left(\frac{(32\tilde{K}^4 + 4K^2\tilde{K}^2(1-5x^2) + K^4(1+x^2))}{((K^2 + 4\tilde{K}^2)^2 - 16K^2\tilde{K}^2x^2)} \right) \\
I_c(K, \tilde{K}) &= \tilde{K}^{2+n} (K^2 + \tilde{K}^2 - 2K\tilde{K}x)^{-1+\frac{n}{2}} \left(\tilde{K}^2 + \frac{1}{4}K(K - 4\tilde{K}x) \right)^{n/2} \\
&\quad \left(\frac{(8\tilde{K}^4 - 24K\tilde{K}^3x + K^4(1+x^2) - 3K^3\tilde{K}x(3+x^2) + K^2\tilde{K}^2(7+19x^2))}{(K^2 + 4\tilde{K}^2 - 4K\tilde{K}x)} \right).
\end{aligned} \tag{A.7}$$

We note that due to the symmetry $\tilde{K} \rightarrow -\tilde{K}$ we have $I_a(K) = I_c(K)$ therefore only $I_a(K, \tilde{K})$ and $I_b(K, \tilde{K})$ need to be evaluated.

A.3.1 Integration Domains

The sharp cut-off of the PMF spectrum at the damping scale k_D imposes some conditions on the angle $\hat{K} \cdot \tilde{K}$. To satisfy these conditions is necessary to split the integration domain. The conditions are different for I_a and I_b , therefore for simplicity in the following we consider the two integrations separately.

A.3.2 Domains of I_a

The sharp cut off imposes:

$$\begin{aligned}
&\tilde{K} < 1 \\
&\left(\frac{K^2}{4} + \tilde{K}^2 + K\tilde{K}x \right) < 1 \\
&(K^2 + \tilde{K}^2 + 2K\tilde{K}x) < 1
\end{aligned}$$

This leads to the following integration scheme:

$$\begin{aligned}
& 1) \quad 0 < K < 1 \\
& \quad \int_0^{1-K} d\tilde{K} \int_{-1}^1 dx I_a(\tilde{K}, K) + \int_{1-K}^1 d\tilde{K} \int_{-1}^{\frac{1-K^2-\tilde{K}^2}{2K\tilde{K}}} dx I_a(\tilde{K}, K) \\
& 2) \quad 1 < K < 2 \\
& \quad \int_{K-1}^1 d\tilde{K} \int_{-1}^{\frac{1-K^2-\tilde{K}^2}{2K\tilde{K}}} dx I_a(\tilde{K}, K) \tag{A.8}
\end{aligned}$$

A.3.3 Domains of I_b

The sharp cut off imposes:

$$\begin{aligned}
& \tilde{K} < 1 \\
& \left(\frac{K^2}{4} + \tilde{K}^2 + K\tilde{K}x\right) < 1 \\
& \left(\frac{K^2}{4} + \tilde{K}^2 - K\tilde{K}x\right) < 1
\end{aligned}$$

This leads to the following integration scheme for $0 < K < 2$:

$$\int_0^{\frac{2-K}{2}} d\tilde{K} \int_{-1}^1 dx I_b(\tilde{K}, K) + \int_{\frac{2-K}{2}}^{\frac{\sqrt{4-K^2}}{2}} d\tilde{K} \int_{\frac{-1+K^2/4+\tilde{K}^2}{K\tilde{K}}}^{\frac{1-K^2/4-\tilde{K}^2}{K\tilde{K}}} dx I_b(\tilde{K}, K) \tag{A.9}$$

in the interval $\frac{\sqrt{4-K^2}}{2} < \tilde{K} < 1$ the integral collapses to zero.

A.3.4 $n=2$

We begin with the case $n = 2$ which is the easiest from the point of view of the calculations. The angular integrand functions simply reduce to:

$$\begin{aligned}
I_a(K, \tilde{K}, x) &= \frac{1}{4} \tilde{K}^4 (8\tilde{K}^4 + 24K\tilde{K}^3x + K^4(1+x^2) + 3K^3\tilde{K}x(3+x^2) + K^2\tilde{K}^2(7+19x^2)) \\
I_b(K, \tilde{K}, x) &= \frac{1}{16} \tilde{K}^4 (32\tilde{K}^4 + 4K^2\tilde{K}^2(1-5x^2) + K^4(1+x^2)) \tag{A.10}
\end{aligned}$$

Once performed the angular integrations, the radial integrations are trivial and the result is:

$$I(K)|_{n=2} = \left(\frac{4}{3} - 3K + \frac{20K^2}{7} - \frac{23K^3}{16} + \frac{2K^4}{5} - \frac{K^5}{16} + \frac{K^7}{256} - \frac{17K^9}{53760} \right) \tag{A.11}$$

In Fig. 8.2 we have shown the result for $n = 2$.

A.3.5 $n=-2$

We will now consider the case $n = -2$. The functions I_a and I_b reduce to:

$$\begin{aligned}
 I_a(K, \tilde{K}, x) &= \frac{4(8\tilde{K}^4 + 24K\tilde{K}^3x + K^4(1+x^2) + 3K^3\tilde{K}x(3+x^2) + K^2\tilde{K}^2(7+19x^2))}{(K^2 + \tilde{K}^2 + 2K\tilde{K}x)^2(K^2 + 4\tilde{K}^2 + 4K\tilde{K}x)^2} \\
 I_b(K, \tilde{K}, x) &= \frac{16(32\tilde{K}^4 + 4K^2\tilde{K}^2(1-5x^2) + K^4(1+x^2))}{((K^2 + 4\tilde{K}^2)^2 - 16K^2\tilde{K}^2x^2)^2} \tag{A.12}
 \end{aligned}$$

We note how these functions are far more complicated than the ones for the $n = 2$ case. Once performed the angular integrations in both the integrals we have the appearance of terms like $|K - 2\tilde{K}|$ and $|K - \tilde{K}|$, in order to solve the modula is necessary to split also the radial integration domain into several sub-domains.

The impact on CMB anisotropies of PMF is dominated by the infrared part of the spectrum, therefore we we restricted our computation to the $K < 1/2$ region of the spectrum. The analytical result for $n = -2$ has a very long and complicated form, therefore, for the sake of simplicity, we show only the infrared limit:

$$\begin{aligned}
 I_a(K) &\sim \frac{24.674}{K^3} \\
 I_b(K) &\sim \frac{24.674}{K^3} \\
 I(K) &\sim \frac{73.8367}{K^3}
 \end{aligned}$$

Fig. 8.2 shows the exact result.

Bibliography

- [1] D.J. Fixsen, E.S. Cheng, J.M. Gales, J.C. Mather, R.A. Shafer, E.L. Wright, *Astrophys. J.* 473:576, (1996)
- [2] C. Bennett, A. Kogut, G. Hinshaw, A. Banday, E. Wright, K. Gorski, D. Wilkinson, R. Weiss, G. Smoot, S. Meyer, J. Mather, P. Lubin, K. Loewenstein, C. Lineweaver, P. Keegstra, E. Kaita, P. Jackson, E. Cheng, *Astrophys. J.* 436:423-442, (1994)
- [3] C. L. Bennett, A. Banday, K. M. Gorski, G. Hinshaw, P. Jackson, P. Keegstra, A. Kogut, G. F. Smoot, D. T. Wilkinson, E. L. Wright, *Astrophys. J.* 464:L1-L4, (1996)
- [4] P. de Bernardis, P.A.R. Ade, J.J. Bock, J.R. Bond, J. Borrill et al., arXiv:astro-ph/0011468v1, (2000)
- [5] W. C. Jones, P. Ade, J. Bock, J. Bond, J. Borrill et al., *Astrophys. J.* 647:823-832, (2006)
- [6] [Planck Collaboration], “Planck: The scientific programme”, arXiv:astro-ph/0604069, (2006)
- [7] E. Komatsu *et al.* [WMAP Collaboration], arXiv:0803.0547, (2008)
- [8] E. Komatsu, K. M. Smith, J. Dunkley, C. L. Bennett, B. Gold, G. Hinshaw, N. Jarosik, D. Larson, M. R. Nolta, L. Page, D. N. Spergel, M. Halpern, R. S. Hill, A. Kogut, M. Limon, S. S. Meyer, N. Odegard, G.

- S. Tucker, J. L. Weiland, E. Wollack, E. L. Wright, arXiv:1001.4538v3, (2010)
- [9] D. Larson, J. Dunkley, G. Hinshaw, E. Komatsu, M. R. Nolta, C. L. Bennett, B. Gold, M. Halpern, R. S. Hill, N. Jarosik, A. Kogut, M. Limon, S. S. Meyer, N. Odegard, L. Page, K. M. Smith, D. N. Spergel, G. S. Tucker, J. L. Weiland, E. Wollack, E. L. Wright, arXiv:1001.4635v2, (2010)
- [10] N. Jarosik, C. L. Bennett, J. Dunkley, B. Gold, M. R. Greason, M. Halpern, R. S. Hill, G. Hinshaw, A. Kogut, E. Komatsu, D. Larson, M. Limon, S. S. Meyer, M. R. Nolta, N. Odegard, L. Page, K. M. Smith, D. N. Spergel, G. S. Tucker, J. L. Weiland, E. Wollack, E. L. Wright, arXiv:1001.4744v1, (2010)
- [11] C. L. Reichardt, P. A. R. Ade, J. J. Bock, J. R. Bond, J. A. Brevik, C. R. Contaldi, M. D. Daub, J. T. Dempsey, J. H. Goldstein, W. L. Holzapfel, C. L. Kuo, A. E. Lange, M. Lueker, M. Newcomb, J. B. Peterson, J. Ruhl, M. C. Runyan, Z. Staniszewski, *Astrophys. J.* 694:1200-1219, (2009)
- [12] C.R.Contaldi, J.R.Bond, D.Pogosyan, B.S.Mason, S.T.Myers, T.J.Pearson, U.L.Pen, S.Prunet, A.C.Readhead, M.I.Ruetalo, J.L.Sievers, J.W.Wadsley, P.J.Zhang, arXiv:astro-ph/0210303v1, (2002)
- [13] [QUaD Collaboration], *Astrophys. J.* 700:L187-L191, (2009)
- [14] H. C. C. Hiang, P.A.R.Ade, D.Barkats, J.O.Battle, E.M.Bierman et al., *Astrophys. J.* 711:1123-1140, (2010)
- [15] M. Lueker, C. L. Reichardt, K. K. Schaffer, O. Zahn et al., arXiv:0912.4317v1, (2009)
- [16] S. Das, T A. Marriage, P A. R. Ade, P. Aguirre, M. Amir et al, arXiv:1009.0847v1

-
- [17] V. M. Slipher, *Popular Astronomy* 23: 21–24, (1915)
- [18] Planck Collaboration, arXiv:1101.2041v1, arXiv:1101.2021, arXiv:1101.2022, arXiv:1101.2023, arXiv:1101.2024, arXiv:1101.2025, arXiv:1101.2026, arXiv:1101.2027, arXiv:1101.2028, arXiv:1101.2029, arXiv:1101.2031, arXiv:1101.2032, arXiv:1101.2034, arXiv:1101.2035, arXiv:1101.2036, arXiv:1101.2037, arXiv:1101.2038, arXiv:1101.2039, arXiv:1101.2040, arXiv:1101.2041, arXiv:1101.2043, arXiv:1101.2044, arXiv:1101.2045, arXiv:1101.2046, arXiv:1101.2047, arXiv:1101.2048, (2011)
- [19] E. Hubble, *Proc. Natl. Acad. Sci. USA* 15 168, (1929)
- [20] G. Lemaitre, *MNRAS* 91: 483, (1931)
- [21] R. A. Alpher, G. Gamow, *Physical Review* 73: 803, (1947) ; R. A. Alpher, *Nature* 162, (1948)
- [22] S. H. Suyu, P. J. Marshall, M. W. Auger, S. Hilbert, R. D. Blandford, L. V. E. Koopmans, C. D. Fassnacht and T. Treu, *Astrophys. J.* 711:201, (2010)
- [23] A. Riess et al., *Astronomical Journal*, 116, 1009, (1998)
- [24] S. Perlmutter et al., *Astrophysical Journal*, 517, 565, (1999)
- [25] S. Weinberg, *Rev. Mod. Phys.* 61, 1, (1989)
- [26] R. R. Caldwell and M. Kamionkowski, *Ann. Rev. Nucl. Part. Sci.* 59:397-429, (2009)
- [27] S. Tsujikawa, Arxiv:1101.0191
- [28] Ya B. Zel'dovich, *Sov. Phys. JETP* 21 656, (1965)
- [29] A. H. Guth, *Phys. Rev. D* 23, 347 (1981)
- [30] A. A. Starobinski, *Physics Letters B*91 99, (1980)

-
- [31] D. Langlois, ArXiv:1001.5259, (2010)
- [32] A. A. Starobinski, Physics Letters B117, 175, (1982)
- [33] S. Guth and S- Y. Pi, Phys. Rev. Letters 49, 1110, (1982); Phys. Rev. D 32, 1899, (1985)
- [34] J. M. Bardeen, P.J. Steinard and M. S. Turner, Phys. Rev. D 28, 679, (1983)
- [35] M. Bruni, S. Matarrese, S. Mollerach and S. Sonego, Class. Quant. Grav. 14 2585, (1997)
- [36] A. M. Bardeen, Phys. Rev. D 22, 1882, (1980)
- [37] M. Bucher, K. Moodley and N. Turok, Phys. Rev. D 62 083508, (2000)
- [38] S. Dodelson, *Modern Cosmology*, Academic Press, (2003)
- [39] “*Pre-launch status of the Planck mission*”, Astronomy and Astrophysics Vol.520, (2010)
- [40] A. A. Penzias and R. W. Wilson, Astrophys. Journal Letters 142: 419, (1965); Astrophys. Journal Letters 1149: 1154, (1965)
- [41] http://lambda.gsfc.nasa.gov/toolbox/tb_cmbfast_ov.cfm
- [42] <http://www.thphys.uni-heidelberg.de/~robbers/cmbeasy/>
- [43] <http://cosmologist.info/CAMB>
- [44] <http://www.core-mission.org/>
- [45] N. Christensen and R. Meyer, arXiv:astro-ph/0006401v1, (2000)
- [46] K. Subramanian, arXiv:astro-ph/0601570, (2006)
- [47] M. Abramowitz and I. Stegun, *Handbook of mathematical functions with formulas, graphs, and mathematical table*, New York: Dover Publishing, (1965).

-
- [48] J. L. Han and R. Wielebinski, *Chin. J. Astron. Astrophys.* 2:293-324, 2002
- [49] L.M. Widrow, *Rev. Mod. Phys.* 74 775, (2002)
- [50] M.L. Bernet, F.Miniati, S.J.Lilly, P.P.Kronberg and M.Dessauges-Zavadsky, *Nature* 454 302,(2008)
- [51] A.M.Wolfe, R.A.Jorgenson, T.Robishaw, C.Heiles and J.X.Prochaska, *Nature* 455 638, (2008)
- [52] Y. Xu, P. P. Kronberg, S. Habib and Q. W. Dufton, *Astrophys. J.* 637:19-26, (2006)
- [53] A.C. Davis, M. Lilley and O. Tornkvist, *Phys. Rev. D* 60:021301, (1999)
- [54] J.P. Vallee, *New Astronomy Reviews* 48, 763-841, (2004)
- [55] P. Blasi, S. Burles and A. V. Olinto, *Astrophys. J.* 514 L79-L82, (1999)
- [56] A. Neronov and I. Vovk, *Science* Vol. 328 no. 5974 pp. 73-75, (2010)
- [57] K.Dolag, M.Kachelriess, S.Ostapchenko and R.Tomas, *Astrophys. J. Lett.* 727, L4 (2011)
- [58] T. Vachaspati, *Phys. Lett. B*, 265,258 (1991)
- [59] R. Gopal and S. Sethi, *MNRAS* 363:521-528, (2005)
- [60] S. Matarrese , S. Mollerach , A. Notari and A. Riotto, *Phys. Rev. D* 71 043502, (2005)
- [61] M. Giovannini, UNIL-IPT-01-16, (2001)
- [62] F.Finelli and A. Gruppuso, *Phys.Lett. B*502 216-222, (2001)
- [63] M. S. Turner and L. M. Widrow, *Phys. Rev. D* 37, 2743, (1988)
- [64] A. Lewis and S. Bridle, *Phys. Rev. D* 66, 103511 (2002)

-
- [65] A. Lewis, A. Challinor and A. Lasenby, *Astrophys. J.* 538, 473 (2000).
- [66] C. P. Ma and E. Bertschinger, *Astrophys. J.* 455, 7 (1995)
- [67] A. Lewis, CAMB Notes, <http://cosmologist.info> (2008)
- [68] L. E. Knox, *Phys. Rev. D* 52, 4307-4318, (1995)
- [69] D. Grasso and H. R. Rubinstein, *Phys. Rept.* 348, 163, (2001)
- [70] A. Mack, T. Kahniashvili and A. Kosowsky, *Phys. Rev. D* 65, 123004, (2002)
- [71] A. Lewis, *Phys. Rev. D* 70, 043011, (2000)
- [72] R. Durrer, P. G. Ferreira and T. Kahniashvili, *Phys. Rev. D* 61, 043001, (2000)
- [73] S. Koh, & C. H. Lee, *Phys. Rev. D* 62, 083509, (2000)
- [74] J.A. Adams, U. H. Danielsson, D. Grasso and H. Rubinstein, *Phys. Lett. B* 388, 253, (1996)
- [75] D. Paoletti, F. Finelli and F. Paci, *MNRAS* 396, 523, (2009)
- [76] C. Bonvin and C. Caprini, *JCAP* 1005:022, (2010)
- [77] K. Subramanian and J. D. Barrow, *MNRAS* 335, L57, (2002)
- [78] K. Subramanian and J. D. Barrow, *Phys. Rev. D* 58, 083502 (1998)
- [79] K. Kojima and K. Ichiki, [arXiv:0902.1367v2](https://arxiv.org/abs/0902.1367v2) (2009)
- [80] R. Shaw and A. Lewis, *Phys. Rev. D* 81, 043517 (2010)
- [81] R. Shaw and A. Lewis, [arXiv:1006.4242](https://arxiv.org/abs/1006.4242) (2010)
- [82] A. Lewis, *Phys. Rev. D* 70, 043518, (2004)
- [83] Finelli, F., F. Paci and D. Paoletti, *Phys. Rev. D* 78, 023510, (2008).

-
- [84] D. Paoletti and F. Finelli, arXiv:1005.0148v1, (2010)
- [85] T. Kahniashvili and B. Ratra, Phys. Rev. D 75, 023002 (2007).
- [86] M. Giovannini, Phys. Rev. D 70, 123507, (2004)
- [87] M. Giovannini, Class Quant. Grav. 23:R1, (2006)
- [88] M. Giovannini, Phys. Rev. D 73, 101302, (2006)
- [89] M. Giovannini, Class. Quant. Grav. 23 4991-5026, (2006)
- [90] M. Giovannini, Phys. Rev. D 74, 063002, (2006)
- [91] M. Giovannini, PMCPPhys. A1:5,(2007)
- [92] M. Giovannini and K. E. Kunze, Phys. Rev. D 77, 061301,(2008)
- [93] M. Giovannini and K. E. Kunze, Phys. Rev. D 77, 063003,(2008)
- [94] M. Giovannini and K. E. Kunze, Phys. Rev. D 77, 123001,(2008)
- [95] M. Giovannini and K. E. Kunze, arXiv:0804.2238v1 ,(2008)
- [96] M. Giovannini, Phys. Rev. D 79, 121302, (2009)
- [97] M. Giovannini, Phys. Rev. D 79, 103007, (2009)
- [98] S. Weinberg, Phys. Rev. D 69, 023503, (2004)
- [99] T. Kahniashvili, A. G. Tevzadze, S. K. Sethi, K. Pandey and B. Ratra, Phys. Rev. D 82, 083005, (2010)
- [100] D. G. Yamazaki, K. Ichiki and T. Kajino, Astrophys. J. 625 L1, (2005)
- [101] D. G. Yamazaki, K. Ichiki, T. Kajino and G. J. Mathews, Astrophys. J. 646:719-729, (2006)
- [102] D. G. Yamazaki, K. Ichiki, T. Kajino and G. J. Mathews, Phys. Rev. D 77, 043005, (2008)

-
- [103] D. G. Yamazaki, K. Ichiki, T. Kajino and G. J. Mathews, Phys. Rev. D 81, 023008 (2010)
- [104] D. G. Yamazaki, K. Ichiki, T. Kajino and G. J. Mathews, Phys. Rev. D 81, 103519, (2010)
- [105] K. Kojima, K. Ichiki, D. G. Yamazaki, T. Kajino and G. J. Mathews, Phys. Rev. D 78, 045010, (2008)
- [106] S. K. Sethi and K. Subramanian, MNRAS 356:778-788, (2005)
- [107] S. K. Sethi, B.B. Nath and K. Subramanian, arXiv:0804.3473v1, (2008)
- [108] S. K. Sethi and K. Subramanian, arXiv:0911.0244v1, (2009)
- [109] J.D. Barrow, P. Ferreira and J. Silk, Phys. Rev. Lett. 78, 3610 (1997)
- [110] T. Kahniashvili, G. Lavrelashvili and B. Ratra, Phys. Rev. D 78, 063012 (2008)
- [111] G. Chen, P. Mukherjee, T. Kahniashvili, B. Ratra and Y. Wang, Astrophys. J. 611, 655 (2004)
- [112] P.D. Naselsky, L.Y. Chiang, P. Olesen and O.V. Verkhodhanov, Astrophys. J. 615, 45 (2004)
- [113] Y. Kim and P.D. Naselsky, JCAP07 041 (2009)
- [114] R. Durrer, T. Kahniashvili and A. Yates, Phys. Rev. D 58, 123004 (1998)
- [115] J.R. Kristiansen and P. Ferreira, Phys. Rev. D 77, 123004 (2008)
- [116] C. Caprini and R. Durrer, JCAP 0311 010, (2003)
- [117] R. Durrer, New Astron. Rev. 51:275-280, (2007)
- [118] K. Subramanian, T. R. Seshadri and J. D. Barrow, MNRAS 344 L31, (2003)

- [119] W. K. Hastings, *Biometrika* 57(1), 97 (1970)
- [120] A. Gelman and D. B. Rubin, *Statistical Science* 7, 457 (1992)
- [121] M Tegmark, D Eisenstein, M Strauss, D Weinberg et al., *Phys. Rev. D* 74, 123507, (2006)
- [122] V. Acquaviva, N. Bartolo, S. Matarrese and A. Riotto, *Nucl. Phys. B* 667, 119, (2003); J. Maldacena, *JHEP* 0305, 013, (2003)
- [123] N. Bartolo, S. Matarrese and A. Riotto, *Phys. Rev. D* 65, 103505, (2002); F. Bernardeau and J. P. Uzan, *Phys. Rev. D* 66, 103506, (2002); F. Vernizzi and D. Wands, *JCAP* 0605, 019 (2006).
- [124] D. H. Lyth, C. Ungarelli and D. Wands, *Phys. Rev. D* 67 023503, (2003)
- [125] N. Bartolo, S. Matarrese and A. Riotto, *Phys. Rev. D* 69, 043503, (2004)
- [126] D. H. Lyth, *JCAP* 0511 006, (2005); M. P. Salem, *Phys. Rev. D* 72, 123516, (2005); D. H. Lyth and A. Riotto, *Phys. Rev. Lett.* 97 121301, 2006
- [127] M. Bastero-Gil, V. Di Clemente and S. F. King, *Phys. Rev. D* 70, 023501, (2004); E. W. Kolb, A. Riotto and A. Vallinotto, *Phys. Rev. D* 71, 043513, (2005); E. W. Kolb, A. Riotto and A. Vallinotto, *Phys. Rev. D* 73, 023522, (2006).
- [128] T. Hamazaki and H. Kodama, *Prog. Theor. Phys.* 96 1123, (1996)
- [129] G. Dvali, A. Gruzinov and M. Zaldarriaga, *Phys. Rev. D* 69, 023505, (2004); L. Kofman, arXiv:astro-ph/0303614
- [130] G. Dvali, A. Gruzinov and M. Zaldarriaga, *Phys. Rev. D* 69, 083505, (2004)
- [131] M. Alishahiha, E. Silverstein and D. Tong, *Phys. Rev. D* 70, 123505, (2004)

-
- [132] N. Arkani-Hamed, P. Creminelli, S. Mukohyama and M. Zaldarriaga, JCAP 0404, 001, (2004)
- [133] D. Babich, P. Creminelli and M. Zaldarriaga, JCAP 0408, 009, (2004)
- [134] W. Hu and M. J. White, Phys. Rev. D 56, 596, (1997)
- [135] C. Caprini, R. Durrer and T. Kahniashvili, Phys. Rev. D 69, 063006, (2004)
- [136] E. Komatsu and D. N. Spergel, Phys. Rev. D 63, 063002, (2001)
- [137] L. M. Wang and M. Kamionkowski, Phys. Rev. D 61, 063504, (2000)
- [138] J. R. Fergusson and E. P. S. Shellard, Phys. Rev. D 76, 083523, (2007)
- [139] I.S. Gradshteyn and I.M. Ryzhik, Table of Integrals, Series, and Products, Academic Press, New York and London (1965).
- [140] C. Caprini, F. Finelli, D. Paoletti and A. Riotto, JCAP 0906:021 (2009).
- [141] I. Brown and R. Crittenden, Phys. Rev. D 72, 063002 (2005).
- [142] T. R. Seshadri and K. Subramanian, Phys. Rev. Lett. 103, 081303 (2009).
- [143] D. Babich and M. Zaldarriaga, Phys. Rev. D 70, 083005 (2004)
- [144] W. Hu, Phys. Rev. D 62, 043007 (2000)
- [145] R-G. Cai, B. Hu and H-B. Zhang, JCAP 08 025,(2010)
- [146] U. Seljak and M. Zaldarriaga, Astrophys. J. 469:437-444, (1996)
- [147] U. Seljak and M. Zaldarriaga, Phys. Rev. D55, 1830-1840, (1997)
- [148] C. Caprini, F. Finelli, D. Paoletti and A. Riotto, In preparation (2011).

-
- [149] L. Campanelli, A.D. Dolgov, M. Giannotti and F.L. Villante, *Astrophys. J.* 616 1-7, (2004)
- [150] T. Kahniashvili, Y. Maravin and A. Kosowsky, *Phys. Rev. D* 80, 023009, (2009)
- [151] A.Kosowsky, T.Kahniashvili, G.Lavrelashvili and B.Ratra, *Phys. Rev. D* 71, 043006, (2005)
- [152] M. Giovannini and K. E. Kunze, *Phys. Rev. D* 78, 023010, (2008)
- [153] A. Loeb and A. Kosowsky, *Astrophys. J.* 469 1-6, (1996)
- [154] H. Tashiro and N. Sugiyama, arXiv:0908.0113v3, (2009)
- [155] S. K. Sethi and K. Subramanian, arXiv:0911.0244v1, (2009)
- [156] D.R.G. Schleicher, R. Banerjee and R.S. Klessen, arXiv:0808.1461v2, (2008)
- [157] H. Tashiro and N. Sugiyama, *MNRAS* 372:1060-1068, (2006)
- [158] E. Komatsu and U. Seljak, *MNRAS* 336 1256 (2002)
- [159] P. Vielva, E. Martinez-Gonzalez, J. E. Gallegos, L. Toffolatti and J. L. Sanz, *MNRAS* 344 89, (2003)
- [160] L. Toffolatti, F. Argueso Gomez, G. De Zotti, P. Mazzei, A. Franceschini, L. Danese and C. Burigana, *MNRAS* 297 117-127, (1998)
- [161] L. Toffolatti, M. Negrello, J. Gonzalez-Nuevo, G. De Zotti, L. Silva, G.L. Granato and F. Argueso, *Astron. Astrophys.* 438 475, (2005)
- [162] G. De Zotti, R. Ricci, D. Mesa, L. Silva, P. Mazzotta, L. Toffolatti and J. Gonzalez-Nuevo, arXiv:astro-ph/0410709v1 (2005)
- [163] G. De Zotti, C. Burigana, M. Negrello, S. Tinti, R. Ricci, L. Silva, J. Gonzalez-Nuevo and L. Toffolatti, arXiv:astro-ph/0411182v1 (2005)

-
- [164] L. Danese, A. Franceschini, L. Toffolatti and G. de Zotti, *Astrophys. J. Lett.* 318, L15, (1987)
- [165] M. Tegmark and G. Efstathiou, *MNRAS*, 281, 1297-1314, (1996)
- [166] P. Serra, A. Cooray, A. Amblard, L. Pagano and A. Melchiorri, *Phys. Rev. D* 78, 043004, (2008)
- [167] H. Dole, G. Lagache and J.-L. Puget, "The Spitzer Space Telescope: New Views of the Cosmos", conference proceeding, (2004)
- [168] G. Lagache, H. Dole and J.-L. Puget, *MNRAS* 338:555, (2003)
- [169] N. Fernandez-Conde, G. Lagache, J.-L. Puget and H. Dole, *arXiv:0801.4299v1*, (2008)
- [170] N. Fernandez-Conde, G. Lagache, J.-L. Puget and H. Dole, *arXiv:1004.0123v1*, (2010)
- [171] L. Knox, A. Cooray, D. Eisenstein and Z. Haiman, *Astrophys. J.* 550 7-20, (2001)
- [172] N. Aghanim, S. Majumdar and J. Silk, *Rept. Prog. Phys.* 71:066902, (2008)
- [173] R. K. Sachs and A. M. Wolfe, *Astrophys. J.* 147 73, (1967)
- [174] M.J. Rees and D. W. Sciama, *Nature* 511,611, 1968
- [175] A. Challinor and A. Lewis, *Phys. Rev. D* 71, 103010 (2005)
- [176] J.P. Ostriker and E. T. Vishniac, *Astrophys. J.* 306 L51, (1986)
- [177] R.A. Sunyaev and Ya.B. Zeldovich, *Astrophysics and Space Science* 7: 3, (1970) *Annual review of astronomy and astrophysics* 18: 537,(1980)
- [178] R.A. Sunyaev and Ya.B. Zeldovich, *Comment Astrop. and Space Phys.* 4 173, (1972)

- [179] A. A. Fraisse, J.-A. C. Brown, G. Dobler, J. L. Dotson, B. T. Draine, P. C. Frisch, M. Haverkorn, C. M. Hirata, R. Jansson, A. Lazarian, A. M. Magalhães, A. Waelkens, M. Wolleben, arXiv:0811.3920v1 ,(2008)
- [180] D. Hooper et al., Phys. Rev. D 76, 083012, (2007)
- [181] M. M. Forbes and A. R. Zhitnitsky, Phys. Rev. D 78, 083505, (2008)
- [182] L. La Porta, C. Burigana, W. Reich, P. Reich, A&A, 479, 641, (2008)
- [183] A. Bonaldi, S. Ricciardi., S. Leach et al., MNRAS, 382, 1791, (2006)
- [184] A. Leger and J. L. Puget, A&A, 137, L5 , (1984)
- [185] B.T. Draine and A. Lazarian, ApJ, 494, L19, (1998)
- [186] T. Kelsall et al., Bulletin of the American Astron. Soc., 27, 1336, (1995)
- [187] M. Maris, C. Burigana, S. Fogliani, arXiv:astro-ph/0603048v2, (2006)
- [188] D.E. Backman et al., ApJ, 450, L35, (1995)
- [189] A. Moro-Martin and R. Malhotra, arXiv:astro-ph/0207350v1
- [190] J.M. Diego, M. Cruz, J. Gonzalez-Nuevo, M. Maris, Y. Ascasibar and C. Burigana, MNRAS, 402, 1213, (2010)
- [191] M. Maris, C. Burigana, A. Gruppuso, F. Finelli and J.M. Diego, arXiv:1010.0830, (2010)
- [192] C. L.Bennett C.L. et al., arXiv:1001.4758, (2010)
- [193] W.H. Press, P. Schechter, Astrophysical Journal, Vol. 187, pp. 425-438, (1974)
- [194] R. K. Sheth and G. Tormen, MNRAS 308:119, (1999)
- [195] B. M. Schaefer, C. Pfrommer, M. Bartelmann, V. Springel and L. Hernquist, MNRAS 370:1309-1323, (2006)

- [196] G. Efstathiou and S. Gratton, unpublished, (2009)
- [197] M. Millea et al., in preparation, (2011)
- [198] N. Taburet, N. Aghanim, M. Douspis and M. Langer, MNRAS 392:1153-1158, (2008)
- [199] N. Taburet, N. Aghanim and M. Douspis, arXiv:0908.1653v1, (2009)
- [200] F. Finelli, J. Hamann, S. M. Leach and J. Lesgourgues, JCAP 1004:011, (2010)
- [201] D. Paoletti, N. aghanim, M. Douspis and F. Finelli, in preparation, (2011)

*Dedicated to Gloria,
who taught me that even in the worst situation you can always smile and
hope for the better, your memory will always be one of the dearest things to
me,*

*and to my Xena
my little ball of fur, without your paws on the keyboard and you tail in my
face work will never be the same.*

Acknowledgements

Unfortunately the length of acknowledgements is proportional to the length of the thesis, i.e. the list would be neverending. I will try to do my best to not forget anyone.

First I would like to thank all my supervisors.

A great thanks goes to Reno, or as I'm used to call him the "big boss", for having always believed in me, giving me responsibilities that I never thought I would be able to handle, but I did it, and this helped me more than I would have ever thought. I want to thank him for guiding me in the scientific world. A great thanks goes to Fabio, the person who followed my life in scientific research from the beginning. In four years of work together he never killed me (even if I think sometimes he really wanted to) and this sets a record! I want to thank him for guiding me and helping me in growing as a scientist and as a person. Our collaboration is the demonstration of the theory that to make good science are necessary a very clever person and a completely mad one, where I am the latter.

I wish to thank Carlo for being always a very careful supervisor, without him this thesis would be full of mistakes, but more than that for being a very good friend. With his jokes, which are so funny or sometimes so terrible, lunches and aperitifs are always amusing moments even in the most stressing periods.

Last but not least I wish to thank the francophone side of my supervisor world, Nabila, the busiest woman on Earth but who always found a moment

for my mad ideas and questions. I want to thank her for the support, scientific, logistic and moral, when I was in Paris (remember that you still own me a day in Paris with the snow!).

I want to thank all the people who collaborated to this work. First I wish to thank Chiara Caprini who gave a great contribution to the non-gaussianity part. I wish to thank her also for the advices and the help she gave me during these three years and especially during my parisian period. I wish to thank Antonio Riotto for his contribution to the non-Gaussianity studies and Francesco Paci for his contribution to the study of tensor magnetic perturbations. I want to thank also Marian Douspis and Guilaine Lagache for the support and the contribution to the project on foreground and secondary anisotropy residuals and Gianfranco De Zotti for the very useful discussions on point sources.

I wish to thank prof. Fiorentini for allowing me to participate to the IDAPP project and Paola Fabbri and Alessandra Tonazzo for the technical support in dealing with IDAPP bureaucratic procedures.

A great thanks goes to my institute mates. I want to thank Vale, Marghe, Fernanda, Frank, Ele, Ale and Tiziana who have been great office mates, especially after 6 pm when brains started to give up and the “world” started to fly around the room. I wish to thank Pietro who as been the mate of all the *Planck* meetings organized in Bologna, I think that our sketch with the ladder and the access point will remain a unique piece of comedy in scientific meeting history! I want to thank him for the practical and moral support. I wish to thank Alessandro whose zen attitude to life can always make the most boring, horrible, annoying thing looking not that bad. A great thanks goes to Matteo, our institute saint, for the moral support during these years. I want to thank also Adriano for the informatic support with the evil cluster, and apologize for all the times I treated to rip off his head when the cluster didn't worked. A very special thanks goes to Enrico, a very good friend,

always there for a coffee and a chat (or an anti-stress “bang your head on the wall” session). I wish to thank him also for the technical support, without him my laptop would be dead since long time ago.

I wish to thank also my other institute mates at the IAS in Paris. Thanks to Fabio and Sara for the funny chats in italian, after days of idiotic hand-speaking, thanks to my less than zero french, speaking like a humang being again was heaven. Thanks to Marian, Nicolas, Matthiew, Julien, Guilaine and all the others of the cosmo-group, when I arrived in Paris I was ready to a French-Italian war, instead everyone was always very kind and nice even if I forced everybody to speak in english, and I know it can be very annoying (I still own you a “pot de depart” and I promise I will do it someday).

The greatest thanks of all goes to my family. To my parents who have always supported me and helped me when I needed, all this would not have been possible without their support, I would never say enough thanks. I want to thank Claudia and Giank, my sister and my brother in law, for all the support and the help they gave me, without them I probably would have been freezing to death waiting for the bus at the station on the way home. A big thanks goes to Angela or the “sheep-eater”, who ever thought that going in that city of fog and mosquitos of Ferrara I would have found one of the best friends of my life! I want to thank her for the support, for the patience in reading my mad e-mails and for her mad replies that made me laugh even in the most overstressing moments! (Remember be always careful with the cheesy-goat, that considering your current city becomes the cheesy-beer drunk-goat!) Thanks to Monica for convincing me that sometimes you have to take a day off and enjoy a visit, well considering our pace maybe it is better to say a marathon, of the beautiful cities of this country (even if my legs will never forget the 485 steps, done five times, in Corniglia!).

Thanks to my Ferrara friends especially Mimma, Luca, Elena, Valentina

and Carlo, our closing time tours of pubs and bars where the perfect end of long working days.

Thanks to to Debora, Michela, Sara, Orazio, Alberto, Orchidea and all the others of the “Italian physicist invasion” friends, for making me feel at home in Paris with our invasions of the Maison the Provence de France kitchen!

A special thanks goes to Placebo, uncle David, NIN, The Beatles, Tori Amos, Muse, The Killers, PJ Harvey, Radiohead, Queen, The Ark, Fine Frenzy, The Cure, Joy division, Venus in Furs & co., Kerli, Depeche, The Verve and all the others that I don't have space to mention, their music is the soundtrack of my life and without it this work would have not been possible.

*...crawling on the planet's face, tiny insects called the human race, lost in
time, and lost in space...
and in meaning.*

Narrator, The Rocky Horror Show